POLITECNICO
MILANO 1863

SCUOLA DI INGEGNERIA INDUSTRIALE
E DELL'INFORMAZIONE

A Bioinspired Approach to the Locomotion of Robots

Degree of Doctor of Philosophy in Mechanical Engineering - Ingegneria Meccanica

Doctoral dissertation of **Giovanni Bianchi**

Supervisor: prof. Simone Cinquemani
Tutor: prof. Gaetano Cascini
Chair of the Doctoral Program: prof. Andrea Bernasconi
Academic Year: 2021-2022

Abstract

The objective of this thesis is the development of innovative methods to address the challenges of underwater locomotion. The majority of autonomous underwater vehicles (AUVs) are propelled by thrusters, characterized by low energy efficiency and high noise pollution, whereas many fishes are efficient and agile swimmers that outperform AUVs. Therefore, this research is imprinted to the creation of new knowledge about aquatic propulsion by adopting a bioinspired approach. Nature displays a wide variety of swimming strategies, and this thesis is focused on the locomotion of the cownose ray since it is featured by the best combination of efficiency and maneuverability among fishes. In order to understand the underlying principles of its swimming strategy, a CFD model of cownose ray swimming has been developed. This model solves the coupled equations of fluid dynamics and forward swimming dynamics of the fish using an overset mesh. This analysis confirmed the results present in literature about the swimming performances of the cownose ray and the vortex structures in the flow. In addition, it relates the swimming performances with the kinematic parameters of the fin movement, and a novel way to calculate the energy efficiency of fish swimming is proposed. Then, a biomimetic robot inspired by the cownose ray was designed and realized to provide an innovative example of underwater locomotion. Experimental tests on the fins of a prototype of the robot have shown that the locomotion principle of this fish is a valid source of inspiration for underwater vehicles but also highlighted some limitations of the first version of the robot. Nevertheless, they have been overcome in a new version in which the fins and the electronic circuit have been completely redesigned. The dynamics of the robot have been simulated, and a control algorithm for forward swimming and maneuvers has been proposed.

Keywords: Bioinspired robotics, Swimming locomotion, Fin propulsion, CFD analysis, Mechanical design

Contents

Introduction

Bioinspiration is an engineering approach that involves studying and modeling nature to emulate biological strategies in solving scientific and industrial problems [6, 7]. Live beings, after billions of years of evolution, have developed effective solutions to nature's challenges to adapt to continuously changing and hostile environments. Thus, nature has been a source of inspiration for developing new solutions for thousands of years [6, 36]. Behind these solutions, some common principles can be identified: all live beings use easily retrievable energy sources; they take advantage of cooperation and use recyclable and readily available materials. These principles are valid in all the scale levels, from the nanoscale of bacteria and cellular processes to the macroscale of whales. Therefore, the field of application of bioinspiration is exceptionally vast. It ranges from efficient management of resources, smart cooperation between systems, self-repairing and lightweight materials, perception of the surrounding environment to manipulation and locomotion [7].

Objective of the thesis

The objective of this thesis is to understand how to put into practice the bioinspiration method and to learn how to transpose a biological solution into an engineering application. The context in which this work is developed is underwater locomotion, and the outcome is the realization of a biomimetic swimming robot inspired by the cownose ray.

The propulsion of underwater vehicles usually relies on thrusters, which have a poor energy efficiency and produce high amount of noise. Moreover, thrusters can generate a force only in one direction; thus, several thrusters are required to make underwater vehicles agile and maneuverable [12]. Therefore, it is interesting to investigate alternative methods to achieve propulsion, using different approaches and creating innovation in this field. For this research, the observation of nature is particularly helpful as many species of fishes and cetaceans are efficient and agile swimmers. Hence, the objective of this PhD thesis is to put into practice a bioinspired approach to create new knowledge about locomotion

mechanisms in the water. This is carried out through the development of innovative models to describe and understand the locomotion strategies of such biological systems so that they can be adapted to a technological solution able to provide an example of innovative underwater propulsion.

Furthermore, the design approach used for this project can be extended to any engineering problem taking inspiration from any other living being. A scheme of the adopted design process is presented in Figure 1.
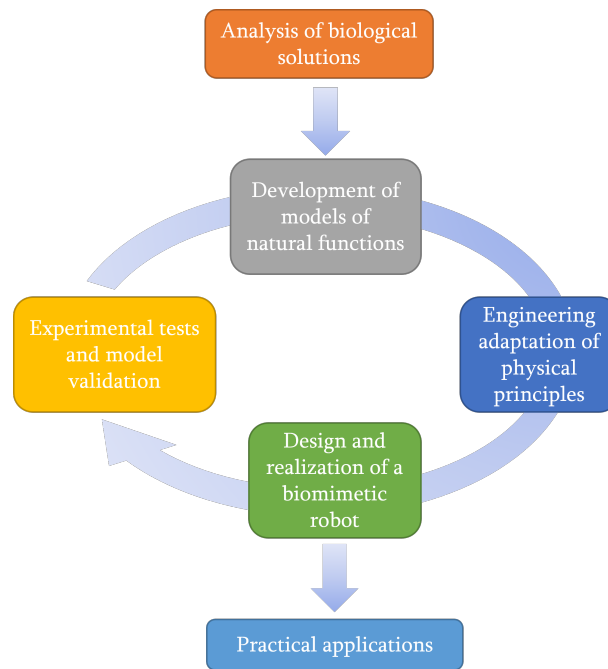
Figure 1: Scheme of the approach adopted during the thesis work

The first step is an analysis of nature's solutions to the challenge of underwater locomotion, finding out the features of each locomotion strategy and their advantages and drawbacks, in order to choose one swimming mode that is possible to emulate and adapt to practical applications. Then, analytic and numerical models are developed to understand the functions necessary to replicate in a biomimetic robot. Afterward, the robot is designed and realized, and, finally, experimental tests are performed. The target of these tests is not only to verify that the robot is functioning but also to assess the validity of the model and our comprehension of the physical principles behind the locomotion strategy.

After identifying the swimming mode of the cownose ray as one of the most promising in terms of maneuverability and efficiency, a kinematic model of the motion of the fins

is developed. Then, a CFD study of fish swimming is carried out to understand the mechanisms underlying thrust generation and the influence of kinematic parameters on swimming performances. Based on the results of numerical simulations, a prototype of the robot and an artificial fin replicating the most important features of the cownose ray motion are designed and built. Some experimental tests on this fin are carried out to assess the validity of the CFD model and to verify the advantages of the cownose ray swimming strategy. Finally, an enhanced version of the biomimetic robot inspired by the cownose ray is realized, and some experimental tests of the robot swimming in the water are performed to evaluate the ability of the robot to exploit the same physical principle as the cownose ray for thrust generation and to assess its swimming performances. The autonomous swimming robot's possible applications developed in this thesis are seabed exploration, environmental monitoring, and underwater search & rescue.

Terminology

Nature has always been a source of inspiration for humans. However, in recent years, bioinspiration has emerged as a widespread approach to engineering, and the systematical knowledge transfer between biology and engineering has taken place. Since there are many fields of study involving the connection between biology and engineering, it is helpful to define some terms with slightly different meaning nuances [36].

- **Bioinspiration**: "the creative approach based on the observation of biological systems", the process of finding a solution to practical problems emulating principles found in nature, which leads to the development of devices meant to operate on the same principles as actual organisms [36, 41, 114];

- **Biomimicry**: "philosophy and interdisciplinary design approach taking nature as a model for sustainable development" [36];

- **Biomimetics**: the study of biological structures or functions to synthesize products that emulate their natural counterpart [36, 41, 114];

- **Bionics**: discipline with the objective of replicating or replacing biological structures or functions with mechanical or electronic equivalents [114].

From an engineering perspective, bioinspiration is a handy tool to find innovative solutions, whereas, at first glance, biomimetics might seem of little utility since the artificial products mimicking plants or animals do not generally have an immediate application. This is far from the truth, especially in robotics, in which there has been a rapid increase in the interest in biomimetic robots. The main reason is that the

principles behind the locomotion of animals are incredibly complex, and they are based on the interaction of several parts with a specific geometry and mechanical properties. Biomimetic robots have the function of validating models of physical and biological processes. A biomimetic robot can address many problems, which would be unfeasible to do relying only on live organisms, whose behavior is challenging to control. For example, it is nearly impossible to make a fish swim in a flow tank in a particular way orienting its fins as desired in a specific instant, but this can be achieved with a biomimetic robot [41].

Methodological approach

Over 3.8 billion years, evolution has led to the survival of the species which present the most successful solutions to nature's challenges, which are constantly improved through natural selection, so that they have reached an outstanding level of optimality [8]. However, while designing a bioinspired system, it is crucial to have clear that natural organisms are optimal for surviving. However, they are not necessarily optimal for their technical performance in a specific function because being part of a living organism introduces several constraints [7]. First of all, the organs of live beings are generally multifunctional, so it could be misleading to think that every characteristic is fundamental for the function of interest. For example, crickets are expertise in jumping, but their legs also host their hearing organs, and they have evolved to comply with this requirement which would not be necessary for a biomimetic robot.

Furthermore, some basic concepts of evolutionary biology must be considered to understand in which sense natural evolution has led to optimal solutions. Live beings have adapted to many evolutionary constraints, and some organs can be part of different life-history contexts. For example, the flexibility of the wings of some insects is the result of the development of the wings during the pupal state when they are stored in a small space. Thus, flexibility is more a requirement than a solution to increase aerodynamic efficiency. The reasons for their excellent flying performances should be searched in other features, such as the corrugation of the wings [106].

These very general considerations are valid for both the possible approaches to bioinspired engineering: the problem-driven approach and the solution-driven approach.

Problem-driven approach

The problem-driven approach consists of researching a bioinspired solution to a practical problem identified at the beginning [36]. The first step is the problem definition, in

which the function of interest is identified. Then a biological solution is searched and studied. Once the solution is understood, its principles are abstracted, removing the specific structural and environmental constraints. Finally, these principles are translated into the problem domain introducing practical constraints such as technological feasibility [36, 52]. This approach is summarized in the scheme presented in Figure 2, where an example of its application is provided [70].

Figure 2: Scheme of the solution-driven approach with the development of a micro-invasive needle provided as an example

Solution-driven approach

The starting point of the bioinspired design with a solution-driven approach is the knowledge of biological systems able to perform a function that can be of interest to develop new technology. Then, the principle underlying the solution is understood and abstracted. Subsequently, the solution's utility for engineering problems is searched, and a specific problem is defined. Finally, the principle of the biological solution is applied to the engineering problem [36, 52]. This approach is summarized in the scheme presented in Figure 3, where an example of its application is provided.

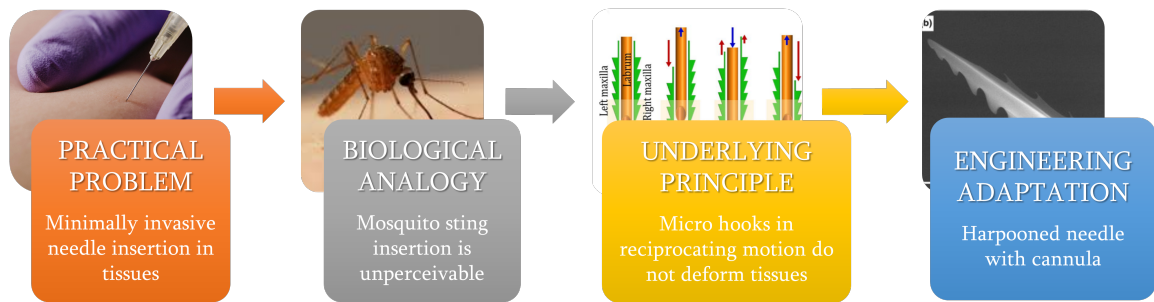Figure 3: Scheme of the problem-driven approach with the invention of Velcro as an example

A solution-driven approach is used for this research as it is aimed at recreating the efficient swimming locomotion of fishes in underwater vehicles.

Structure of the thesis

In Chapter 1 examples of the bioinspiration method to all engineering fields are presented, with particular emphasis on bioinspired robotics, except for underwater locomotion strategies and swimming robots, which are described more in detail in the following chapters. In Chapter 2, classification of swimming locomotion strategies and general concepts of the hydrodynamics of fish swimming are provided. In Chapter 3, the most significant examples of already existing fish robots are described, and the possible applications of these robots are presented. Chapter 4 is dedicated to the description of the CFD model of a swimming cownose ray and the discussion of the results. In Chapter 5, the prototype of the bioinspired robot is described, from the design of the mechanisms to the dynamic analysis and the components' sizing. In Chapter 6, the control algorithm of the robot is described. In Chapter 7, the experimental tests on the fin motion are presented. In Chapter 8, the final design of the bioinspired robot is described. Finally, conclusions are drawn in chapter 9.

1 | Applications of Bioinspiration

THE biological functions that can serve as a source of inspiration are countless and extremely varied, and so are the fields of application of bioinspired engineering.
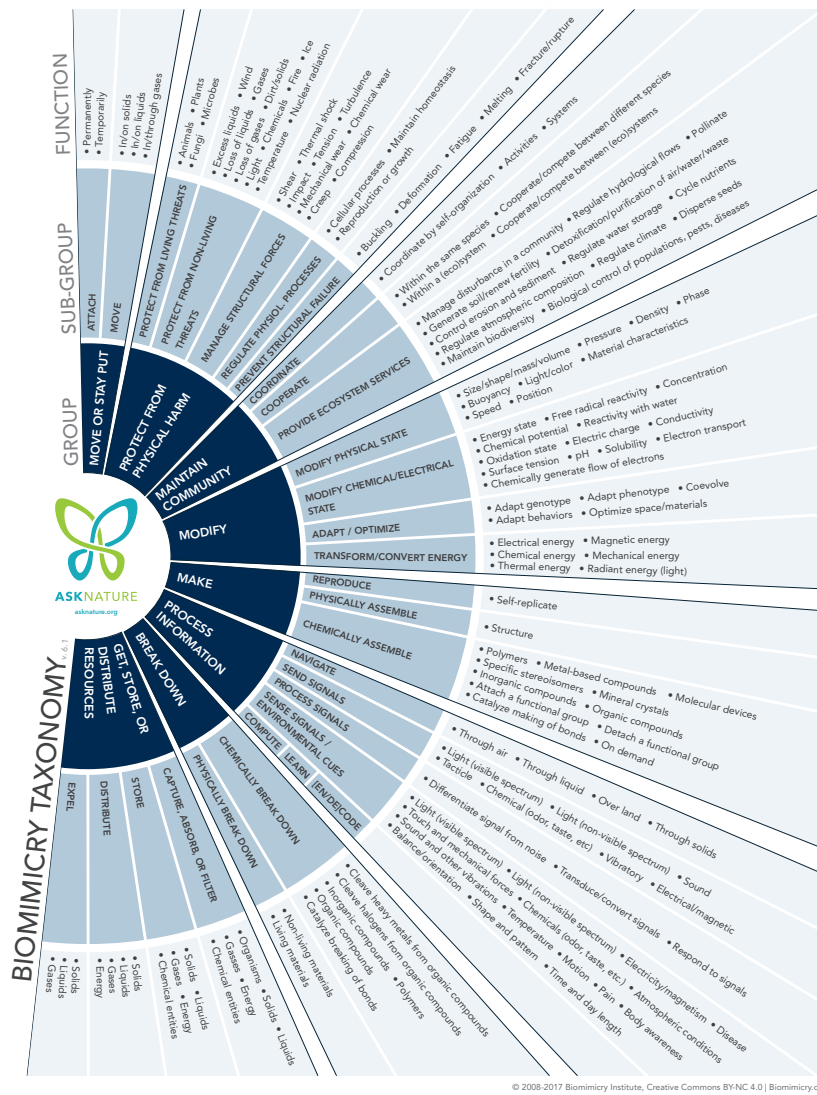

Figure 1.1: Biomimicry Taxonomy (AskNature ©)

The biomimicry taxonomy, reported in Figure 1.1, is a classification of biological functions, which can help engineers identify nature's examples of the function they are trying to emulate [2]. An example for every field of application is reported in the following sections.

1.1. Cooperation

Insect colonies perform complex group tasks through many simple individual interactions without central control or supervision. The teamwork is self-organized, and each individual finds its tasks only following chemical traces left by other individuals. The potential of self-organization in nature is enormous, and ant colonies and termite mounds rely just on this type of coordination [13]. This is the source of inspiration for many algorithms used to control robot swarms. These complex systems are composed of many small robots, and it would be tough for a single computer to communicate with all the components in real time. However, robots able to communicate and interact with nearby members can swarm and perform complex tasks [100].

(a) Termite colony inside a mound   (b) Swarm of robots, Rubenstein, 2014, Harvard University [100]

Figure 1.2: Termites in a mound and a swarm of robots

1.2. Self-assembly

Tissues composing both plants and animals are self-assembled, and they are synthesized thanks to the complex chemical interactions among enzymes and other complex compounds. Exploiting the same principle, self-repairing and self-assembling materials can be obtained. They are called supra-molecular materials because they are composed of many molecules which form functional systems. As it occurs for proteins complexes, the non-covalent bonds are fundamental in defining the function and the possible interactions with different compounds, as summarized in Figure 1.3 [32].
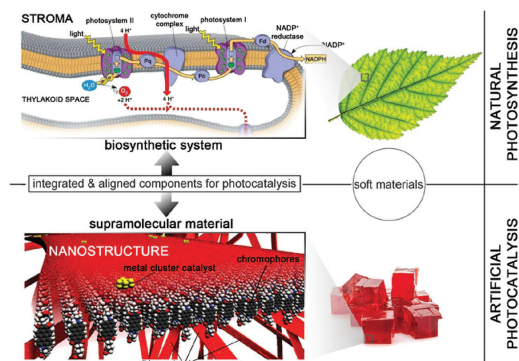
Figure 1.3: Self-assembled systems with integrated functionality by non-covalent interactions, Dumele, 2020, Northwestern University [32]

1.3. Sensing

(a) Rat whiskers
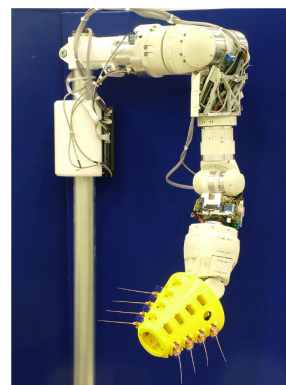
(b) Artificial BIO-TACT sensor, Sullivan, 2012, University of the West of England [122]

Figure 1.4: Rat whiskers and bioinspired tactile sensor

Many mammals, such as rodents and seals, use for tactile sensing some hairs on their snout called whiskers or *vibrissae*, that they use to explore the surroundings keeping at a slight distance or detect hydrodynamic wakes. They are long tapered hairs that bend as they come in contact with an object. They are extremely sensitive and can even detect textures on a surface [93]. They have been the source of inspiration for touch sensors that apply minimal force on the objects they are supposed to detect. Mounted on robotic arms, they are valuable tools for manipulating delicate objects [122]. Rat whiskers and bioinspired touch sensors are shown in Figure 1.4.

1.4.   Energy conversion

The oriental hornet, shown in Figure 1.5, has some pigments in its cuticles that can absorb solar energy and convert it into electrical energy. In addition, the outer brown layer of its body is covered in grooves that funnel solar rays, and the yellow segments contain a pigment that absorbs solar energy and generates electrical energy, which is used for liver functionality and to give muscles a boost of energy. This is the source of inspiration for organic solar cells with high conversion efficiency [92].

Figure 1.5: Oriental hornet

1.5.   Optical properties

The wings of the Morpho Butterfly are featured by nanoscale structures on their surface which cause light waves to diffract and interfere. As a result, some color wavelengths cancel out, and others are intensified and reflected. The result is that the butterfly wings appear of a very intense iridescent blue, as shown in Figure 1.6 [132]. This property is called structural color. It has inspired the creation of artificial self-assembling coatings that reflect ultraviolet, visible, or infrared light without using any toxic pigment or dye [3].

Figure 1.6: Iridescent blue Morpho Butterfly wings

1.6. Protection from physical harm

The beak of the Golden-fronted woodpecker (*Melanerpes Auriforms*) and its skull bone have a shape and a material composition that protects the brain from vibrations and shocks deriving from impacts. The woodpeckers drum the wood of a tree about 20 times per second, reaching an acceleration of 1200 g without damage to their brain. This structure inspired the design of a shock-absorbing mechanism consisting of close-packed micro glasses within a visco-elastic layer, arranged like the spongy bone and the skull of the woodpecker [143].

Figure 1.7: Golden-fronted woodpecker

1.7. Breaking down materials

The ovipositor of the parasitic wasp *Megarhyssa Ichneumon*, shown in Figure 1.8, can drill through the wood to lay its eggs. This organ is lightweight and highly flexible, and its surface is featured by small teeth which cut wood when the ovipositor moves with a reciprocating motion. A bioinspired drilling mechanism has been derived emulating this principle, and it is a lightweight and energy-efficient solution advantageous for space exploration [43].

Figure 1.8: Megarhyssa Ichneumon with its long ovipositor

1.8. Adhesive properties

Geckos can climb any surface thanks to their sticky feet. Their toes are covered with thousands of tiny hair-like projections which branch in smaller nanostructures ending with small disks called spatulae, giving to the gecko feet a vast contact surface. Spatulae interact with surfaces thanks to Van Der Waals forces, which are very weak attraction forces between molecules. Nevertheless, being the contact surface very large, the sum of all Van Der Waals forces is high and gives geckos their outstanding climbing ability [4]. Materials inspired by gecko feet have been developed showing great adhesive performances [48].

(a) Gecko foot
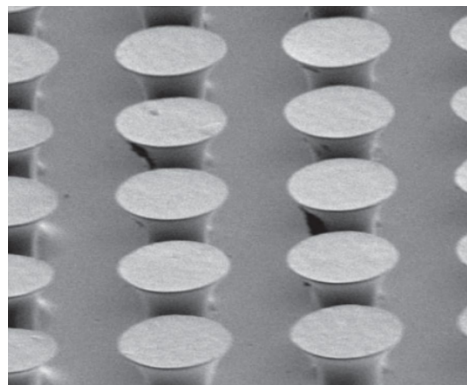
(b) Bioinspired adhesive material seen at the microscope, Gorumlu, 2017, Texas Tech University [48]

Figure 1.9: Gecko foot and bioinspired adhesive material

1.9. Bioinspired robotics

Robots taking inspiration from nature usually imitate live organisms in how they move or manipulate objects.

1.9.1. Manipulation

Manipulation of objects is a fundamental operation in the industry, which is conventionally carried out using traditional rigid robots, unsuitable for handling delicate objects such as food. On the other hand, biomimetic manipulators are usually soft and made of compliant material, which gives them the ability to deal with uncertainties and makes them safer for human-robot interaction [59].

Manipulators inspired by tentacles or trunks

(a) Octopus

(b) Octopus robot, Laschi, 2012, BioRobotics Institute, Scuola Superiore Sant'Anna [68]

Figure 1.10: Octopus and bioinspired robot

Octopus tentacles and elephant trunks are long muscle appendages able to grasp objects and lift weights while remaining highly compliant and deformable. The primary ability that a soft robot can emulate from octopuses is the ability to stretch, bend, tighten the arm around an object and regulate stiffness to adapt to the environment, thanks to the particular muscle tissue arrangement in the tentacles, which lack a skeletal structure. This ability has been replicated in an octopus robot with tentacles characterized by actuators oriented in multiple directions and SMAs springs to adapt stiffness [68]. The robot is shown in Figure 1.10.

Another bioinspired manipulator is the BionicMotionRobot, inspired by an elephant's trunk and shown in Figure 1.11. This robotic arm consists of a structure with 12 degrees of freedom, pneumatically actuated. This robot can perform natural movement

patterns, and its inherent flexibility represents an enormous advantage for safe human-robot interaction [118].
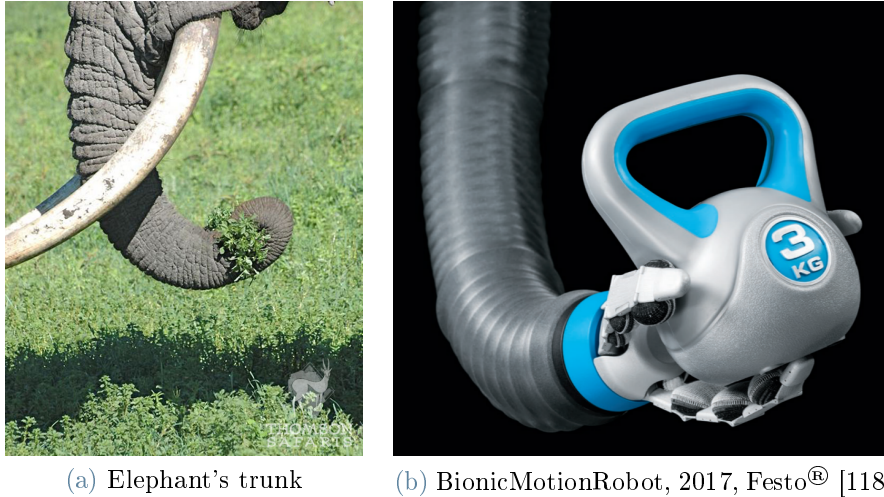
<table>
<tr><td>(a) Elephant's trunk</td><td>(b) BionicMotionRobot, 2017, Festo® [118]</td></tr>
</table>

Figure 1.11: Elephant trunk and the bioinspired manipulator BionicMotionRobot

Several other examples of bioinspired manipulators inspired by this principle can be found, and they can find applications also for minimally invasive surgery [96].

Manipulators inspired by the chameleon's tongue

A bioinspired gripper can take inspiration also from the chameleon's tongue. The chameleon shoots out at more than 3.5 m/s its tongue to catch its prey, which elongates more than six times with respect to its rest length. This mechanism, combined with the super-sticky tongue end, gives the chameleon a prey catch rate of 99.6 %. A catching robot has been developed using a coilgun to accelerate a magnet that can catch metallic objects [28]. Another bioinspired manipulator that takes inspiration from the chameleon's tongue exploits the principle which makes the tongue's end so sticky. The chameleon puts the tongue over the prey and securely encloses it in a tight fit. The bioinspired gripper consists of a silicone chamber that deforms when it comes in contact with the object to grasp, and then negative pressure is created so that the object is sucked in, as shown in Figure 1.12 [120].
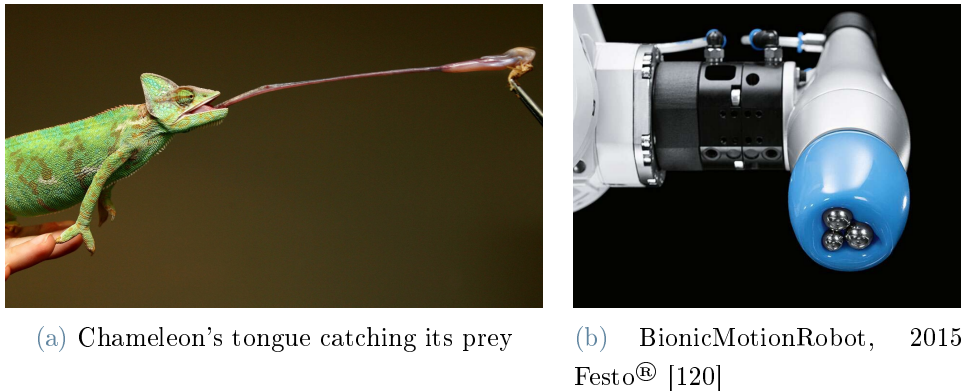
(a) Chameleon's tongue catching its prey

(b) BionicMotionRobot, 2015, Festo® [120]

Figure 1.12: Chameleon's tongue and bioinspired manipulator

1.9.2. Locomotion

The vast majority of bioinspired robots emulates from live beings their locomotion strategies. In nature, it is possible to find animals of all sizes that live in significantly different environments. Therefore, there is a wide variety of biological locomotion strategies that can serve as a source of inspiration for the design of robots.

Walking robots

One way of moving across the land is to walk or run. The main advantage of this kind of locomotion is the ability to move on uneven and unstructured terrains. Furthermore, each leg is featured by several degrees of freedom so that these animals can perform different gaits. For example, they can move their legs to change their body's height or orientation [82]. Therefore, the walking gaits differ significantly depending on the number of legs.

(a) Scorpion

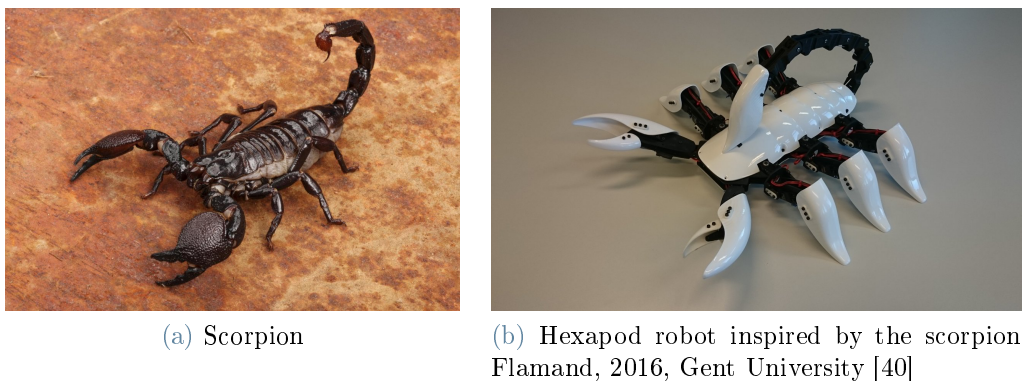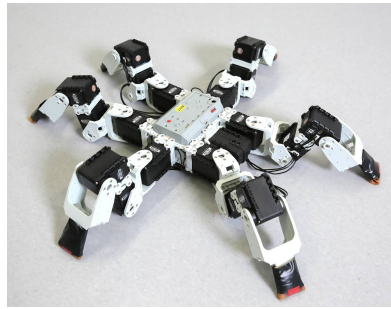(b) Hexapod robot inspired by the scorpion, Flamand, 2016, Gent University [40]

Figure 1.13: Scorpion and a bioinspired robot

Several robots are taking inspiration from invertebrates, mainly insects, spiders, and

scorpions, with six or eight legs. Having a high number of legs makes them very stable and provides them a large number of degrees of freedom so that many gaits are possible; however, their motion is generally slow. For example, in Figure 1.13, a hexapod robot [40] is shown, inspired by the scorpion, and, in Figure 1.14, a robot inspired by the spider is displayed [94].

(a) Spider

(b) Hexapod robot inspired by the spider, Ramdya, 2017, EPFL [94]

Figure 1.14: Spider and a bioinspired robot

Quadruped robots can move very fast and with high energy efficiency. Their legs are composed of multiple links with many actuators. As a result, these robots can be very agile, and some of them, like the robot presented in Figure 1.15 can even perform jumps and flips [11]. Quadruped robots find applications in space exploration, search and rescue operations, and surveillance.


(a) Cheetah

(b) Cheetah robot, Bledt, 2018, MIT [11]

Figure 1.15: Cheetah and a bioinspired quadruped robot

Finally, robots can take inspiration also from humans, who walk with just two legs. Like other walking robots, they can move on unstructured terrains, but they also have two arms they can use to perform other tasks. Although biped robots require very complex

algorithms to stabilize and control their motion, they can perform even difficult stunts and replace human workers carrying out simple tasks, as shown in Figure 1.16 [67].
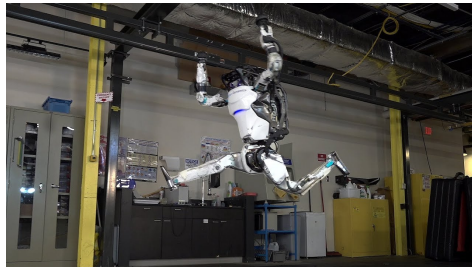
(a) Jumping humanoid robot, Kuindersma, 2016, MIT [67]
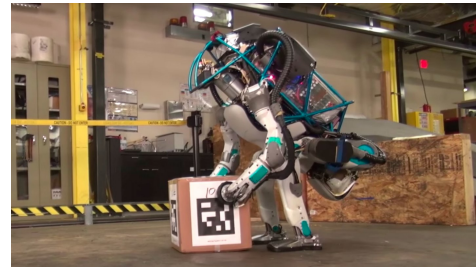
(b) Humanoid robot moving a box, Kuindersma, 2016, MIT [67]

Figure 1.16: Humanoid robot

Jumping robots

Another function that biomimetic robots emulate from nature is the ability to jump. This locomotion strategy is similar to walking, and it is an alternative to it for most animals. The difference is that all legs are used synchronously, and springs or other elastic elements are required in the legs to absorb impacts that occur during landing. The potential elastic energy that springs accumulate in an impact can be stored and recovered to perform the next jump, obtaining a gait with high energy efficiency [76]. An example of jumping robot is the Bionic Kangaroo, shown in Figure 1.17, which takes inspiration from a kangaroo [119].

(a) Kangaroo

(b) Bionic Kangaroo, 2014, Festo® [119]

Figure 1.17: Kangaroo and biomimetic kangaroo robot

Biomimetic jumping robots can take inspiration also from insects, like the cricket, the grasshopper, or the locust, which, while jumping, spread their wings and glide so that the traveled distance is increased, and the impact force during landing is reduced, resulting

in locomotion characterized by great energy efficiency. For example, in Figure 1.18 a grasshopper and a bioinspired jumping-gliding robot are presented. This robot is actuated by a motor attached to a cam which compresses a spring and then releases the stored energy. The combination of jumping and gliding makes it able to travel a double distance with respect to pure jumping and reduce of 50% the impact force [130].

(a) Grasshopper

(b) Bioinspired jumping-gliding robot, Vidyasagar, 2015, EPFL [130]

Figure 1.18: Grasshopper and jumping-gliding robot

Crawling robots

Crawling locomotion is typical of snakes and worms, which are biologically very different, but they all lack legs and have thin elongated bodies. This body shape, with a thin body and a compact cross-section, not only makes them able to move in unstructured terrains but also gives them the ability to move inside tiny gaps and holes. Furthermore, since most of their body is always in contact with the ground, their gaits are very stable. Being constantly in contact with the soil means that a high friction force is developed during motion; nevertheless, their energy efficiency is comparable to other animals with legged locomotion because the aforementioned drawback is balanced by the advantage of not needing to lift any part of their body. Furthermore, their body is very simple to emulate in a biomimetic robot since it consists of the same structures and joints repeated many times. Finally, snakes are also able to climb trees and wrap around their prey, thanks to their shape, similar to the one of elephants' trunks or octopuses' tentacles. Thus, bioinspired snake robots are extremely versatile since they could be used both for locomotion and manipulation while remaining with a simple structure [55].

The most common crawling locomotion strategy is the serpentine or slithering locomotion, adopted in nature by most snakes and consisting of waves of lateral bending that propagate from the head to the tail. The generation of a net propulsive force is based on the anisotropic dynamic friction coefficient of snakes' skin, which is covered by rigid scales overlapping in a longitudinal direction, which makes the friction coefficient very small

in a longitudinal direction and very high in a transverse direction [20, 56], as shown in Figure 1.19. Moreover, snakes can take advantage from the presence of obstacles on their path pushing against them, so that the lateral forces cancel out and a net propulsive force is generated [74]. This property makes them very suitable for locomotion on uneven terrains.

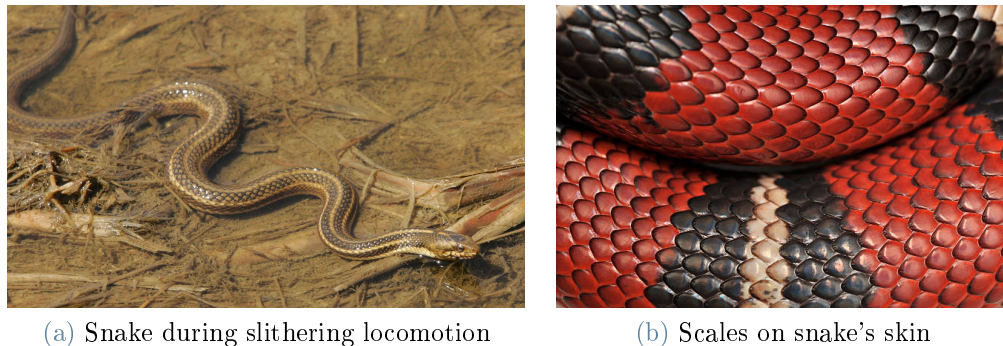(a) Snake during slithering locomotion

(b) Scales on snake's skin

Figure 1.19: Slithering snake and zoom on the scales of its skin

The anisotropic friction of snakes' skin can be achieved using passive wheels, as the one shown in Figure 1.20a [55].

Snakes also use other types of crawling locomotion, such as sidewinding, typical of the rattlesnake. The bending waves are similar to those occurring in slithering locomotion. However, the part of the body remaining straight is slightly lifted from the ground, and static friction is present in bents. A bioinspired robot exploiting this principle is presented in Figure 1.20b [85].

(a) Slithering snake robot with passive wheels, Crespi, 2005, EPFL [26]

(b) Sidewinding snake robot, Marvi, 2014, Georgia Institute of Technology [85]

Figure 1.20: Biomimetic snake robots

Two-anchor crawling is a different type of crawling locomotion used by inchworms. First, they bend their body in an "Ω" shape, then, keeping their tail attached to the ground,

stretch their body pushing forward their head; finally, they attach their head to the ground and bend their body again, pulling forward their tail. This principle is advantageous for tiny robots, which can make use of actuators made of smart materials such as piezoelectric or shape-memory-alloys, like the robot shown in Figure 1.21 [65].

(a) Inchworm

(b) Bioinspired inchworm robot with SMAs actuators, Koh, 2013, Seoul National University [65]
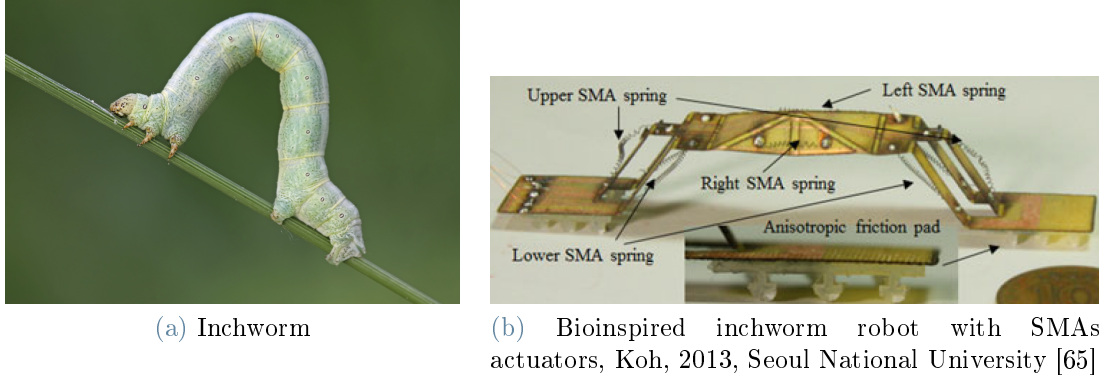
Figure 1.21: Inchworm and bioinspired inchworm robot

Peristaltic locomotion is characteristic of earthworms and sea cucumbers. They enlarge the cross-section of their body sequentially, in a wave propagating from the head to the tail. The enlarged segments are in contact with the soil, whereas the others stretch and contract periodically, making the animal move forward. This locomotion principle is quite similar to the two-anchor crawling. It is a source of inspiration for small robots, actuated by smart materials, like the robot shown in Figure 1.22 [110].
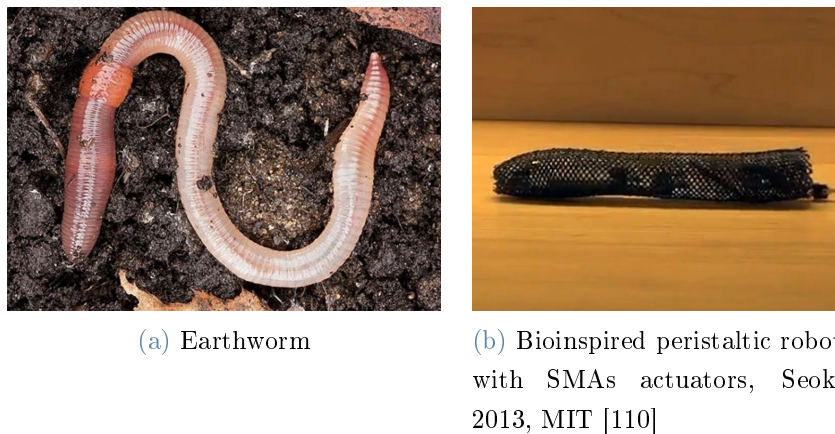

(a) Earthworm

(b) Bioinspired peristaltic robot with SMAs actuators, Seok, 2013, MIT [110]

Figure 1.22: Earthworm and bioinspired peristaltic robot

Digging robots

Moving underground represents a tremendous challenge in biology and robotics because of the presence of many obstacles and the high contact forces both due to pressure and friction with the soil particles. Nevertheless, many animals have developed the ability to dig, move soil and burrow underground. The Atlantic razor clam can dig as deep as 70 cm under the seabed. It uses a combination of movements of its valves and its foot: the repeated expansion and contraction of valves moves the surrounding sand particles, which unpack, leaving some space between them, and water is pulled inside these pores, creating a fluid buffer around the animal. Hence, the clam can advance downwards, facing a small resistance. This principle has inspired the development of RoboClam, a bioinspired robot that could find application in seabed exploration and in laying cables under the sea, as shown in Figure 1.23 [135].

Figure 1.23: Atlantic Razor Clam and RoboClam, Winter, 2014, MIT [135]

The vast majority of biomimetic robots take inspiration from animals, but the most efficient diggers in nature are plants. Their roots can penetrate the soil at any angle, and their motion has very high energy efficiency. The growing locomotion of roots is a very slow movement. Nevertheless, since only the root tip is in motion and the rest of the body is still, the energy dissipation due to friction is minimized, and the overall inertia of the motion is minimal.

The Plantoid robot, displayed in Figure 1.24, takes inspiration from plants roots, and it emulates the addition of cells to the tip exploiting the 3D printing of material with the fused deposition modeling technique. The robot's head is also equipped with chemical and temperature sensors used to imitate other plant functions. The direction of growth can be given with an asymmetry of the thickness of material deposition or of the number of layers [103].
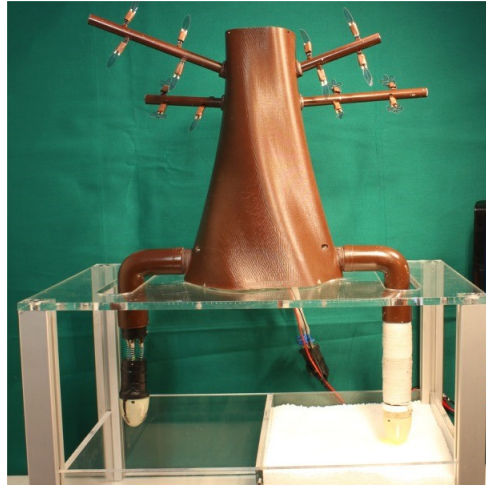
Figure 1.24: Plantoid robot, Sadeghi, 2017, IIT [103]

Flying robots

The recent interest in the development of drones has promoted the research for novel propulsion mechanisms for aerial vehicles. Thus, several bioinspired flying robots have been developed trying to replicate the maneuverability and energy efficiency of bird or insect flight. The majority of birds and bats fly by flapping their wings in a particular motion pattern that allows generating at the same time lift and thrust force. The wing kinematics is complex since the wings flex, bend, rotate and twist during a flapping cycle. Thus, the resulting flow is unsteady and three-dimensional. Hence, complex phenomena such as wake capture or leading-edge vortex formation and detachment combined with the aeroelasticity of wings cannot be neglected [53]. Taking inspiration from nature is particularly convenient in developing small unmanned aerial vehicles, which require very high maneuverability and a low forward speed [53].
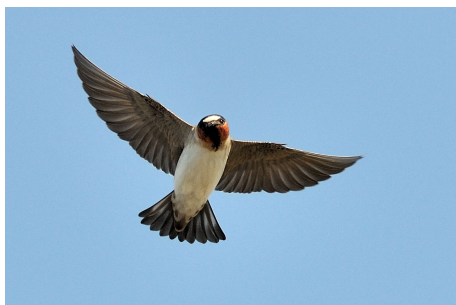

(a) Swallow with spread wings
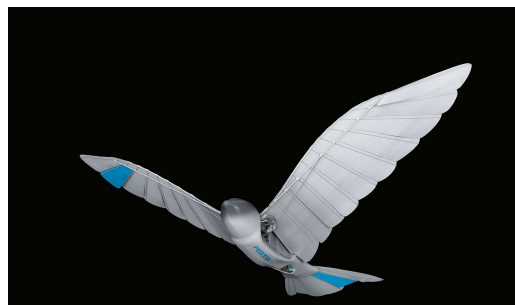
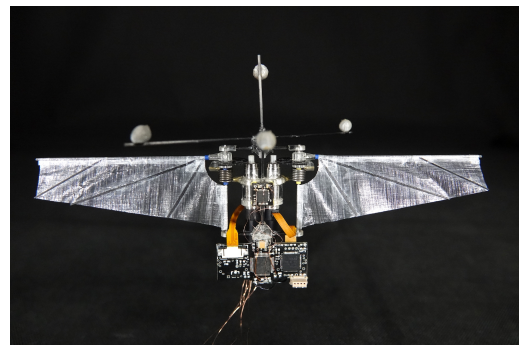(b) Biomimetic robot Bionic Swift, 2021, Festo® [121]

Figure 1.25: Swallow and biomimetic flying robot

A biomimetic flying robot is the Bionic Swift, inspired by the swallow and shown in Figure 1.25. Not only the wing-beating kinematics emulates the flight of a real bird, but the presence of artificial feathers also features its wings. They are arranged in such a way that, during the wing upstroke, they fan out, letting air flow through the wing, whereas, during the wing downstroke, feathers tighten, making the wing surface seamless. This means that the force required to move wings upwards is smaller than the force needed to move them downwards, resulting in an efficient flying strategy [121].

Among birds, the most agile is the hummingbird, which can hover and perform unparalleled fast escape maneuvers. The ability to hover, the small dimension, and the high wing-beat frequency ($\sim 30\,\mathrm{Hz}$) create an analogy with insects' flight, but the wing shape and orientation are very distinct. Therefore, a simplified bioinspired hummingbird robot has been developed, and it can perform agile maneuvers and fly as silently as its natural counterpart [37].
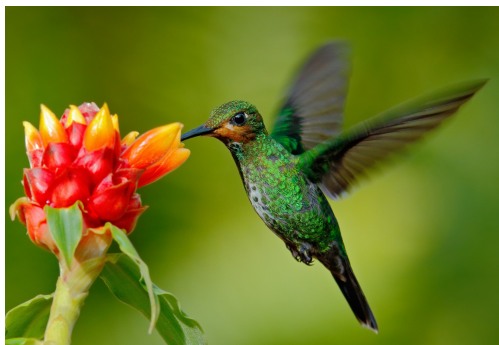


(a) Hovering hummingbird   (b) Robot inspired by the hummingbird, Fei, 2019, Purdue University [37]

Figure 1.26: Hummingbird and bioinspired robot

Insects are masters of flight agility, and they are a source of inspiration for micro-air vehicles. They fly at very low Reynolds numbers, and many of them can glide, hover, suddenly change direction, and even fly backward. The insect with the most interesting characteristics is the dragonfly, whose wings are featured by corrugations and a particular camber angle optimized for gliding. Furthermore, they have two pairs of wings that are moved independently, making them able to hover and take off vertically [128]. The BionicOpter, displayed in Figure 1.27, is a biomimetic robot inspired by the dragonfly. It can equal all the flight characteristics of the dragonfly since the amplitude of wing flapping, and the tilting angle can be controlled independently for each wing [117].

(a) Dragonfly
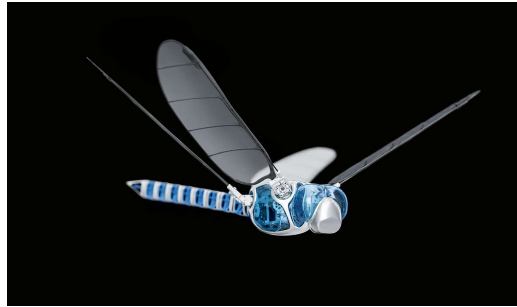
(b) Robot inspired by the dragonfly, 2013, Festo® [117]

Figure 1.27: Dragonfly and biomimetic robot

2 | Hydrodynamics of swimming

THE earliest life forms were aquatic; thus, swimming is the first kind of locomotion that appeared on Earth [141]. This means that, over billions of years, swimming live beings have evolved through natural selection, differentiating in a tremendously vast number of species, each featured by a particular shape or motion strategy [47, 72, 138, 141]. Furthermore, such a long evolutionary history guarantees that aquatic organisms have developed highly efficient locomotion strategies, although not necessarily optimal. Therefore, aquatic organisms are promising sources of inspiration for a large number of engineering applications [72, 111].

The locomotion of a body through a medium is based on momentum transfer between some part of it, the propeller, to the surrounding fluid [133], and the properties of water as a locomotion medium have played a crucial role in the evolution of swimming animals. The main characteristics are its incompressibility and its high density. The water incompressibility implies that any movement of the swimming animal will set in motion the water surrounding it and vice versa for every possible flow generated by animal locomotion. The density of water ($\sim 1000\,\mathrm{kg/m^3}$) is close to the body density of animals, so hydrostatic force and gravity almost counterbalance each other, and the weight of the animal does not affect its motion [111].

2.1. Classification of swimming modes

Swimming propulsion is exploited by aquatic animals covering a wide range of body sizes and speeds, from blue whales, which are 30 m long and can reach a cruise speed of 12 m/s, to protists, characterized by a length of 50 μm, and by a swimming velocity of 80 μm/s. The physical principles used by live beings to swim differ according to their size since the characteristics of the flow in which swimming animals are immersed depend considerably on the animal dimensions. The dimensionless parameter that allows quantifying the contribution of the different forces to momentum transfer is the Reynolds number, defined

as follows:

$$Re = \frac{Ul}{\nu} \tag{2.1}$$

where U is the velocity of the flow, l is the characteristic length of the animal, and ν is the kinematic viscosity of the fluid, which for water is equal to $1 \times 10^{-6} \, \mathrm{m^2/s}$. The Reynolds number represents the ratio between inertia and viscous forces in a flow. The flow of a large cetacean is mainly dominated by inertia forces, as its Reynolds number is about 10^8, whereas microorganisms swim with a Reynolds number of 10^{-3}, as at that scale viscous forces are predominant over inertia, as shown in Figure 4.28 [44, 138].
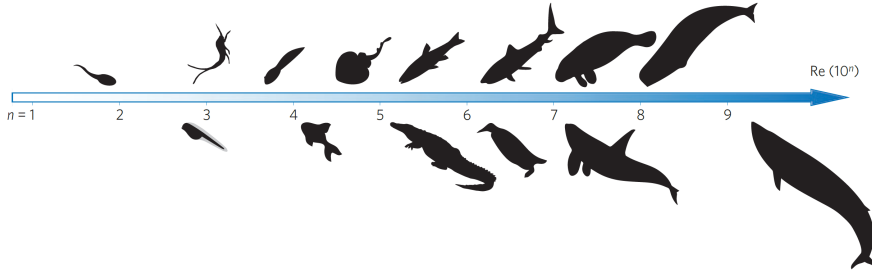

Figure 2.1: Reynolds number characterizing swimming locomotion of different species, Gazzola, *Nature Phys* (2014) [44]

While it is straightforward to identify the kinematic viscosity of the fluid, it not as easy to define the characteristic length and the velocity of the flow since the characteristic length is related both to the kinematics of fin movements and to the dimensions of the animal, and the velocity of the flow is the superimposition of forward locomotion and fin movement. Hence, it is necessary to introduce the Swimming number, a new dimensionless parameter capturing both length and motion scales [44]:

$$Sw = \frac{\omega A L}{\nu} \tag{2.2}$$

where ω is the circular frequency of fin movement, A is the maximum amplitude of fin displacement, L is the length of the animal, and ν is again the kinematic viscosity of water. In an incompressible and inviscid flow, a deforming body accelerates a mass of surrounding fluid that scales with ρL^2 per unit span, and the fluid acceleration scales with $A\omega^2$, so that the inertia force of the fluid scales with $\rho L^2 A\omega^2$. Since the amplitude of fin movement is generally proportional to the animal length, the local angle formed by the fin scales with A/L, and the thrust force is $\approx \rho L A^2 \omega^2$ [44]. For a low Reynolds number $(< 10^4)$, the boundary layer is laminar and the viscous drag resisting to motion scales with $\rho(\nu L)^{1/2} U^{3/2}$ according to Blasius theory. Writing an equilibrium of forces in

the longitudinal direction so that thrust is equal to drag, it is possible to obtain that the scaling of the forward velocity U:

$$U \approx L^{1/3}\nu^{-1/3}A^{4/3}\omega^{4/3} \tag{2.3}$$

Substituting the scaling of U into Equation 2.1, it is possible to obtain:

$$Re \approx \frac{L^{1/3}\nu^{-1/3}A^{4/3}\omega^{4/3}L}{\nu} = Sw^{4/3} \tag{2.4}$$

On the other side, for a high Reynolds number ($> 10^4$), the boundary layer becomes turbulent and the pressure drag is predominant over the viscous drag, so that the drag force per unit span scales with $\rho U^2 L$. Therefore, the scaling of the velocity U corresponds to [44]:

$$U \approx A\omega, \tag{2.5}$$

and substituting it into Equation 2.1, it results that:

$$Re \approx \frac{A\omega L}{\nu} = Sw \tag{2.6}$$

This scaling law is confirmed by experimental observations, as shown in Figure 2.2, and it allows computing the Reynolds number of the flow combining the characteristic dimensions of the animal and of its swimming gait [44].
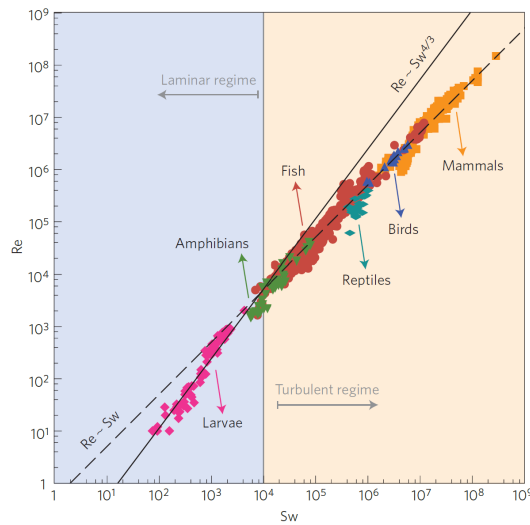

Figure 2.2: Relation between Reynolds number and Swimming number of different species, Gazzola, *Nature Phys* (2014) [44]

The momentum transfer mechanisms adopted by live beings can be based on four different forces:

- *viscous drag*: friction between the animal skin and the fluid. It is the consequence of the viscosity of water and a velocity gradient in the boundary layer. It depends on the swimming speed and the nature of the boundary layer.

- *pressure/form drag*: pressure caused by the flow distortion as the body pushes water aside to pass. It depends on the shape of the animal, and the majority of fast-swimming animals have a streamlined shape to reduce this force.

- *acceleration reaction*: the inertia of water accelerated by the fins. It is strongly dependent on the size of the fish and it is fundamental in periodic movements.

- *lift*: hydrodynamic force acting in a direction perpendicular to the fin. It contributes to propulsion when the fin rotates about the pitch or yaw axis.

The relative contribution of these forces to propulsion is different according to the Reynolds number of the flow, as shown in Figure 2.3 [111].
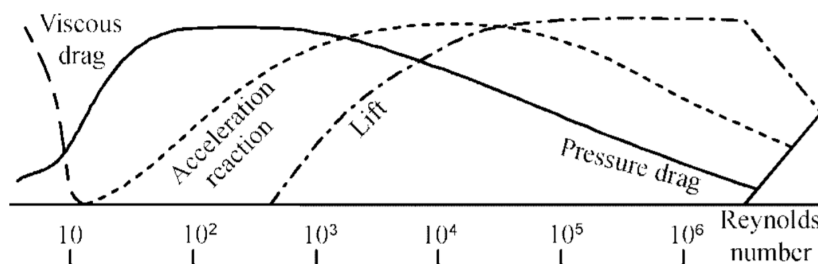

Figure 2.3: Relative contribution of forces to propulsion as function of the Reynolds number, Sfakiotakis, *IEEE Journal of Oceanic Engineering* (1999) [111]

Swimming propulsion mechanisms can be classified in four categories, whose main characteristics are summarized in Figure 2.4 and described in the following sections.
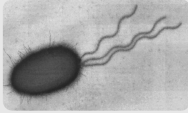
	Flagellar propulsion	Jet propulsion	Median paired fin	Body caudal fin
Speed	80 μm/s ~ 1 mm/s	2 cm/s ~ 1 m/s	0.1 m/s ~ 5 m/s	0.2 m/s ~ 30 m/s
Reynolds number	10^{-4} ~ 1	1 ~ 10^2	10^3 ~ 10^6	10^3 ~ 10^8
Efficiency	10 ~ 20 %	20 ~ 50 %	50 ~ 90 %	40 ~ 90 %
Maneuverability	Very low	Very low	Very high	High

Figure 2.4: Classification of biological swimming modes and their main characteristics

Combining the information contained in Figure 2.4 and in Figure 2.3, it is possible to observe that the Reynolds number of flagellar propulsion is extremely low, so viscous forces govern their motion and that for jet propulsion, featured by a medium-low Reynolds number, there is a contribution of drag, as well as of inertia. Finally, body-caudal fin (BCF) and median paired fin (MPF) locomotion strategies are featured by high Reynolds number, so inertia and lift forces are predominant. This means that the physical principles of flagellar and jet propulsion swimming are peculiar to these swimming strategies. In contrast, the body-caudal fin and median-paired fin swimming are based on similar principles, and they mainly differ by the parts of the body performing the movements responsible for thrust generation. Referring to the nomenclature presented in Figure 2.5, the body-caudal fin swimming strategy involves propagating a wave along the body, culminating in a sizeable periodic displacement of the tail. Conversely, in the median-paired fin swimming mode, thrust is generated by the coupled movements of pectoral fins or dorsal and anal fins. Their movement often consists of a traveling wave similar to BCF swimming mode, but with the substantial difference that the body remains still, and the wave is present only on the surface of the fin.

The BCF swimming mode is predominant among fishes, as only 15% use MPF swimming for propulsion. Nevertheless, BCF swimming animals can use MPF swimming strategies for maneuvering and stabilization.

In this chapter, flagellar and jet propulsion are described, and their fluid mechanics are briefly presented, then the hydrodynamic principles underlying fish and cetacean locomotion are analyzed, and the peculiarity of both locomotion strategies are highlighted.
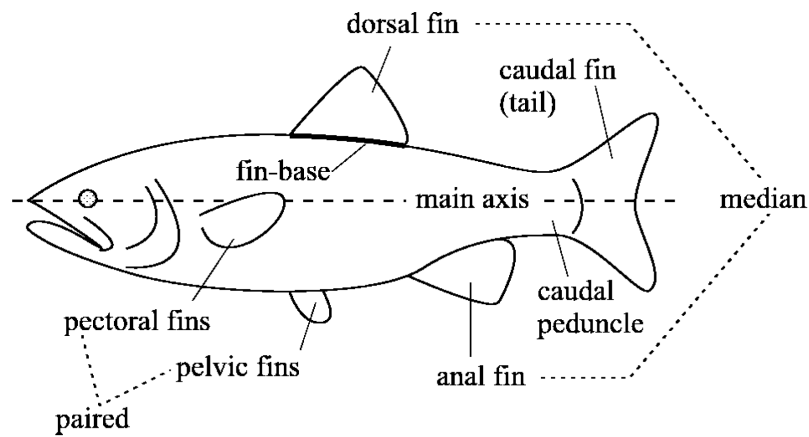
Figure 2.5: Terminology used to identify the fins of fishes, Sfakiotakis, *IEEE Journal of Oceanic Engineering* (1999) [111]

Finally, some examples of bioinspired applications are provided for each swimming mode, except for robots inspired by mantas and rays, which are the topic of the following chapter.

2.2. Flagellar propulsion

Flagellar propulsion is the swimming mechanism adopted by several microorganisms called *flagellata*, precisely. An example is shown in Figure 2.6, where the flagellum is the thin, flexible filament attached to the cell. The flagellum either performs a whip-like motion caused by the action of molecular motors distributed along the filament, or it assumes the form of a helix, rotating about its axis [69, 72].

Figure 2.6: Protist *Peranema* seen at the microscope with its flagellum

Due to their small dimensions, the Reynolds number of flagellates ranges from 10^{-4} to 1, meaning that the inertia forces are negligible with respect to viscous forces and that the drag force dominates the motion. Since inertia contribution is irrelevant, the generated

thrust depends only on the propeller's position during a cycle, and that any symmetric motion, like the flapping of the caudal fin of a fish, at this scale, would not result in a net forward movement. Thus, propulsive organs of microorganisms are either featured by non superimposable mirror images, like helical swimmers, or they assume different geometries during the cycle, like in the planar wave propulsion [129]. In planar wave prpulsion, the motion of the flagellum is a wave propagating in a direction opposite to swimming and it is possible to assume that the flagellum is deformable, and that the amplitude of oscillations is much smaller than their wavelength [69]. The principle at the base of flagellate propulsion is the anisotropy of viscous friction, and it can be understood looking at Figure 2.7, where the forces acting on an infinitesimal element of the flagellum are shown.
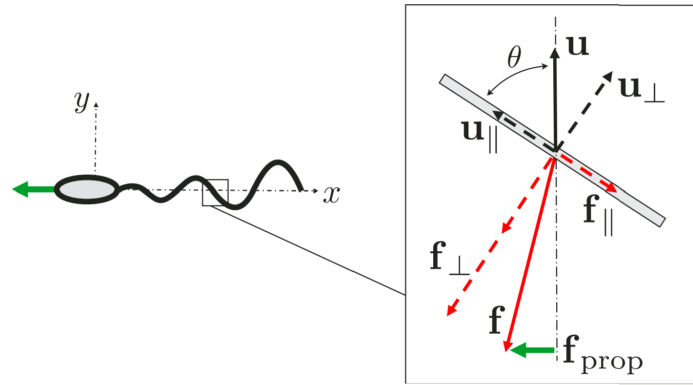

Figure 2.7: Physical interpretation of the drag-induced propulsion for flagellate organisms, Lauga, *Rep. Prog. Phys.* (2009) [69]

Any element of the filament moves in a direction perpendicular to the motion direction, and its tangent is rotated by an angle θ with respect to its local velocity. The velocity can be projected on the local normal and tangential directions, and the same can be done for the drag force, which is opposite to the element velocity. Because of the difference of drag coefficient in the normal and tangential directions, the drag force does not have the same direction as the element velocity, but a component in a perpendicular direction arises. This component is the propulsive force generated by the flagellum [69]. The same principle is also valid for more complex flagellar deformations, such as the helical motion, which induces a three-dimensional flow. The power exerted by the flagellum on the fluid is directly proportional to kinematic viscosity if the internal work of deformation is neglected [69]. A similar simple undulatory mode of propulsion is at the base of the swimming mode of the majority of aquatic animals, even though the difference in shape and size make the flow around them very distinct [72].

This kind of propulsion does not show great swimming performances. However, it is studied to develop biomimetic microscopic robots that could reach inaccessible places inside the human body to perform minimally invasive surgery, localized drug delivery, or screening for diseases at early stages [129]. In Figure 2.8, a biomimetic robot inspired by flagellates is presented. It uses a flexible paramagnetic filament, which deforms like a flagellum in response to the variation of an external magnetic field [69].
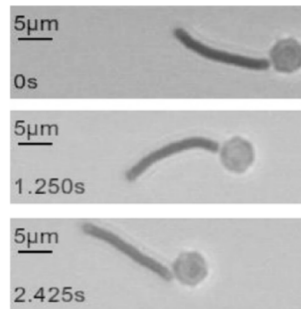

Figure 2.8: Biomimetic robot exploiting flagellate propulsion, Lauga, 2009, University of California [69]

2.3.　Jet propulsion

The jet propulsion mechanism is exploited by several invertebrates such as jellyfish, octopus, scallop, and squid. It consists in filling with water a cavity and expelling it at greater velocity. This kind of locomotion can be subdivided into three categories: bell constriction, mantel constriction, and shell compression, shown in Figure 2.9. They differ according to the different organs driving the movement, but the basic principles are very similar. In this paragraph, only the locomotion strategy of the jellyfish is described since the other two are analogous and only differ for geometry and dimensions.
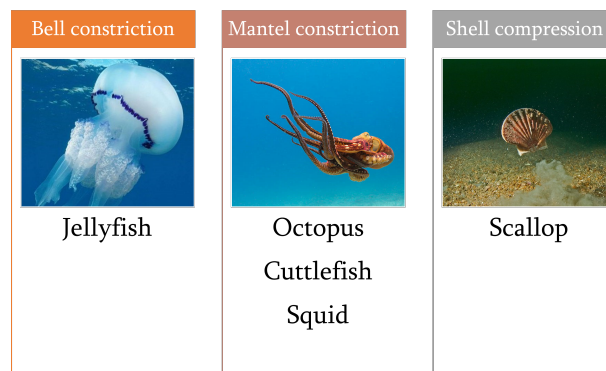

Figure 2.9: Simplified classification of biological jet propulsion swimming mechanism

The jellyfish's body is mainly composed of a bell, also called umbrella, shaped like a hemiellipsoid, with some tentacles attached. These animals periodically contract and relax the muscles of the bell, ejecting water during the constriction phase of the bell. Consequently, the animal receives a forward thrust, so movement is possible. However, the generated propulsive force is small, and the motion of jellyfishes is strongly affected by currents, which are impossible for them to resist [111].

The propulsive mechanism adopted by the jellyfish can be understood by analyzing the vortices shed in the wake during a contraction and expansion cycle, shown in Figure 2.10 [45].
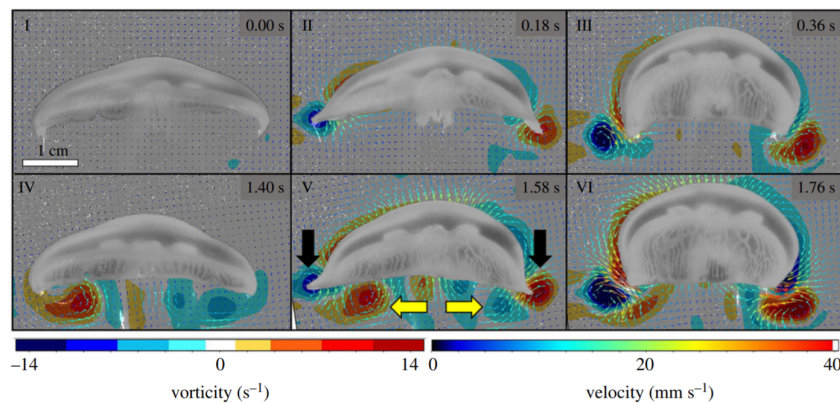

Figure 2.10: Vorticity and velocity vector around the bell margin of a jellyfish, Gemmel *Proc. R. Soc. B.* (2020) [45]

During the contraction phase, the water is ejected backward from the center of the bell, and due to the reduction of volume, the pressure inside the bell is higher than outside. Thus, at the bell margin, water moves outwards, generating a toroidal vortex, called starting vortex, shed in the wake at the end of the contraction phase. When the expansion phase begins, a vortex rotating in the opposite direction, called stopping vortex, is formed inside the bell, as water is sucked inwards. This vortex remains inside the bell after the bell expansion, and it interacts with the starting vortex that forms as another contraction phase begins. At the interface between stopping and starting vortices, near the bell margin, there is a convergent backward flow that increases the velocity of the ejected fluid and the strength of the starting vortex, enhancing the swimming performance of the jellyfish. The stopping vortex vanishes, and in the wake, only starting vortices can be observed, which form a jet flow directed downwards in the center of the bell [45, 54]. The vortex interface acceleration is a fundamental feature of this type of locomotion, and it has been observed that it improves of 30 % the swimming speed and of 40% the propulsive force [45].

This locomotion principle has been used for the realization of Robojelly, shown in Figure 2.11a, which is made of soft silicone and it uses bioinspired composite shape-memory-alloys (SMA) to actuate the bell [131]. Another example of a robot inspired by the jellyfish is shown in Figure 2.11b, whose bell is driven by ionic polymer metal composites [89]. In Figure 2.11c, a miniaturized soft jellyfish robot is presented, capable of five different swimming modes and featured by high maneuverability [97].

(a) Robojelly, Villanueva, 2011, (CIMSS) Virginia Tech [131]

(b) Jellyfish robot using IPMC, Najem, 2012, Virginia Tech [89]
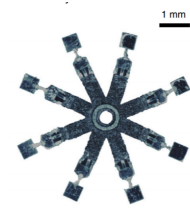
(c) Miniaturized jelyfish robot, Ren, 2019, Max Planck Institute for Intelligent Systems [97]

Figure 2.11: Bioinpsired jellyfish robots

2.4.   Body-caudal fin (BCF)

The body-caudal fin swimming strategy consists of the generation of a traveling wave along the fish's body in a direction opposite to the swimming movement. This wave travels faster than swimming velocity, and it has an increasing amplitude toward the tail. As a result, the wave accelerates water backward, and the fish gains a forward thrust because of momentum conservation. This movement of the fish is called *undulatory* if the length of the body is smaller than half wavelength, and *oscillatory* otherwise [111].
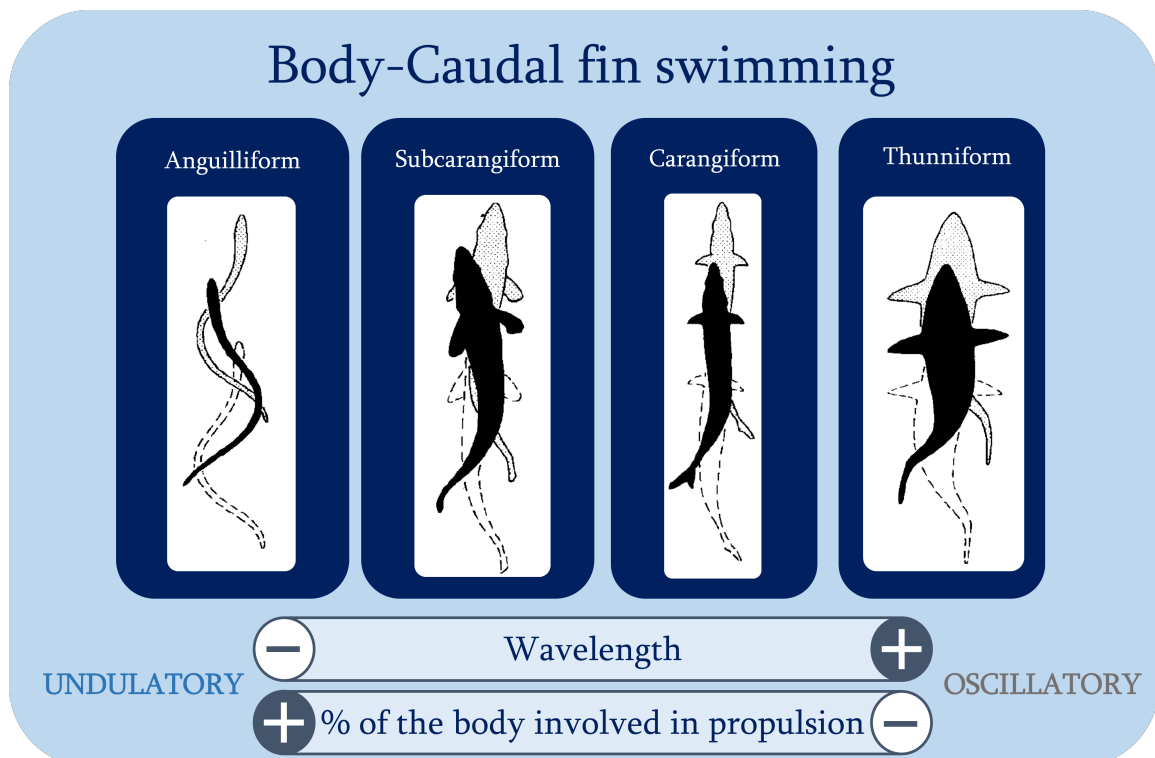

Figure 2.12: Classification of BCF swimming modes according to the wavelength and to the percentage of the body contributing to propulsion movement

The Body-caudal fin locomotion is typical of the majority of fishes and of the totality of cetaceans, and BCF swimmers can be subdivided into four main categories, created just to classify the kinematics of locomotion, without any connection with taxonomy, as shown in Figure 2.12 [105, 111]. As it is possible to observe in Figure 2.12, there is no neat distinction between categories. However, the body's movements change continuously from the undulatory motion of the whole body typical of anguilliforms to an oscillatory motion involving only the tail characterizing thunniforms.

2.4.1. Anguilliform swimming

Anguilliform swimming is the category showing the largest body undulation among BCF swimmers. This category includes eels, lampreys, salamanders, and swimming snakes with long, slender, and highly flexible bodies. A wavelength shorter than the length of the body ensures that all lateral forces are always perfectly balanced, but it also implies that the wave propagation velocity is small. Thus, these animals swim rather slowly, not exceeding $0.3\,\text{m/s}$. Nevertheless, several migratory fish, like many species of eels, adopt this type of locomotion, suggesting that its energy efficiency must be high to allow such a long endurance. Furthermore, these animals are extremely agile, being capable of turning with a small curvature and even swimming backward [105]. Examples of anguilliform swimming animals are presented in Figure 2.13.
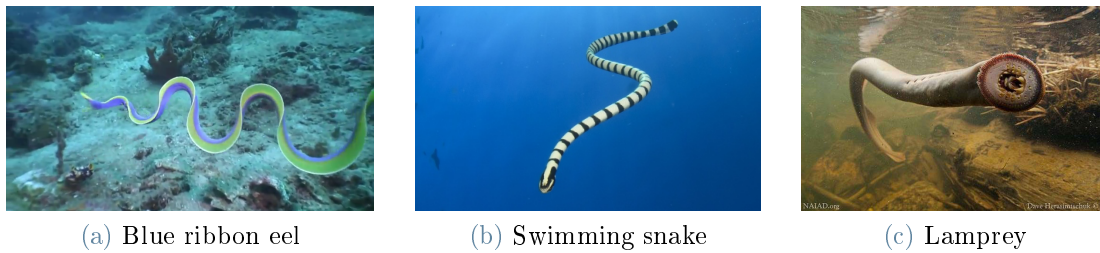

(a) Blue ribbon eel   (b) Swimming snake   (c) Lamprey

Figure 2.13: Anguilliform swimmers

The flexibility of their body is due to the high number of vertebrae (> 100), and it can be reproduced in bioinspired robots using a modular structure of actuators and joints, similar to the structure of crawling snake robots.

An example of a robot of this kind is Amphibot, shown in Figure 2.14a. It is a modular robot in which every module is a box containing an actuator for the neighboring module. This robot floats on the water surface, and it is capable of just in-plane movements. Its swimming velocity is comparable to a human's, and it can perform rapid and agile maneuvers. Moreover, it is an amphibious robot as it can also crawl on land, exploiting the same principles as snake robots [25].

A similar anguilliform robot is the Mamba, shown in Figure 2.14b, and its modules contain two actuators. Thus the robot is capable of performing 3D movements. This robot is equipped with force contact sensors, so it can measure environment contact forces, which could be useful to perform complex operations underwater [75].

(a) Amphibot, Ijspert, 2017, EPFL [61]

(b) Mamba, Liljeback, 2014, Norwegian University of Science and Technology [75]

Figure 2.14: Robots inspired by anguilliform swimmers

2.4.2. Subcarangiform and carangiform swimming

The subcarangiform and carangiform swimming strategies are very similar, and they both involve the propagation of a wave along the fish's body. For subcarangiforms the body undulation also involves the fish's head, which performs a limited amplitude motion, whereas carangiforms only move the posterior part of their body. Conventionally, a fish is considered subcarangiform if it moves more than one third of its body and carangiform if movements are concentrated in the posterior part of the body. Carangiforms have a stiffer body than subcarangiforms and anguilliforms, so they do not show excellent turning capabilities, but they can swim faster. Subcarangiforms' and carangiforms' bodies are shorter than a complete wavelength; thus, lateral forces are not balanced. In order to reduce the tendency to recoil, their mass is concentrated in the anterior part of their body, which performs a limited movement, and the thickness of their body is reduced near the attachment of the caudal fin [111]. Both categories include a huge variety of fish species with different sizes and swimming speeds, and, in general, they are considered efficient swimmers. In Figure 2.15 some examples of subcarangiform fishes are provided, and Figure 2.16 shows examples of carangiform fishes.

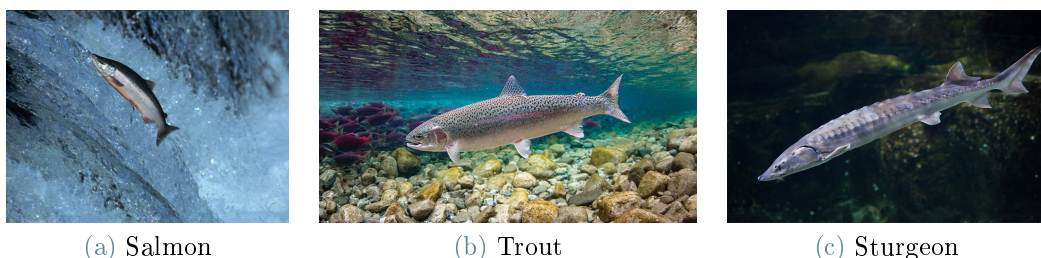(a) Salmon (b) Trout (c) Sturgeon

Figure 2.15: Subcarangiform swimmers

There is a great variety of robots inspired to subcarangiform or carangiform swimmers, in general, composed of a large rigid head, housing for electronics and batteries, and three
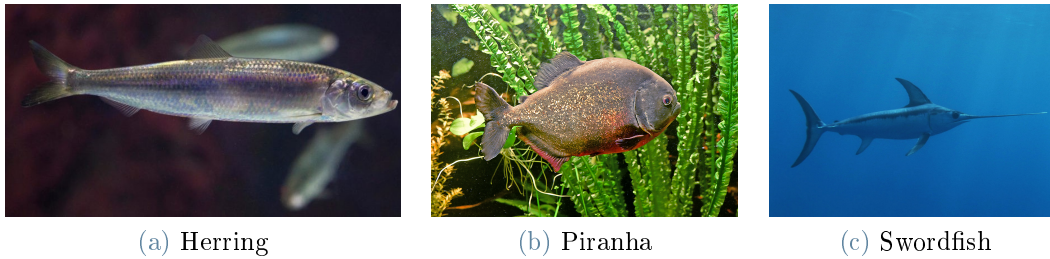
(a) Herring   (b) Piranha   (c) Swordfish

Figure 2.16: Carangiform swimmers

or four links in series reproducing the kinematics of the posterior part of the body and the tail. A robot of this kind is the G9 fish, shown in Figure 2.17a, whose motion is characterized by three links in series actuated independently by servomotors. Its skin is covered with rigid scales overlapping each other, and it is capable of highly maneuverable turns [57]. The Carp robot, shown in Figure 2.17b, is featured by with a rigid head and a flexible tail actuated by five links in series. This robot can swim up to $0.6\,\mathrm{m/s}$, and is also equipped with pectoral fins, which enhance the turning capabilities, and with a ballast pump controlling buoyancy [60]. Another bioinspired carangiform robot is shown in Figure 2.17c, it has a small rigid head, and the rest of its body is composed of four links and a rigid tail. In addition, several proximity sensors are mounted on the robot to avoid obstacles and plan its trajectory to reach the target position following the shortest path [64].
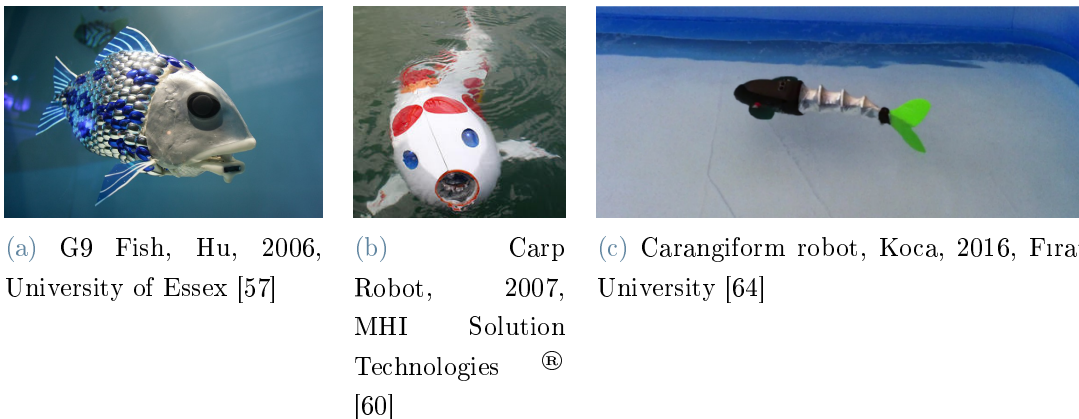
(a) G9 Fish, Hu, 2006, University of Essex [57]

(b)   Carp Robot, 2007, MHI Solution Technologies ® [60]

(c) Carangiform robot, Koca, 2016, Fırat University [64]

Figure 2.17: Subcarangiform and carangiform inspired robots

2.4.3. Thunniform swimming

Thunniform animals are characterized by a streamlined body and a sizeable rigid tail performing large oscillations. In thunniform locomotion, only the rearmost quarter of the body takes part in propulsion-generating movements, and most of the thrust is generated by the tail, which for many species assumes a half-moon crescent shape, and it is called lunate tail. These animals are usually predators in the high levels of the food chain, and they have evolved to maintain high cruising speeds for long periods and reach great burst acceleration.

Thunniform swimming is typical of varied groups of animals, such as teleost fishes, sharks, and cetaceans, so that it is considered a culminating point of the natural evolution of swimming strategies, as animals with different evolutionary paths have developed such similar swimming kinematics. The only difference between thunniform fishes and cetaceans is that fishes move their tail laterally, and cetaceans move it vertically, but the form of the traveling wave and the fin's geometry are very similar. The thrust generation is dominated by the lift force acting on the fin, and it is considered among the most efficient swimming strategies found in nature [105, 111].

Thunniforms outperform in velocity all the other swimming modes. The fastest cruising animal belongs to this category, and it is the killer whale, able to maintain a constant velocity of 4 m/s for days. The black marlin, too, the fastest animal in absolute, is a thunniform swimmer, able to reach a speed of 36 m/sfor a few seconds as it leaps out of water. However, the kinematics of thunniform swimming is not optimized for agile maneuvering and rapid direction changes. In Figure 2.18, some animals belonging to this category are displayed.


(a) Tuna   (b) Killer whale   (c) Mackerel
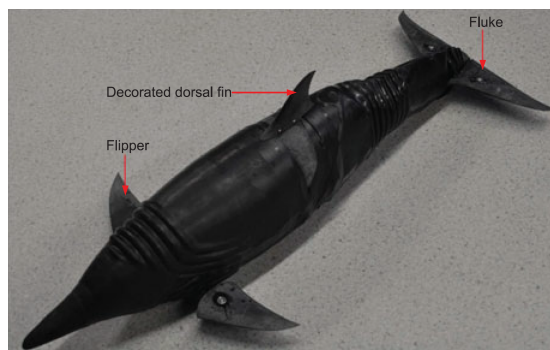
Figure 2.18: Thunniform swimmers

Such outstanding performances of thunniform swimmers have triggered the interest in developing many bioinpsired robots mimicking this kind of locomotion. An example is So-Fi, a soft fish robot inspired by the tuna, similar in size and performance to its natural counterpart. Its tail is flexible, and it is moved by fluidic elastomer actuators. In addition,

it is featured by a buoyancy control chamber to perform diving maneuvers. The robot, shown in Figure 2.19a, can swim at several meters of depth and it is controlled wireless using ultrasounds [62].

Another robot designed to reproduce this locomotion strategy is the Dolphin robot, shown in Figure 2.19b, which can reach a swimming speed of $2\,\mathrm{m/s}$ and leap out of the water, like real dolphins. Two DC motors drive the posterior part of the body and the tail, and three servomotors move the two pectoral fins and the neck to improve the agility during turning and leaping [144].
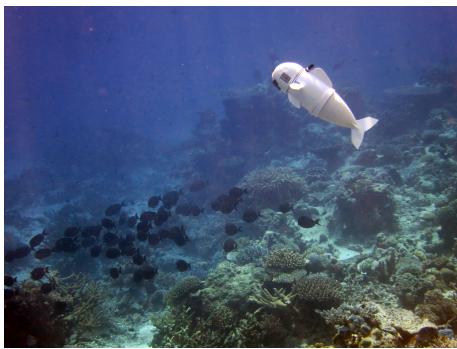
(a) So-Fi, Katzschmann, 2018, MIT [62]

(b) Dolphin Robot, Yu, 2016, Chinese Academy of Sciences [144]

Figure 2.19: Biomimetic robots inspired by thunniforms

2.4.4. Ostraciiform swimming

The ostraciiform swimming strategy is a particular category, which lies in between BCF and MPF swimming since they simultaneously use all their fins to generate thrust, so they perform a complex combination of movements involving pectoral, dorsal, anal, and caudal fins.

This category includes a small variety of fishes, among which the cowfish and the boxfish, shown in Figure 2.20a, are the most representative examples. These fishes have a rigid body, and they move their fins like paddles without showing any wave propagation. They swim very slowly, and their energy efficiency is poor, but they have developed great agility in maneuvering, as they live in narrow spaces among rocks in coral reefs [105, 111].

A robot inspired to the boxfish, shown in Figure 2.20b, has an entirely rigid body subdivided into many compartments to host motors and electronics, each fin has one degree of freedom, and the main contribution to thrust is given by the caudal fin, whereas the pectoral fins are used for maneuvering [84].

(a) Boxfish
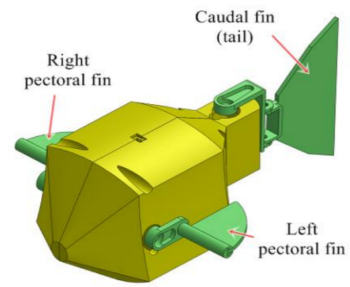
(b) Boxfish Robot, Mainong, 2017, Universiti Malaysia [84]

Figure 2.20: Boxfish and biomimetic boxfish robot
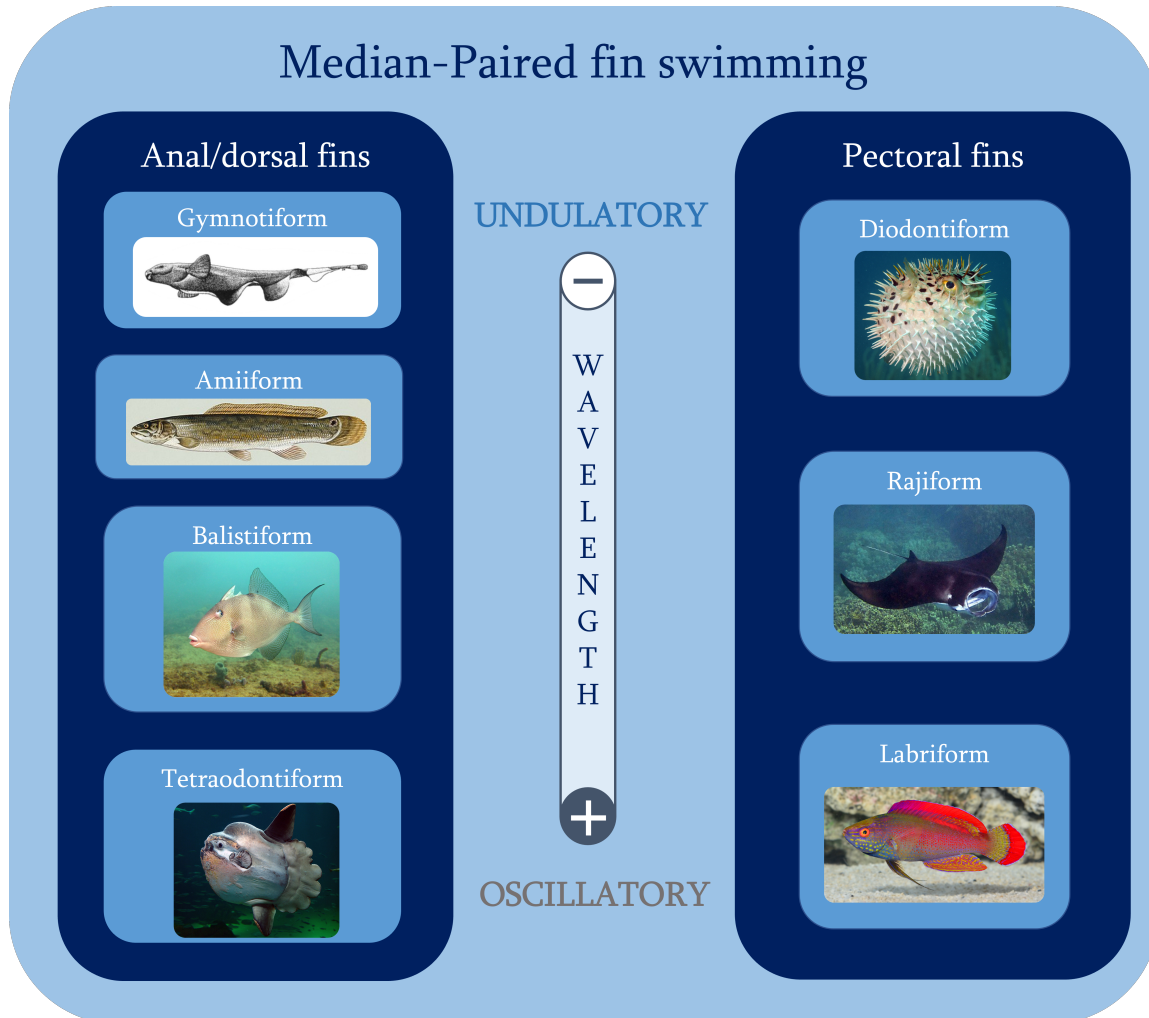
2.5.   Median paired fin (MPF)

Figure 2.21: Classification of MPF swimming modes according to the wavelength and to the fins used for propulsion

Median paired fin swimming strategy includes a large variety of animals of different sizes and shapes. A first classification can be done by dividing fishes that use the dorsal and the anal fins from fishes using pectoral fins, and in these subcategories, swimming modes can be classified according to whether they are undulatory or oscillatory. In the same way, as BCF swimmers, they produce a traveling wave on the fin to push water backward to receive a forward-directed force. The classification of MPF swimming modes is shown in Figure 2.21.

2.5.1. Amiiform, gymnotiform and balistiform swimming

Amiiform animals swim by undulating their dorsal fin, which runs over the entire length of their body, and it is composed of a flexible membrane that is moved by compact fin ribs. These fishes are slow swimmers, but they are quite agile, as they can swim backward, inverting the direction of wave propagation, and they can tilt the axis of their fin to generate lateral forces and moments for turning. Amiiform swimming is characteristic of a small number of species, like the bowfin and the Aba Aba knifefish, shown in Figure 2.22a [105].

Gymnotiform fishes are analogous to amiiforms, as they move their anal fin in the same way as amiiforms move their dorsal fin, so their swimming performances are comparable. Amiiforms and gymnotiforms are ambush predators and prefer living in closed environments near the seabed, where they can hide to protect from larger predators and ambush their prey. Gymnotiforms swimming too is characteristic of a few species, one of which is the ghost knifefish, shown in Figure 2.22b [105].
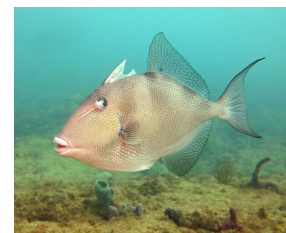
Balistiform fishes generate a traveling wave on both their dorsal and anal fin to achieve propulsion, and their fins are usually shorter than those of amiiform and gymnotiforms. Their body is flat and compressed laterally, and they have a caudal fin that they occasionally move to increase endurance [105]. The most common species found in this category is the triggerfish, shown in Figure 2.22c.

(a) Aba Aba knifefish - Amiiform   (b) Ghost knifefish - Gymnotiform   (c) Triggerfish - Balistiform

Figure 2.22: Amiiform, gymnotiform and balistiform fishes

The Bionic Undulating Fin Robot, shown in Figure 2.23a, is characterized by a locomotion strategy inspired by amiiform swimming. Its dorsal fin comprises a thin membrane enclosing some rigid equispaced ribs. Each rib is actuated by a scotch-yoke mechanism, which takes its motion from the rotation of a cam. A single motor drives all the fin ribs, as all the cams are mounted on the same shaft with a proper relative angle to obtain a traveling wave. In a successive version of this robot, ribs are actuated independently to allow more flexibility in the choice of kinematic parameters [142]. The Robotic Knifefish, shown in Figure 2.23b, is inspired by the black ghost knifefish and it falls into the

gymnotiform category. It is featured by a rigid body and a flexible anal fin composed of 20 ribs, each actuated independently by a servomotor [27].
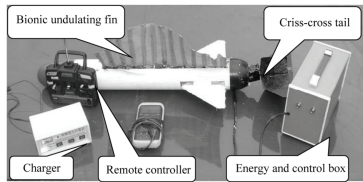
(a) Bionic Undulating Fin Robot, Xie, 2016, National University of Defense Technology [142]
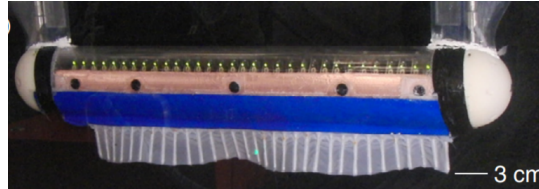
(b) Robotic Knifefish, Curet, 2011, Northwestern University [27]

Figure 2.23: Robots insired by amiiforms and gymnotiforms

2.5.2. Tetraodontiform swimming

Tetraodontiform swimming mode is very particular, and only a minimal number of species belong to this category. The ocean sunfish, shown in Figure 2.24, is the largest and the most representative. Its body is 2 m wide and it is featured by very tall dorsal and anal fins. Its body is rigid and does not have a caudal fin, so it propels itself only with the paired movements of dorsal and anal fins, which show an oscillatory behavior since the ribs moving the fins have a very small phase difference. This kind of locomotion does not allow high speed, and its energy efficiency is lower than other fishes. In addition, the large size of the fish and the small force developed by the fins make it also very clumsy in maneuvering in closed environments. For these reasons, there is no interest in developing robots inspired by this category of fishes[105].

Figure 2.24: Ocean Sunfish

2.5.3.   Diodontiform swimming

Fishes found in this category use undulating pectoral fins and oscillating dorsal and anal fins to generate thrust. The movement of their pectoral fins is quite complex since a wave with a very short wavelength can be superimposed to an oscillation of the fin with a longer wavelength. The most common examples of diodontiform fishes are the porcupine fish and the pufferfish, shown in Figure 2.25. They live in shallow water reefs, and they are slow and quite inefficient swimmers, relying on spines or poison to chase away predators [105].

Figure 2.25: Pufferfish

Due to their poor swimming performances, diodontiform fishes are not a source of inspiration for biomimetic robots.

2.5.4.   Rajiform swimming

Rajiform swimming is typical of fishes like skates and rays, belonging to the order *Batoidea*. Batoids are characterized by a unique morphology, having dorsoventrally flattened bodies and large pectoral fins fused to the head, forming a wide flat structure, with the shape of a disc or diamond [98, 99].
Their fins are extremely flexible, since their skeleton is made of cartilaginous ribs extending laterally from the body into the fin, as shown in Figure 2.26 [99, 105].

(a) Skeleton of the Common Stingray, Salazar, *Ocean Enigeering* (2018) [105]

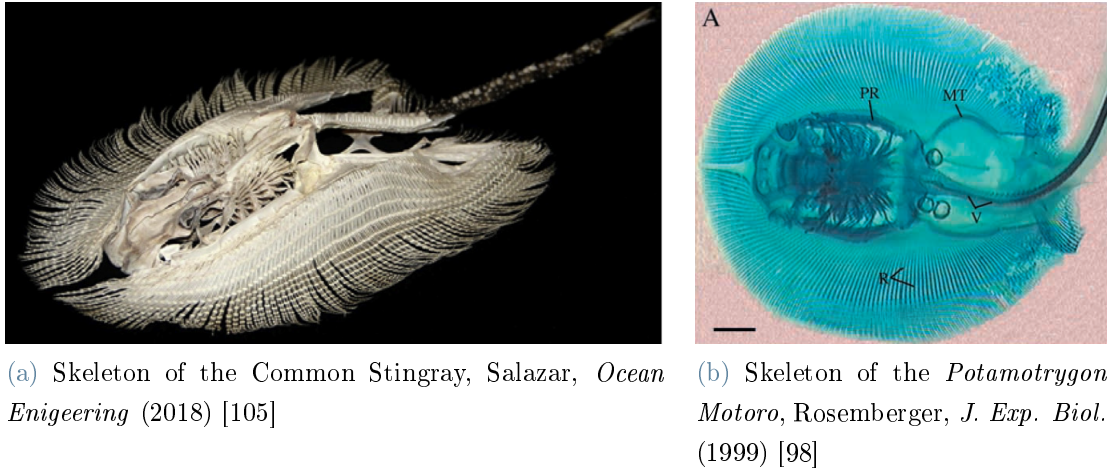(b) Skeleton of the *Potamotrygon Motoro*, Rosemberger, *J. Exp. Biol.* (1999) [98]

Figure 2.26: Skeletons of batoid fishes

These ribs are moved individually in a vertical direction, creating a wave along the fin length, whose kinematics differ according to the species. Fishes with both undulatory and oscillatory behaviors are found in this category, as shown in Figure 2.27, where some batoid species are presented, highlighting the number of waves present on the fish's body during its movement. It is possible to observe that batoid fishes fully occupy the continuum between oscillation and undulation and that the shape of the fins passes from being circular for fully undulatory locomotion to being triangular for fully oscillatory locomotion. Many species lying in the middle of this continuum can vary their wavelength to get the advantages of oscillatory or undulatory swimming according to the situation. The completely oscillatory swimming mode of batoids can also be called *Mobuliform* [98].

Figure 2.27: Batoid fishes ordered according to the number of waves along the fish body during swimming

Undulatory pectoral fins have evolved to optimize their flexibility, as this feature is not only fundamental for the generation of the traveling wave, which allows propulsion, but also for feeding. These fishes live near the seabed, and they hunt smaller prey with

a tactic called *tenting*. They cover their prey with their body and trap it by pressing the edges of their fins against the seabed so that it cannot escape. Fins with extreme flexibility make these fishes extremely agile in turning maneuvers, giving them the ability to perform turns with a very small or even null curvature radius [49]. On the other side, oscillatory pectoral fins do not show this level of multifunctionality, and they have evolved only to optimize swimming performances. Although very flexible, they are slightly more rigid than undulatory batoid fins, particularly in the region surrounding the leading edge, where stress concentration is the highest. This gives them the possibility of generating more thrust and achieving a higher speed, with the drawback of reduced maneuverability. These fishes live in pelagic environments and may exploit oceanic currents to glide, moving without consuming energy. Moreover, some species, like the giant manta, never stop swimming throughout their entire lifespan because they need to keep in motion to push oxygenated water into their gills and absorb plankton with their mouth, suggesting that their motion is characterized by a high energy efficiency [49]. Some batoids are negatively buoyant, and their fin movements are slightly asymmetric, with a downstroke more powerful than the upstroke, so that they can generate a lift force in a similar way to the flapping flight of birds [107].

The difference between undulatory and oscillatory swimming can be appreciated by looking at Figure 2.28, where the fin deformation of three different species occurs during fin movement. It is possible to note that the *Dasyatis Sabina* (Figure 2.28A) shows more than an entire wavelength along its body, while the *Gymnura Micrura* (Figure 2.28B) exhibits approximately one wavelength, and the *Rhinoptera Bonasus* is characterized by a more oscillatory behavior, with less than a half wavelength along its body [98].
The differences in fin movements not only concern the wavelength but also amplitude and frequency of motion vary among the species. It has been observed that undulatory species, characterized by a shorter wavelength, exhibit a small amplitude of fin movement, about $0.2 \sim 0.3$ times the fin width, since their stretching capability is limited, despite the high flexibility of the fins. The frequency of the fin movement is quite high, and it can reach 3 Hz for *Dasyatis Sabina*. Conversely, oscillatory species display less than half of a wave along the fin length; thus, they can exploit all the flexibility of their fins to achieve a high amplitude of movement, up to about $0.4 \sim 0.5$ times the fin width. The frequency of fin movement decreases as the locomotion behavior becomes more oscillatory, with the cownose ray moving their fins at about 0.9 Hz and the giant manta at about 0.3 Hz.
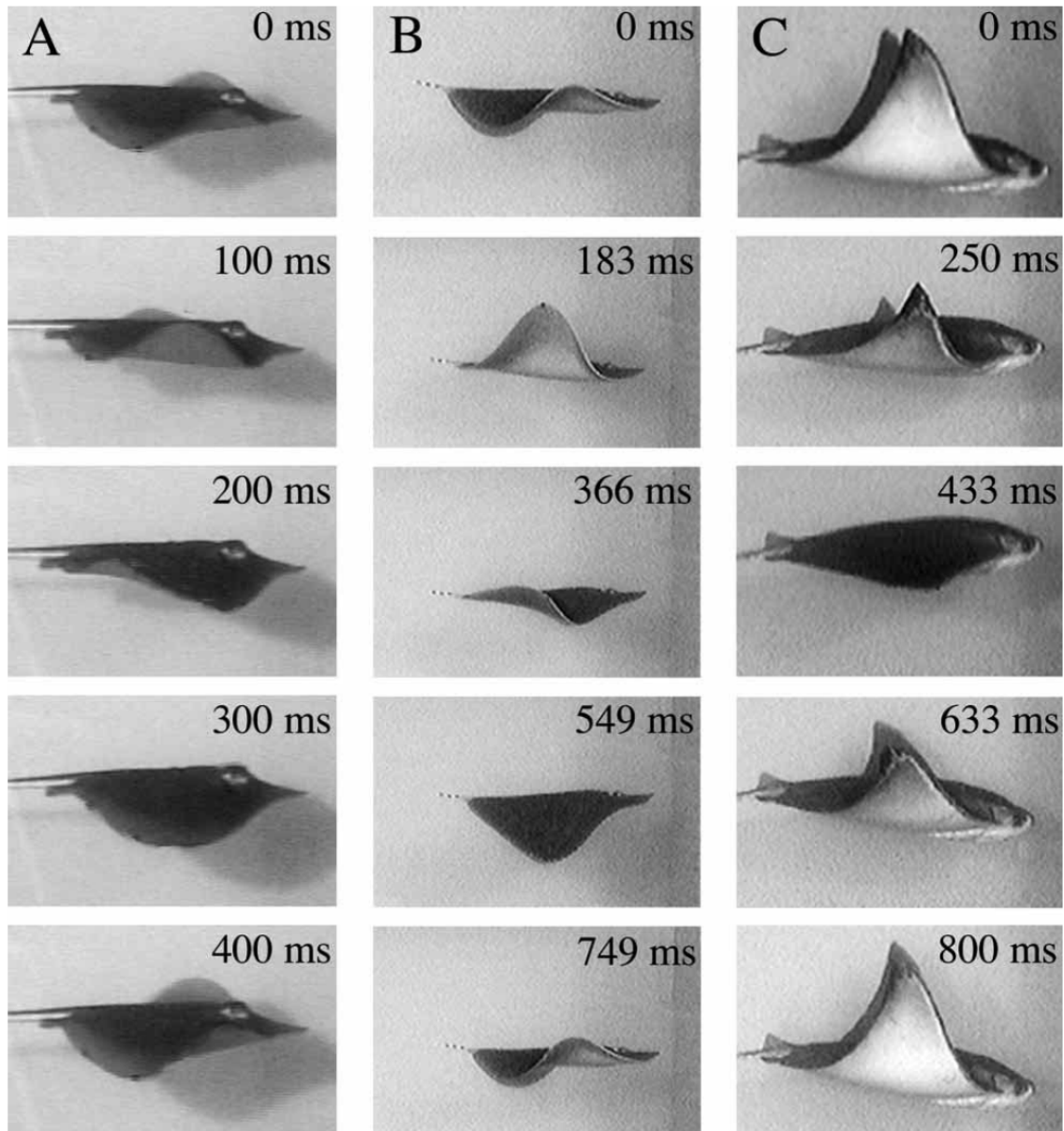
Figure 2.28: Successive lateral video images of (A) *Dasyatis Sabina*, (B) *Gymnura Micrura* and (C) *Rhinoptera bonasus*, Rosemberger, *Journ. Exp. Biol.* (2001) [98]

Being the frequency inversely proportional to the wavelength, the propagation velocity of the wave on the fin, normalized with respect to the fish size, is approximately the same for all batoids. Moreover, the ratio between the swimming speed and the wave propagation velocity is $0.8 \sim 0.9$ for all species [98]. This implies that the water is pushed backward by the traveling wave with a velocity just slightly greater than the relative velocity between the fish and the surrounding water, meaning that the energy lost in the wake is a small fraction of the consumed energy, and the efficiency of rajiform

swimming mode is very high, reaching 90% for the largest species, and making them efficient swimmers on a par with thunniform fishes [39].

Different behavior between oscillatory and undulatory species is also observed during turning maneuvers, as shown in Figure 2.29. Fishes with a more undulatory behavior perform turning maneuvers propagating waves on the fins in opposite directions so that they generate two equal and opposite forces on the two fins, which produce a moment about the yaw axis. This technique gives them very high maneuverability since they can curve even with a null curvature radius. However, this kind of maneuver is quite energy demanding since their wide flat shape is characterized by a significant moment of inertia about the yaw axis, so that high forces need to be generated on the fins. Instead, fishes with a more oscillatory swimming mode do not need such small curvature radii, as they tend to live in pelagic environments where no obstacles are present; thus, they prefer using a more energy-efficient turning maneuver called banking, which is similar to the one performed by airplanes. During turning, they stop fin flapping, and, assisted by the high swimming velocity, they glide by tilting their body about the rolling axis so that the generated lift force is directed laterally, and a moment about the yaw axis is produced. Fishes do not consume energy to move their fins during this maneuver, but the curvature radius is large. Some species with behavior between fully undulatory and fully oscillatory can perform a combination of these two maneuvers, banking and generating small amplitude waves on their fins [91].

(a) Turning maneuver of a bat ray (undulatory)
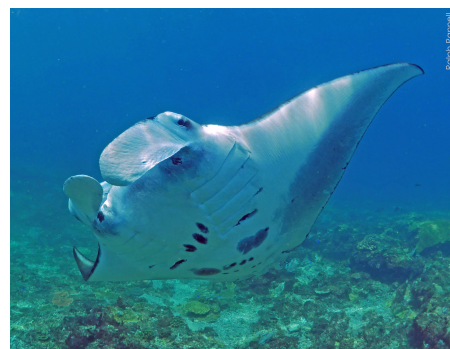
(b) Banking maneuver of a giant manta (oscillatory)

Figure 2.29: Different turning maneuvers of batoid fishes

The high efficiency of rajiform locomotion, combined with their excellent turning performances, makes these fishes a valuable source of inspiration for many biomimetic robots, which are described in the following chapter.

2.5.5. Labriform swimming

The labriform swimming category includes most MPF swimming fishes, like wrasses and parrotfish, shown in Figure 2.30. They adapted their swimming strategy to live in closed quarter environments, so they swim at low speed and are very agile in turning and diving maneuvers.
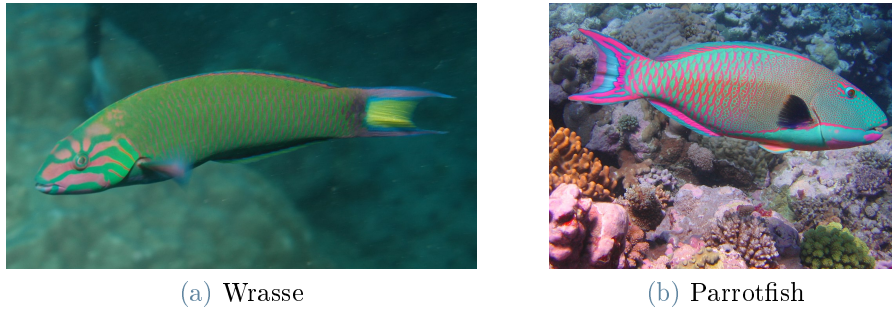

(a) Wrasse

(b) Parrotfish

Figure 2.30: Labriform fishes

The fin movements of labriforms are of two types: flapping and rowing. Rowing motion consists of a power stroke when fins are moved backward and towards the body axis and a recovery stroke when the fins are brought forward. During the recovery stroke, the fins are more open than in the power stroke to allow water to pass through the fin and reduce the drag force.

Nevertheless, the energy efficiency of this motion is very low, and the generated thrust is discontinuous, as only the power stroke contributes to propulsion. On the other hand, flapping motion is more efficient because the thrust is produced in almost all the phases of fin movement, which consists of a periodical vertical displacement of the leading edge while the rest of the fin remains passive.

The fin is moved downwards and away from the body in the first phase. Then, although the fin's leading edge is pushed forward, the downward movement gives it a high angle of attack, generating lift on the fin, which is pulled forward. Then, the fin is moved backward and toward the body, pushing water backward, and finally, the leading edge of the fin is moved upwards while the fin is closed. The flapping mode allows to generate a propulsive force in all phases of the movement; thus, it is more efficient than rowing mode, but its efficiency is still not comparable to one of the other swimming modes [111].
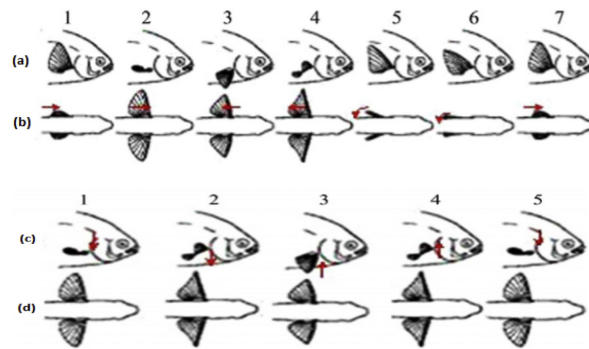
Figure 2.31: (a) Side view of rowing - (b) Top view of rowing - (c) Side view of flapping - (d) Top view of flapping, Sfakiotakis, *IEEE Journal of Oceanic Engineering* (1999) [111]

In Figure 2.31 the kinematics of fin motion for rowing and flapping modes of labriform swimming are displayed.

In Figure 2.32a, a fish robot inspired to labriform swimming is presented. Two servomotors actuate each fin of this robot: one is used to perform the basic flapping or rowing movement, and the other to rotate the fin during flapping to change its orientation and the angle of attack [115]. Many other bioinspired robots have pectoral fins, which mimic labriform swimming, and an example is the robot shown in Figure 2.32b, which can perform both flapping and rowing locomotion. In addition, its pectoral fins are connected to the fish body with flexible feathering joints, which enhance swimming performances at high frequencies of fin flapping, and it can use a caudal fin as a secondary way of propulsion when a greater velocity is required [10].
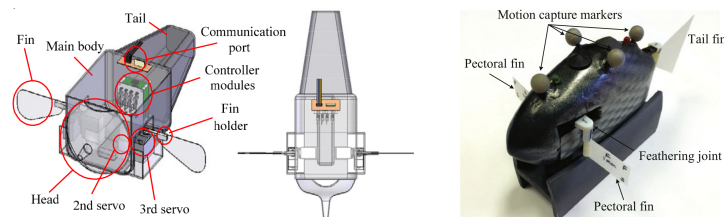
(a) Labriform Fish robot, Sitorus, 2009, Bandung Institute of Technology [115]

(b) Robotic fish with flexible pectoral fins, Behbahani, 2016, Michigan State University [10]

Figure 2.32: Biomimetic robots inspired by labriform fishes

2.6.   Hydrodynamic principles of fishes and cetacean locomotion

Fishes and cetaceans move with a high Reynolds number, and their swimming propulsion depends primarily on the inertia force. The fluid's viscosity has an important role in creating the vorticity shed into the wake, whereas the viscous drag causing skin friction is of marginal importance, as it affects the flow only in a thin boundary layer surrounding the body surface. This means that thrust generation and drag resistance can be studied separately [138].
Both BCF and MPF swimming modes are characterized by a periodic motion of the fins pushing water backward, so a forward thrust is obtained thanks to momentum conservation. During constant velocity swimming, the momentum in the backward jet created by the fin movement is counterbalanced by the momentum created by viscous friction as the fish drags forward some of the fluid surrounding its body.

The mechanism of thrust generation is a very complex phenomenon, as it depends on the pressure distribution of a three-dimensional, unsteady flow, where the interaction between vortices is of fundamental importance. Moreover, each species is characterized by a peculiar fin geometry and kinematics, which significantly affect swimming performances.

Nevertheless, the general basic principles behind fish propulsion, which are common to both BCF and MPF swimmers, can be understood making some simplifications:

- **inviscid flow**: the role of viscosity is marginal in thrust generation; thus, the propulsive forces can be analyzed considering only the variation of momentum in the flow caused by the movement of the fins. The drag resistance acting on the body surface can be studied separately.

- **amplitude of fin displacement much smaller than body length**: the fin moves only in a direction perpendicular to the swimming direction of the fish, and the amplitude of motion is much smaller than the fish length [73, 137, 139].

- **fin of infinitesimal thickness**: this assumption is valid for the vast majority of MPF fishes and BCF swimmers having tails with a high aspect ratio, such as rays, tunas, and sharks [73, 137, 139].

Lying on these assumptions, two models that capture the mechanism of fish swimming propulsion have been developed, leading to similar results.

2.6.1. Swimming of a waving plate

In the first model, developed by Wu, the fin can be regarded as a deformable flat plate, producing a waving motion, as shown in Figure 2.33. The fin is considered to have an infinite span, so to neglect the side effects occurring at the fin extremities. These are different for every fish species and give rise to a spanwise flow of secondary importance. Thus, the flow can be considered only two-dimensional [139].
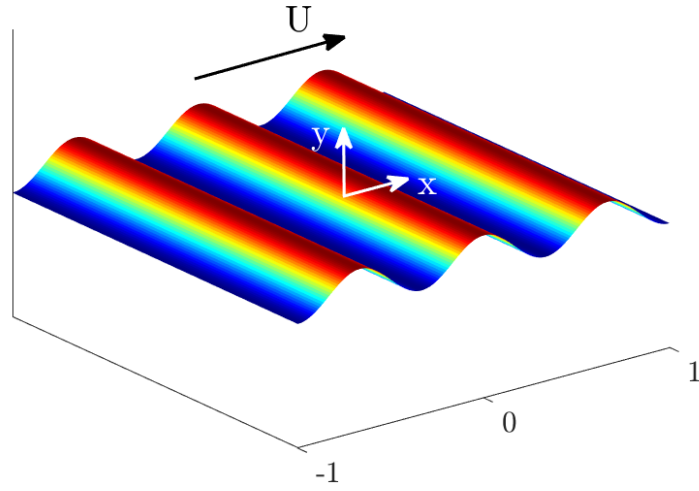

Figure 2.33: Plate of infinitesimal thickness producing a waving motion

The flow generated by the plate satisfies the continuity equation and the Navier-Stokes equation for incompressible and inviscid fluids (Eq. 2.7), where $\mathbf{v} = (U + u)\mathbf{i} + v\mathbf{j}$.

$$\begin{cases} \dfrac{\partial \mathbf{v}}{\partial t} + (\mathbf{v} \cdot \nabla)\,\mathbf{v} = -\dfrac{1}{\rho}\nabla p \\ \nabla \cdot \mathbf{v} = 0 \end{cases} \tag{2.7}$$

Considering the swimming velocity of the fish U constant and much greater than the fin displacement velocity components in u and v, it is possible to simplify the Navier-Stokes equation, obtaining Equation 2.8.

$$\frac{\partial \mathbf{v}}{\partial t} + U\frac{\partial \mathbf{v}}{\partial x} = -\frac{1}{\rho}\nabla p \tag{2.8}$$

The acceleration of the fluid is also equal to the gradient of a function $\phi(\mathbf{x}, t)$, called

acceleration potential, defined as follows:

$$\phi(\mathbf{x}, t) = \frac{p_\infty - p}{\rho}, \tag{2.9}$$

where p_∞ is the pressure of the fluid at infinite distance from the body.

Combining Equation 2.9 and the continuity equation (Equation 2.7) it is possible to obtain:

$$\nabla^2 \phi = 0 \tag{2.10}$$

This means that velocity and pressure fields can be found by solving the Laplace equation for the acceleration potential. Moreover, working with the acceleration potential is particularly convenient because it is a regular function in the whole domain, as pressure is continuous everywhere inside the flow, particularly in the wake, unlike velocity that, for an inviscid flow, may allow discontinuities in the wake [137].

The motion of the plate can be written in the most general form as:

$$y = h(x, t) \qquad -\frac{L}{2} < x < \frac{L}{2} \tag{2.11}$$

where L is the length of the plate, and the amplitude of $h(x, t)$ and of $\dfrac{\partial h}{\partial x}$ are much smaller than L.

The normal component of the velocity in correspondence of the plate surface is equal to the velocity of the deformation of the plate itself, thus:

$$v = \frac{\partial h}{\partial t} + U \frac{\partial h}{\partial x} \qquad \text{for} \quad y = 0^\pm, \quad -\frac{L}{2} < x < \frac{L}{2} \tag{2.12}$$

The same boundary condition can be expressed in terms of the potential $\phi(\mathbf{x}, t)$:

$$\frac{\partial \phi}{\partial y} = \frac{\partial^2 h}{\partial t^2} + 2U \frac{\partial^2 h}{\partial t \partial x} + U^2 \frac{\partial^2 h}{\partial x^2} \qquad \text{for} \quad y = 0^\pm, \quad -\frac{L}{2} < x < \frac{L}{2} \tag{2.13}$$

Since $\dfrac{\partial \phi}{\partial y}$ is an even function with respect to y, ϕ is an odd function with respect to y, and being ϕ also a regular function, it results that:

$$\phi(x, 0^\pm, t) = 0 \qquad \text{for } |x| \geq \frac{L}{2} \tag{2.14}$$

Since viscous forces are neglected in this analysis, the problem has infinite solutions, and another boundary condition should be added to complete the definition of the problem. It

is necessary to impose the Kutta condition at the trailing edge of the plate, which means that, for a constant velocity U, the streamlines on the top and bottom sides of the plate are parallel. This condition can be expressed as:

$$|\phi(\frac{L}{2}, 0^\pm, t)| < \infty \tag{2.15}$$

The solution of Equation 2.10 satisfying the aforementioned boundary condition can be found by expressing $h(x, t)$ as a Fourier series and making use of conformal transformations [137]. Having found the potential ϕ the pressure difference across the plate can be evaluated, according to Equation 2.9:

$$\Delta p = \rho \left[\phi(x, 0^-, t) - \phi(x, 0^+, t) \right] \tag{2.16}$$

Hence, the forces acting on the plate can be found by integrating the pressure difference on the plate surface:

$$
\begin{aligned}
L &= \int_{-\frac{L}{2}}^{\frac{L}{2}} \Delta p \, \mathrm{d}x \\
T &= \int_{-\frac{L}{2}}^{\frac{L}{2}} \Delta p \left(\frac{\partial h}{\partial x} \right) dx + T_s = T_p + T_s,
\end{aligned}
\tag{2.17}
$$

where L is the lift force, i.e. the force acting in the y direction, normal to the plate, and T is the thrust force, acting in the x direction. This last is characterized by two contributions, the former T_p is due to the pressure difference across the plate, the latter T_s is due to the pressure singularity next to the leading edge, and it is called leading-edge suction [137]. Since the thickness of the plate is zero, the flow is required to make a 180° turn around the leading edge, as shown in Figure 2.34, giving rise to a theoretically infinite centrifugal inertia, pulling the fin forward [95].
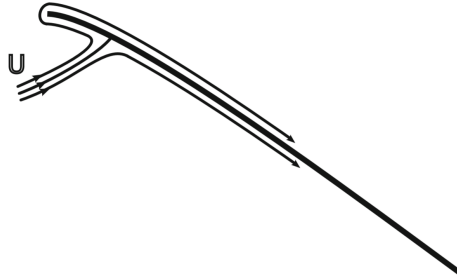

Figure 2.34: Flow around the leading edge of a zero thickness plate, Ramesh, *Theor. Comput. Fluid Dyn.* (2018) [95]

Therefore, the force acting on the leading edge should be evaluated using the Blasius

formula:

$$T + iL = \frac{i\rho}{2} \oint_{\epsilon} w \mathrm{d}z, \tag{2.18}$$

where the circulation of the complex velocity $w = u + iv$ is evaluated on a small circle of radius ϵ centered in the leading edge.

As far as fish locomotion is concerned, the deformation of the fin $h(x,t)$ appears in the form:

$$h(x,t) = A(x)\cos{(kx - \omega t)}, \tag{2.19}$$

where k is the wavenumber, ω is the circular frequency, and $A(x)$ is the amplitude of fin displacement.

$A(x)$ is usually a constant for most MPF fishes since the amplitude of fin motion does not vary along the fin length; for most species, it varies along the fin span, but the effect of the amplitude variation along the span cannot be considered in a two-dimensional flow analysis. For BCF swimmers, $A(x)$ is a linear or quadratic function of x, as the amplitude of fin displacement increases towards the fish's tail. Equation 2.19describes a wave propagating from the head to the fish's tail. This movement pushes the surrounding water backward with a velocity equal to the wave propagation velocity $c = \dfrac{\omega}{k}$. This means that the wave propagation velocity c must be greater than the swimming velocity U to transfer momentum to the surrounding water. Figure 2.35 displays the thrust generated by the wave propagation on a flat plate per unit of span for both a uniform amplitude and a linearly varying amplitude of deformation. The obtained values are referred to a plate of length $2\,\mathrm{m}$, and for a swimming velocity of $1\,\mathrm{m/s}$, and they have been calculated using the solution of Equations 2.17 and 2.18, obtained by Wu [137].

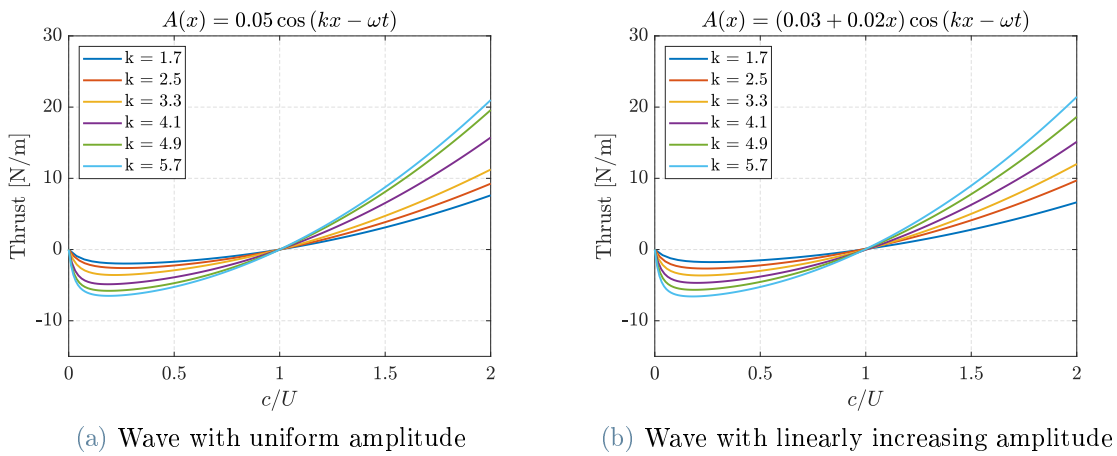(a) Wave with uniform amplitude   (b) Wave with linearly increasing amplitude

Figure 2.35: Thrust generated by the wave propagation on a flat plate

It is possible to observe that a positive thrust is generated only for $c > U$, whereas for

$c = U$ the generated force is zero. If $c = U$, the plate moves following a sinusoidal path fixed in space, without exchanging momentum with the surrounding fluid. Finally, in the case $c < U$, the propulsive force is negative, as the movement of the fin subtracts momentum from water [137].

According to the energy conservation principle, the input power due to the movement of the fin is the sum of the useful power of the thrust force and the time derivative of the kinetic energy in the fluid [137].

$$P = TU + \frac{\mathrm{d}E}{\mathrm{d}t} \tag{2.20}$$

The total power spent by the body to perform this movement corresponds to the product between the lateral velocity of the plate and the lift force $-L$ exerted by the body on the fluid:

$$P = -\int_{-\frac{L}{2}}^{\frac{L}{2}} \Delta p \frac{\partial h}{\partial t} \mathrm{d}x \tag{2.21}$$

The rate of change of kinetic energy in a fluid can be expressed as the scalar product of the pressure force and velocity at the boundaries of the domain [116]:

$$\frac{\mathrm{d}E}{\mathrm{d}t} = -\int_{S_B} \mathbf{v} \cdot p\mathbf{n} \mathrm{d}S_B \tag{2.22}$$

where $\mathbf{n}$ is the vector normal to the surface pointing outwards. The integral over the surface S_B, in this case, is the integral along the length of the plate plus the power of the leading-edge suction. Therefore, substituting to $\mathbf{v}$, its expression obtained in Equation 2.12, the time derivative of the kinetic energy becomes:

$$\frac{\mathrm{d}E}{\mathrm{d}t} = -\int_{-\frac{L}{2}}^{\frac{L}{2}} \Delta p \left(\frac{\partial h}{\partial t} + U \frac{\partial h}{\partial x} \right) \mathrm{d}x - T_s U \tag{2.23}$$

Finally, the useful power is the product between the thrust force T, obtained in Equation 2.17, and the forward velocity U:

$$TU = U \int_{-\frac{L}{2}}^{\frac{L}{2}} \Delta p \frac{\partial h}{\partial x} \mathrm{d}x + T_s U \tag{2.24}$$

The energy balance expressed in Equation 2.20 states that not all the power spent by the fish is transformed into power useful to propel its body, but some power is lost to increase the kinetic energy in the wake. As the flow generated by the fin motion is unsteady, some of the lost kinetic energy is recovered in successive instants; however, a complete recovery is only possible if no vorticity is generated. Nevertheless, a body performing a

periodic motion in a fluid cannot exert a non-zero mean force without shedding vorticity
[116]. Thus, as the fin generates a thrust force, some kinetic energy is lost to the wake.
The amount of this lost power depends on the kinematics of fin motion, and it can be
quantified using the Froude efficiency.

$$\eta = \frac{\bar{T}U}{\bar{P}} \qquad \text{where} \qquad \bar{f} = \frac{1}{T} \int_{t}^{(t+T)} f(\tau) \mathrm{d}\tau \qquad (2.25)$$

In Figure 2.36, it is possible to observe the efficiency of a waving plate for a constant and
for a linearly varying amplitude.

(a) Wave with uniform amplitude   (b) Wave with linearly increasing amplitude
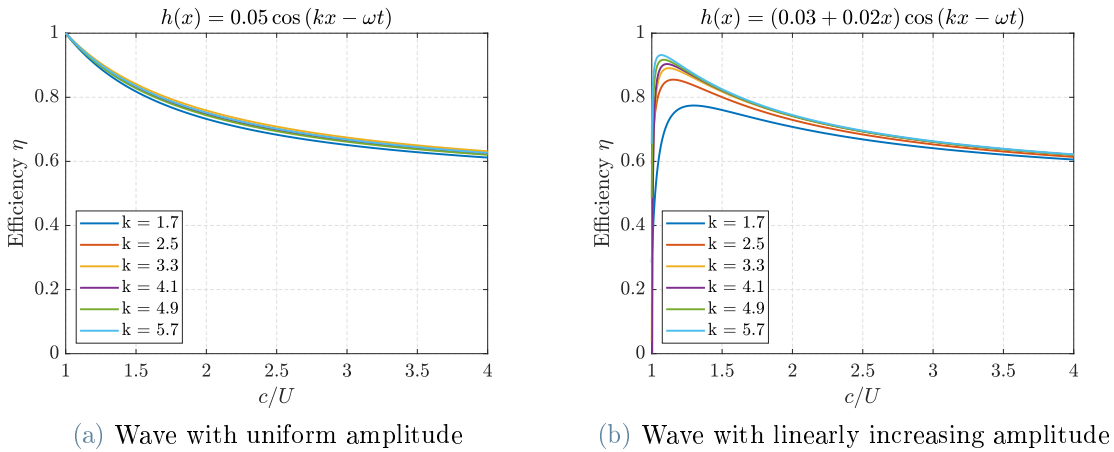
Figure 2.36: Energy efficiency of the wave propagation on a flat plate

The efficiency depends mainly on the ratio between the wave propagation velocity c and
the forward swimming velocity U, and that the dependency on wavelength and the type
of motion are less relevant. An important result is that when $c \to U$, the efficiency tends
to one, which means that no energy is wasted generating vortices in the wake. However,
it is not possible to generate a propulsive force without generating vortices [116], so the
thrust for $c = U$ is zero. Therefore, the kinematic parameters determining the wave
propagation velocity c are a trade-off between high energy efficiency and high propulsive
force. This model is able to explain the basic principle behind the swimming propulsion of
fishes, highlighting that the thrust generation is achieved thanks to the wave propagation
along the fin and that the efficiency of propulsion is related to the traveling wave velocity.
Nevertheless, the hypotheses of this model introduce several simplifications, such as the
bi-dimensionality of the flow and the infinitesimal thickness of the fin. Therefore, this
model is useful to understand the main mechanism of fish swimming, but it is not able to
reproduce the complex flow generated by the fin movements.

2.6.2. Slender body theory

The other model of fish swimming has been developed by Lighthill, and it considers the fish a slender body, which means that its dimensions and its movements perpendicular to its direction of locomotion are much smaller than its length and that its cross-section varies gradually along its length [73].
A drawing of a fish with these characteristics is displayed in Figure 2.37, where also the coordinate system adopted in the following discussion is shown. Since the fish is slender and the fin movement is only in one direction, the flow around it can be considered two-dimensional [73, 116].
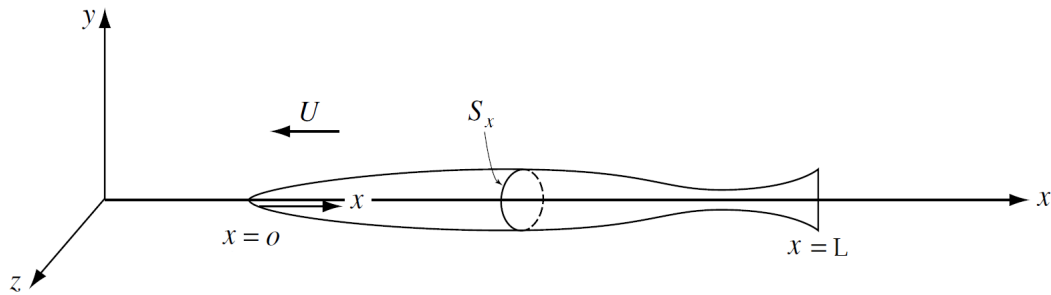
Figure 2.37: Slender fish of length L swimming in the negative x direction with velocity U, Sparemberg, *Journal of Engineering Mathematics* (2002) [116]

The flow is determined by the superimposition of the flow of constant velocity U in the swimming direction and the flow induced by the fin displacement described by the function $h(x,t)$. The velocity v induced by the fin movement is:

$$v = \frac{\partial h}{\partial t} + U\frac{\partial h}{\partial x} \tag{2.26}$$

where the time derivative accounts for the velocity caused by the motion of the fin itself, and the space derivative reflects the effect of the deformation of the fin in deflecting the flow from the x to the y direction. The y component of the momentum per unit of length of the fluid is:

$$p_y = \rho A(x)v(x,t) \tag{2.27}$$

where the ρ is the density of water and the term $\rho A(x)$ is called virtual or added mass. The added mass of a body is the mass of the surrounding fluid set into motion along with the body because of the pressure field around it.
For a uniform rectilinear motion of the body, the added mass is constant and depends only on the dimensions and the shape of the body; however, for more complex types of

motion, it depends also on the relative magnitude of linear and angular accelerations, and it varies with time [47]. For the hypothesis of a slender fish the added mass varies gradually along the length of the body and $\rho A(x)$ is a continuous function in the whole domain. This means that $\rho A(0) = 0$ for any possible shape or motion of the fish as the added mass upstream is null and $\rho A(x)$ is continuous.

The lift force in the y direction per unit length can be found as the time derivative of the momentum:

$$L = \frac{\mathrm{D}}{\mathrm{D}t} \left(\rho A(x) v(x,t) \right) = \left(\frac{\partial}{\partial t} + U \frac{\partial}{\partial x} \right) [\rho A(x) v(x,t)] \tag{2.28}$$

The total thrust is given by two contributions: the first T_1 is the resultant of the lift directed in the longitudinal direction, the second T_2 is the pressure force due to the gradual change of shape of the body along its length. The first contribution T_1 can be found by just multiplying the lift force for the tangent of the bending angle of the body:

$$T_1 = -\left(\frac{\partial}{\partial t} + U \frac{\partial}{\partial x} \right) [\rho A(x) v(x,t)] \frac{\partial h}{\partial x} \tag{2.29}$$

Integrating the force over the body length the instantaneous total thrust T_1 becomes:

$$T_1 = -\rho \int_0^L \left(\frac{\partial}{\partial t} + U \frac{\partial}{\partial x} \right) \left(\rho A(x) v(x,t) \frac{\partial h}{\partial x} \right) \mathrm{d}x + \rho \int_0^L \frac{\partial v}{\partial x} v(x,t) A(x) \mathrm{d}x \tag{2.30}$$

Hence, T_1 results:

$$T_1 = -\rho \int_0^L \frac{\partial}{\partial t} \left(A v \frac{\partial h}{\partial x} \right) \mathrm{d}x - \rho U \int_0^L \frac{\partial}{\partial x} \left(\rho A v \frac{\partial h}{\partial x} \right) \mathrm{d}x + \rho \int_0^L \frac{\partial v}{\partial x} v A \mathrm{d}x \tag{2.31}$$

The average thrust over a period can be evaluated taking the mean integral of each of these terms. For a periodic motion the first integral is zero, and the force T_1 reduces to:

$$T_1 = -\rho U \overline{\int_0^L \frac{\partial}{\partial x} \left(A v \frac{\partial h}{\partial x} \right) \mathrm{d}x} + \rho \overline{\int_0^L \frac{\partial v}{\partial x} v A \mathrm{d}x} \tag{2.32}$$

where

$$\bar{f} = \frac{1}{T} \int_t^{(t+T)} f(\tau) \mathrm{d}\tau \tag{2.33}$$

The first integral in equation 2.32 is elementary, whereas the second can be integrated by parts, leading to:

$$T_1 = -\rho U \overline{\left(A v \frac{\partial h}{\partial x} \right) \Big|_0^L} + \rho \overline{\frac{1}{2} v^2 A \Big|_0^L} - \frac{1}{2} \rho \overline{\int_0^L v^2 \frac{\partial A}{\partial x} \mathrm{d}x} \tag{2.34}$$

The force T_2 can be written as the integral of pressure p of the fluid around the cross section S_x of the slender body translating in x direction.
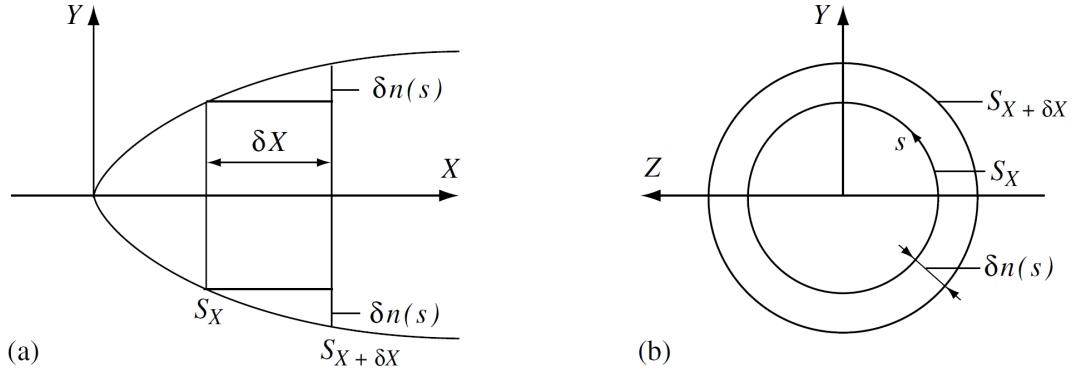

Figure 2.38: The cross sections S_x and $S_{x+\delta x}$, the length parameter s and $\delta n(s)$, Sparemberg, *Journal of Engineering Mathematics* (2002) [116]

Using the notation of Figure 2.38, it is possible to write:

$$T_2 = - \int_{S_x} p(s)\delta n(s)\mathrm{d}s \tag{2.35}$$

where both pressure and the normal versor vary along the circumferential coordinate s as the fish is undergoing the movement $h(x,t)$. The y component of the momentum of the fluid is $\rho v A(x)$, and due to the change of cross-section, there is a momentum variation equal to:

$$\rho v \delta A = \rho v \left[A(x+\delta x) - A(x)\right] = \rho v \frac{\mathrm{d}A}{\mathrm{d}x}\delta x \tag{2.36}$$

The work done by the body to produce this change of momentum is equal to $\rho v^2 \frac{\mathrm{d}A}{\mathrm{d}x}\delta x$, as the body is moving with velocity v. During this motion, the body moves the fluid outwards of a distance δn against the pressure p. Thus, the body does an amount of work per unit of length equal to:

$$\int_{S_x} p(s)\delta n(s)\mathrm{d}s \tag{2.37}$$

The total amount of work per unit length is then equal to the variation of kinetic energy in the fluid, so:

$$\frac{1}{2}\rho v^2 \frac{\mathrm{d}A}{\mathrm{d}x}\delta x = \int_{S_x} p(s)\delta n(s)\mathrm{d}s + \rho v^2 \frac{\mathrm{d}A}{\mathrm{d}x}\delta x \tag{2.38}$$

Combining Equation 2.35 and Equation 2.38 and integrating over the length of the body,

it is possible to find the average force T_2:

$$T_2 = \overline{\int_0^L \frac{1}{2}\rho v^2 \frac{\mathrm{d}A}{\mathrm{d}x}\mathrm{d}x} \tag{2.39}$$

Hence, the total thrust resulting from the sum of T_1 and T_2 can be found from Equation 2.34 and Equation 2.39.

$$T = T_1 + T_2 = -\rho U \overline{\left(Av\frac{\partial h}{\partial x}\right)}\Big|_0^L + \rho\overline{\frac{1}{2}v^2 A}\Big|_0^L \tag{2.40}$$

Remembering that $A(0) = 0$ for the hypothesis of a slender fish, Equation 2.40 can be evaluated and rearranged in the following final form [73, 116].

$$T = \frac{1}{2}\rho A(L)\left[\overline{\left(\frac{\partial h}{\partial t}\right)^2} - U^2\overline{\left(\frac{\partial h}{\partial x}\right)^2}\right]_{x=L} \tag{2.41}$$

This model allows determining the generated thrust considering the interaction with the fluid occurring only at the trailing edge, implying that the tail dynamics represent the cumulative effect of the hydrodynamics of the upstream flow over the rest of the body [47]. As far as fish locomotion is concerned, the function $h(x,t)$ usually appears in the form:

$$h(x,t) = A(x)\cos(kx - \omega t), \tag{2.42}$$

and the total thrust for a motion with uniform amplitude is shown in Figure 2.39. The same graph can be obtained with any function $A(x)$, provided that the amplitude of motion at the trailing edge of the tail is the same.
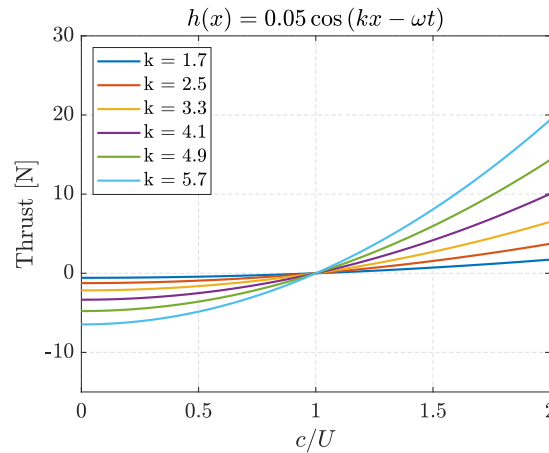
Figure 2.39: Thrust generated by the waving motion of a slender fish

By comparing this graph with Figure 2.35, it is possible to observe that both models capture the main characteristic of this motion, which is that a positive thrust can be generated only for a wave propagation velocity greater than the swimming velocity ($c > U$), and that the generated force increases as the wavelength ($2\pi/k$) decreases.

The work done by the fish to perform this movement $h(x,t)$ can be calculated as the product between the lift force and the velocity of the movement:

$$P = -\int_0^L L(x,t)\frac{\partial h}{\partial t}\mathrm{d}x \tag{2.43}$$

Equation 2.43 can be rearranged in the form:

$$
\begin{aligned}
P &= \rho \int_0^L \frac{\partial h}{\partial t}\left(\frac{\partial}{\partial t} + U\frac{\partial}{\partial x}\right)[A(x)v(x,t)]\,\mathrm{d}x \\
&= \rho \int_0^L \left(\frac{\partial}{\partial t} + U\frac{\partial}{\partial x}\right)\left[\frac{\partial h}{\partial t}A(x)v(x,t)\right]\mathrm{d}x - \rho\int_0^L \frac{\partial v}{\partial t}v(x,t)A(x)\mathrm{d}x \\
&= \frac{\partial}{\partial t}\left[\rho\int_0^L \frac{\partial h}{\partial t}v(x,t)A(x)\mathrm{d}x - \frac{1}{2}\rho\int_0^L v(x,t)^2 A(x)\mathrm{d}x\right] + \rho U\left(\frac{\partial h}{\partial t}v(x,t)A(x)\right)\Big|_0^L
\end{aligned}
\tag{2.44}
$$

Taking the average over one period of this last expression, the time derivative is null, and only the last term remains, which can be expressed in the following form since $A(0) = 0$.

$$P = \rho U A(L)\left[\overline{\frac{\partial h}{\partial t}\left(\frac{\partial h}{\partial t} + U\frac{\partial h}{\partial x}\right)}\right]_{x=L} \tag{2.45}$$

This corresponds to the product of the lateral velocity of the tail and the rate of shedding lateral momentum [73]. According to this model, the loss of kinetic energy into the fluid occurs at the trailing edge of the tail too, and its rate at which kinetic energy is shed is the product of the kinetic energy due to the lateral movement of the trailing edge and the forward velocity U:

$$\frac{\mathrm{d}E}{\mathrm{d}t} = \frac{1}{2}\rho v(L,t)^2 A(L)U, \tag{2.46}$$

which averaged over one period gives:

$$E = \frac{1}{2}\rho U A(L)\left[\overline{\frac{\partial h}{\partial t} + U\frac{\partial h}{\partial x}}\right]_{x=L} \tag{2.47}$$

Combining Equation 2.41, Equation 2.45, and Equation 2.47 it is possible to verify that the principle of conservation of energy is respected, as the total input power P is the sum of the power lost to the fluid $\frac{\mathrm{d}E}{\mathrm{d}t}$ and the power of the forward thrust TU. The Froude

efficiency of this kind of propulsion can be evaluated as:

$$\eta = \frac{\overline{T}U}{\overline{P}} \tag{2.48}$$

Generally, the lateral deformation of a fish can be described by a traveling wave:

$$h(x,t) = f(x)g\left(x - \frac{t}{c}\right) \tag{2.49}$$

where g is a periodic function. Substituting Equation 2.49 into Equation 2.45 and Equation 2.41, it is possible to obtain:

$$\eta = 1 - \frac{1}{2}\frac{\left(1 - \frac{U}{c}\right)^2 f^2(L)\overline{g'^2} + U^2 f'(L)^2\overline{g^2}}{\left(1 - \frac{U}{c}\right)f^2(L)\overline{g'^2}} \tag{2.50}$$

The efficiency depends on the ratio between the traveling wave velocity c and the swimming velocity U, and, as for the waving plate model, when $c \to U$, the efficiency tends to one, but the generated thrust is null. Thus, frequency and wavelength, which determine the traveling wave velocity, are tuned to find the best trade-off between high thrust and efficiency. The efficiency for a sine wave is shown in Figure 2.40.

(a) Wave with uniform amplitude   (b) Wave with linearly increasing amplitude
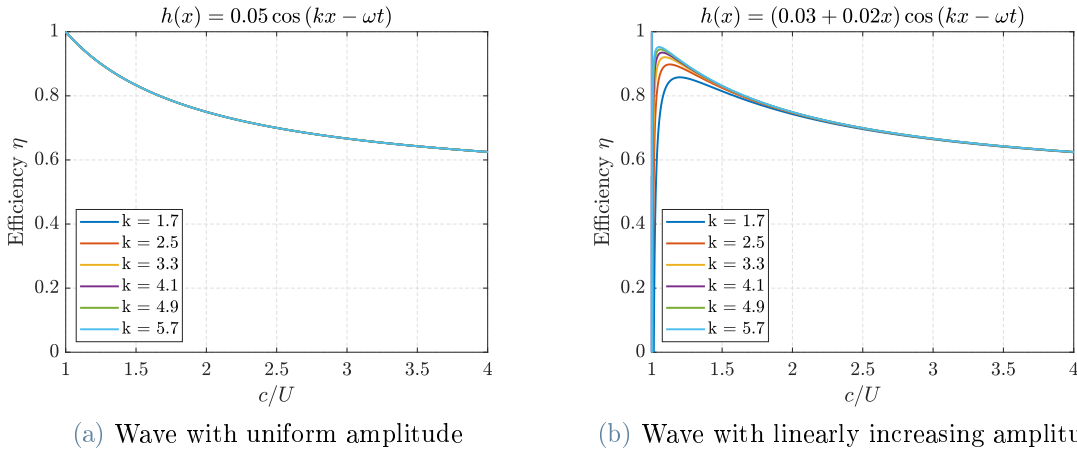
Figure 2.40: Energy efficiency of a slender fish swimming with a constant amplitude

These plots can be compared with the plots in Figure 2.36, showing the efficiency of the same motions obtained with the waving plate model, and it is possible to observe that the results are very similar.

2.6.3. Vortices in the wake

The swimming locomotion of a body immersed in a fluid is characterized by the transfer of both linear and angular momentum to the surrounding water. The angular momentum of the fluid appears in its vorticity, which is defined as the curl of the velocity.

$$\boldsymbol{\omega} = \nabla \times \mathbf{v} \tag{2.51}$$

There is a deep connection between the vorticity of the fluid and the forces generated by the body, and in most cases, the study of fish locomotion results more effective, following an approach that accounts for the variation of vorticity in the wake rather than the variation of velocity [47].

Taking the curl of the Navier-Stokes equation, the following expression can be obtained:

$$\frac{\partial \boldsymbol{\omega}}{\partial t} = \underbrace{\nabla \times (\mathbf{v} \times \boldsymbol{\omega})}_{\text{advection}} - \underbrace{\nu \nabla \times (\nabla \times \boldsymbol{\omega})}_{\text{diffusion}} \tag{2.52}$$

Equation 2.52 states that the local vorticity can vary because of two mechanisms: the advective transport by the velocity field and the diffusion caused by viscosity. Another important quantity is the circulation Γ, which is defined as:

$$\Gamma = \oint_c \mathbf{v} \cdot d\mathbf{c} \tag{2.53}$$

and which is related to the vorticity with the Stokes theorem, stating that the integral of the curl of a vector over a surface S is equal to the line integral of that vector over any closed material curve c lying on the surface S (Equation 2.54).

$$\int_S \boldsymbol{\omega} \cdot \mathbf{n} dS = \int_S (\nabla \times \mathbf{v}) \cdot \mathbf{n} dS = \oint_c \mathbf{v} \cdot d\mathbf{c} = \Gamma \tag{2.54}$$

Thus, applying the Stokes theorem, it is possible to rewrite Equation 2.52 as a function of the circulation.

$$\frac{\partial \Gamma}{\partial t} = \oint_c \nu (\nabla \times \boldsymbol{\omega}) \cdot d\mathbf{c} \tag{2.55}$$

It is, then, possible to observe that the circulation on a closed material curve can change only by viscous diffusion, the advective transport does not affect the total circulation since the contour c is a material curve, and it is advected with the fluid as well.

At high Reynolds numbers, as in the case of fish swimming, the viscous forces can be neglected, so the circulation remains conserved as stated by Kelvin's circulation theorem.

$$\frac{\partial \Gamma}{\partial t} = 0 \qquad (2.56)$$

According to Equation 2.56 and Equation 2.54, in a contour C_0 at a great distance from the moving body where the velocity of the fluid is null, the circulation Γ is null and remains constant over time, implying that the total vorticity in the area enclosed by the contour C_0 is constant. Nevertheless, inside the contour, the flow caused by the movement of the fish can generate regions of the flow with equal and opposite vorticity.

During locomotion, vorticity is generated at the interface between the fluid and the body as a result of the presence of a viscous boundary layer.

The fluid velocity then advects the vorticity generated in the boundary layer, and it is shed into the wake. Since viscosity tends to oppose velocity gradients, when a rotating fluid particle enters the wake, it induces a velocity to the particles surrounding it, dragging them in rotation. The result is that the boundary layer separated from the surface starts rolling up like a scroll, and eventually, it can generate a vortex in the wake, as shown in Figure 2.41. [47].
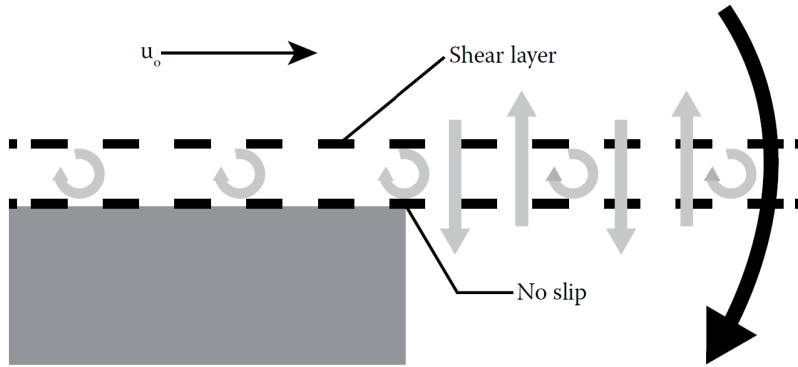
Figure 2.41: Boundary layer roll-up, Gordon, *Animal locomotion: physical principles and adaptations* (2017) [47]

The velocity induced by a vortex can be calculated using the Biot-Savart equation, which for a point vortex is:

$$\mathbf{u_{pv}}(\mathbf{x}) = \frac{\Gamma_{pv}}{2\pi|\mathbf{r}|} \qquad (2.57)$$

where Γ_{pv} is the circulation of the point vortex.

As the presence of vortices induces velocity in the fluid, the vortices generation is connected to the transfer of momentum between the fish and the fluid, thus studying the

vortex patterns in the wake allows understanding the forces exchanged between the fish and the fluid.

Since the variation of momentum in the fluid can be determined from vortex patterns in the wake, and since the vortices in the wake are the result of vorticity shedding at the trailing edge of the tail, it appears clear why the forces acting on the fish can be described only with the movement of the trailing edge of the tail, as in the slender body theory.

The force applied by the fish to the fluid can be calculated by analyzing the momentum of the fluid in a control volume surrounding the fish, and for a steady-state or for a time-averaged velocity profile, the two possible cases are shown in Figure 2.42.

In the first case, there is a velocity defect in the wake, meaning that the body has subtracted momentum from the fluid and is receiving a net drag force from the fluid. The opposite happens in the second case, where the wake presents a velocity surplus and the body receives a net thrust.

(a) Wake momentum defect   (b) Wake momentum surplus
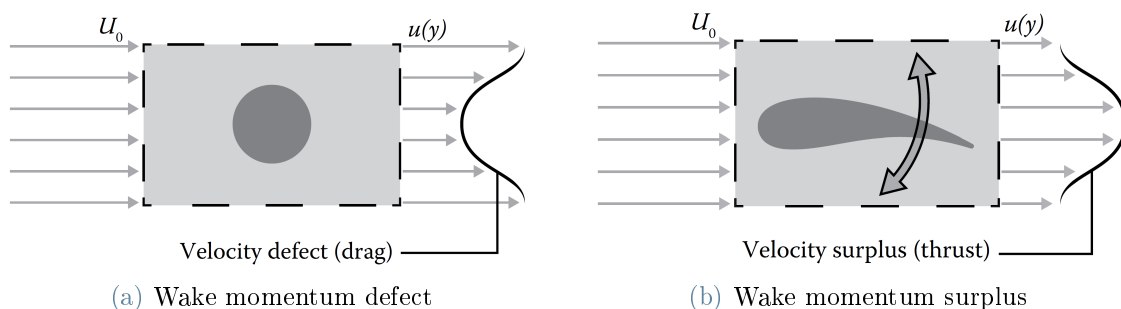
Figure 2.42: Time-averaged velocity profiles in the wake, Boundary layer roll-up, Gordon, *Animal locomotion: physical principles and adaptations* (2017) [47]

The structure of the wake and the vortex patterns can be derived from Kelvin's circulation theorem (Equation 2.56). The circulation around a fin section, shown in Figure 2.43 is equal to the difference in longitudinal velocity between the two sides of the fin.

In the time instant represented in Figure 2.43, the fish is swimming leftwards at speed U and the fin is moving upwards with a velocity v. As the fluid is pushed upwards, on the upper side of the fin, the pressure is higher than on the lower side of the fin, thus, according to the Bernoulli principle, the velocity on the lower side is greater than the velocity on the upper side.

Even though the flow characterizing fish swimming is unsteady, such qualitative considerations about the relation between velocity and pressure can be done using the

Bernoulli principle.
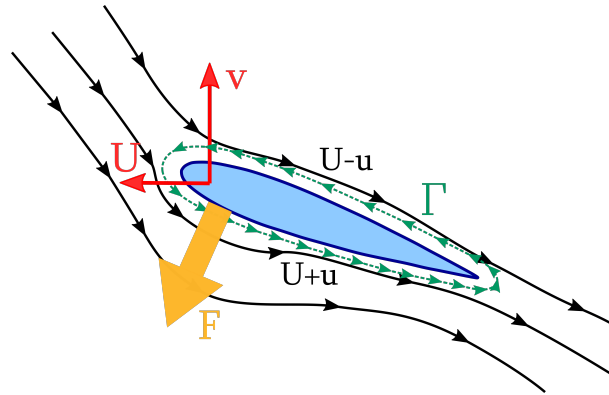
Figure 2.43: Circulation around a section of the fin

Since the longitudinal velocity perturbation u is odd with respect to y [139], it can be calculated that:

$$\Gamma = \oint_c \mathbf{v}d\mathbf{c} = u^+ - u^- = 2u^+ \tag{2.58}$$

The circulation around the fin is proportional to the velocity $v(x,t)$ [140], thus it varies periodically during the fin movement. Since the total amount of circulation remains constant according to Kelvin's circulation theorem, to any variation of circulation around the fin corresponds an equal and opposite variation of circulation inside the fluid.

Hence, the vorticity shed at the trailing edge of the tail varies periodically as well, and this leads to the formation of vortices of alternate sign in the wake, as shown in Figure 2.44.
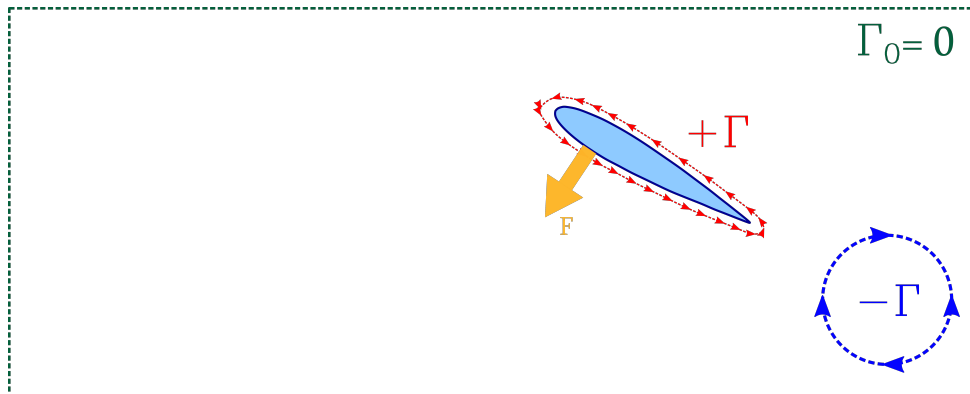
(a) As the fin stars moving and gaining positive circulation a vortex with negative circulation is shed in the wake
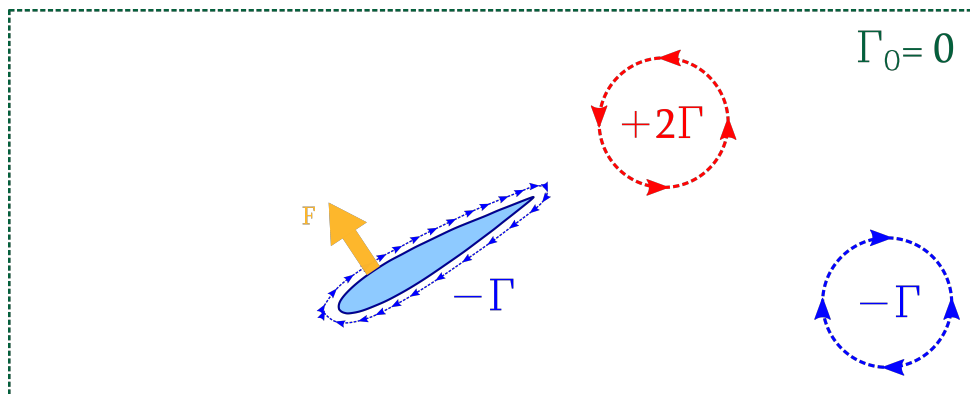
(b) When the movement of the fin changes direction, the circulation on the fin becomes negative and a vortex with positive circulation is shed in the wake
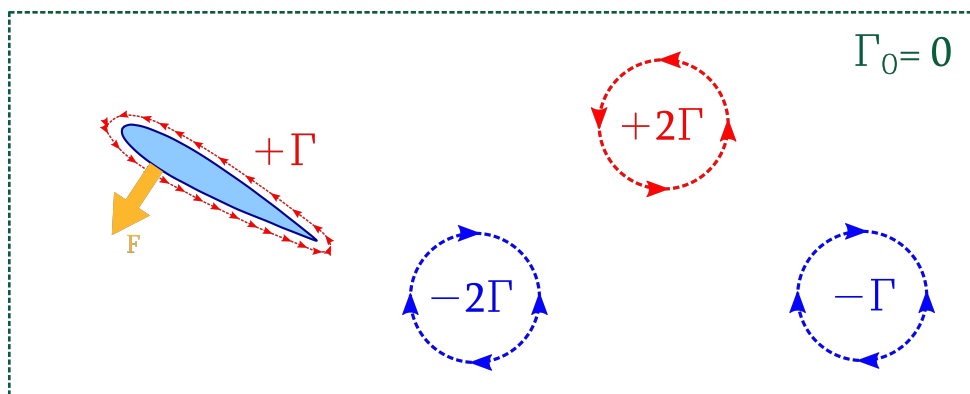
(c) When the movement of the fin changes direction again, the circulation on the fin becomes positive and a vortex with negative circulation is shed in the wake

Figure 2.44: Formation of vortices of alternate sign in the wake, as a result of the changes of the circulation around the fin

This particular vortex pattern is called Reverse Karman Street, and it consists of vortices of alternate signs shed by the fin every time it changes direction. These vortices cause a

momentum surplus in the center of the wake, forming a sort of propulsive jet resulting
from water being pushed backward by the traveling wave. In a real, viscous fluid, where
also a drag force is acting on the fish, at the top and the bottom of the wake, a counterflow
is present, so that when the fish is swimming at a constant speed, and thrust and drag
are balanced, no net momentum is given to the wake.

The vortex pattern of the Reverse Karman Street resembles that of the Karman Street,
but its vortices have an inverted sign. The Karman street is the wake generated by the
flow around a bluff body at a high Reynolds number, consisting of vortices of alternate
signs detached from the body. A Karman street always implies a momentum defect in
the wake, indicating that the body is subject to a drag force. The Karman Street and
the Reverse Karman street are shown in Figure 4.34, where the time-averaged velocity
perturbation in the wake is displayed [34].
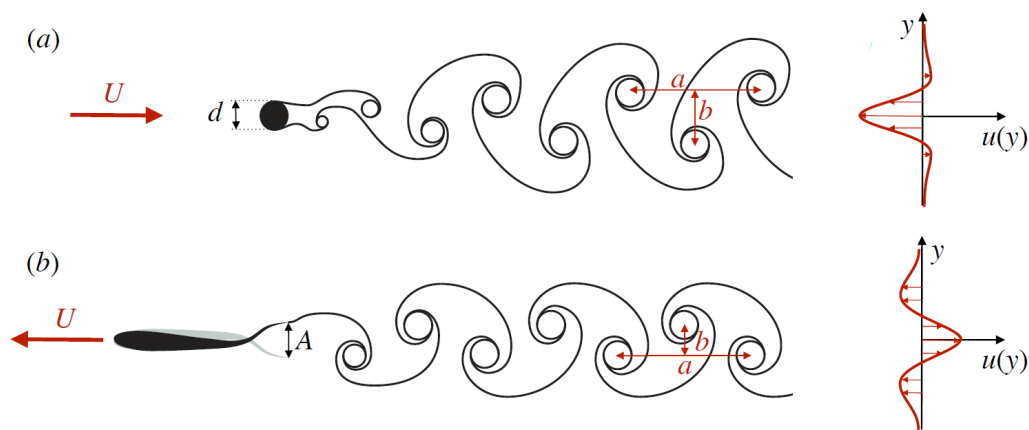
Figure 2.45: Karman Street generated by a bluff body (a) and Reverse Karman Street
generated by the fish propulsion (b), Eloy, *Journal of Fluids and Structures* (2012) [34]

The vortices presented in Figure 4.34 are the most important feature of the wake behind
a swimming fish, but they only describe spanwise vorticity. In the absence of viscous
diffusion, the total circulation inside the wake is constant; thus, the circulation around
vortex lines, i.e. the lines tangent to the local vorticity vectors, cannot vary along the
line. This means that these vortex lines can either terminate on the surface of the fish or
form closed loops in the wake.

In the wake of fishes, rings and chains of rings are often observed, and, in order to
appreciate the mechanism of their formation, the spanwise flow on the fin must be
considered too. At the fin's spanwise extremities, the fluid on the high-pressure side
tends to pass to the low-pressure side, rotating around the fin tips, gaining vorticity,
which is left in the wake as the fish advances. This leads to the formation of two vortices,

one for each extremity, rotating in opposite directions and with vorticity perpendicular to the one characterizing vortices of the Reverse Karman Street. The fin tip vortices are connected to the vortices in the Reverse Karman Street, as the vortex line forms a closed loop, thus in the wake, a chain of toroidal vortices can be observed. The three-dimensional view of vortices behind a swimming fish is shown in Figure 2.46 [30, 34, 47].
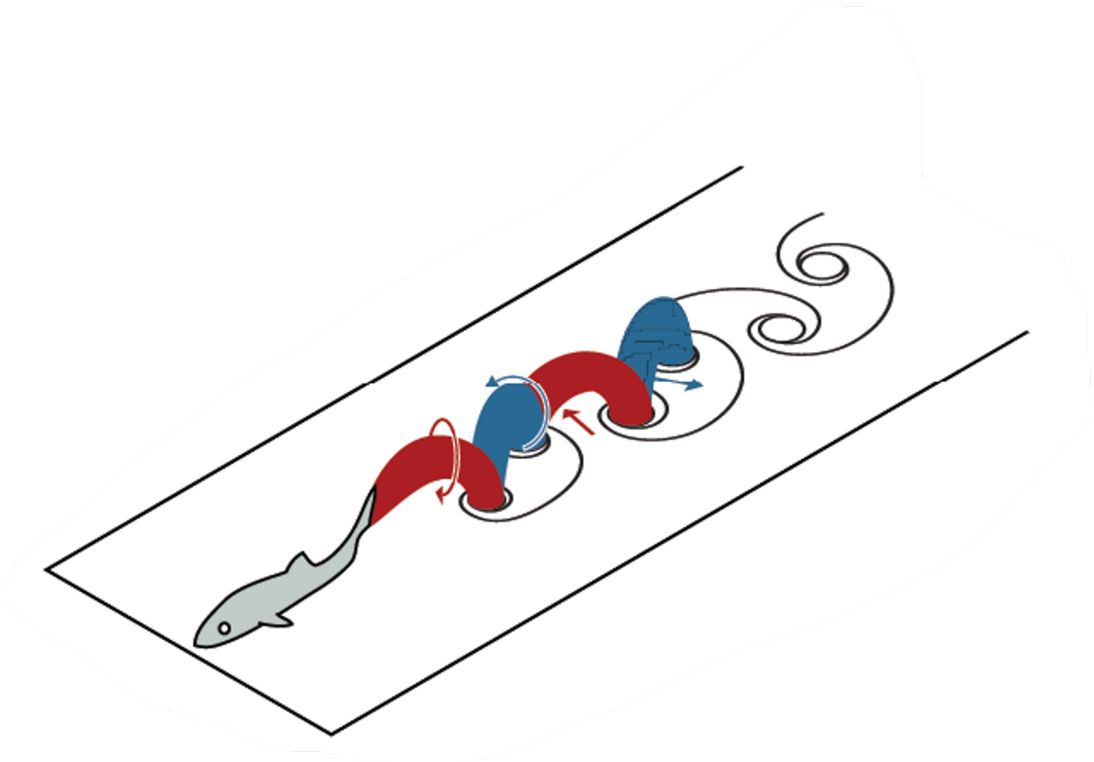
Figure 2.46: 3D view of vortices in the wake of a swimming fish forming a chain of closed loops, Eloy, *Journal of Fluids and Structures* (2012) [34]

To relate the momentum in the wake to vorticity, the vortex impulse is introduced:

$$\mathbf{I} = \frac{\rho}{2} \int_V \mathbf{r} \times \boldsymbol{\omega} \mathrm{d}V \tag{2.59}$$

If the volume V is sufficiently large so that the velocity at its boundaries is undisturbed by the fish motion, the vortex impulse corresponds to the momentum contained inside the volume [47, 104, 136]. Thus, the force acting on the fish can be calculated as the derivative of the vortex impulse.

$$\mathbf{F} = \frac{\mathrm{d}\mathbf{I}}{\mathrm{d}t} \tag{2.60}$$

The impulse of a toroidal vortex can be calculated using Equation 2.57, and it is equal

to:

$$\mathbf{I} = \rho \Gamma A \mathbf{n_l} \tag{2.61}$$

where A is the area of the loop and $\mathbf{n_l}$ is the versor perpendicular to the plane in which the loop is contained. The force, then, can be calculated taking the derivative of the impulse in Equation 2.61. This result, in the case of a fin with span dimension W, steadily translating with velocity U, leads to the relation between circulation and the steady hydrodynamic lift, known as Kutta-Joukowski theorem [47].

$$\mathbf{F} = \frac{d\mathbf{I}}{dt} = \rho \Gamma \frac{dA}{dt} \mathbf{n_l} = \rho \Gamma U W \mathbf{n_l} \tag{2.62}$$

In the real case of an unsteady flow around the fin, the circulation Γ is also dependent on time, and the expression of the force includes a term related to the change of circulation on the fin.

The geometry and the dimensions of the vortices depend on the fish species, and generally, their vertical extension is approximately equal to the fin span, whereas their longitudinal size is approximately equal to the distance covered during half a period. Despite vortex sizes being different for every fish species, the Strouhal number, the adimensional parameter describing the vortex distribution in the wake, is similar for all swimming animals. The Strouhal number is defined as follows:

$$St = \frac{fd}{U} \tag{2.63}$$

where f is the frequency of vortex shedding, d is the characteristic size of the body, and U is the free-stream velocity. The Strouhal number is linked to vortex spacing in the wake, as the vertical distance between vortices b can be assumed to be equal to the size of the body d, and the horizontal distance a is equal to the free-stream velocity multiplied the time $1/f$ between the shedding of two vortices with vorticity of the same sign [34]. For swimming animals, the Strouhal number can be expressed in the following way:

$$St = \frac{f2A}{U} \tag{2.64}$$

where f is the frequency of the fin movement, and the characteristic size is equal to $2A$, corresponding to the peak-to-peak amplitude of fin motion [34, 127]. The Strouhal number characterizing the swimming locomotion at cruising speed of fishes and cetaceans is between 0.2 and 0.4, regardless of the dimensions and of the locomotion strategy of the animal, as can be observed in Figure 2.47, where the Strouhal number at different

swimming velocities is plotted for several species [102].
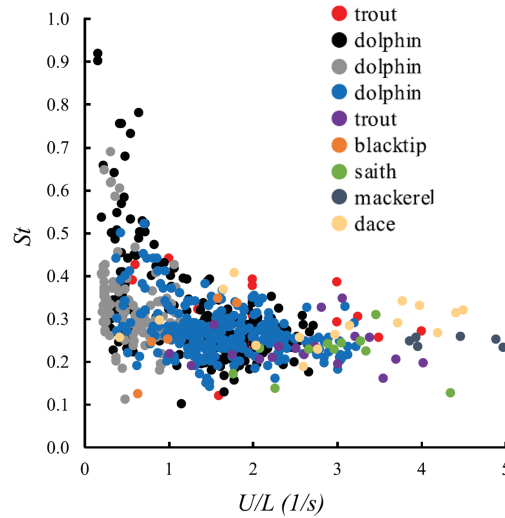
Figure 2.47: Strouhal number variation with swimming speed for different species of fishes and cetaceans, Saadat, *Phys. Rev. Fluids* (2017) [102]

This range of Strouhal numbers is associated with the maximum propulsive efficiency, and it is also common to many species of flying animals [34, 102, 124, 126, 127].A high value of energy efficiency in this range is because only for such Strouhal numbers can a stable Reverse Karman street be developed in the wake. or a Strouhal number smaller than 0.2, the wake appears wavy, and vortices are not present. There is a momentum defect, and the fish experiences a net drag because the frequency or the amplitude of fin motion is too small to swim at that velocity. For a Strouhal number higher than 0.4, vortices are generated near the leading edge of the fin, and they are shed in the wake every half-cycle as well. These vortices have smaller strength and opposite circulation with respect to vortices released at the trailing edge of the fin. The wake shows a momentum excess, meaning that thrust is generated, but the kinetic energy given to the fluid is higher than in the Reverse Karman Street because, with a higher Strouhal number, more vortices are present in the wake [1]. This characteristic of the wake of an oscillating profile would explain why all swimming animals have evolved their gait to optimize the formation of a Reverse Karman Street in the wake.

In addition to the vorticity in the wake, a vortex can also form near the fin's leading edge. However, this vortex is observed only in animals characterized by an oscillatory movement, such as carangiforms, thunniforms, cetaceans and myliobatoids, whose

propulsion mechanism is dominated by the lift force acting on the fin [14]. For a fin with a finite thickness, the flow turning around the leading edge does not perform a 180° turn, as modeled in the waving plate theory, but it detaches from the surface of the fin, and it rolls up, forming a vortex, as shown in Figure 4.42. A similar phenomenon is observed on insect wings, aerodynamic profiles with a high angle of attack and the wings of delta-shaped airplanes.
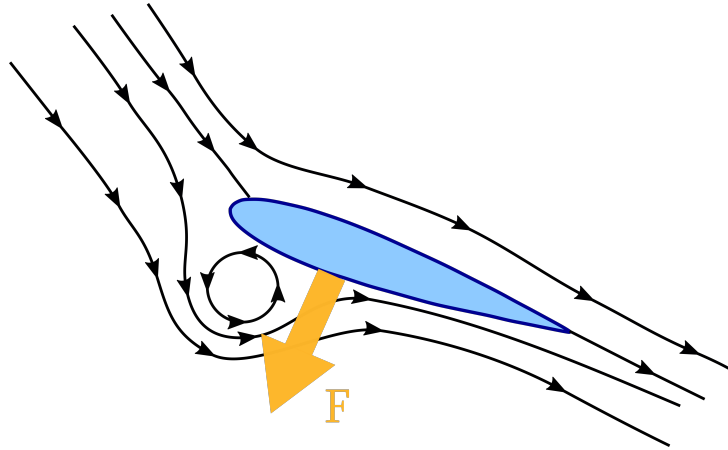
Figure 2.48: Leading-edge vortex

At the core of the leading-edge vortex, a low-pressure region is present, enhancing the lift acting on the fin, and as a consequence also the thrust force increases. On bi-dimensional wings with a high angle of attack, the leading-edge vortex formation is unstable, so it grows indefinitely until it becomes too large and is advected by the flow velocity and shed in the wake [33]. Conversely, in fish swimming, the leading-edge vortex is not shed in the wake, but it remains attached to the surface of the fin, enhancing lift during the whole flapping cycle. The reason for the stabilization of this vortex is the spanwise flow from the fin root to the fin tip, caused by the pressure difference on the two sides of the fin. This flow convects vorticity outwards, preventing the vorticity from accumulating and causing an unstable growth of this vortex. The spanwise flow causes a spiraling motion of the fluid in the vortex, eventually reaching the fin tip, where this vortex is connected to the fin-tip vortex.

An attached leading-edge vortex can be observed in fins of all shapes, but a delta shape promotes the spanwise flow in the vortex and promotes its stabilization. Hence, most fishes whose locomotion strategy is characterized by the presence of a leading-edge vortex have fins with a delta shape, as shown in Figure 2.49 [14].

(a) Caudal fin of a yellow-finned tuna

(b) Caudal fin of a whale

(c) Manta Ray

Figure 2.49: Delta-shaped fins of animals showing a leading-edge vortex on the fin

At $St > 0.4$, the spanwise flow is not strong enough to stabilize the leading-edge vortex; thus, it becomes unstable, and it is shed in the wake, interacting with the vortices in the Reverse Karman Street in a detrimental way and reducing energy efficiency [1, 14].

For the vast majority of BCF swimming animals, the caudal fin is the primary source of propulsion. However, the flow in its proximity is generally disturbed by other appendages such as dorsal or anal fins. These fins also shed vortices in the wake, which interact with vortices formed by the caudal fin, playing an essential role in propulsion efficiency. Although the main role of dorsal and anal fins is a stabilization function in turning maneuvers, they also increase the propulsive efficiency of steady-state swimming. The dorsal and the caudal fin can be regarded as two oscillating foils in tandem, and there is a phase difference in the motion of the two fins induced by the wave propagation on the animal body. The wake generated by the dorsal fin is a Reverse Karman Street too, with a smaller width and with vortices of smaller strength, since its motion is characterized by a smaller amplitude. The caudal fin intercepts these vortices, and they have the same rotational sense as the developing circulation around them. Enhancing the circulation, they increase the force generated by the fin and the strength of the vortices in the Reverse Karman Street in the wake [31, 50].

Swimming animals not only take advantage of the interaction between vortices generated by their fins but also exploit the vorticity already present in the flow. For example, when a bluff obstacle is present in a river or inside a stream of water, it releases a Karman Street in its wake. Swimming behind the obstacles, fishes reduce the drag force, as they are in a region of reduced flow velocity. However, the most significant advantage can be achieved if they synchronize their motion with the periodic vortex shedding of the obstacle to interact constructively with such vortices and extract energy from the wake, as shown in Figure 2.50a [9, 71]. Moreover, when fishes swim in schools, they encounter the wakes

of the preceding members, and they can recapture some energy from the wake arranging themselves in a diamond formation. When two fishes swim side by side, each of them releases a Reverse Karman Street, with a jet stream in the center of the individual wake and counterflow at the two sides, as shown in Figure 2.50b. Thus, in the middle of the two wakes, a Karman Street analogous to the one generated by a bluff body is present, so the fish behind can exploit the strong counterflow in this region to interact with vortices and reduce the energy consumption of locomotion [71].
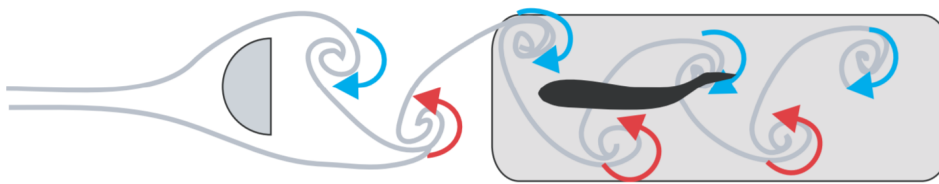
(a) Fish exploiting the counterflow in a Karman Street of an obstacle
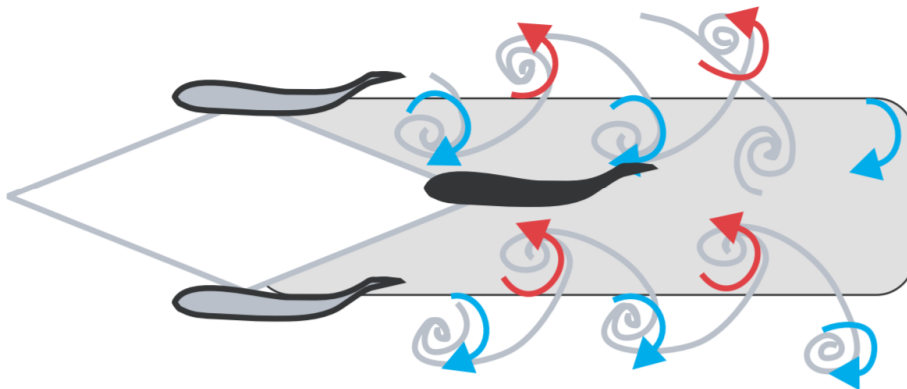
(b) Fish exploiting the counterflow between two Reverse Karman Streets of preceding fish in the school

Figure 2.50: Mechanism of energy extraction from vortices present in the flow, Liao, *Phil. Trans. R. Soc. B* (2007) [71]

2.7.   Efficiency of fish propulsion

The efficiency of propulsion is the ratio between the useful work and the consumed energy in the condition of constant speed motion. The useful work is the work of the thrust force, corresponding to the energy required to overcome the resisting drag force of the fluid. For most vehicles, the propeller is isolated from the rest of the body, and the thrust generated by the propeller is balanced by the drag acting on the hull of a ship or a rigid part of a different vehicle. Thus, it is straightforward to identify the useful work, as it is possible to separate the contributions of thrust and drag, since they act on different parts of the vehicle, and the energy efficiency is defined as the Froude efficiency:

$$\eta = \frac{\overline{TU}}{\overline{P_{in}}} \tag{2.65}$$

where the overbar means the average over one period.

Conversely, in the case of fish swimming, or, more in general, of a self-propelled deformable body, the quantification of the energy efficiency is much more challenging since both thrust and drag are generated by the movements of the fins or of the body, and it is complicated to separate them. Moreover, in the case of steady-state swimming, the net force acting on the fish body is zero, and it does not perform any useful work, despite consuming some power, so that the energy efficiency would always be zero [83].

Nevertheless, this limitation can be overcome by introducing different measures of energy efficiency, one of which is the cost of transport (COT). The COT is defined as the total energy consumed per unit distance traveled [5, 83]:

$$COT = \frac{E_{tot}}{S} \tag{2.66}$$

The metabolic COT is calculated considering all the energy consumed by the animal as input energy. Thus, it includes the inefficiencies in the conversion from metabolic power to muscle power and from muscle power to kinetic power, and it is usually estimated by measuring the oxygen flow rate in the breathing of the animal [5]. On the other side, the mechanical COT considers as input energy only the energy spent to deform the body or the fin, and it is a much more useful measure of the energy efficiency of propulsion. The main drawback of using COT is that it is a dimensional quantity [J/m], and there is no universal way to normalize it, so this coefficient depends on the dimensions of the animal and its mass. Hence, it could only be used to compare different gaits of the same animal,

but it cannot provide any information about the absolute energy efficiency of locomotion
[83]. Usually, this coefficient is normalized with respect to the mass of the animal, but
COT does not scale linearly with mass, so it does not allow any fair comparison of the
energy efficiency between different fish species [63]. The cost of transport of several
swimming animals is plotted in Figure 2.51 [63].
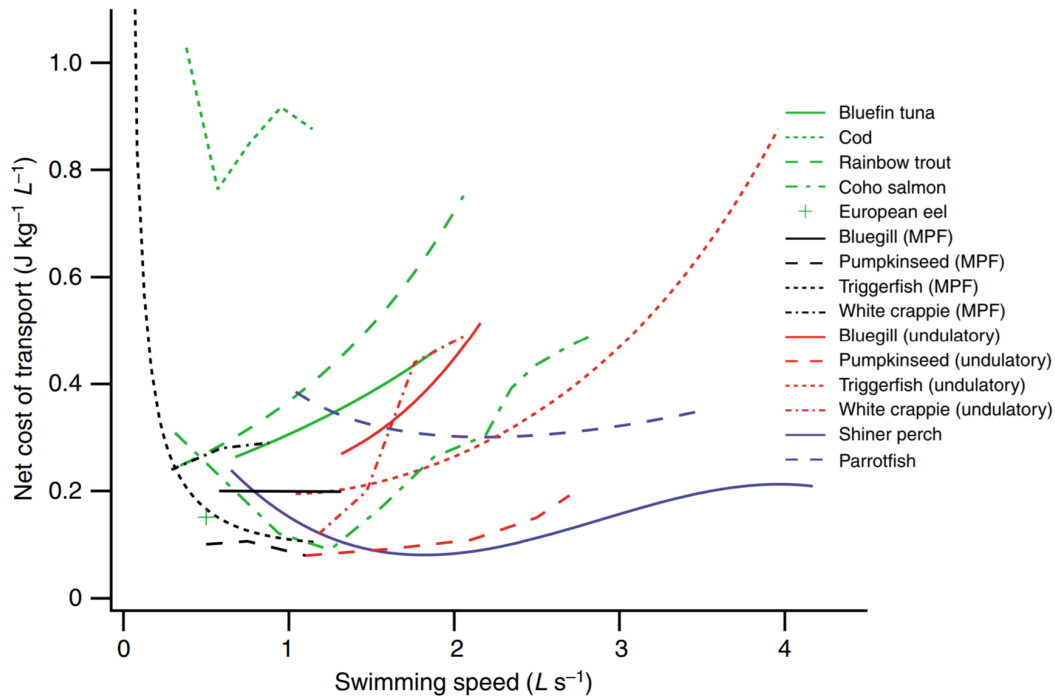
Figure 2.51: Cost of transport (COT) of different swimming animals, Kendall, *Journ.
Exp. Biol.* (2007) [63]

Some ways to normalize the COT and to obtain a dimensionless quantity have been
developed, but with such normalizations, it may result that gaits of the same animal
with the same COT have a different normalized COT if they are characterized by
different wavelength or frequency, which make this measure useless to investigate the
best combination of kinematic parameters that allows obtaining high energy efficiency
[5, 83].

Another measure of the energy efficiency of a self-propelled body is the quasi-propulsive
efficiency (η_{QP}), defined as:

$$\eta_{QP} = \frac{RU}{\overline{P_{in}}} \tag{2.67}$$

where R is the towed resistance of the body [83]. Since the efficiency has a meaning
only in steady-state conditions, the towed resistance is equal to the thrust force, and the

numerator of Equation 2.67 corresponds to the useful power of swimming. Nevertheless, the resistance R is not equal to the drag force at every time instant of fish movement, but it is the drag force measured towing the fish at a constant speed U. The advantage of using η_{QP} is that it captures the hydrodynamic characteristics of the body, and it can be used to compare fishes or AUVs with different shapes or sizes. Nevertheless, the resistance R is not measured in natural swimming conditions, introducing a considerable limitation to measuring the efficiency of fish locomotion, as the drag force acting on the fish is variable during swimming. These variations occur not only because the fish changes its shape and, consequently, the drag coefficient changes, but also because the flow surrounding a fish moving its fins is very different from the flow surrounding a towed dead fish, even if the velocity U is the same. Therefore, this coefficient may even be greater than 1 if, during swimming, the interaction between the body and the fluid makes the drag coefficient drop substantially [83].

In order to quantify the energy efficiency of fish propulsion, it is necessary to separate the contributions of thrust and drag that act together on the same body. This work provides a different definition of efficiency, which is suitable for calculating analytically or numerically the efficiency of self-propelled bodies like swimming fishes. Since data coming from numerical analyses allow distinguishing the contributions of pressure and viscous forces, it is possible to define efficiency properly. The input power P_{in} is the power spent by the fish to move its fins, so it is obtained as the scalar product between the forces acting on the fins and the relative velocity of the fins with respect to the fish body $\mathbf{v_{rel}}$. Since fins are moved only in a lateral or vertical direction, the power P_{in} is independent of the swimming velocity and the forces acting in a longitudinal direction. Hence, the input power is obtained as:

$$P_{in} = - \int_{\Sigma} (p\mathbf{n} + \boldsymbol{\tau}) \, \mathrm{d}\Sigma \tag{2.68}$$

where the infinitesimal forces acting on each infinitesimal element of the fin are the pressure force $p\mathbf{n}$, being $\mathbf{n}$ the normal versor of the fin surface, and the viscous tangential stresses τ. The useful output power P_{out} is the result of the pressure acting on the fins projected on the swimming direction, whereas the pressure acting on the rigid part of the body and the tangential stresses acting on the whole surface contribute to the resistance.

$$P_{out} = - \int_{\Sigma_{fins}} p_x n_x \mathrm{d}\Sigma_{fins} \tag{2.69}$$

Finally the efficiency can be computed as:

$$\eta = \frac{P_{out}}{P_{in}} \tag{2.70}$$

This definition of efficiency is indicative of how much power contributes to generating a force propelling the fish in the swimming direction. This is because the tangential forces acting on the surface result from dissipative viscous effects, and the pressure force acting on the rigid part of the body always resists forward motion.

3 | State of the art

FISHES show excellent swimming performances. Thus, there is a growing interest in designing bioinspired autonomous underwater vehicles (AUVs), which mimic their swimming propulsion. These robots can find applications in seabed exploration, environmental monitoring, underwater farming, or surveillance. As shown in the previous chapter, almost all kinds of biological swimming locomotion inspire the design of biomimetic robots, and the rajiform swimming of batoid fishes is one of the most interesting, since they combine high efficiency and great maneuverability. Therefore, the project of this thesis is focused on the design of a biomimetic robot inspired by a cownose ray. In this chapter, the most advanced existing robots exploiting rajiform swimming propulsion are briefly described, focusing on the robots that reproduce fishes with an oscillatory behavior, inspired by the cownose ray, or by fishes with similar size and fin kinematics.

These robots are quite different from each other, and they can be classified according to how they move the pectoral fins and reproduce the traveling wave typical of fish swimming.

3.1. Robots with a single actuator per fin

Many robots that take inspiration from a batoid fish use a single actuator to move each pectoral fin, and the undulatory motion is obtained with the passive flexibility of the fin itself.

3.1.1. Robo-Ray II

As shown in Figure 3.1, this robot has fins made of silicone rubber whose shape is approximated with aerodynamic profiles. The leading edges of the fins are reinforced with flexible ribs, connected to the pneumatic artificial muscles which move the fins. A servo-motor moves the tail, that acts as a rudder during floating and diving maneuvers. This robot moves its fins at 1.2 Hz, and it can reach a cruising swimming velocity of 0.16 m/s, corresponding to 0.5 body lengths per second [17].

(a) Robo-Ray II
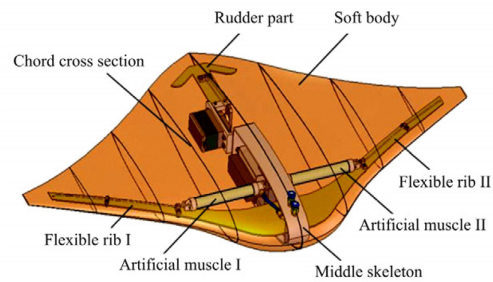
(b) Scheme fo Robo-Ray II

Figure 3.1: Robo-Ray II, Cai, 2010, Beihang University [17]

3.1.2.   Robo-Ray III

Robo-Ray III is an evolution of Robo-Ray II, which has pectoral fins made of a very flexible rubber plate, with a more rigid fiberboard leading edge. During forward swimming, the amplitude of fin movement is 30°, and each fin, moved at 2 Hz, generates a force of 2.75 N, achieving a steady-state velocity of 0.7 body lengths per second. This robot, shown in Figure 3.2, is equipped with a pressure sensor to control depth and with an infrared sensor to detect obstacles [16, 90].
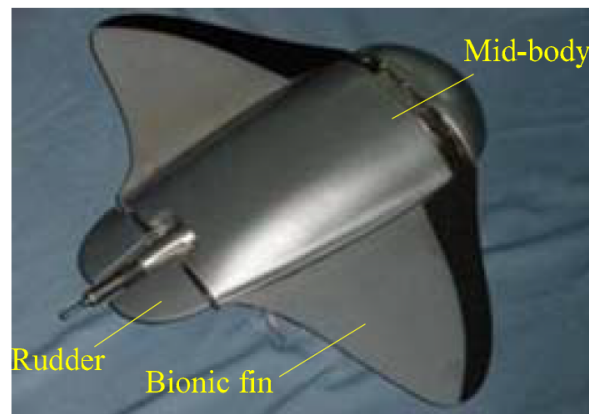
Figure 3.2: Robo-Ray III, Cai, 2010, Beihang University [17]

3.1.3.   Robot Manta Ray

The fins of the Robot Manta Ray are very similar to those of Robo-Ray III, having a rigid leading edge made of ABS and thin foil of PVC for the rest of their surface. he fins are actuated by servomotors placed in the front part of the robot. This robot's dimensions and fin kinematics are inspired by a giant manta cub, which has flexible fins with a rigid

leading edge, as grown giant mantas, but it is much smaller and moves them at a higher frequency. Flapping fins at 0.9 Hz, this robot is able to achieve a speed of 1.7 body lengths per second [22].
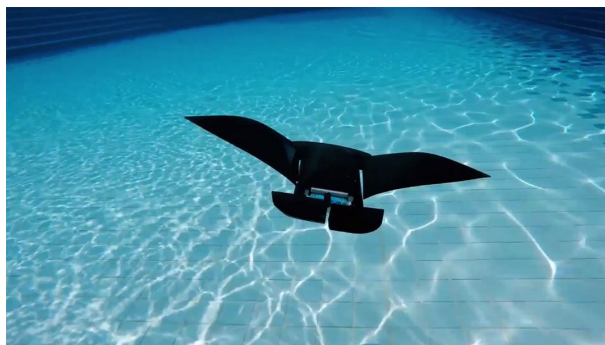
Figure 3.3: Robot Manta Ray, Chew, 2015, National University of Singapore [22]

3.1.4. Manta Ray Robot

Another robot falling in this category is the *Manta Ray robot*, shown in Figure 3.4. Its pectoral fins are made of very flexible silicone rubber sheets 1 mm thick, which are actuated by a cranck-rocker mechanism connected to servo-motors. This robot moves its fins at 0.8 Hz, reaching a maximum speed of 1.4 body lengths per second [42].
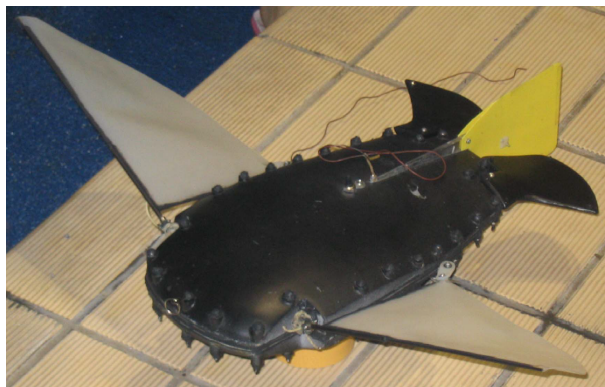
Figure 3.4: Manta Ray Robot, Gao, 2007, Robotics Institute Beijing University [43]

3.1.5. Robotic Cownose Ray

The fins of this robot are obtained by combining an ionic polymer-metal composite (IPMC) actuator with a molded elastomer recreating the shape of the cownose ray fin. IPMCs are electroactive polymers, also known as *artificial muscles*, generating large deflection in response to electric stimuli. The IPMC actuator is placed near the leading

edge, and the rest of the fin deforms passively. As a result, the fins can generate a deflection of 40% with less than 1 W of power consumption. Nevertheless, this robot swims very slowly, with a maximum speed of 0.034 body length per second [21].
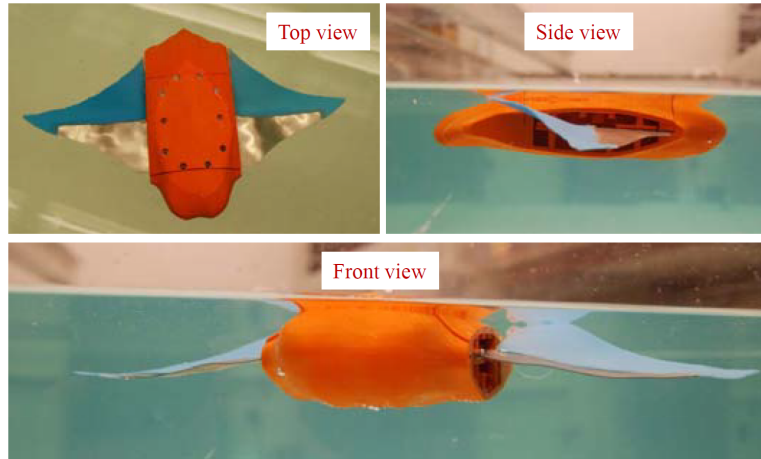
Figure 3.5: Robotic Cownose Ray, Chen, 2011, University of Virginia [21]

3.2.   Robots having fins with two degrees of freedom

Some other robots use a single mechanism to move each fin, but they actuate two degrees of freedom: the flapping motion and the pitch angle of the fin, so that, with the appropriate combination of the two movements, they are able to recreate the oscillating motion of the fin of a batoid fish.

3.2.1.   Biomimetic Cownose Ray

The Biomimetic Cownose Ray, shown in Figure 3.6, combines the flapping motion of the fin with the chordwise twisting movement to reproduce the oscillating motion. The twisting mechanism is positioned at the middle of the fin root, and a flexible shaft transmits the twisting torque from the fin root to the fin tip. The fin sections are obtained with flexible silicone ribs, which are mounted on the flexible shaft. It can reach a speed of 0.4 m/s, and it is highly maneuverable, being able to perform a pivot turning [81].

(a) Biomimetic Cownose Ray
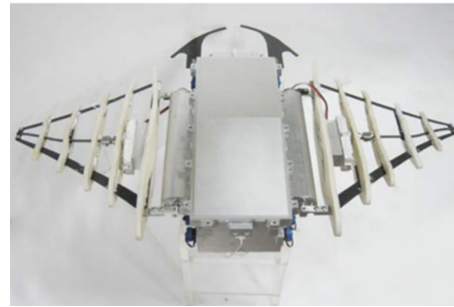
(b) Biomimetic Cownose Ray without elastic skin

Figure 3.6: Biomimetic Cownose Ray, Ma, 2015, Beihang University [81]

3.2.2. Bionic Manta Ray Robot

This robot, shown in Figure 3.7, combines a flexible mechanism and a flexible fin structure to reproduce at best the deformation of the fin of a real manta ray. The fin flapping is driven by two cables, one on the upper side and one on the lower side, connected to a servomotor positioned at the fin root, and elongating one and shortening the other, the fin deforms. In the center of the fin, a flexible mechanism is present, and on its tip, another servomotor controlling the twisting angle of the fin is mounted. This robot flaps its fins at $2.5\,\mathrm{Hz}$, and it can sustain for 25 minutes a velocity of $0.4\,\mathrm{m/s}$, corresponding to 0.8 body lengths per second [146].

Figure 3.7: Bionic Manta Ray Robot, Zhang, 2018, Beihang University [146]

3.2.3. Aqua Ray

Aqua Ray robot, shown in Figure 3.8, moves its fins thanks to a water-hydraulic drive unit, with Bionic Fluidic muscles used as actuators. They consist of hollow elastomer

cylinders that increase their diameter and longitudinally contract when filled with water. The generated force is transferred to the fin tip with artificial tendons giving rise to a smooth and large-amplitude fin deflection. On this robot, a large caudal fin is mounted too, which is not only used for maneuvering but also to help pectoral fins in propulsion. Aqua Ray can swim for 30 minutes at 0.5 m/s, corresponding to 0.8 body lengths per second [38].

Figure 3.8: Festo's Aqua Ray, 2007, Festo® [38]

3.2.4. Manta Ray AUV

This robot, shown in Figure 3.9, has a fin structure similar to the Aqua Ray robot, but it is larger and has the same dimensions as a real manta ray. In addition, it is equipped with jet propellers, thanks to which the robot can reach a very high velocity. Moreover, they help stabilization so that the trajectory can be maintained more precisely, and the robot can also be used for delicate operations, such as sonar measurement or seabed mapping [35].

(a) Manta Ray AUV without coating

(b) Manta Ray AUV with coating

Figure 3.9: Manta Ray AUV, 2017, Boss EvoLogics® [35]

3.3. Robots having fins with several independent mechanisms

Finally, other robots have several independent mechanisms actuating each fin, which give the possibility to modulate the chordwise wave propagation very accurately, enhancing the robot's maneuverability.

3.3.1. Mantabot

Mantabot is a biomimetic autonomous vehicle inspired by the giant manta, shown in Figure 3.10. The form of its fins is derived from computer tomography, and their motion is replicated with active tensegrity beams surrounded by a flexible elastomer. The amplitude of fin flapping is 0.4 body lengths and qualitatively is very similar to the fin movements of a manta ray. The vortices in the wake of this robot have been compared with those present in the wake of a manta ray, and this study has shown that the robot can replicate the same vortical structures, although it generates a wider wake, resulting in a less efficient movement than the natural one [7, 39, 77]. The robot moves fins at 2 Hz, and it can reach a top speed of 0.8 body lengths per second.

Figure 3.10: Mantabot, Fish, 2016, West Chester University, [39]

3.3.2. Roman III and Roman IV

Each fin of Roman III consists of a flexible silicone sheet with three ribs attached to it, which are parallel-connected and actuated by three independent brushless motors. The phase shift between the three mechanisms and the synchronization of the two fins are maintained using a central pattern generator (CPG) control algorithm. A water pump

and a bladder are used to control the robot's buoyancy and perform diving and floating maneuvers. Roman III can also glide, controlling the angle of attack of the fins. The steady forward swimming reaches 0.8 body lengths per second [79].
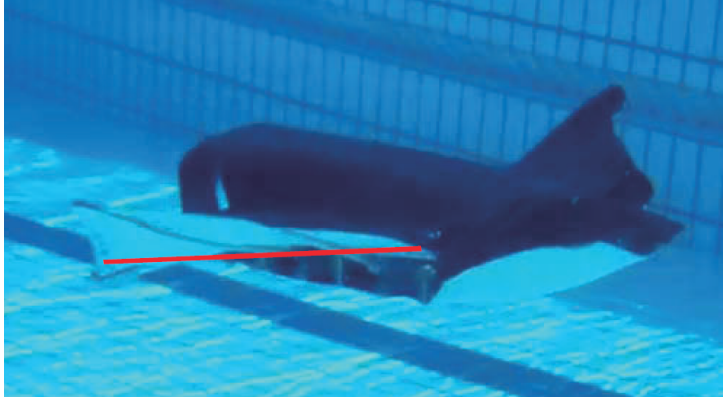
Figure 3.11: Roman III, Low, 2011, Nanyang University [79]

Roman IV is an evolution of Roman III, with more flexible fins, as its ribs are not rigid, but they are composed of elastic materials exploiting the Festo's Fin Ray effect, obtaining a high curvature at the fin tip and better swimming performances [23].

3.3.3.   Bionic Fish

This biomimetic robot is inspired by the cownose ray, and it replicates the fin deformation using three mechanisms for each fin, and a tail is used as a rudder during maneuvers. The traveling wave is created with a phase delay in the rotation of the motors. The fin's mechanisms consist of one-stage or two-stage slider-rockers to create a curvature at the fin tip. The three mechanisms are connected with flexible carbon fiber plates, which maintain the shape of the outer edges of the fin, and some flexible rubber bridges are mounted on the mechanisms to ensure the correct thickness along the fin span. The skin of the robot is made of nylon cloth. This robot, shown in Figure 3.12, can swim at 0.4 m/s, corresponding to 0.7 body lengths per second, and perform a null radius pivot turning [19].

(a) Components of the Bionic Fish inspired by the cownose ray

(b) Bionic Fish inspired by the cownose ray
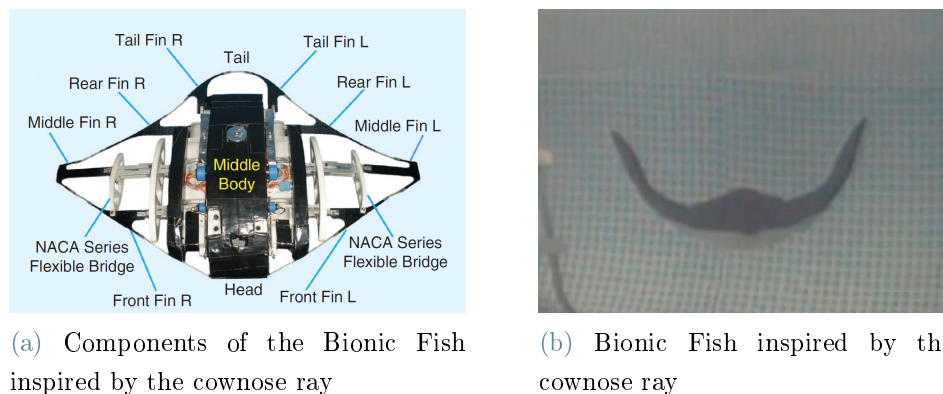
Figure 3.12: Bionic Fish inspired by the cownose ray, Cai, 2018, Beihang University [19]

3.3.4. Bionic Manta Ray Robot

The bionic manta ray robot, shown in Figure 3.13, uses three mechanisms for each fin to reproduce the oscillating movement, and its skeleton consists of a series of cross-spring pivots made of carbon fiber. Its skin is made of polyurethane-coated spandex, and since it is not waterproof, all the electronics are contained in a sealed box. This robot can swim at 0.8 body lengths per second, and it is able to perform a turn with a null curvature radius and swim backward [51].

Figure 3.13: Bionic Manta Ray Robot, He, 2020, Northwestern Polytechnical University [51]

3.3.5. Robotic Manta

This robotic manta has fins moved by two independent crank-rocker mechanisms, actuated by two servomotors. These mechanisms are made of aluminum and attached to flexible latex sheets. The buoyancy mechanism consists of a pump and a system of valves

controlling the water level in two reservoirs placed in the front and the rear so that, also when they are filled with water, the robot is balanced. This robot, shown in Figure 3.14, can swim at $0.3\,\mathrm{m/s}$, corresponding to 0.7 body lengths per second, and perform rapid diving and turning maneuvers [86].
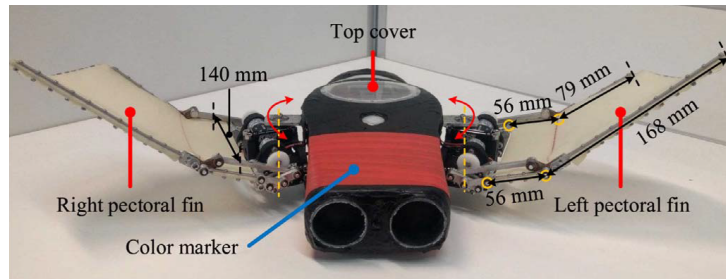
Figure 3.14: Robotic Manta, Meng, 2020, Chinese Academy of Sciences [86]

4 | Model of cownose ray locomotion

THE starting point of designing a biomimetic robot is the biological and biomechanical analysis of the target biological sample. The robot fish designed for this work is based on the morphological and kinematic analysis conducted on a *Rhinoptera Bonasus*, shown in Figure 4.1, commonly known as cownose ray.
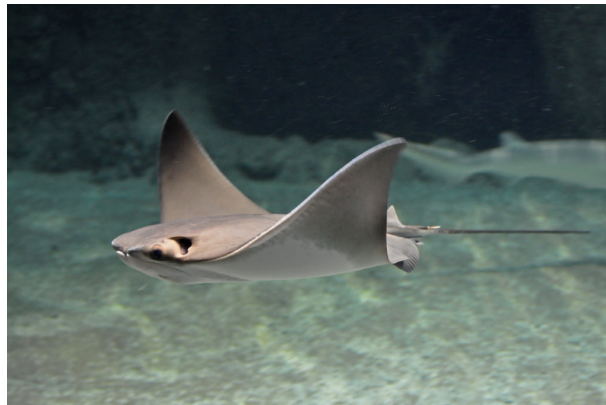
Figure 4.1: Cownose Ray (*Rhinoptera Bonasus*)

The cownose ray is a batoid fish, which presents a skeleton inside its pectoral fins composed of hundreds of segmental cartilages. This skeletal cartilaginous structure involves a large flapping of the pectoral fins that can be obtained with small movements of the single cartilage segments. The cownose ray is one of the most efficient swimmers in the ocean, which can migrate over a long distance at a speed of $0.6 \sim 0.8$ body lengths per second, accomplishing high swimming efficiency. The flexible pectoral fins employed as propulsive source guarantee stability and maneuverability. For this reason, many researchers are dedicated to investigating its locomotion in order to develop bio-mimetic and bio-inspired applications. The kinematic model of the motion of its fins is used as input of a simplified

dynamic model useful to estimate the thrust generated by the fin, and of a more complex CFD model which allows highlighting the flow generated by the movement of the fins so that the mechanism of thrust generation can be understood and a more accurate calculation of the forces can be achieved.

4.1. Bio-mechanical model of fin kinematics

The scope of the developed biomechanical model is the simulation of the 3D kinematic locomotion of a batoid fish and the estimation of the thrust force produced by its motion. The fins of a batoid fish are composed of $100 \sim 200$ cartilage segments connected in series by joints forming structures, called radial elements. These radial elements are the structural support of the fin, and they extend radially from the fin root attached to the main body to the fin tip. In addition, the radial elements are connected with some "cross-bracing" connective tissue. The disposition of these components varies significantly among species: undulatory species are featured by staggered joints positioned at the extremity of the fin, which guarantee very high flexibility, whereas oscillatory species present cross-braced joints in the center, which stiffen the fin, making it capable of bearing higher loads [108]. A computerized tomography image of the cownose ray skeleton is presented in Figure 4.2, where the anatomical components of the skeleton are visible, and it is possible to identify radial segments, joints, and connective tissue [101].
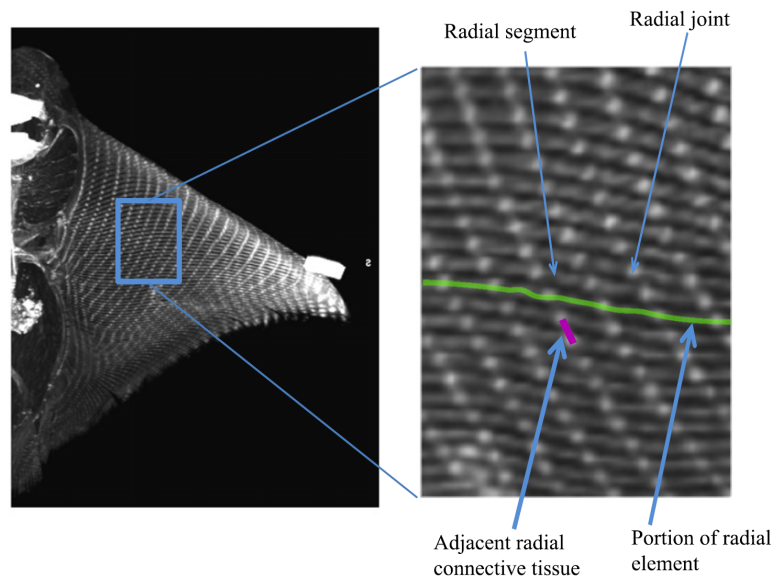
Figure 4.2: Computerized tomography image of the skeleton of a cownose ray, Russo, *Bioinspiration & Biomimetics* (2015) [101]

The kinematic parameters characterizing the cownose ray swimming are listed below and summarized in Table 4.1 [98]:

- **fin-beat frequency** f: number of fin-beats per second;

- **mid-disc amplitude** A: half of the total dorsoventral displacement of the widest portion of the fin, usually non-dimensionalized with respect to the disc width;

- **number of waves** N: number of waves present along the fin, it is obtained dividing the length L of the body from the snout to the beginning of the tail for the wavelength λ;

- **propulsive wavespeed** c: velocity of the traveling wave along the fin, it is obtained multiplying wavelength λ and frequency f;

- **phase velocity** U/c: ratio between forward velocity U and velocity of the traveling wave;

- **stride length** U/f: the distance traveled in one fin-beat period.

Table 4.1: Average dimensions of the cownose ray and kinematic parameters of its swimming

Disc length	0.45	[m]
Disc width	0.7	[m]
Frequency	1.04	[Hz]
Mid-disc amplitude (proportion of disc width)	0.35	[-]
Wavespeed (proportion of disc length)	2.62	[-]
Number of waves	0.4	[-]
Phase velocity	0.76	[-]
Stride length	0.6	[m]
Mass	12	[kg]

The qualitative and quantitative kinematic analysis is based on observing cownose ray swimming in an aquarium [18, 19] and analyzing its skeletal structure [101]. First of all, a reference frame is set, as it can be seen in Figure 4.3. The origin of the coordinate system is set on the root point of the leading edge, i.e., the intersection point between the leading edge and the foil baseline, where deformation does not occur during linear cruising motion. The x-axis is parallel to the pitch axis, i.e., the lateral body axis, and points to

the tail direction; the y-axis is parallel to the roll axis, i.e., the spanwise direction; the z-axis is with the yaw axis, i.e., the dorso-ventral body axis.
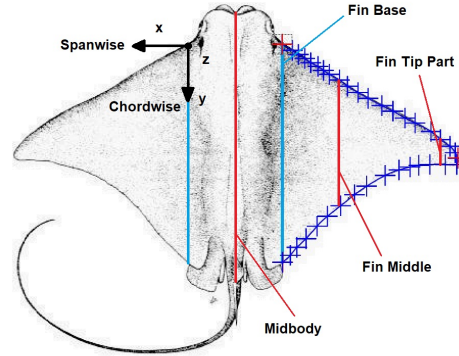
Figure 4.3: Dorsal shape of a cownose ray sample. Representation of the coordinate system (black), the fin bases (light blue), and three key sections (red): midbody, fin middle and fin tip part, the blue crosses are the extracted point of the dorsal shape of the right pectoral fin., Cai, *IEEE Robotics and Automation Magazine* (2018) [19]

The contour of the fin is reconstructed from the interpolation of markers positioned on the edge of the fin, as shown in Figure 4.3, and it is shown in Figure 4.4. The values on the axes are dimensionless: the dimensions of the pectoral fin were normalized by the chordwise length of the fin base, which is the maximum length of the pectoral fin along the chordwise direction. The shape of the fin is triangular, with a rounded and swept back tip [18].
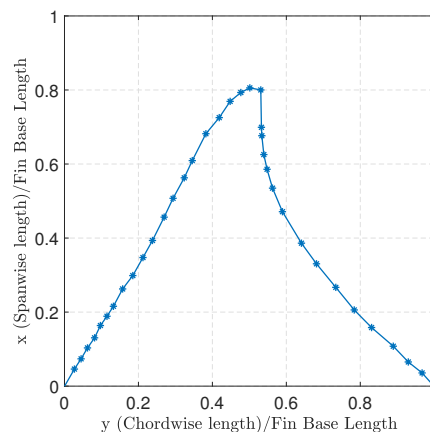
Figure 4.4: Edge of the right pectoral fin of a cownose ray

The movement of the fins is shown in Figure 4.5 and in Figure 4.6, where successive frames of a cownose ray swimming are presented [18].
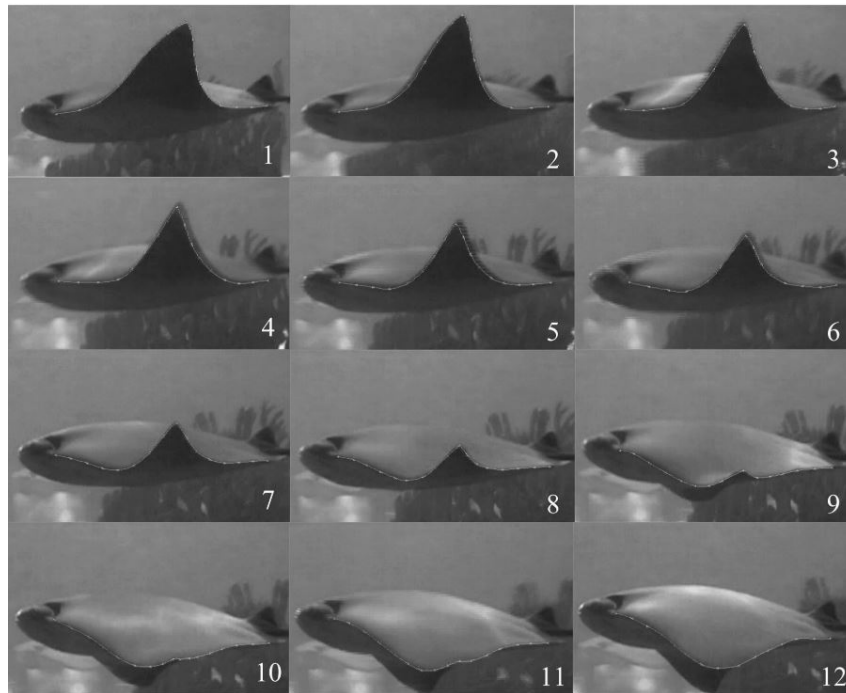
Figure 4.5: Video frames of the cownose ray linear cruising from the lateral view, Cai, *Advanced Robotics* (2012) [18]
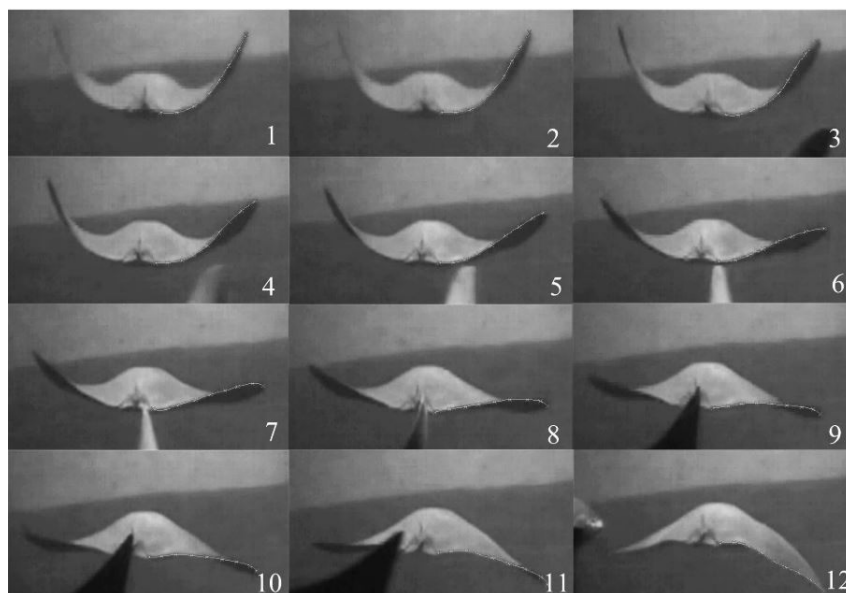
Figure 4.6: Video frames of the cownose ray linear cruising from the back view, Cai, *Advanced Robotics* (2012) [18]

The video analysis of the oscillation of the pectoral fin clearly shows the effect of the flexibility of the fin, especially the distal part in the spanwise direction and the presence

of a traveling wave in the chordwise direction. Furthermore, the flapping motion of
the pectoral fin is perpendicular to the forward direction, without the exhibition of a
rowing motion, and no horizontal displacement appears for the fin tip. Conversely, a clear
sinusoidal discipline can be seen in the vertical direction along the chordwise direction
(y-direction) [18]. The kinematic analysis of fin movement is based on the observation of
the skeletal structure of the fin, and the fin deformation is calculated from the position
and the relative rotation of the joints composing the fin skeleton. The cartilage structure
of the fin is depicted in Figure 4.7, where the radial segments are represented as grey lines
and the joints as red dots [101].
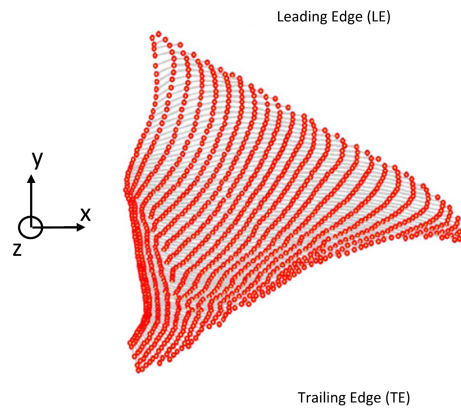
Figure 4.7:   Scheme of the fin skeleton of a cownose ray, Russo, *Bioinspiration &
Biomimetics* (2015) [101]

To provide a representation of the pectoral fin movement, source of cownose ray
propulsion, a set of geometrical and kinematic input parameters has been defined:

- Non-dimensional wave number, i.e. the number of waves traveling along a defined
  direction:

    - N_c: chordwise direction

    - N_s: spanwise direction

- Deflection angle of the fin tip with respect to the horizontal plane θ_{max}

- Fin-beat frequency $\omega = 2\pi f$

- Asymmetric flapping coefficient δ, to achieve an asymmetric flapping movement

The fin-beat frequency f and the number of chordwise wave N_c allow the computation of

the wavespeed c, i.e., the velocity of propagation of the traveling chordwise wave:

$$c = \frac{\omega}{\gamma} = \frac{L_y f}{N_c} \tag{4.1}$$

where γ is the wavenumber, which is equal to $\frac{2\pi}{\lambda}$, and $\lambda = \frac{L_y}{N_c}$ is the wavelength of the traveling chordwise wave [101]. It is possible to introduce an additional reference system, with the coordinates r and s, with s representing the curvilinear abscissa in spanwise direction with origin on the fin root, and r representing the curvilinear abscissa in chordwise direction with origin on the leading edge, as shown in Figure 4.8.
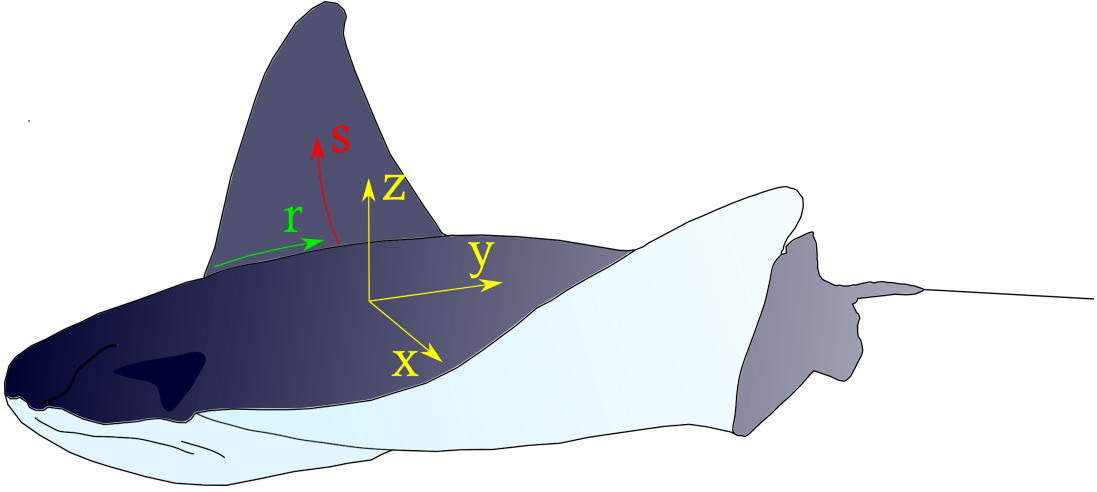
Figure 4.8: Representation of the reference systems on the fish body and on the fin

The absolute rotation in each joint is expressed as:

$$\theta_{rs} = \frac{1}{L_x} \left[\theta_{max} s \cos\left(\Phi r + \Psi s - \omega t\right) + \delta s \right] \tag{4.2}$$

The variables Φ and Ψ in Equation 4.2 represent the angular phases of the traveling wave in the chordwise and in the spanwise direction, and they can be calculated as:

$$\Phi = \frac{2\pi N_c}{L_y} \qquad \Psi = \frac{2\pi N_s}{L_x} \tag{4.3}$$

Once the rotation in each joint is computed, it is possible to obtain the position of the joints at every time instant of the periodic fin movement. The position of each joint i is obtained from the previous joint $i-1$ along the spanwise direction, as shown in Figure 4.9 and in Equation 4.4, where L is the length of each radial element, and β is the orientation

of the radial element with respect to the longitudinal axis [101].

$$
\begin{cases}
x_i(r,s,t) = L\cos\theta(r,s,t)\sin\beta(r,s) + x_{i-1}(r,s,t) \\
y_i(r,s,t) = L\cos\theta(r,s,t)\cos\beta(r,s) + y_{i-1}(r,s,t) \\
z_i(r,s,t) = L\sin\theta(r,s,t) + z_{i-1}(r,s,t)
\end{cases}
\tag{4.4}
$$

(a) Oscillatory motion inputs θ_{max}, Φ, Ψ, δ (b) Spanwise curvature by radial segment rotation about joints
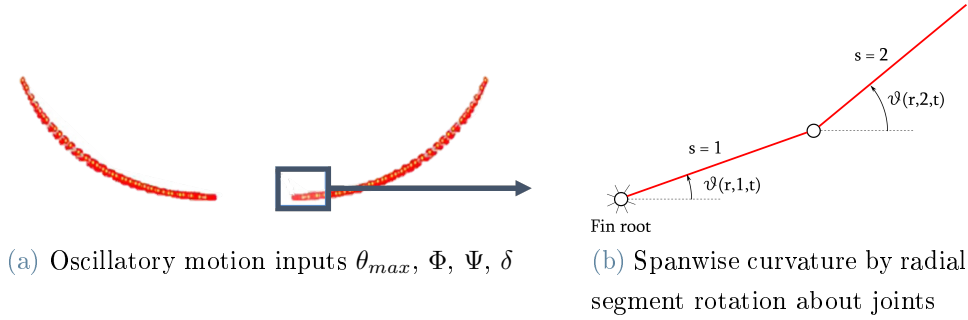
Figure 4.9: Kinematic inputs and method to obtain spanwise curvature

As all the radial elements are almost parallel and aligned with the spanwise direction, as it can be observed in Figure 4.7, it is possible to consider $\beta = \dfrac{\pi}{2}$ for all elements without introducing any significant error in the model.

The input geometrical and kinematic parameters given to the model are based on the observation of biologists [18, 101], and they are summarized in Table 4.2.

Table 4.2: Geometrical and kinematic parameters used to describe the movement of the pectoral fin

Geometrical parameters			
Fin baseline length	L_y	0.5	[m]
Spanwise elements	S	404	[-]
Chordwise elements	R	501	[-]
Transverse segment angle	$\beta(r,s)$	$\pi/2$	[rad]
Kinematic parameters			
Number of chordwise waves	N_c	0.4	[-]
Number of spanwise waves	N_s	0.2	[-]
Maximum element angular amplitude	θ_{max}	65	[deg]
Asymmetric flapping coefficient	δ	0.05	[deg]
Fin-beat frequency	f	1.04	[Hz]
Scaled wavespeed	c/L_y	2.60	[-]

The fin deformation resulting from this kinematic model is presented in Figure 4.10, where a perspective view of the fin in different time instants of a period is shown, and in Figure 4.11, where the contours of the vertical displacement of the fin surface are displayed.

The red portions of the contour plot represent a motion with a positive altitude ($z > 0$), whereas the blue portions represent a negative one ($z < 0$). The contour plot reveals the oscillatory behavior: for $t < T/2$, where T is the oscillation period, the pectoral fin moves downwards (downstroke phase), indeed the fin tip region is blue-colored; analogously, for $t > T/2$, the pectoral fin is moving upwards (upstroke phase).

Furthermore, the contour plot highlights the longitudinal traveling of the chordwise wave, as can be seen looking at the longitudinal transfer of color on the fin surface.

(a) T/6

(b) T/3

(c) T/2

(d) 2/3 T

(e) 5/6 T

(f) T
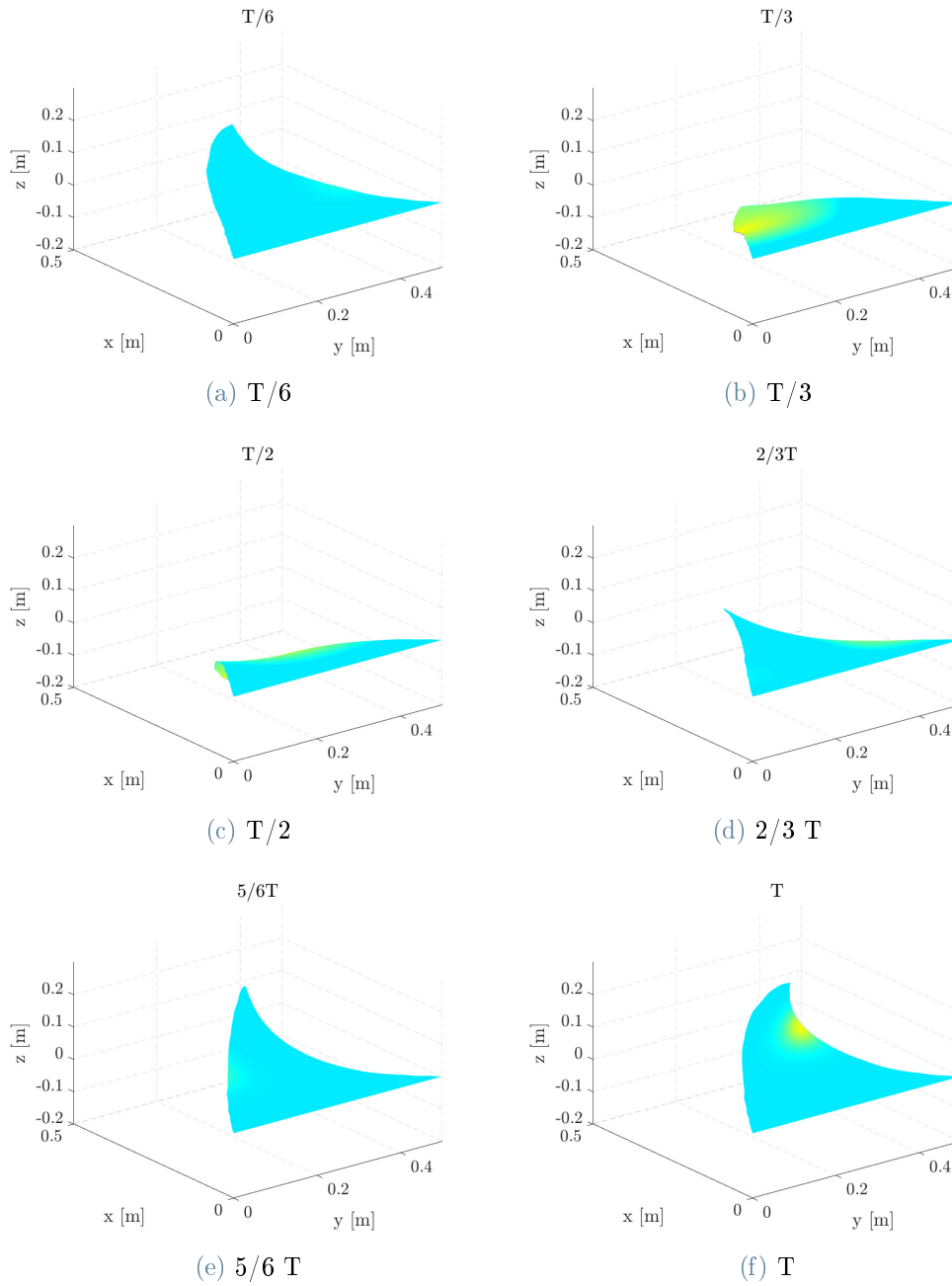
Figure 4.10: 3D deformed pectoral fin during a period

(a) T/6

(b) T/3

(c) T/2

(d) 2/3 T

(e) 5/6 T

(f) T
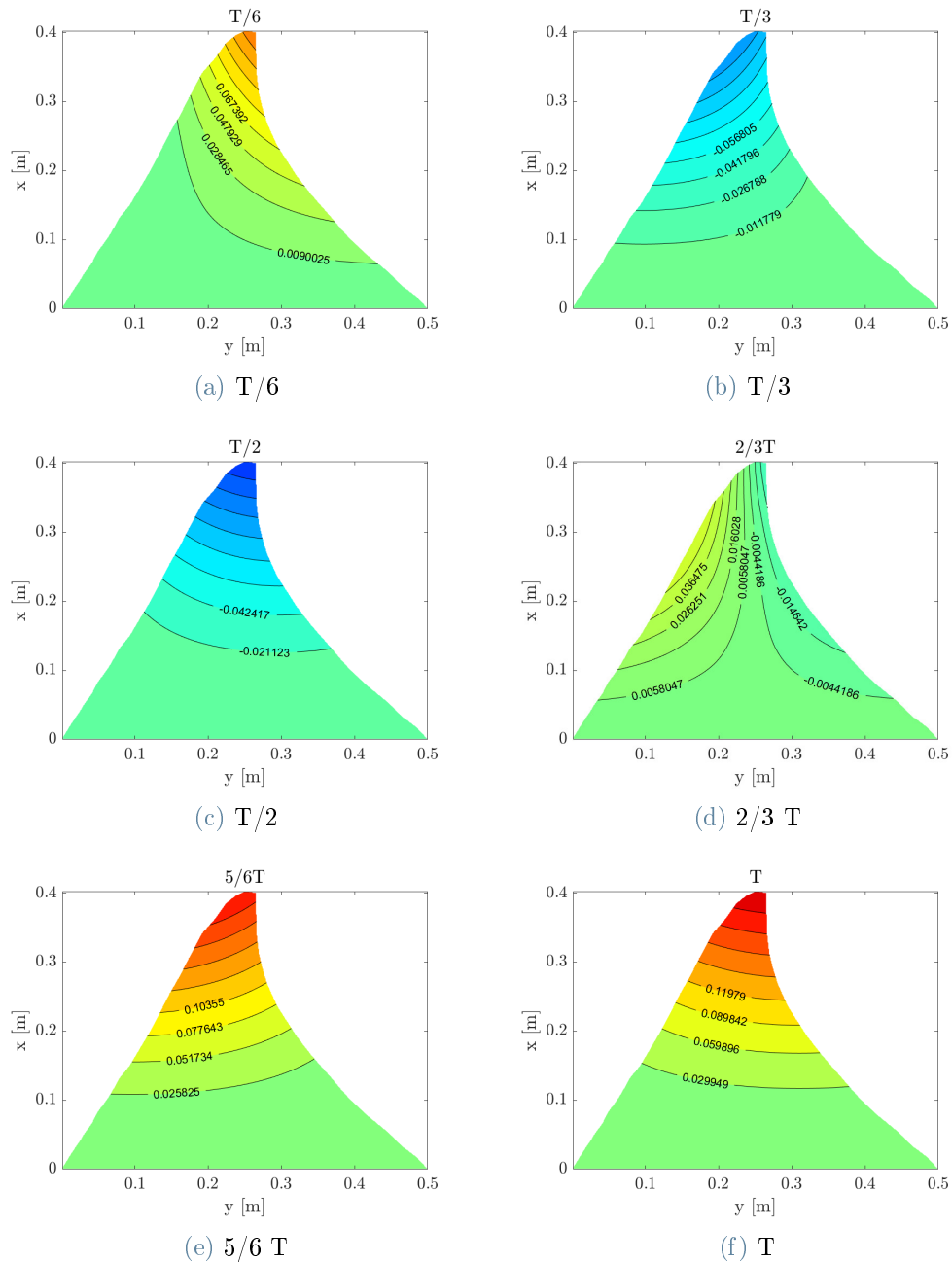
Figure 4.11: Contour plot of the vertical displacement (z-direction) of the pectoral fin during a period

The fin tip spanwise cross-section is endowed with the most significant spanwise dimension. Thus, it is characterized by the largest amplitude of oscillation, and it is the most representative in the analysis of the pectoral fin motion. In Figure 4.12, the position of the fin tip spanwise cross-section is displayed for several time instants during a period of fin oscillation. The position at the beginning of the downstroke is colored green, and the

line gradually shifts to blue, becoming dark blue at the end of the upstroke. It is possible
to note that the fin positions during upstroke and downstroke are very similar, but they
do not precisely match. The reason for this difference is the spanwise wave propagation,
which induces a slight delay on the fin tip. Due to the asymmetric flapping coefficient
δ, the amplitude of the upstroke is greater than that of the downstroke, matching the
observation of biologists [18, 101].
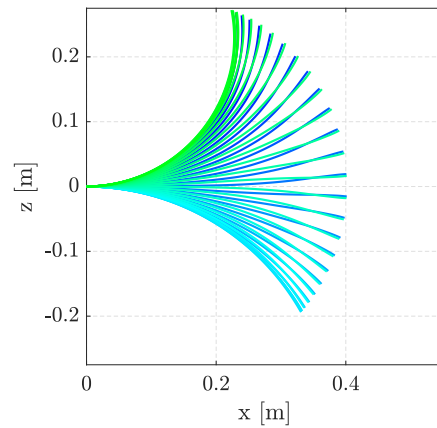
Figure 4.12: Flapping of the fin tip spanwise cross-section of the pectoral fin during a
period

The presence of a traveling wave on the fin surface can also be appreciated looking at
Figure 4.13, where the vertical positions during a period of a point at the middle of the
leading edge, of a point on the fin tip, and a point in the middle of the trailing edge are
shown. The fin tip, being more distal from the fin root, is characterized by a movement
of greater amplitude, and there is a phase delay between the three points.
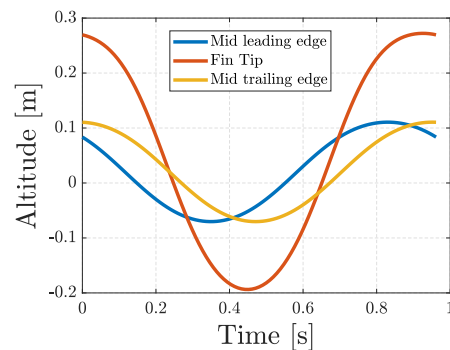
Figure 4.13: The harmonic altitude of three key points along chordwise direction: middle
point on the leading edge (MPL), fin tip (FT), middle point on the trailing edge (MPT)

4.2. Simplified dynamical model

Once the kinematics of the pectoral fin movement is known, it is possible to develop a simple dynamical model to estimate the thrust, power, and efficiency of this kind of locomotion. The high Reynolds number ($\sim 10^5$) associated with the cownose ray swimming involves that viscous forces can be considered negligible due to the characteristic length of the pectoral fin (fin baseline) and the swimming cruising speed. Therefore, the presented model takes into account only the reactive forces computed considering the change of momentum induced by the movement of a mass of water surrounding the fin. The presented model adopts the same frame of reference and coordinate system as shown in Figure 4.8. Since the chordwise cross-section ($y - z$ plane) movement on the pectoral fin is characterized by a traveling chordwise wave, passing from the leading edge to the trailing edge along the y direction, it is possible to consider the pectoral foil as if it were composed by a series of parallel mono-dimensional (1D) flexible foils moving in the $y - z$ plane. Hence, each chordwise cross-section along the x direction is assumed to be a 1D flexible foil, whose movement is characterized by its kinematic parameters, i.e., oscillation amplitude, oscillation frequency f, and wavelength λ of the traveling wave. The 1D flexible pectoral foil is conceptually modeled as depicted in Figure 4.14 [19].
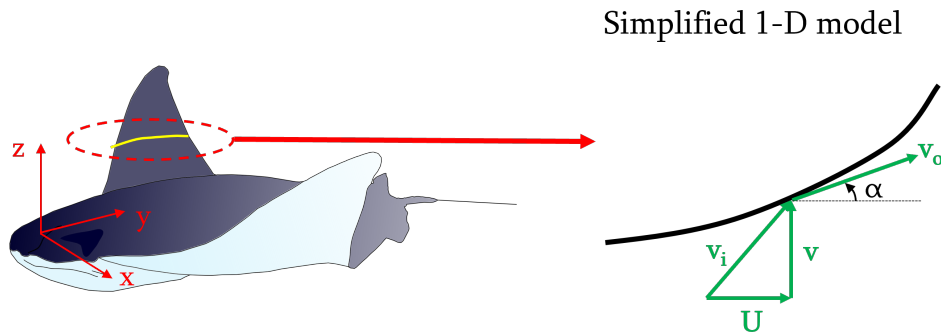
Figure 4.14: Model of the 1D flapping foil, represented during a downstroke

Considering each fin element as mono-dimensional, the lateral velocity of the fin is neglected, and the lateral flow is not taken into account in this analysis. Thus, the spanwise traveling wave is not considered in this model and N_s is set to 0. Each element of the fin extends in the chordwise direction and its velocity is only vertical. Moreover, being $\beta = \dfrac{\pi}{2}$, the r coordinate coincides with the y coordinate. The vertical displacement of each infinitesimal fin element can be computed according to Equation 4.4. It results to be a sinusoidal movement with an amplitude depending on the distance from the fin root, and with a mean value different from zero because of the asymmetric flapping coefficient

δ, which can be summarized as:

$$z(x, y, t) = A(x) \sin (\Phi y - \omega t) + c(\delta, x) \tag{4.5}$$

Then, the vertical velocity can be easily computed taking the derivative of the displacement:

$$\mathbf{v} = -\dot{z}(x, y, t) = A(x)\omega \cos (\Phi y - \omega t) \tag{4.6}$$

Finally, the relative velocity between the element of the fin and the fluid $\mathbf{v_i}$ is obtained as the sum of the vertical velocity and the longitudinal swimming velocity of the fish U, as shown in Figure 4.14.

$$\mathbf{v_i} = \mathbf{U} + \mathbf{v} \tag{4.7}$$

The infinitesimal element of length $\mathrm{d}l$, is so small that it can be considered as linear, and it is rotated about the horizontal axis of an angle α, which can be calculated as:

$$\tan \alpha = \frac{\partial z}{\partial y} = A(x)\Phi \cos (\Phi y - \omega t) \tag{4.8}$$

The incoming flow, with velocity $\mathbf{v_i}$, cannot cross the fin element; thus, after the interaction with the fin, it has a velocity $\mathbf{v_o}$ parallel to the fin element itself. The force, normal to the fin element, can be computed as the derivative of the momentum of the water. In an infinitesimal time $\mathrm{d}t$, the fin element sweeps an area $\mathrm{d}S$, as shown in Figure 4.15.
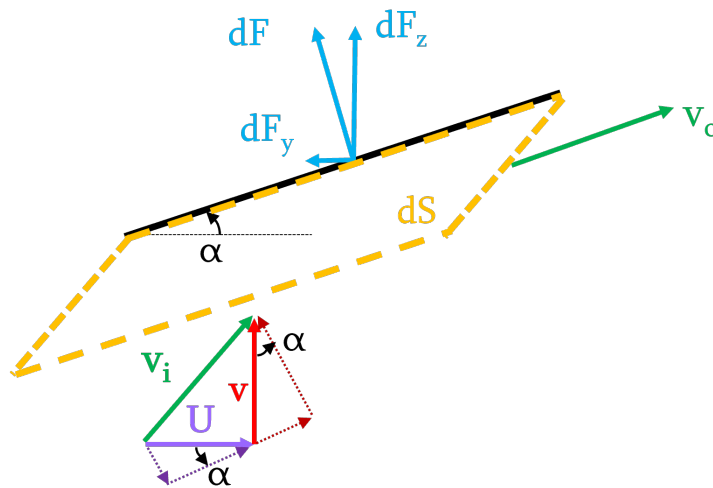
Figure 4.15: Force model of an infinitesimal element of the 1D flapping foil

The area $\mathrm{d}S$ can be calculated by multiplying the base of the parallelogram $\mathrm{d}l$ with its

height, which is the distance traveled in the normal direction within the time $\mathrm{d}t$, obtained by multiplying the time $\mathrm{d}t$ with the normal component of the velocity $\mathbf{v_i}$:

$$\mathrm{d}S = (v\cos\alpha - U\sin\alpha)\,\mathrm{d}t\mathrm{d}l \tag{4.9}$$

Hence, the mass of water accelerated by the fin element is:

$$\mathrm{d}m = \rho\,(v\cos\alpha - U\sin\alpha)\,\mathrm{d}t\mathrm{d}l \tag{4.10}$$

The force acting on the fin can be computed as the variation of momentum of the water:

$$\mathrm{d}\mathbf{F} = -\frac{\mathrm{d}m\mathbf{v_o} - \mathrm{d}m\mathbf{v_i}}{\mathrm{d}t} \tag{4.11}$$

Since this model neglects the tangential viscous forces on the fin, the acting force has only a component normal to the fin element, and the normal component of the outflow velocity is zero ($v_{o,n} = 0$). Hence, the infinitesimal force in Equation 4.11 can be simplified, and it can be expressed as a function of the normal component of the outflow velocity $v_{i,n}$:

$$\mathrm{d}F_n = \frac{\mathrm{d}mv_{i,n}}{\mathrm{d}t} \tag{4.12}$$

Combining Equation 5.15 and Equation 4.12, it is possible to obtain the infinitesimal force as a function of vertical and longitudinal velocity:

$$\mathrm{d}F_n = \rho\,(v\cos\alpha - U\sin\alpha)^2\,\mathrm{d}l \tag{4.13}$$

Equation 4.13 can be rearranged as:

$$\mathrm{d}F_n = \rho\sin\alpha\left(\frac{v}{\tan\alpha} - U\right)^2\mathrm{d}l \tag{4.14}$$

Substituting the expression of $\tan\alpha$ obtained in Equation 5.12, the infinitesimal force becomes:

$$\mathrm{d}F_n = \rho\sin^2\alpha\left(\frac{\omega}{\Phi} - U\right)^2\mathrm{d}l \tag{4.15}$$

where the term $\dfrac{\omega}{\Phi}$ is equal to the traveling wave velocity c. Finally, the thrust can be obtained by projecting in the longitudinal direction the normal force on the fin and integrating it on the fin surface Σ:

$$F_y = (c - U)^2\,\rho\iint_\Sigma |\sin^3\alpha(x,y)|\mathrm{d}l\mathrm{d}x \tag{4.16}$$

Following the same procedure also the force in the vertical direction can be calculated:

$$F_z = (c - U)^2 \rho \iint_\Sigma \sin^2 \alpha(x, y) \cos \alpha(x, y) \mathrm{d}l\mathrm{d}x \tag{4.17}$$

It is possible to observe that the forces generated by the fin vanish when $c = U$, as predicted by the waving plate and the slender fish models [73, 137], since the traveling wave is not able to give any momentum to the water, and the fin moves following a sinusoidal path in space. The generated thrust and vertical force obtained with the kinematic parameters presented in Table 4.1 are shown in Figure 4.16. According to the reference system present in Figure 4.14 a negative longitudinal force represents thrust whereas a positive force represents drag.

(a) Thrust　　　　　　　　　　　　　　　(b) Vertical force
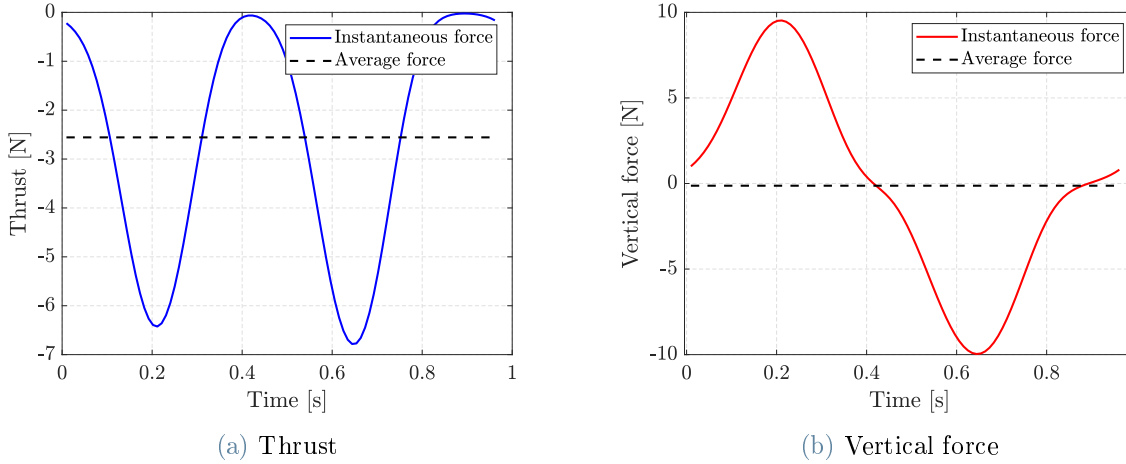
Figure 4.16: Forces acting on one fin swimming with the motion parameters shown in Table 4.1

Due to the asymmetry of fin movement, the mean value of the vertical force is not zero but slightly positive. The asymmetry of fin flapping is exploited by many batoid fishes, which are slightly negatively buoyant, to sustain their weight while swimming or to perform maneuvers. This asymmetry also implies that the thrust generated during the upstroke and the downstroke is not equal. Nevertheless, the asymmetry just slightly modifies the average value of the thrust force, as shown in Figure 4.17, where thrust and vertical force obtained with $\delta = 0$ are plotted.

(a) Thrust
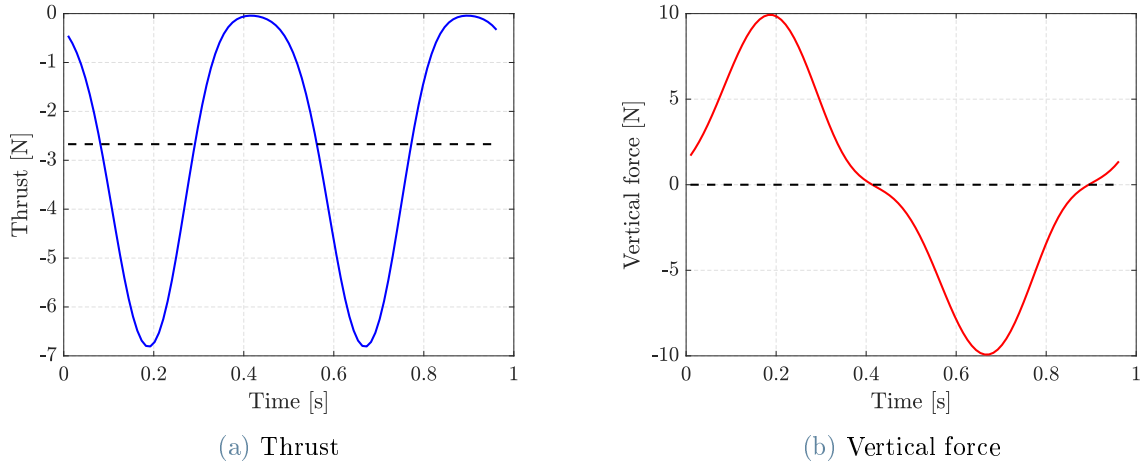
(b) Vertical force

Figure 4.17: Forces acting on one fin swimming with wavelength and frequency as in Table 4.1 and $\delta = 0$

A comparison between Figure 4.16 and Figure 4.17 confirms that the role of asymmetric flapping is to provide a vertical force without any significant effect on propulsion. Therefore, considering that the designed bioinspired robot is neutrally buoyant, this asymmetry can be neglected, and in the following analysis, δ is always equal to 0, so symmetrical movement is considered.

The efficiency of propulsion is computed as the ratio between the power of the thrust force, and the power of the vertical force acting on the fin element, which is the power exerted by the fish to move its fins.

$$\eta = \frac{1}{T} \int_T \frac{\mathrm{d}F_y U}{\mathrm{d}F_z v} \mathrm{d}t \tag{4.18}$$

Substituting the expressions of F_y and F_z previously obtained into Equation 4.18, the energy efficiency becomes:

$$\eta = \frac{1}{T} \int_T \frac{\rho \left(v \cos\alpha - U \sin\alpha\right)^2 \sin\alpha}{\rho \left(v \cos\alpha - U \sin\alpha\right)^2 \cos\alpha} \frac{U}{v} \mathrm{d}t = \frac{1}{T} \int_T \frac{\tan\alpha}{v} \frac{U}{v} \mathrm{d}t = \frac{U}{c} \tag{4.19}$$

This result is remarkable since Equation 4.19 states that the energy efficiency of fish swimming only depends on the ratio between the forward speed and the traveling wave velocity, and that when the two velocities coincide, so that no thrust force is generated, the efficiency is 1, in accordance with the models of the slender fish and of the waving plate.

To understand the mechanism of propulsion, the effect on thrust and efficiency of each kinematic parameter is studied.

Wavelength effect   The thrust generated with different wavelengths at different velocities is plotted in Figure 4.18.

(a) Thrust at different velocities

(b) Thrust at different ratios between wave velocity and swimming velocity
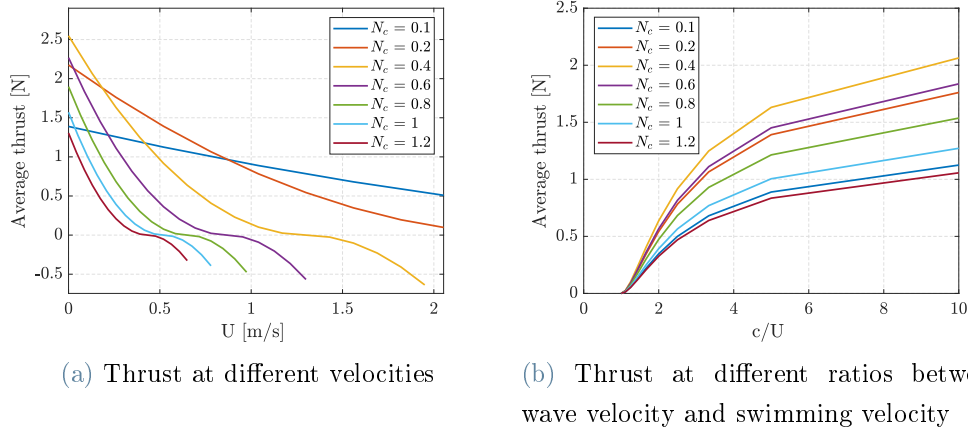
Figure 4.18: Thrust generated with different wavelengths with $f = 1.04\,\mathrm{Hz}$ and $\theta_{max} = 65°$

According to Equation 4.16, the generated force is null when the swimming velocity reaches the traveling wave velocity for every wavelength. Increasing the wavelength, i.e., decreasing the number of chordwise waves N_c, the traveling wave velocity increases, thus the forward thrust increases since the velocity at which water is pushed backward is greater.

Nevertheless, as the wavelength becomes greater, the fin becomes flatter, and the angle α reduces. Therefore, the force tends to be directed more in a vertical direction than in a horizontal one, and when this effect becomes predominant over the other one, the generated thrust decreases.

Frequency effect In Figure 4.19 the effect of a variation of frequency on the generated thrust is presented.

(a) Thrust at different velocities

(b) Thrust at different ratios between wave velocity and swimming velocity
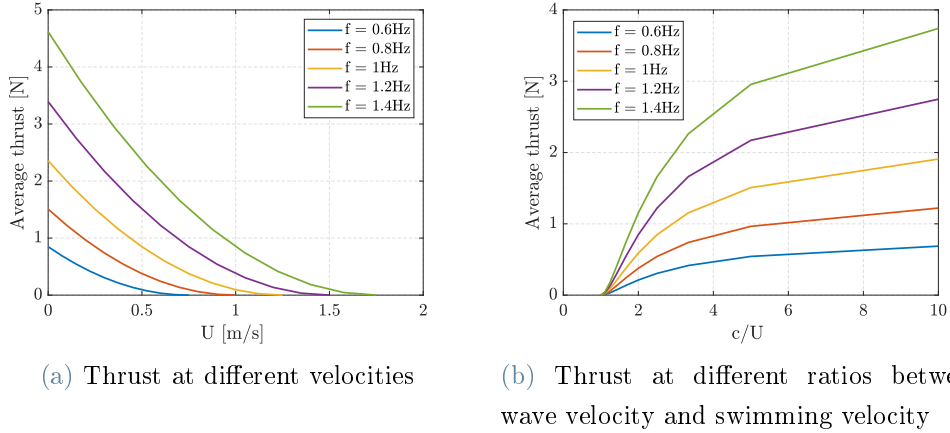
Figure 4.19: Thrust generated with different frequencies with $N_c = 0.4$ and $\theta_{max} = 65°$

The flapping frequency is proportional to the traveling wave velocity; thus, the steady-state speed, for which the generated thrust is zero, is proportional to frequency. Since a frequency variation does not modify the fin orientation during a flapping period, the generated thrust always increases as the frequency increases.

Amplitude effect The last kinematic parameter considered in this analysis is the flapping amplitude, and in Figure 4.20, the effects of an amplitude variation on the propulsive thrust are presented.

(a) Thrust at different velocities

(b) Thrust at different ratios between wave velocity and swimming velocity
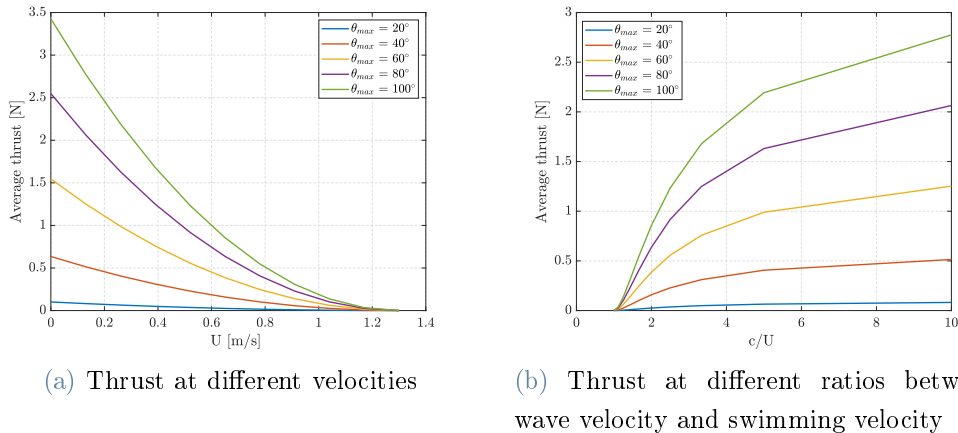
Figure 4.20: Thrust generated with different amplitudes with $N_c = 0.4$ and $f = 1.04\,\text{Hz}$

Increasing the amplitude of fin movement, the generated thrust increases, nevertheless the steady-state velocity corresponding to a null thrust does not change, suggesting that increasing the amplitude cannot be an effective strategy to swim faster, but it can be useful to increase the thrust during acceleration phases. In Figure 4.21, the energy efficiency at different velocities obtained varying the kinematic parameters is presented. It is possible to observe that the swimming efficiency corresponds to the ratio U/c and is not dependent on any kinematic parameter.
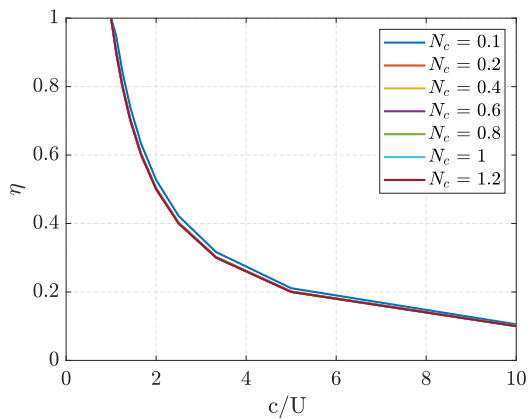
(a) Efficiency at different velocities with different wavelengths
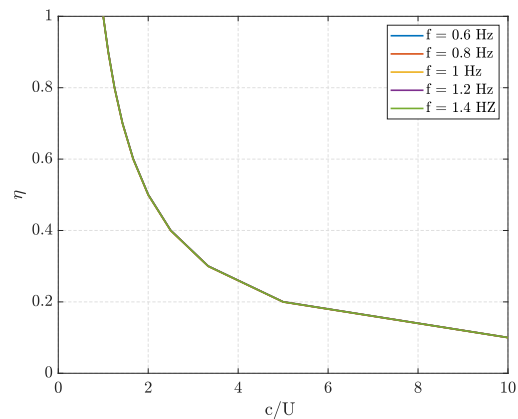
(b) Efficiency at different velocities with different frequencies
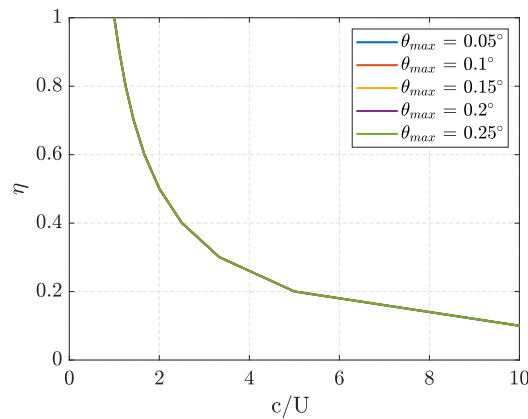
(c) Efficiency at different velocities with different amplitudes

Figure 4.21: Efficiency obtained varying the kinematic parameters

In an ideal inviscid fluid, where drag force is not present, the steady-state velocity always corresponds to the traveling wave velocity, and the swimming efficiency is one for any possible combination of kinematic parameters. Nevertheless, in real swimming conditions,

the drag force is present so that the fish cannot find an equilibrium for $U = c$, but the equilibrium between thrust and drag is reached for $U < c$. Hence, a combination of kinematic parameters for which the equilibrium is reached at a swimming velocity U close to the traveling wave velocity c is expected to be very efficient, whereas a different combination, for which the equilibrium is reached at a velocity $U \ll c$ is expected to have low efficiency. Thus, to study the efficiency of this kind of swimming propulsion it is necessary to consider in the analysis also the drag force, which depends on kinematic parameters as well, since the fin shape and its angle of attack are dependent on the wavelength and the amplitude of the movement. Therefore, it is impossible to study the efficiency with such a simplified model, and a more complex numerical simulation is required.

4.3.   CFD model of forward swimming

The models presented so far provide an accurate explanation of the main principles behind fish locomotion; however, their analytical approach is based on several simplifying assumptions that do not capture the complexity of the fin motion. Conversely, a numerical approach is more suitable to investigate the forces acting on the fins and the wake structure, relating them to the kinematic parameters of fin deformation. Computational fluid dynamics (CFD) is a widespread tool used to investigate fish locomotion and, in particular, the swimming of batoid fishes.

Previous studies include the work of Fish, who investigated the dynamics of steady-state swimming of a manta ray with an immersed boundary element method. In their analysis the fish is still and it is immersed in a constant velocity flow opposite to the swimming direction, they studied the vortices in the wake and the efficiency of this kind of propulsion relating it to the Strouhal number [39]. Liu's research also uses numerical tools to analyze a robot's wake structure inspired by a batoid fish swimming at a constant velocity [77]. In the work of Zhan, the gliding of a manta under the sea surface is simulated, obtaining drag and lift coefficients of still fins at different angles of attack [145]. The numerical investigation of Sharp regards the forces acting on a fin performing an undulatory motion, and it is carried out using Multiparticle Collision Dynamics [112]. The dynamics of the interaction with water of a deformable fin has been explored by Liu who modeled the fin as a series of panels connected by springs [78], and by Wei-Shan, who performed a dynamic analysis of the motion of a *Raja Eglanteria* coupling the CFD with a dynamic solver [134]. Bottom performed numerical simulations of swimming locomotion of stingrays, analyzing vortices in the wake [15].

Similarly, Thekkethil studied the hydrodynamics of batoid fishes describing the

three-dimensional vortex structure, and they highlighted that the cownose ray has one of the highest thrust coefficients among batoid fishes [125]. Huang performed a hydrodynamic analysis coupled with a complete six-degree-of-freedom (6DOF) simulation of a bioinspired robot with undulating fins and two propellers; they have found a relation between fin flapping frequency and speed of the robot and they studied the stability of the robot during forward swimming and maneuvers [58].

The work object of this thesis improves the results of the aforementioned researches analyzing the forward swimming of a cownose ray accelerating from rest to the steady-state velocity. The deformation of the fin is imposed, whereas the forward swimming motion is calculated together with the pressure and velocity fields of the surrounding fluid. In terms of thrust, efficiency, and steady-state velocity, the wake structure and the results are then compared and put in relation to the frequency and wavelength of fin deformation. This analysis aims to explain the complex phenomena, which allow batoid fishes to have high efficiency and relate them to wavelength and frequency of fin motion.

4.3.1. Description of the CFD model

The shape and dimensions of the fins are taken from the literature [19], and they are shown in Figure 4.22. The cross-section of the fin is approximated as a series of symmetric airfoils smoothly tapering toward the fin tip: at the body center the cross-section is approximated with a NACA 0020, at the fin midspan with a NACA 0015, and near the fin tip with a NACA 0012.

(a) Airfoils approximating the fin cross-section　　　(b) Dimensions of the fin for the numerical analysis
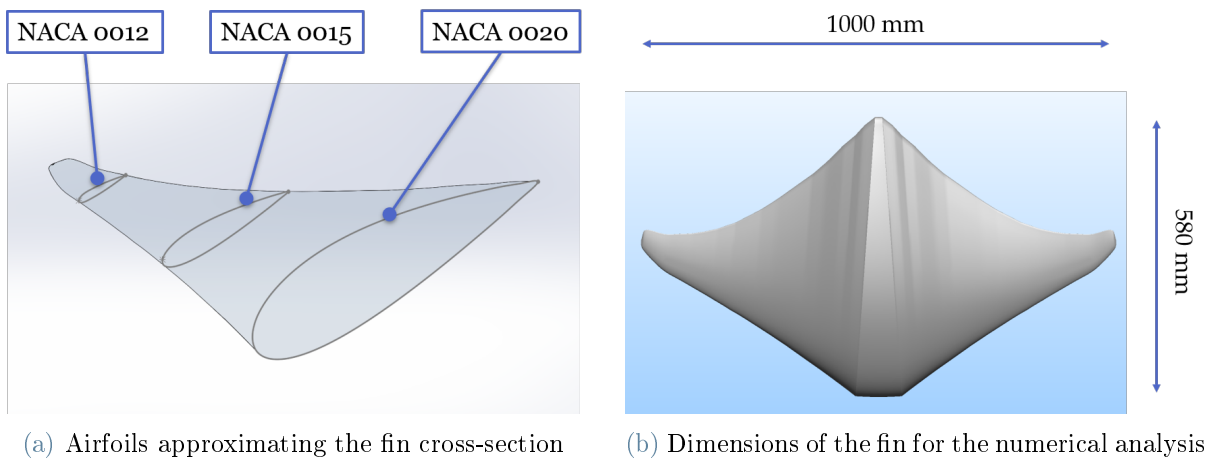
Figure 4.22: Shape and dimensions of the fin for the numerical analysis

The kinematics of fin motion, presented in the previous section, is slightly simplified in order to obtain a continuous function and make the calculation of the displacement of the points belonging to the fin surface independent from each other. First of all, the asymmetry coefficient δ is neglected, since its influence is not relevant, as shown in the previous section. Moreover, it has been observed that the tip deflection lag, determined by the spanwise traveling wave, gives a minor contribution in thrust generation with respect to the chordwise wave [88]; therefore, Ψ can be ignored. It has been hypothesized that the tip lag contribution consists of reducing losses due to the tip vortices [39]; however, this effect will be analyzed in future work.

Lying on these assumptions, Equation 4.2 becomes

$$\theta(s, y, t) = \frac{1}{L_y} \theta_{max} s \sin\left(\Phi y - \omega t\right) \tag{4.20}$$

and x and z coordinates of each point of the fin can be calculated as:

$$x(s, t) = \int_0^s \cos\left[\theta(\sigma, y, t)\right] \mathrm{d}\sigma = \frac{\sin\left[\theta_{max} s \sin\left(\Phi y - \omega t\right)\right]}{L_x \theta_{max} \sin\left(\Phi y - \omega t\right)} \tag{4.21}$$

$$z(s, t) = \int_0^s \sin\left[\theta(\sigma, y, t)\right] \mathrm{d}\sigma = \frac{1 - \cos\left[\theta_{max} s \sin\left(\Phi y - \omega t\right)\right]}{L_x \theta_{max} \sin\left(\Phi y - \omega t\right)} \tag{4.22}$$

The CFD model of a forward swimming cownose ray is implemented in theopen-source software OpenFOAM. The three-dimensional unsteady simulation is carried out using an overset mesh. It consists of two mesh grids merged: the first encompasses all the domains and remains still, the second includes a portion of fluid around the fish and moves jointly with it. The two meshes occupy the same space, and the software interpolates between overlapping elements to find a unique solution [113].

The motion of the internal mesh surrounding the fish results from the superimposition of two motions: forward swimming and fin deformation. As far as the fin deformation is concerned, every point of the mesh surrounding the fish is moved according to Equations 5.1 and 5.2, resulting in a mesh deformation correspondent to the motion of the fin. This motion depends only on the kinematics of fins, which are imposed.

On the other side, for forward swimming, the fish and its surrounding mesh are treated as a rigid body. The dynamics along the longitudinal axis of the fish are solved with a Newmark solver featured by $\beta = 0.25$ and $\gamma = 0.5$. The only degree of freedom of the fish is the forward displacement, whereas all the other DOFs are constrained. Therefore, at every time-step, the fins are moved, deforming the internal mesh, and the solver

calculates the forces acting on the fins and the forward displacement of the fish.

The solved equations are unsteady Reynolds-averaged Navier-Stokes (URANS), and the solver used in OpenFOAM is overPimpleDyMFoam, capable of solving unsteady, incompressible, turbulent flows with an overset mesh.
The domain is shown in Figure 4.23, the stationary mesh is colored in blue and the moving mesh in red.
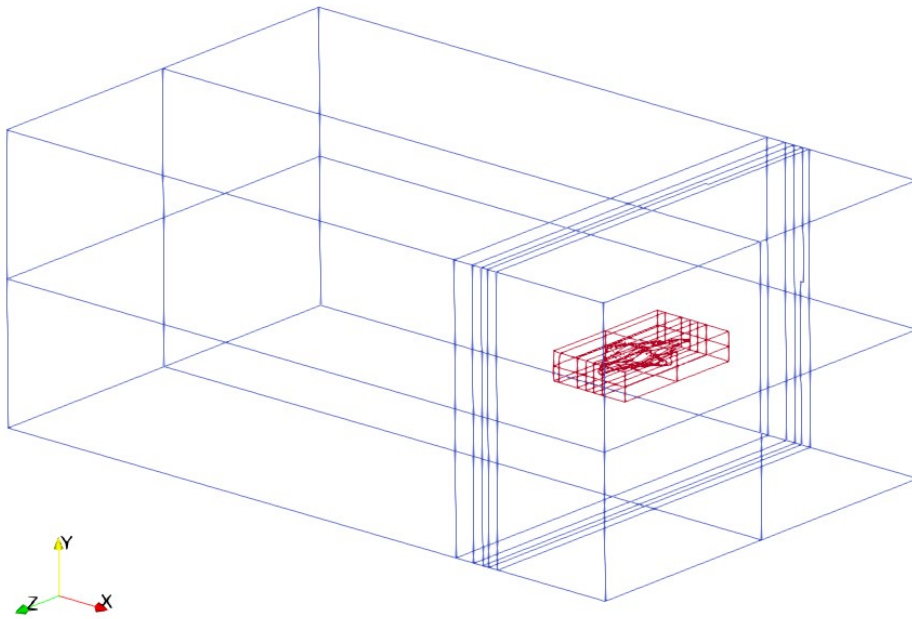
Figure 4.23: Domain of the CFD simulations, with the background mesh colored in blue and the overset mesh colored in red

The background domain comprises 300,000 (200x30x50) hexahedral cells, with a gradual refinement toward the zone occupied by the moving mesh. Its dimensions are 5m x 3m x 2m, and it is shown in Figure 4.24a.
The moving mesh is obtained using snappyHexMesh on a 0.6m x 0.2m x 1.1m block, with three levels of refinement on the surface of the fish, resulting in a mesh of 1,462,199 cells, shown in Figure 4.24b. To reduce interpolation errors, cells at the boundary of the moving mesh have similar dimensions to cells in the background.

(a) Background mesh   (b) Overset mesh surrounding the fish
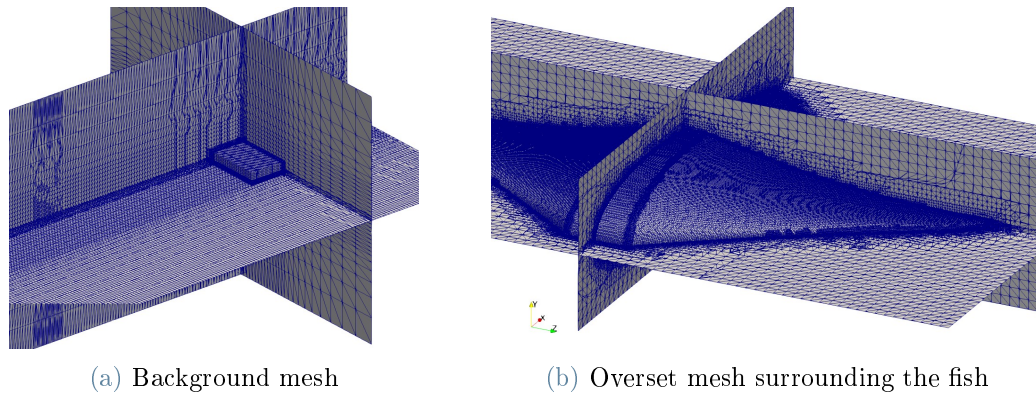
Figure 4.24: Mesh used in the CFD simulations

The results of the grid sensitivity analysis are shown in Figure 4.25, where the velocities obtained with different mesh grids are shown. The coarsest mesh has two levels of refinement on the fish surface, and the cells in the background are twice as large as the cells of the chosen mesh, whereas the most refined mesh grid has four levels of refinement and its cells are twice as small. It is possible to note that the results obtained are independent of mesh size since the average error between the normal and the most refined mesh is 1.25 %.
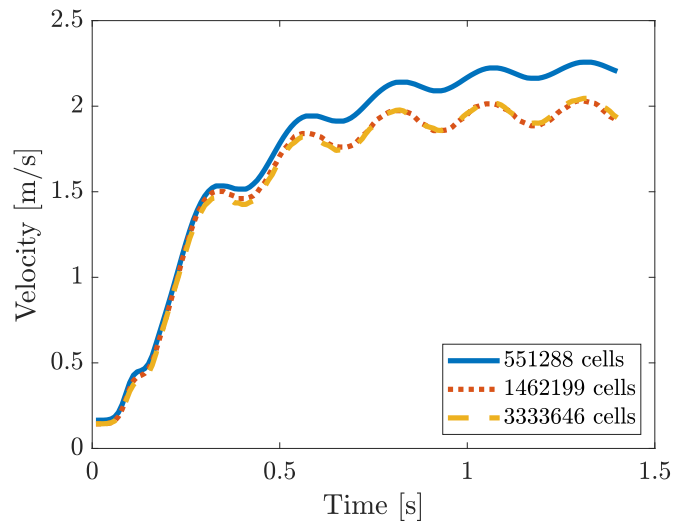
Figure 4.25: Grid sensitivity analysis showing the velocity obtained with meshes of different sizes

The turbulence is resolved using a $k - \omega \ SST$ (shear stress transport) turbulence model with standard wall functions. The validity of the chosen mesh size for the adopted

turbulence model is evaluated by calculating the y^+ parameter which represents the dimensionless distance from a wall and is calculated as follows:

$$y^+ = \frac{y u_T}{\nu} \tag{4.23}$$

where y is the distance from the wall, ν is the kinematic viscosity of the fluid, and u_T is the friction velocity. The friction velocity is calculated as shown in Equation 4.24, and represents the velocity related to the shear stresses τ_w between layers of the flow.

$$u_T = \sqrt{\frac{\tau_w}{\rho}} \tag{4.24}$$

In Figure 4.26, the surface of the fish is colored with y^+ for the standard mesh: the values are smaller than 300 everywhere meaning that the results obtained with this turbulent model are reliable.
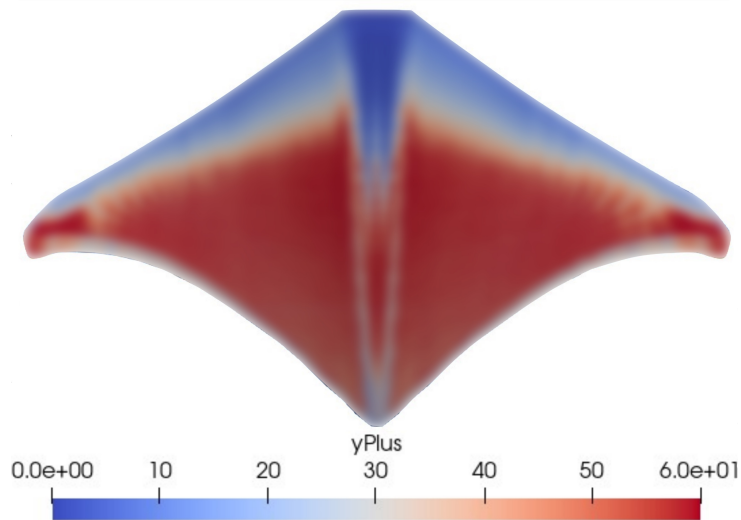
Figure 4.26: y^+ on the fish surface

A similar analysis has been performed to assess the independence of the results from the domain size. The results are compared in Figure 4.27, where it is possible to note that by increasing the size of the domains, the difference in velocity is negligible.

For this analysis, the sizes of the overset domain have been changed with the same proportions as the background domain. The analysis of the independence of the domain size is performed on a different simulation with different kinematic parameters from the analysis of the mesh size.
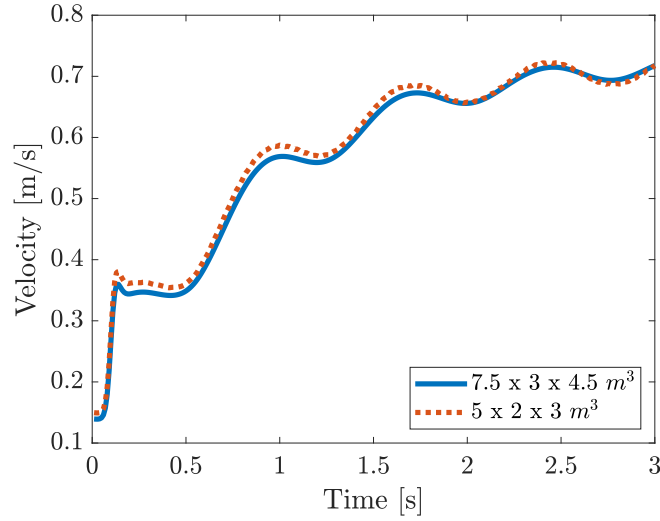
Figure 4.27: Domain size sensitivity analysis showing the velocity obtained with domains of different sizes

At the initial time step, the fins are undeformed, and pressure is zero all over the domain. The velocity has been set to a very small value of 1×10^{-3} m/s on one extremity of the boundary; zero-gradient velocity boundary conditions are applied to the other sides of the domain, and a moving wall velocity condition is applied on the surface of the cownose ray. Pressure is set to a zero value on one extremity of the domain, and a zero-gradient condition is applied to all the other boundaries. The mesh deformation due to fin motion is imposed on all the moving mesh. This is obtained by including Equations 5.1 and 5.2 in the rigid body motion solver of OpenFOAM for all the cells belonging to the moving domain.

The Reynolds number characterizing this problem cannot be calculated a priori since the steady-state velocity of the fish is unknown. Nevertheless, it is possible to estimate this speed as all the kinematic parameters of the fin motion are determined, and the speed of the traveling wave can be computed as $c = \dfrac{\omega}{\Phi}$. Thrust can only be obtained if the speed of the traveling wave c is greater than the forward swimming speed of the fish U. As a matter of fact, when equilibrium is reached, and the cownose ray is swimming at a constant speed, the generated thrust is small, just the amount needed to overcome the drag, and the steady-state speed is slightly smaller than the traveling wave velocity. This prediction allows having an estimation of the Reynolds number. For a swimming gait, it

can be calculated as reported in Equation 7.4 [44]:

$$Re \approx Sw = \frac{\omega A L}{\nu} \tag{4.25}$$

where ω is the frequency of flapping, A is the amplitude of fin-tip displacement, and L is the average chord length of the fin, as shown in Figure 4.28. The Reynolds number results to be $\sim 10^5$ for all the analyses.
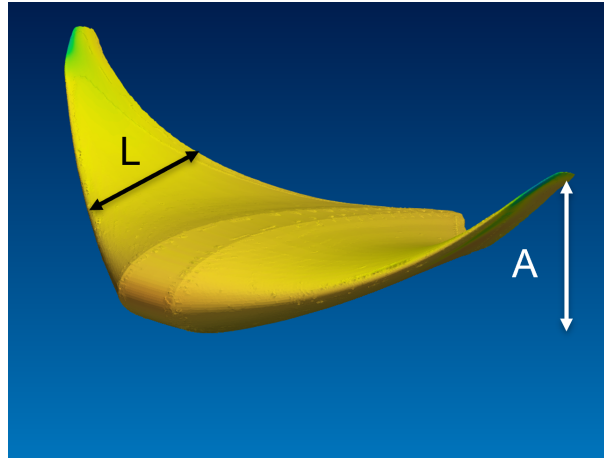
Figure 4.28: Characteristic dimensions of the cownose ray for Reynolds number calculation

4.3.2.   Vortex structures in the wake and leading-edge vortex

The description of the thrust generation principle and of the structure of the wake is performed referring to the simulation with $\omega = 4\pi$ rad/s and $\lambda = 2.5$ body length (BL), but the qualitative description of the results can be extended to all the cases analyzed in this work.

Thrust generation is concentrated on the external parts of the fins, where the motion is of higher amplitude, whereas the central part of the body generates most of the drag, as other researchers have highlighted [77]. The contribution to thrust generation over the fin surface is shown in Figure 4.29, where the force acting in the swimming direction divided by the area of the element is presented. A negative value, shown in blue, means a contribution to thrust, and a positive value, shown in red, represents a contribution to drag.
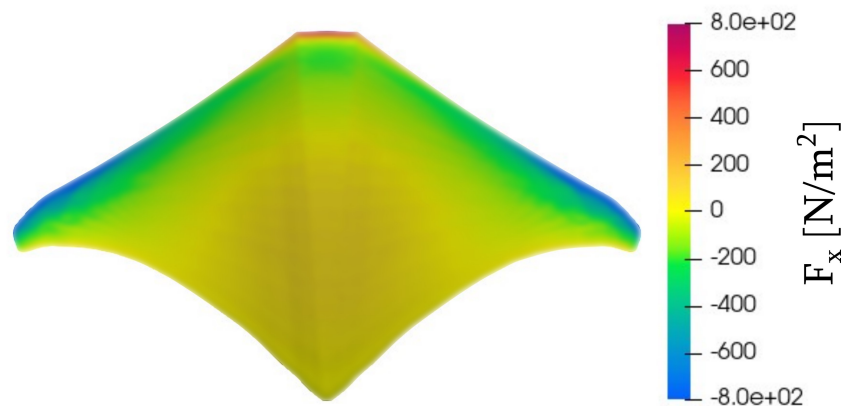
Figure 4.29: Force in swimming direction on the bottom side of the fish during upstroke

Figure 4.30 illustrates the pressure distribution during upstroke and downstroke in the plane at midspan of the fin, shown in Figure 4.30a. The fin movement creates a large negative pressure area in front of the fish, which is pushed forward by this pressure difference.

Observing the pressure distribution on the fins and the time profile of thrust, it is possible to notice that a propulsive force is generated during both upstroke and downstroke with equal values because both the profile and the fin motion are symmetric.

(a) Plane of the section shown in Figures 4.30b and 4.30c

(b) Pressure distribution around the fin during upstroke

(c) Pressure distribution around the fin during downstroke
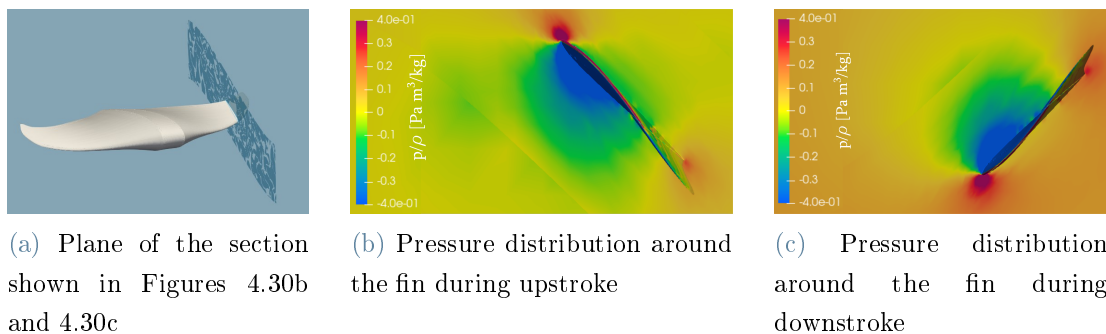
Figure 4.30: Pressure distribution around a section in the middle of the fin

Hence, during a flapping cycle, thrust generation is subject to a sinusoidal variation with a double frequency with respect to the frequency of flapping. The generation of propulsive force is proportional to the fin velocity; thus, it is maximum in the midpoint of flapping, and it is minimum at the upper and lower limits of its stroke.

A null thrust is generated when the fin tips reach the top and bottom extremities, whereas thrust is maximum in the middle of their motion. When the fin is at one end of its stroke, the velocity of its motion is zero; thus, it cannot impress any momentum to the

surrounding water, so it does not generate any thrust. This can be observed in Figure 4.31a, showing the thrust variation over four periods of fin flapping. It is possible to note that at the beginning, when the fish is accelerating, there is a propulsive net force over one period, whereas, when it has reached the steady state, the average force over one period is zero.

As shown in Figure 5.19a, steady-state velocity is reached after a few cycles, and it follows the same sinusoidal variations as thrust. When the steady state is reached, the oscillations around the average velocity do not exceed 5% of the average velocity. The velocity of the fish is non-dimensionalized with respect to its dimensions, and it is represented in body length per second (BL/s), where the body length is $0.58\,\mathrm{m}$, as shown in Figure 4.22b.
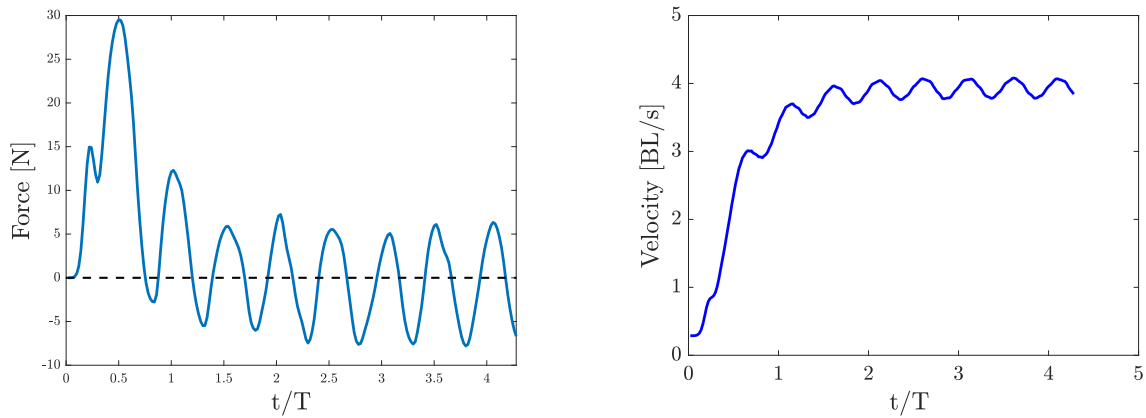
(a) Force in the swimming direction during four periods

(b) Velocity of the fish during four periods

Figure 4.31: Force in the swimming direction and velocity of the fish

The force in the longitudinal direction is the sum of thrust and drag, and when the steady state is reached, it oscillates around a zero mean value. To calculate the efficiency, thrust and drag contributions need to be separated, as discussed in Chapter 2. Thus, according to the definition of energy efficiency provided in Chapter 2, the forces contributing to the useful power are only those acting in a normal direction to the surface of the fins, whereas the tangential viscous forces and the forces acting on the rigid central body are resistive forces opposing to forward motion.

This decomposition of the longitudinal force is shown in Figure 4.32, where it is possible to observe that the thrust force, normal to the fin surface, is always positive, and it has a null value in correspondence of top and bottom extremities of fin movement, when the velocity is null, showing the same trend as obtained with the simplified dynamical model.

The drag force is quadratically proportional to the velocity, and it increases as the fish accelerates, but it also displays oscillations during the period due to variation of shape and angle of attack of the fin, which modify the drag coefficient of the fin.
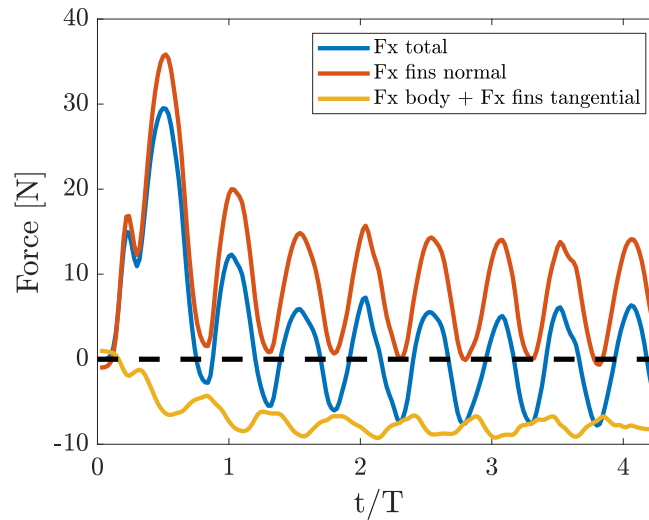
Figure 4.32: Forces acting on the fish along the swimming direction

This decomposition of the longitudinal forces allows computing the efficiency of swimming locomotion for every combination of kinematic parameters, which will be discussed in the following paragraphs.

To understand how the fins move the fluid and why a thrust is generated, it is essential to investigate the structure of vortices in the wake. The vortices in the wake are shown in Figure 4.33, seen from different perspectives.

For each fin, it is possible to divide the wake into three different parts:

- fin tip vortices

- vortices behind the middle of the fin

- vortices behind the center of the body

The vortices in the wake are very similar to those obtained by Fish [39]. The only difference is the absence of the vortices near the body center in their work. This could be because they are simulating a different species of batoid fish, which has a larger body than the cownose ray; thus, the fluid motion around the body center is less affected by

the fin flapping.

(a)

(b)
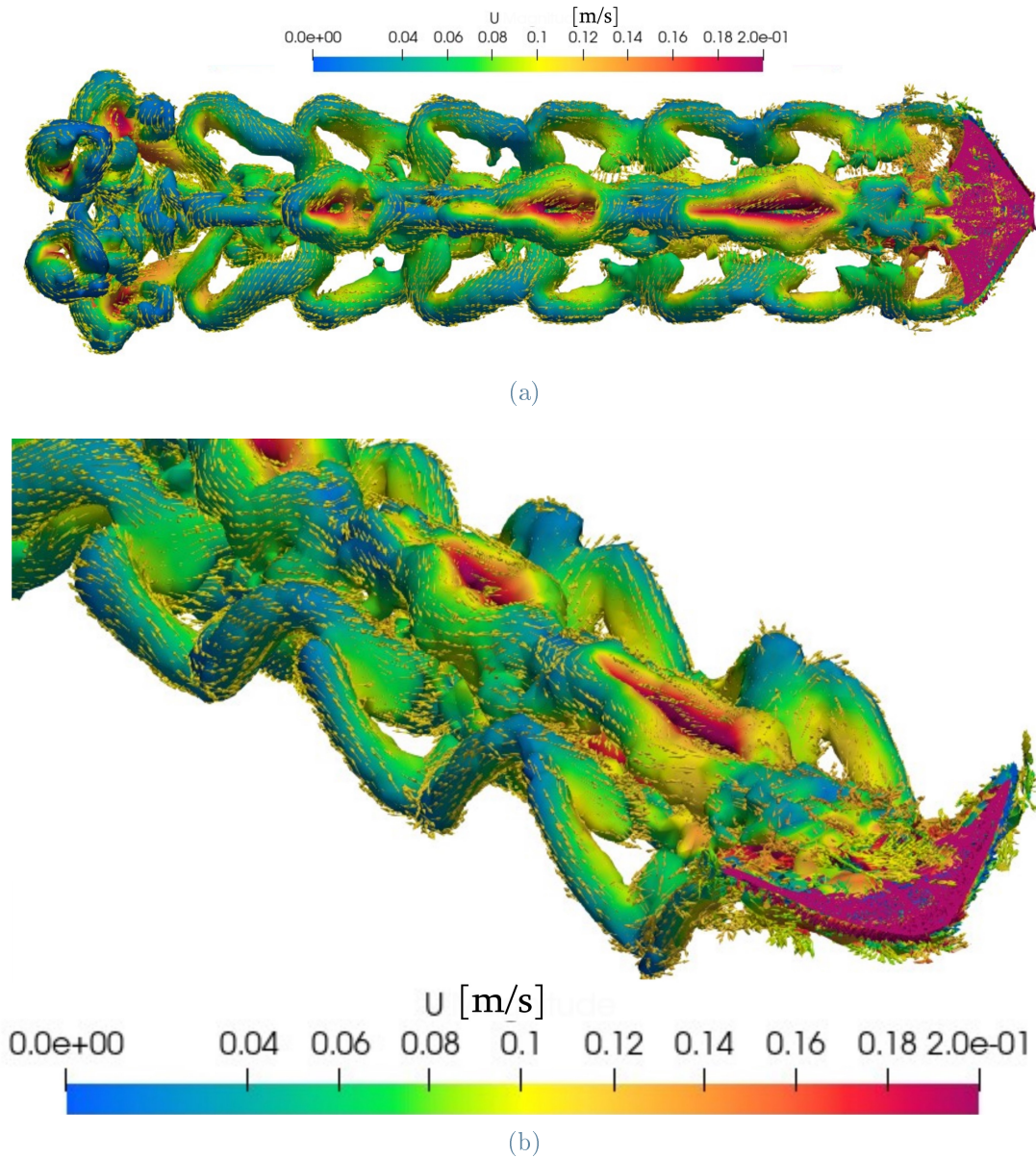
Figure 4.33: Contour of surfaces with $\lambda_2 = 0$, with vorticity vectors

An interesting result of this numerical analysis is the comprehension of the mechanism allowing high efficiency of these fishes based on vortices shedding. Like many other fishes, cownose rays shed a vortex in the wake at each half flapping period every time the fin reaches the top or the bottom of its motion. Such vortices rotate clockwise or counterclockwise depending on whether the fin has performed an upstroke or a downstroke [77].

Observing the wake structure in a plane perpendicular to the fin span shown in Figure

4.30a, it can be noticed that vortices are arranged like in a reverse Karman Street, as presented in Figure 4.34 with counterclockwise vorticity on the top and clockwise vorticity at the bottom, with the fish swimming leftward. This vortices arrangement produces a sort of propulsive jet in the center of the wake, whereas there is a counterflow in the surrounding volume. In case the fish swims at a constant speed, jet stream and counterflow are balanced, and the net streamwise momentum in the wake is null [34, 72].
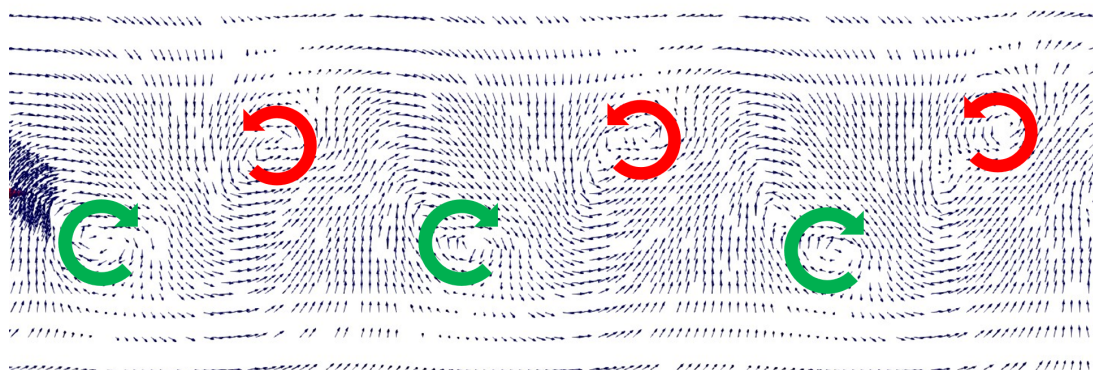
Figure 4.34: Vortices in the wake forming a Reverse Karman Street

The vortex detachment mechanism is illustrated in Figure 4.35, where a section perpendicular to the span-axis of the fin is shown at different time instants, with the streamlines of absolute velocity. The fish is swimming from left to right, and the first time step is shown on the left:

a) The fish is swimming rightwards, performing an upstroke. A negative pressure area is formed on the lower side of the fin; therefore, water from the top side flows on the opposite side, rotating around the fin's leading edge. On the rest of the fin, the water is pushed upward and backward following the motion of the traveling wave.

b) When the fin reaches the upper extremity of its motion, its velocity is null, as it is about to reverse the vertical direction of fin flapping. Hence, the pressure difference between the two sides is absent, and the vortex around the leading edge disappears, while water behind the trailing edge has an upward and backward velocity, impressed by the fin at the previous time instant.

c) Then, when the fin begins its downward motion, the flow surrounding the fin is opposite to the one described in the first time instant, and the water behind the trailing edge is pushed downward. Just behind, the water still conserves its upward velocity given by the upstroke; thus, a vortex forms.

This mechanism of vortex formation is the same highlighted on heaving and pitching airfoil [1, 109].

(a)　　　　　　　　　　　　(b)　　　　　　　　　　　　(c)
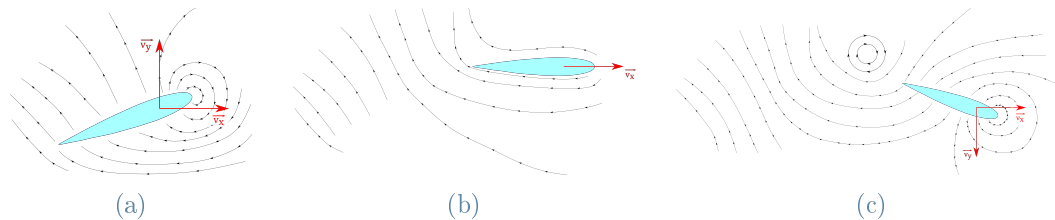
Figure 4.35: Sequence of time steps during a quarter of flapping cycle, highlighting the detachment of one of the vortices forming the reverse Karman street

Although vortices in the wake cause dissipations, it is unavoidable that some vortices are generated when a body moves periodically in a viscous fluid, as discussed in Chapter 2. The vortices highlighted in the previous paragraph are a direct consequence of this kind of motion, responsible for thrust production [72].

Therefore, although it is desirable to keep them as small as possible, they result from a thrust-producing movement of high energy efficiency.

In Figure 4.36, it is also evident that a momentum surplus in the opposite direction to swimming is present in the wake during acceleration, remembering that the fish is swimming from right to left. On the top, velocity vectors in the wake are shown: water is pushed backward by fin motion and alternately upward and downward following the fin displacement.

In the beginning, when the acceleration is greater, the amplitude of velocity vectors is higher. At the bottom, the velocity component in the swimming direction is presented in a color scale. It is possible to note that a propulsive jet stream is present in the center, whereas on the top and at the bottom, in correspondence of vortices, some water moves in the opposite direction.

(a)

(b)
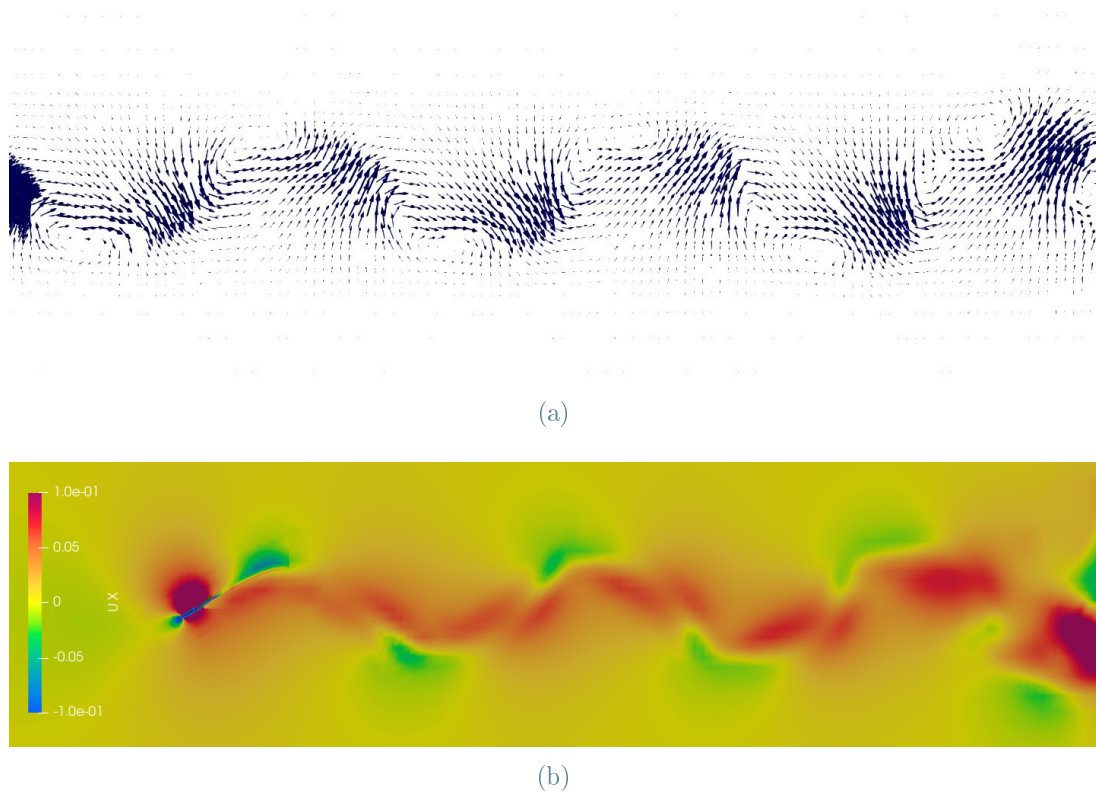
Figure 4.36: On the top velocity vectors; at the bottom velocity component in the swimming direction

Another vortex is shown in Figure 4.37b, where the velocity vectors are drawn on the plane shown in Figure 4.37a. It is generated around each fin tip due to the pressure difference between the two sides of the fin. During downstroke, the fin motion creates negative pressure on the upward-facing side; thus, the fluid on the downward-facing side tends to rotate around the fin tip and move to the other side, generating a vortex. The same mechanism is repeated during the upstroke, with a vortex rotating in the opposite direction. The generation of this vortex occurs only behind the fin tip because of the shape of the fish because the spanwise velocity of water that tends to move on the opposite side is smaller than the forward velocity of the fish divided the tangent of the sweep angle of the fin. The curvature of the fin is optimized to reduce the strength of this vortex. The high curvature of the fin makes its tip act as a winglet and obstructs the passage of water from one side to the other.

(a) Plane just behind the fin tip   (b) Fin tip vortex
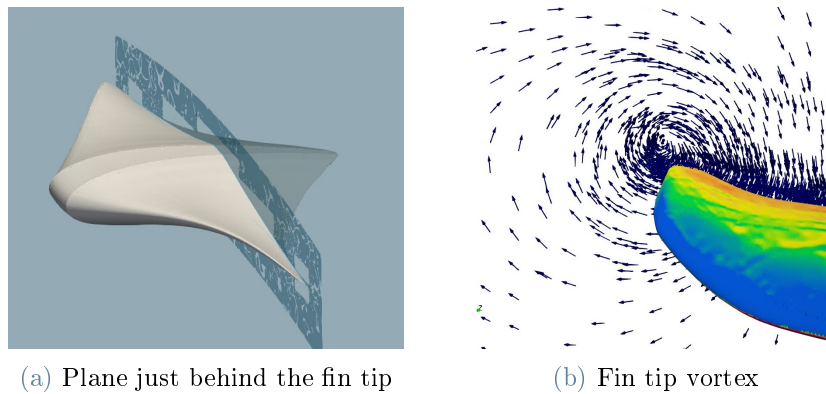
Figure 4.37: Velocity vectors of the vortex around the fin tip during a downstroke

Finally, another vortex in the body center is presented in Figure 4.38. Its presence is due to the alternate motion of the fin tips inward and outward during their motion. These vortices rotate in opposite directions on the two sides of the fish and they reverse their vorticity between upstroke and downstroke.

(a) Plane near the tail of the fish   (b) Central body vortex
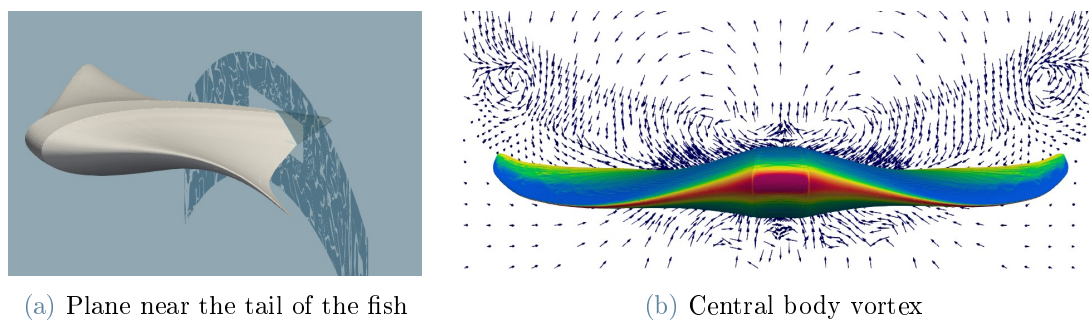
Figure 4.38: Velocity vectors of the vortex below the central part of the fish body

The obtained results are consistent with the results obtained experimentally by Clark [24], as shown in Figure 4.39, and numerically by Dewey [29], who performed experiments on a batoid-inspired fin actuated in a traveling wave motion. They have highlighted that vortices in the wake have an alternate sign, and they are arranged similarly to a reverse Karman street, and they have put in evidence a vortex around the fin tip.
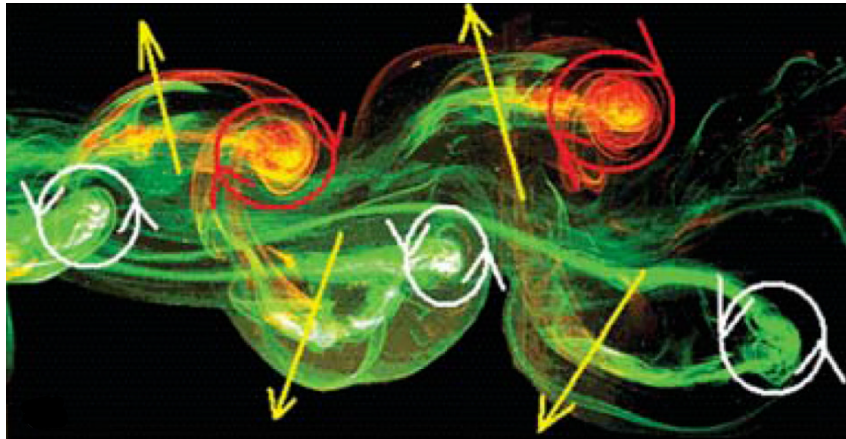
Figure 4.39: Vortex cores of alternating sign in the wake in the region near the mid-span found experimentally, Clark, *Journal of Fluid Mechanics* (2006) [24]

Conversely, the results differ significantly from those obtained numerically by Bottom [15] since they have studied a stingray, whose fin has a different shape from the cownose ray and which undulate their fins with a much shorter wavelength.
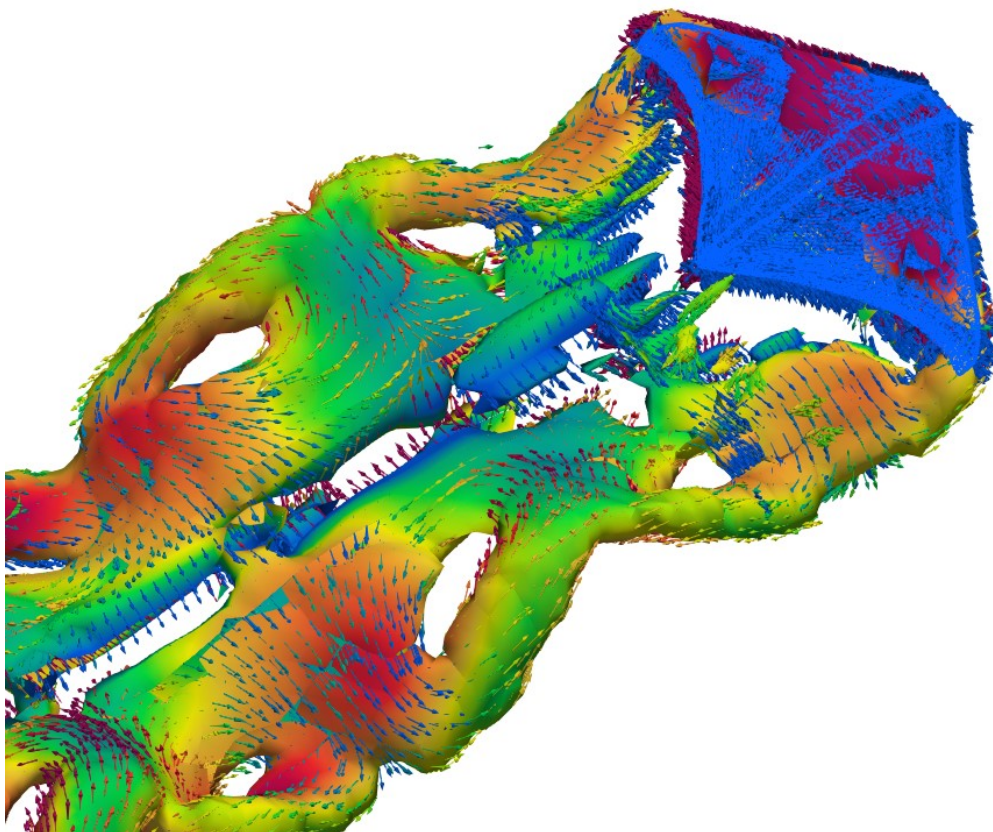
Figure 4.40: Surface of $\lambda_2 = 0$ identifying vortices in the wake that form ring structures

In Figure 4.40, the vortices in the wake are shown with vorticity vectors. It is possible to observe that the vortices forming the reverse Karman street, with the vorticity vectors directed laterally, are connected with the vortices that have been formed by the flow around the fin tip, which have vorticity vectors directed longitudinally and vertically, and with the vortices forming behind the center of the body with vorticity vectors directed longitudinally. These vortices are connected and form a coherent ring structure, typical of the wake generated by fish locomotion, as described in Chapter 2.

Leading-edge vortex A vortex on the leading edge (LEV) of the fins is typical of animals swimming with lift-based propulsion, like carangiform and thunniform fishes [14, 15]. In this kind of locomotion, the fin acts as a heaving and pitching airfoil, with a high angle of attack, generating a lift force in the front of the fin that pulls the fish forward. A stable leading-edge vortex is very common in nature since it enhances lift generation, and it is observed too on the wings of flying insects [15]. Cownose ray fin motion can be described by Equations 5.1 and 5.2 regardless of wavelength, but according to the wavelength, the motion can be oscillatory or undulatory, and only oscillatory locomotion, in general, is characterized by a leading-edge vortex [14]. In this work, the swimming performances with different wavelengths are compared, and the influence of this parameter on the LEV is discussed.

In Figure 4.41a, the streamlines of absolute velocity on the fin tip for a short wavelength $(\lambda = 1.67BL)$ are shown during a downstroke. It is possible to observe the vortex around the fin tip, with the fluid moving in a lateral direction, passing from the bottom side to the top side of the fin. However, there is no vortex on the leading edge, as the streamlines of the fluid passing around the leading edge remain parallel, and no flow separation is observed on the fin surface. Looking at Figure 4.41b, where the relative velocity vectors are represented, the same observations can be done since the velocity vectors always remain almost parallel to the swimming direction. This relative velocity is calculated as the difference of the fluid velocity and the forward velocity of the fish; thus, it is different from the relative velocity between each section of the fin and the fluid since the fin is also moving in a vertical direction.

(a) Streamlines of absolute velocity around the fin tip

(b) Relative velocity vectors near the fin tip
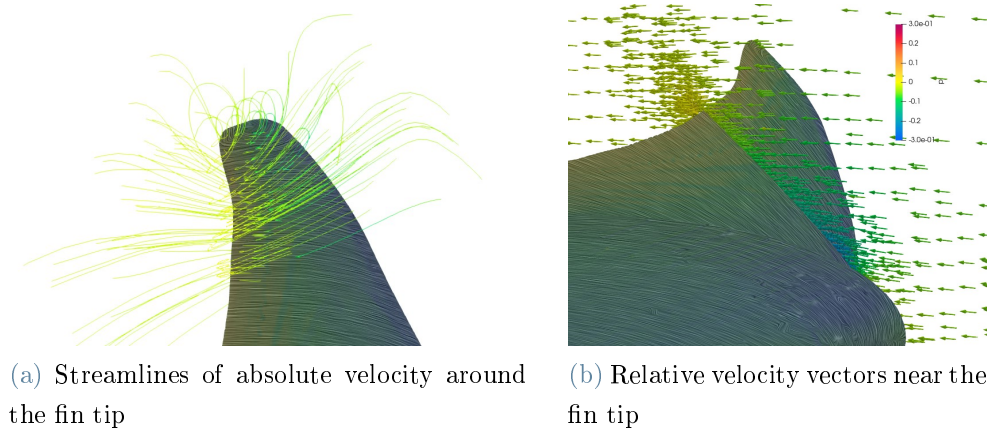
Figure 4.41: Velocity vectors and streamlines near the fin tip for $\lambda = 1.67BL$

Conversely, a vortex near the leading edge is formed when the wavelength is larger and the motion is oscillatory. The streamlines of absolute velocity around the fin tip during a downstroke are shown in Figure 4.42a. It is possible to observe that around the leading edge, a vortex is present. The water near the leading edge flows from the top side to the bottom side, and it rotates, generating a vortex connected with the vortex around the fin tip. This vortex can also be observed in Figure 4.42b, where the relative velocity vectors are displayed. This vortex generates a low-pressure area near the leading edge at its center, which enhances thrust. The formation of an LEV for oscillatory fin motion of batoid fishes has been observed by Lu too [80], who studied the vortex formed by the fin motion of a manta, characterized by a longer wavelength than the cownose ray. They also have highlighted that the LEV strength increases with an increasing wavelength.

(a) Streamlines of absolute velocity around the fin tip

(b) Relative velocity vectors near the fin tip
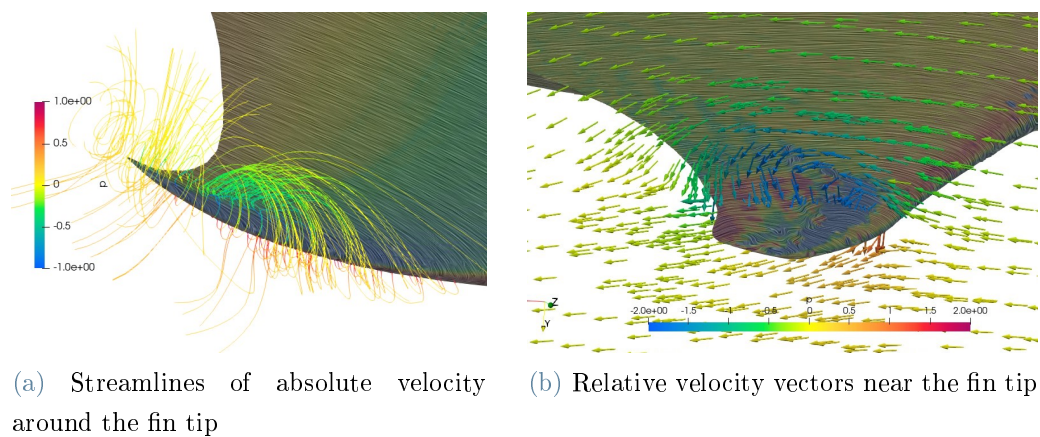
Figure 4.42: Velocity vectors and streamlines near the fin tip for $\lambda = 20BL$

4.3.3. Influence of kinematic parameters on swimming performances

In this work, several dynamic analyses have been carried out, changing frequency, amplitude, and wavelength of fin motion to investigate the performances of these fishes and understand the *secret* of its efficiency.

Wavelength effect

Figure 4.43 shows the velocity of the fish with different wavelengths. The cownose ray is featured by oscillatory swimming, and it moves its fins with a wave traveling at 2.5 body lengths (BL) per second at about 1 Hz [98, 101]. However, it adjusts wavelength and frequency to tune maneuverability, power consumption, and acceleration according to its needs.

In Figure 4.43, it is evident that increasing the wavelength, the steady-state velocity increases, then it reaches a maximum, and, with an extremely high wavelength, it starts decreasing again. This happens because a longer wavelength means a greater wave propagation velocity; thus, water is pushed backward at a higher speed, giving more momentum to the fish. Nevertheless, a long wavelength also implies that the fin is flat, and it pushes water more in a vertical direction than backward; therefore, it is more difficult to generate thrust.
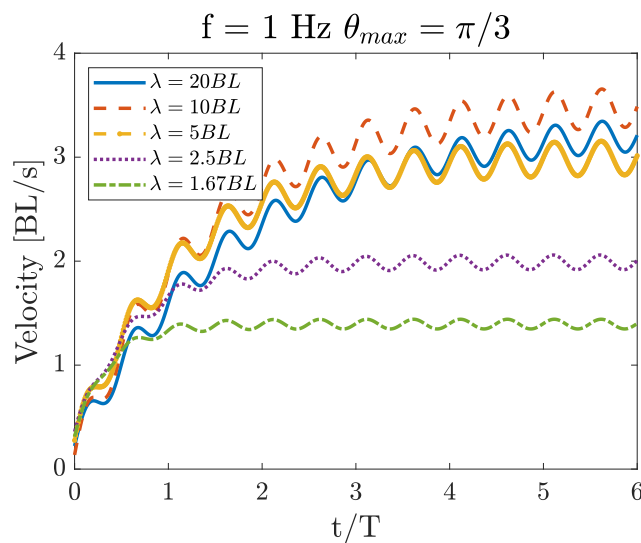
Figure 4.43: Forward velocity of the swimming fish for different wavelengths at 1 Hz

This result is consistent with the observation that batoid fishes with an oscillatory behavior, i.e., a longer wavelength, swim faster, and their motion is suitable to roam across the oceans, whereas fishes with an undulatory behavior, i.e., a shorter wavelength, are featured by small velocities and live in coral reefs or closed environments [98].

During steady-state swimming, force oscillates around a zero average value, as represented in Figure 4.31. In Figure 4.44a, the amplitude of these oscillations is represented for different wavelengths λ. The force is enhanced by increasing the wavelength; however, as for the velocity, for very long wavelengths, further increasing the wavelength does not have any positive effect on the generated thrust. When the fish swims with a large wavelength, the behavior is very similar even though the wavelength is significantly different. This happens because the number of waves on the fin, the reciprocal of the wavelength, is very similar.

The amplitude of the oscillations of the power consumed at the steady-state by the fish and the efficiency of fish swimming are plotted in Figure 4.44b for different wavelengths λ.
Swimming strategies involving a higher wavelength entail that the fins remain flatter, so the water is pushed more vertically, making a short wavelength a more efficient swimming strategy. The efficiency is calculated averaging the power over a period, and it is meaningful only when the fish has reached the steady-state velocity.
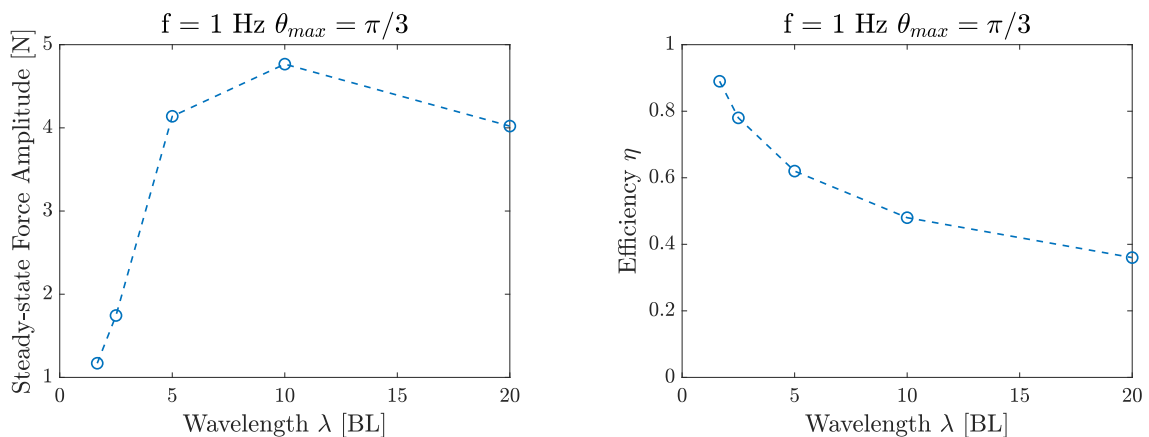
(a) Force in the swimming direction acting on the fish for different wavelengths at 1 Hz

(b) Efficiency of the fish for different wavelengths at 1 Hz

Figure 4.44: Steady-state force and efficiency at different wavelengths

Frequency effect

As far as the study of the effect of frequency on swimming performances is concerned, it has been chosen to perform simulations with different frequencies and with a wavelength of 2.5 BL. This number has been chosen since it is a good compromise between forward velocity at the steady-state and energy efficiency, as shown in the previous paragraph, and because it is close to the real behavior of a cownose ray in nature [98, 101]. In Figure 4.45, the forward velocity of the fish swimming with different frequencies is presented, and it can be observed that the steady-state velocity is proportional to frequency, consistently with the results obtained by Huang [58]. The curves shown in Figure 4.45 have different lengths because the time unit of this graph is non-dimensionalized with respect to the period. Therefore, although they last approximately the same time, there are different periods in each simulation.
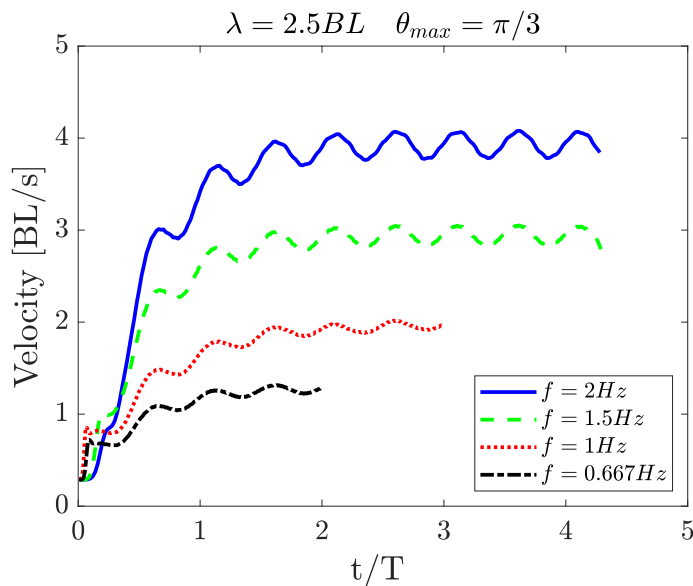
Figure 4.45: Forward velocity of the swimming fish for different frequencies with $\lambda = 2.5$ BL

The force is proportional to the square of frequency, as it can be observed in Figure 4.46a, where the dotted red line represents the fitting parabolic curve and the yellow area is the 95% confidence interval of the fitting. This result is expected since the predominant force is the inertia of the moving water, proportional to the square of the frequency. This is a remarkable finding because it means that the swimming of batoid fishes can be scaled with frequency in a linear fashion, and, as a consequence, the efficiency is not affected by frequency variations, as shown in Figure 4.46b.
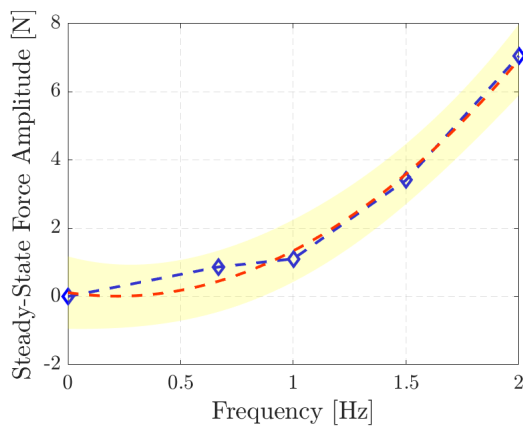
(a) Force in the swimming direction acting on the fish for different frequencies with $\lambda = 2.5$ BL
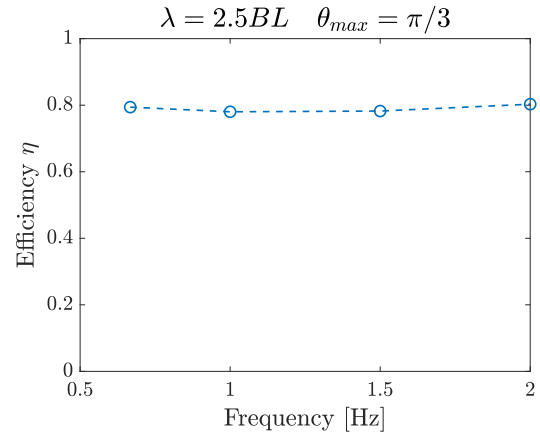
(b) Efficiency of the fish for different frequencies with $\lambda = 2.5$ BL

Figure 4.46: Steady-state force and efficiency at different frequencies

The effects of wavelength and frequency on swimming performances are summarized in Figure 4.47. It appears clear that the velocity increases with frequency and has a maximum for a particular wavelength and that the efficiency only depends on wavelength. Therefore, in terms of energy consumption, the swimming of batoid fishes can reach high efficiency, up to 89% for some swimming conditions, and it is more convenient to change the frequency instead of wavelength to accelerate.
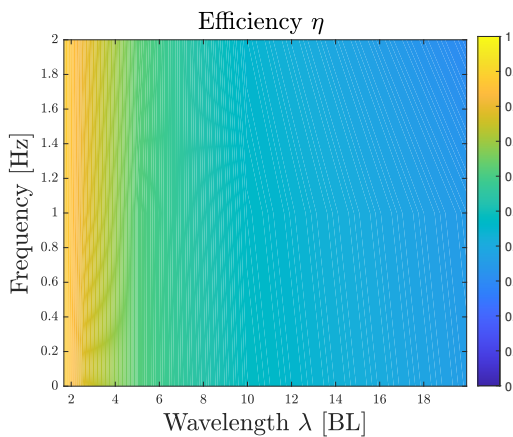
(a) Steady-state velocity for different wavelengths and frequencies
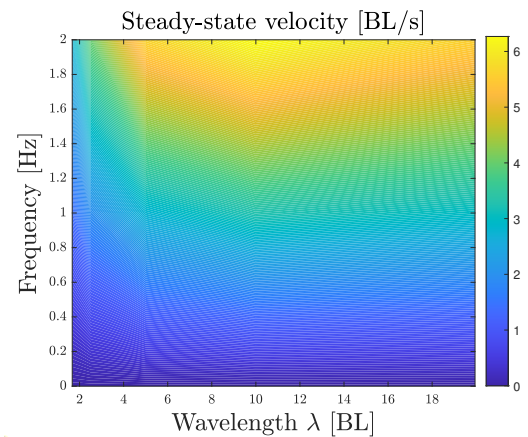
(b) Efficiency for different wavelengths and frequencies

Figure 4.47: Steady-state velocity and efficiency for different wavelengths and frequencies

4.3.4.   Angle of attack

Since the deformation of the fins of a cownose ray is featured by a small number of waves, about 0.4 [98], it is possible to consider every section of the fin as a heaving and pitching airfoil, and an angle of attack can be defined. The angle of attack α is the angle between the chord of the fin and the relative velocity of water with respect to the fin, as shown in Fig. 24(a), where ψ is the pitch angle of the fin section. The horizontal velocity of the fins v_x is the same for every section of the fin, whereas the vertical velocity v_y and the pitch angle ψ are different since the fin tip motion has a larger amplitude than the fin root. Therefore, the angle of attack is different for every fin section. The angle of attack is the difference between the angle of the relative velocity and the pitch angle ψ:

$$\alpha = \psi - \arctan \frac{v_y}{v_x} \tag{4.26}$$
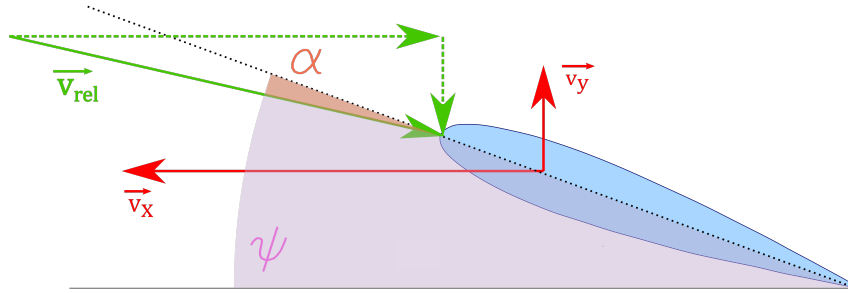
Figure 4.48: Angle of attack of a fin section

Neglecting the motion of the fin section along the lateral axis, i.e., out of the plane shown in Figure 4.48, which is smaller than the other two components, the relative velocity v_{rel} has two components: a horizontal component v_x equal to the forward velocity of the fish, and a vertical component v_y, which is $\dot{z}(s,t)$, the derivative of Equation 5.2. For a determined fin section, the velocity v_y is linearly dependent on frequency, and, as previously shown, the forward velocity v_x too results to be proportional to frequency. On the other side, a wavelength variation does not affect the velocity v_y, but it significantly changes the forward velocity v_x, as shown in Figure 4.43. Hence, the angle of the relative velocity does not depend on frequency but only on wavelength of fin motion. Furthermore, the pitch angle ψ too is independent of the frequency, and it is dependent only on wavelength. In particular, the larger is the wavelength, the flatter is the fin, and, as a consequence, the smaller is the pitch angle. Thus, the angle of attack of any section of the fin is a function of the wavelength of fin motion, and in Figure 4.49, the variation of the angle of attack of a section near the fin tip over a period is presented.
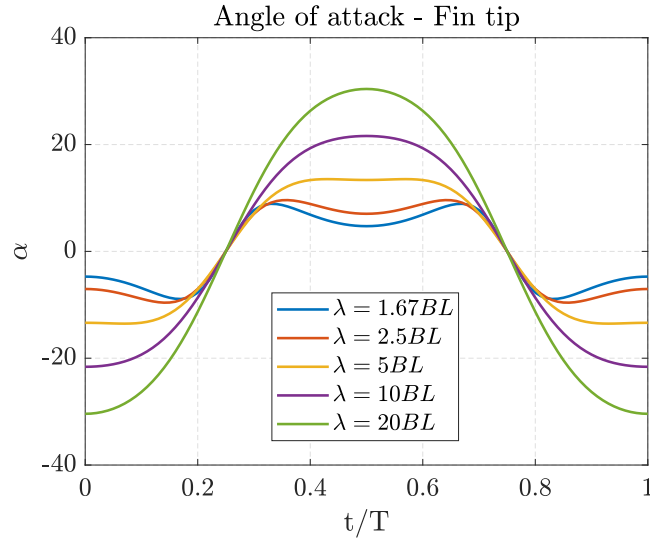
Figure 4.49: Variation of the angle of attack of a fin section positioned at 90 of fin span over a period

A change in wavelength has two conflicting effects on the angle of attack: the first is due to the variation of ψ, which would make α increase for smaller wavelengths; the second is due to the different forward velocity, which would make α decrease for shorter wavelengths. Near the fin tip, where the thrust generation is concentrated, the second effect is prevailing, so the angle of attack is larger for longer wavelengths. This means that when the fin is performing an upstroke the angle of attack is negative, whereas it is positive during a downstroke.

The angle of attack is also a key parameter governing the dynamics of the leading-edge vortex, and it is possible to observe that an LEV is formed only when the fish swims with a long wavelength, i.e., with a high angle of attack, in accordance with other researchers [33], which state that a high angle of attack is fundamental for the formation of the LEV.

4.3.5. Strouhal number

The Strouhal number for a swimming fish is defined as described in Chapter 2:

$$St = \frac{fA}{U} \tag{4.27}$$

where f is the flapping frequency, A is the peak-to-peak amplitude of the trailing edge of the fin, and U is the swimming velocity [34]. For a batoid fish, the trailing edge amplitude is variable along the span of the fin; thus, it is better to measure the vertical distance between two vortex cores directly from the wake. It results that this distance is the

peak-to-peak amplitude of the farthest span of the fin before the beginning of the fin tip vortex. The Strouhal number for different wavelengths and frequencies is presented in Figure 4.50.

(a) Strouhal number for different wavelengths

(b) Strouhal number for different frequencies
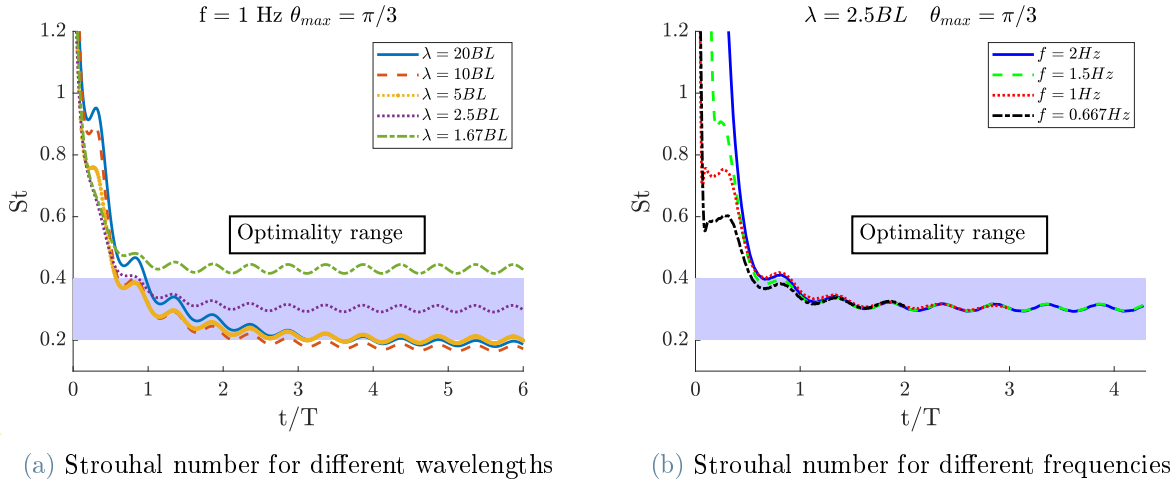
Figure 4.50: Strouhal number of cownose ray locomotion

Since the steady-state velocity is proportional to frequency, the Strouhal number does not depend on frequency, whereas it varies with wavelength. The Strouhal number of the cownose ray swimming results to be between 0.2 and 0.4 for most of the simulated swimming modes. This result fits with observations of scientists [34, 39, 123, 124], and it is a remarkable confirmation of the ability of the model to catch and reproduce the real behavior of the cownose ray.

Furthermore, for the simulation with $f = 1\,\text{Hz}$ and $\lambda = 2.5$ BL, the most typical swimming parameters for the cownose ray, the Strouhal number is perfectly in the middle of this optimal range. For a greater wavelength, the Strouhal number decreases below 0.2, and the propulsive efficiency decreases. Conversely, for a short wavelength, the Strouhal number results to be higher and outside the optimal range, although the energy efficiency is the highest among all the simulations, and the trend of the efficiency with respect to wavelength suggests that the efficiency can increase indefinitely by reducing the wavelength. However, this is not possible in practice because it would induce a great deformation on the fin surface that could be impossible to achieve for a real fish. The Strouhal number also influences the formation of the LEV, as stated by Bottom [15], who investigated the vortices formed by a stingray. They have found that an LEV can form even though the stingray swims with an undulatory motion. However, they found that the leading-edge vortex formation is favored by a Strouhal number of about 0.3, which corresponds to the same Strouhal numbers as for the cownose ray swimming with

a large wavelength resulting from this work. The stingray fin analyzed by Bottom [15] is featured by a significantly different geometry, and its motion is characterized by a smaller amplitude than the motion of the fins of a cownose ray.

In conclusion, a CFD model coupled with a dynamic solver has been developed, making use of a deformable overset grid. This method has been applied to simulate the swimming of a cownose ray with an imposed deformation on the fin, taken from the observations of the real fish made by biologists, and it could be applied for any different fish once its movement is known. The superimposition of the two movements of the overset mesh has been obtained by writing custom libraries developed for this scope.

The wake structure has been analyzed, highlighting the presence of vortices forming a reverse Karman street. This is related to thrust generation with an oscillatory motion, and it is present in the wake of the majority of fishes. Furthermore, other vortices around the fin tips and near the body center have been pointed out. Such simulations have been carried out with different wavelengths and frequencies of fin motion, and the swimming performances have been compared. The presence of a leading-edge vortex has been highlighted for fin motion with a long wavelength; nevertheless, such a long wavelength is not typical of the motion of a cownose ray, and its energy efficiency is small. Despite the presence of a leading-edge vortex, the main contribution to thrust is given by the traveling wave pushing water in the opposite direction. The analysis of the flow carried out in this thesis confirmed the results obtained by previous researches about the presence of a Reverse Karman Street and leading-edge vortices, and explained the effect of different kinematic parameters on the flow in the wake and on swimming performances. In particular, the energy efficiency of swimming locomotion has been calculated in a novel way.

The steady-state velocity is proportional to frequency, and it is maximum for a particular value of wavelength. The energy efficiency is remarkably high, and it does not depend on frequency but only on wavelength, and the calculated Strouhal number results in the same optimal range as other swimming animals.

The developed model is a useful tool that will also be used in future work to analyze the dynamics of maneuvering of batoid fishes and understand the effect of spanwise wave propagation on the fin. The results obtained are the starting point for the design of the bio-inspired underwater robot object of this thesis and for the choice of its kinematics and its motion law, as they reveal the effect of different swimming strategies on motion performances.

5 | Design of a prototype of the biomimetic robot

A prototype of a biomimetic robot has been built to assess the validity of the principles behind the locomotion strategy of the cownose ray. The objective of building this prototype is to perform some experimental tests on its fins to verify our understanding of the locomotion strategy of batoids and to measure the forces and the moments acting on the fins to properly choose the actuators of the final version of the robot. The first step of the project is the analysis of fin geometry and fin motion; then,kinematic synthesis of a mechanism reproducing the fin is performed. After these steps, the robot dynamics are modeled, and a control algorithm is designed. Finally, the robot is built and tested.

5.1. Design of the robot

5.1.1. Kinematic synthesis of the fins

This robot recreates the cownose ray fin deformation using three mechanisms, which are independently actuated so that it is possible to modulate the frequency and the wavelength of the movement, obtaining several different combinations of kinematic parameters. Since the number of waves on the fin is about 0.4 [98], three mechanisms are enough to reproduce the traveling wave, and they are positioned near the head, in the center, and near the tail, as in other previous bioinspired robots [19]. The fin ray mechanism design aims to mimic the flapping motion of the cownose ray, and the three designed fin mechanisms (front, middle, and rear) must be driven by independent servomotors because the respective motion laws must account for a phase delay, responsible for the chordwise kinematic wave, which should be variable according to the swimming mode and the maneuvers so that it cannot be achieved by connecting links with a mechanical transmission. The kinematics of the mechanisms is the same as in the robot developed by Cai [19], and the kinematic

diagram of the mechanism moving the central part of the fin is displayed in Figure 5.1 .
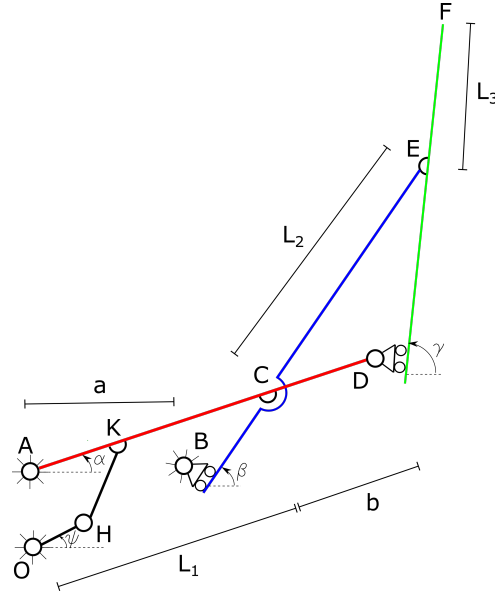
Figure 5.1: Kinematic diagram of the mechanism moving the central mechanism of the pectoral fin

The four-bar linkage actuated by the motor is connected to the first link (A-D), which moves the second (B-E) and third (D-F) links through sliders and hinges. The lengths of the links are selected using an optimization method to approximate as accurately as possible the deformed shape of the fin, neglecting in this first step the presence of the four-bar linkage OHKA. The optimization method is the minimum area error method [18], which consists in finding the optimal combination of link lengths that minimizes the area between the real deformed curve and the shape obtained with the three links. The optimization procedure is performed considering a dimensionless problem and considering the overall length of the fin span in the central section.

By recalling the equation that describes the deformation of the fin in the central section,

$$x(s,t) = \frac{\sin\left[\theta_{max}s\sin\left(\Phi y - \omega t\right)\right]}{L_x\theta_{max}\sin\left(\Phi y - \omega t\right)} \tag{5.1}$$

$$z(s,t) = \frac{1 - \cos\left[\theta_{max}s\sin\left(\Phi y - \omega t\right)\right]}{L_x\theta_{max}\sin\left(\Phi y - \omega t\right)} \tag{5.2}$$

it is possible to find the area below the curve integrating Equation 5.2, which represents the vertical displacement, along the lateral coordinate x. Hence, firstly it is necessary to combine Equations 5.1 and 5.2 to obtain an expression of the vertical displacement $z(x,t)$

dependent on the lateral coordinate instead of the curvilinear abscissa s:

$$s = \frac{\arcsin\left(x\theta_{max}L_x\sin\left(\Phi y - \omega t\right)\right)}{\theta_{max}\sin\left(\Phi y - \omega t\right)} \tag{5.3}$$

$$z(x,t) = \frac{1 - \cos\left[\arcsin\left(x\theta_{max}L_x\sin\left(\Phi y - \omega t\right)\right)\right]}{L_x\theta_{max}\sin\left(\Phi y - \omega t\right)} \tag{5.4}$$

Integrating Equation 5.4 along x from 0 to the lateral coordinate of the fin tip x_{max}, the area below the deformed curve of the fin is obtained:

$$A = \int_0^{X_{max}} z(x,t)\mathrm{d}x = \frac{x_{max}}{\theta_{max}\sin\left(\Phi y - \omega t\right)}\mp$$
$$\mp\frac{1}{2}\left(x_{max}\sqrt{\frac{1}{(\theta_{max}\sin\left(\Phi y - \omega t\right))^2} - x_{max}^2} \pm \frac{\arcsin\left(x_{max}\theta_{max}\sin\left(\Phi y - \omega t\right)\right)}{(\theta_{max}\sin\left(\Phi y - \omega t\right))^2}\right). \tag{5.5}$$

The area below the links, instead, is:

$$\tilde{A} = \frac{L_1^2\sin\alpha\cos\alpha}{2}+$$
$$+\frac{(2L_1\sin\alpha + L_2\sin\beta)L_2\cos\beta}{2} + \frac{(2L_1\sin\alpha + 2L_2\sin\beta + L_3\sin\gamma)L_3\cos\gamma}{2} \tag{5.6}$$

The angle α is a sinusoidal function of time, and the variable θ can be introduced as a cyclical variable. The amplitude of the oscillation of α is unknown, and it is determined together with the other parameters of the optimization:

$$\alpha = X\sin\left(\Phi y - \omega t\right) = X\sin\theta. \tag{5.7}$$

The angles β and γ can be written as functions of α:

$$\beta = \arctan\left(\frac{L_1\sin\alpha}{L_1\cos\alpha - a}\right), \tag{5.8}$$

$$\gamma = \arctan\left(\frac{L_2\sin\beta - b\sin\alpha}{L_2\cos\beta - b\cos\alpha}\right). \tag{5.9}$$

Considering that the sum of the lengths of the three links must be equal to the length of the span of the fin, it is possible to write:

$$L_3 = 1 - L_1 - L_2. \tag{5.10}$$

Therefore, the area below the links $\tilde{A}$ of Equation 5.6 is a function of five variables: L_1, L_2, a, b, X. The function to minimize is the difference between the two areas for all the

time instants of a period of fin oscillation, i.e., for all the angles θ from 0 to 2π, and it is written as:

$$S = \sum_{\theta=0}^{2\pi} |A(\theta) - \tilde{A}(\theta)|. \tag{5.11}$$

The result of the optimization is shown in Figure 5.2.

(a)   (b)

(c)   (d)
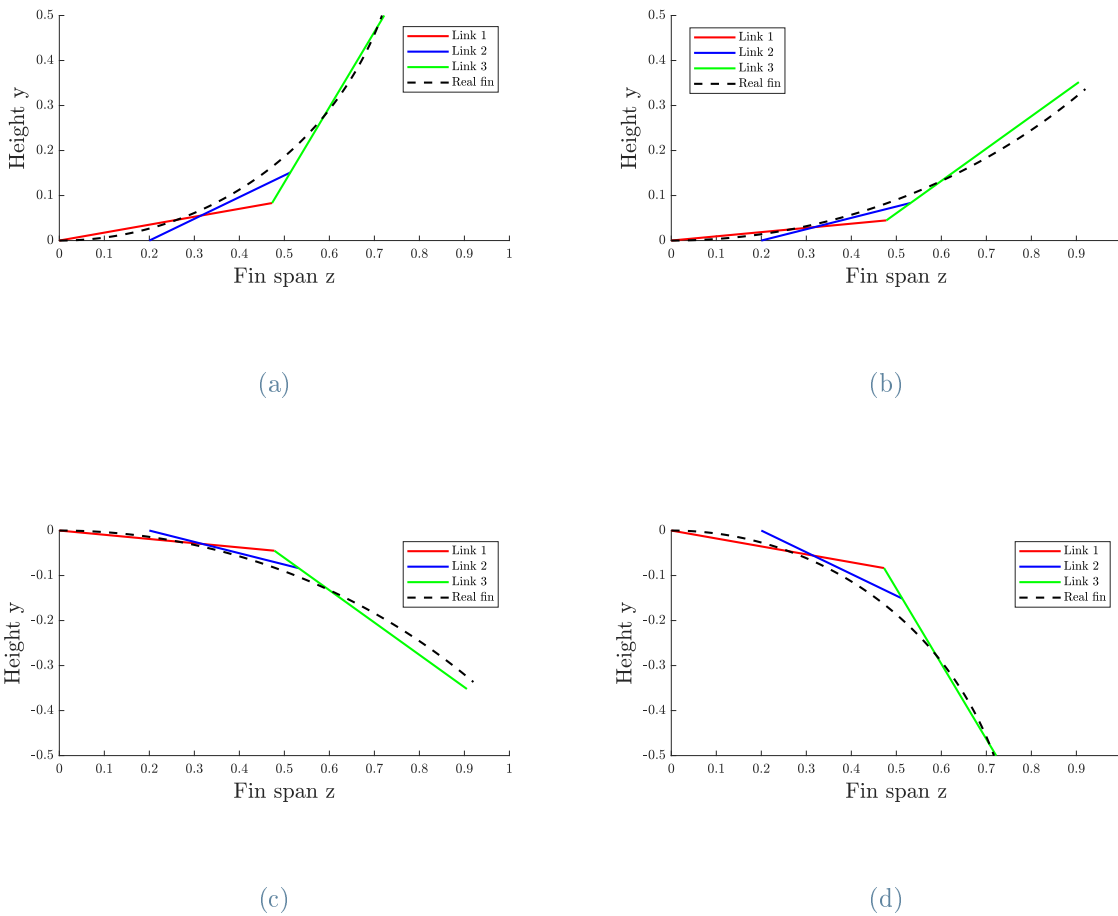
Figure 5.2: Comparison between the curve of the deformation of a real cownose ray and the shape obtained by the links of the mechanism of the central fin

The other two mechanisms moving the fin are designed with the same optimization method. Since the fin deformation in every section is described by the same equations as in the central section, the only difference between the real deformation of the front or back section and the central section is in the length of the fin span. Given that the result obtained with the optimization of the mechanism of the central part of the fin is more than satisfactory, the same kinematic diagram is used for the mechanisms on the front

and back of the fin. To account for different lengths of the fin span, the mechanism for the frontal part of the fin (5.4a) lacks the third link; similarly, the link in the back of the fin (5.8b) lacks both the second and the third link.

The structure of the three fin mechanisms is depicted in Figure 5.3:

- Front fin ray: one-stage slider rocker mechanism

- Center fin ray: two-stage slider rocker mechanism

- Rear fin ray: one link, an oscillating plate
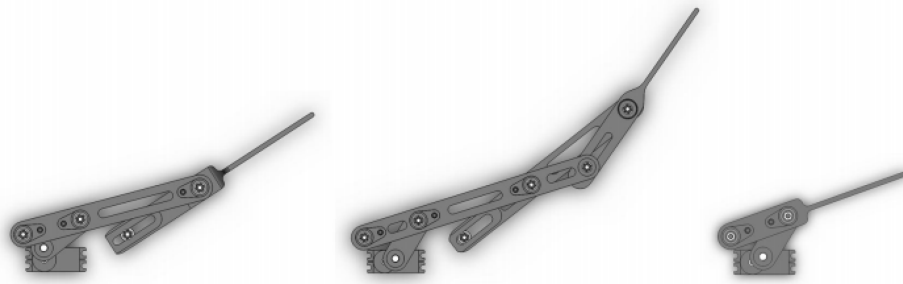
Figure 5.3: Frontal, central and rear fin (respectively from left to right)

Since both the curve defining the deformation of the fin and the kinematic diagram are the same for all mechanisms, the optimization gives the same results, and the link lengths are equal to those of the central mechanism of the fin, as shown in Figure 5.4.
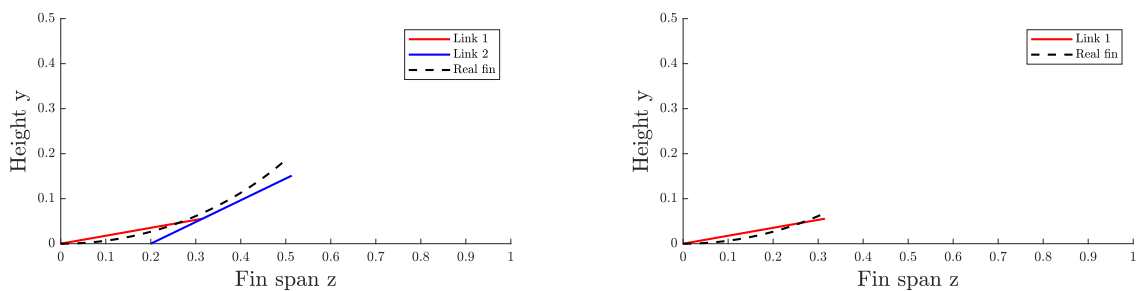
(a) Kinematic diagram of the mechanism in the front of the fin after optimization

(b) Kinematic diagram of the mechanism in the rear of the fin after optimization

Figure 5.4: Comparison between the curve of the deformation of a real cownose ray and the shape obtained by the links of the mechanism of the central fin

The actuators chosen for this prototype are continuous rotation servomotors, which rotate at a constant speed, so a four-bar linkage is needed to transform the unidirectional rotation of the motor into an alternate rotation of the first link of the fin mechanism. Considering Figure 5.1, the angle α is written as a function of the angle ψ and the lengths of the links composing the four-bar linkage, and the error function is then minimized. The optimization result is shown in Figure 5.5, where the angle α obtained with the four-bar linkage and the desired angle α of Equation 5.7 are plotted.
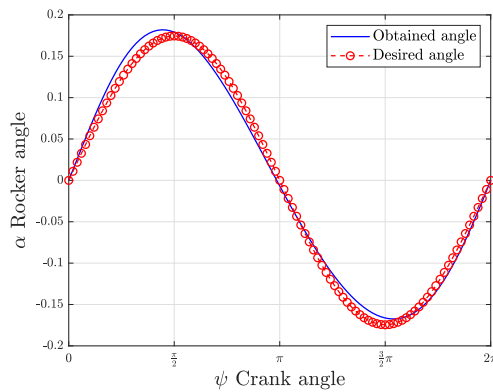
Figure 5.5: Comparison between the desired angle α and the one obtained with the four-bar linkage

Finally, the complete mechanism can be designed, and its superimposition on the curve of a real deformed fin is shown in Figure 5.6.
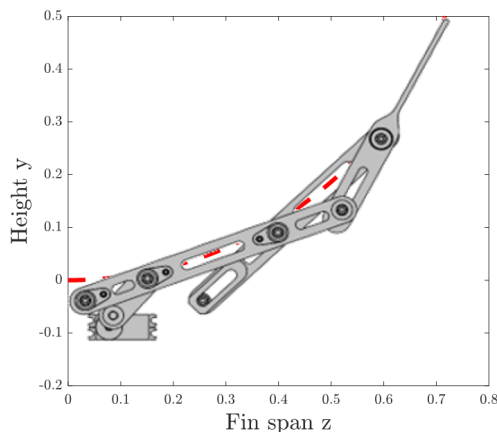
Figure 5.6: Superimposition of the designed mechanism and deformed curve of the central cross-section of a cownose ray fin

5.1.2. Tail

Another important simplification introduced in the robot design is the tail. Manta rays just like their sting rays cousins have a long whip-like tail that plays no role in locomotion. The fish is able to balance itself during complex motions thanks only to the pectoral fins which, therefore, guarantee both movement and balance. Due to the complexity of the movements of the fin, a tail has been introduced, which, properly controlled, acts like lift rudders, assisting the pectoral foils in floating and diving maneuvers and balancing the pitch rotation during forward swimming. The tail is formed by two rudders, as shown in Figure 8.7, and it is also useful during the turning phase in the horizontal plane by reducing the radius of curvature.
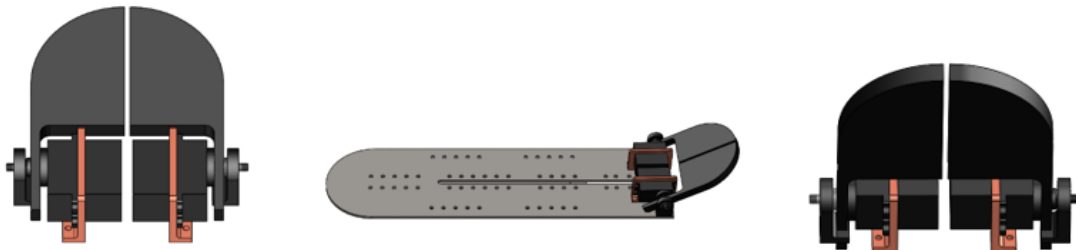
Figure 5.7: Tail of the robot

All the servomotors actuating the fin mechanisms and the tail are fixed to 3D printed frames attached to a base made of aluminum, as shown in Figure 5.8.
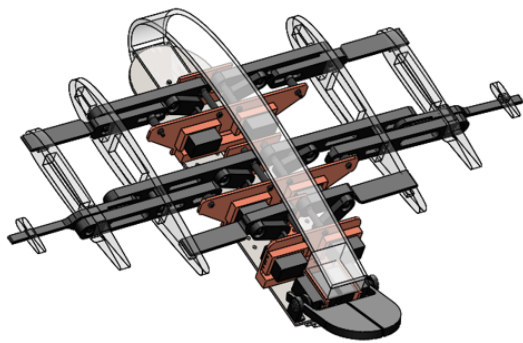
(a) Final design of the robot
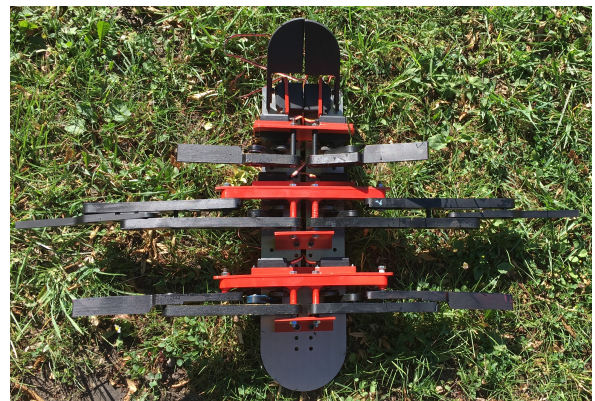
(b) Robot without the external surface

Figure 5.8: Final design of the prototype of the biomimetic robot

5.1.3. Shape and external surface of the robot

The reconstructed shape of the cownose ray obtained by Cai [18] and used to develop the CFD model described in Chapter 4 has been reproduced in the robot too. Thus, the pectoral fin of the robot has a triangular shape with a swept-back tip, and each cross-section of the fin is an aerodynamic profile getting thinner towards the fin tip. A NACA 0024 profile is used for the central body of the robot, it is rigid, and it is obtained by 3D printing with Z-UltraT, a material specifically designed for the Zortrax 3D printer, with mechanical properties similar to ABS. Instead, the other aerodynamic profiles are flexible to guarantee the deformation of the fin. They are made of silicone rubber, and they have been manufactured using molding. The positioning of the NACA profiles is shown in Figure 5.9.
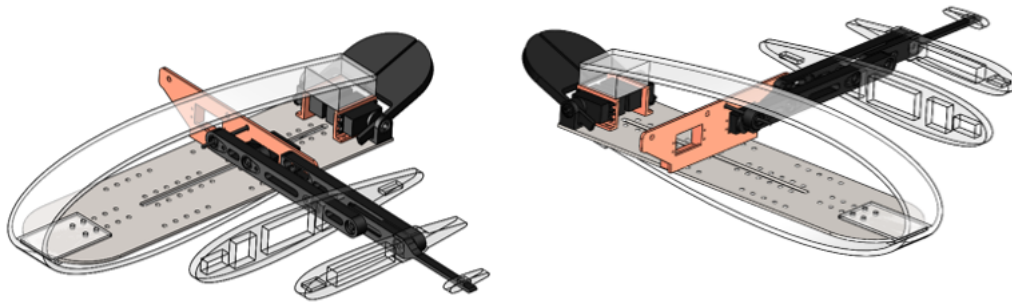
Figure 5.9: NACA profiles giving the shape to the pectoral fins

A pocket has been introduced in the bottom part of the rigid central profile, with the purpose of holding the electronic components in a part that can be extracted without disassembling any other part of the robot. This pocket is placed below the mechanism, and its external shape follows the NACA profile so that there is no loss in hydrodynamic efficiency. It is divided into two floors: the upper floor is reserved for the electronic board, and the lower floor is for the battery. The electronic devices are boxed in this structure with an opening on the side, which allows the cables to be connected with the motors placed above. The shelf that separates the two floors is just placed on four bulges without being fixed because, otherwise, it would be impossible to extract the battery. At the extremities, four holes allow the assembly of this part with the NACA profile using screws. The overall arrangement is shown in Figure 5.10.
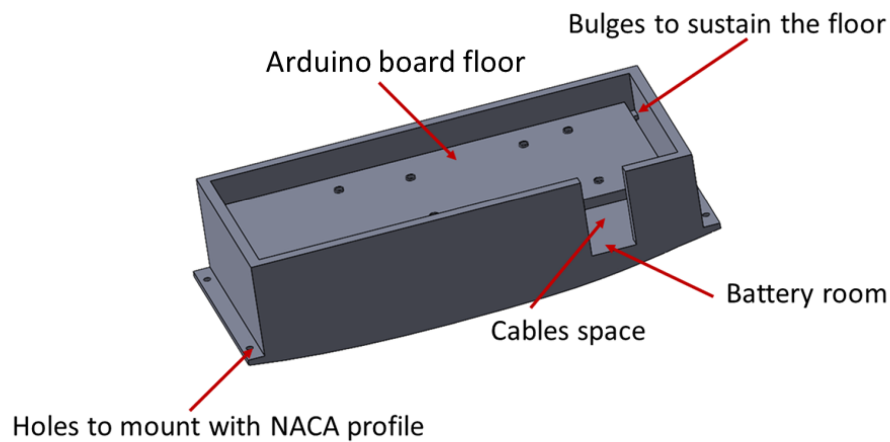
Figure 5.10: Slot holding battery, board and electronic components

Finally, the external surface is obtained by welding together two polyethylene sheets along the contour of the robot. This cover is fundamental as it preserves the shape of the robot throughout the movement of the fins, and it waterproofs the robot.

The coating plays a fundamental role since it protects the robot from the water, avoiding damage to the electronic components and the sinking of the robot itself. Furthermore, to generate the thrust force, it is necessary to replicate the wave given by the three mechanisms in the best possible way. Thus, the desired coating should stay attached at its best to the mechanisms during their movement. Therefore, for each side, two polyethylene sheets have been cut following the shape of the fin, and they are welded together and attached to the NACA profile to guarantee impermeability. The cut plastic sheets are slightly oversized with respect to the original shape of the fin due to the limited deformability of polyethylene. Hence, undesired stresses can be avoided on the links and the servomotors. Although a larger coating creates some folds while the fin is in motion and does not follow exactly the desired deformed fin shape, the silicone supports placed in the middle of the fins relieve this problem.

The assembled robot with coating and silicone rubber NACA profiles is presented in Figure 5.11.

Figure 5.11: Assembled robot with coating

5.2. Dynamic analysis of the robot

A numerical analysis of the robot dynamics has been performed using SimMechanics, a graphical environment working on Simulink, used for modeling dynamic systems. In addition, the CAD model developed in Solidworks has been simplified removing, screws, pins, and small components that are not relevant for the study of the dynamics, and it has been exported in Simulink, leaving only the main components: the aluminum bases, the frames, fins mechanisms, and the motors.

The fluid-dynamics forces acting on the robot for all combinations of different kinematic parameters have been exported from the CFD simulations using the software Paraview. This dynamic analysis aims to study the 6-DOF dynamics of the robot to design the control algorithm for forward swimming and maneuvers.
A diagram showing the process followed to obtain the multi-body simulation of the robot is presented in Figure 5.12.
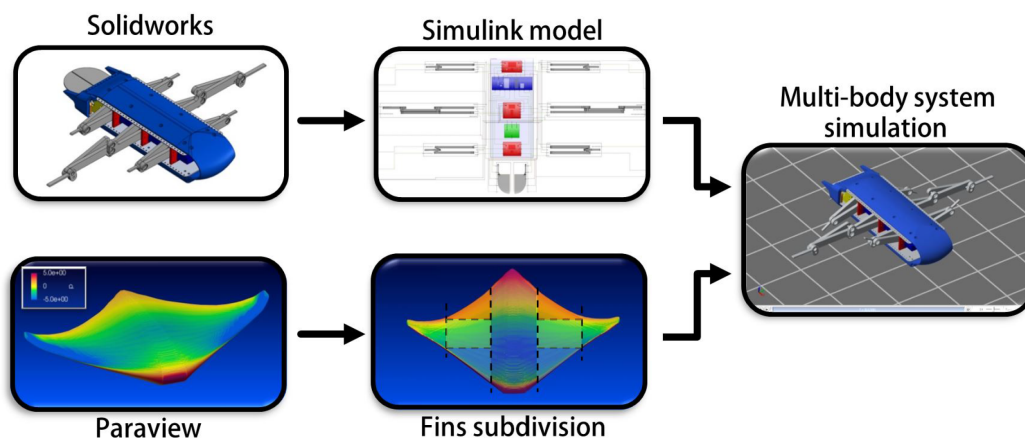
Figure 5.12: Diagram with the steps followed to obtain the final simulation model

This dynamic analysis has been performed both on the first version of the robot and of an improved version of the robot described in Chapter 6. The results of this dynamic analysis refer to the improved version of the robot, where the kinematics of the fin mechanisms is different; however, the conclusion are analogous.

5.2.1. Forces extraction from CFD analyses

The CFD study gives the total pressure distribution over the surface in contact with the fluid. In order to introduce the fluid dynamic actions in the simulation, the idea is to

split the total surface of the fins into subsections (Figure 8.24a) and evaluate in each slice the distribution of forces and torques along active directions to calculate their resultants in each center of mass.

F_x, F_y, F_z, M_x, M_y, and M_z were calculated for each section. Then, these actions were applied in the relative references system of the Simscape model, corresponding to the fin slices, as shown in Figure 8.24b. Since the two fins move symmetrically during forward swimming, the forces acting on them are mirrored with respect to the longitudinal axis, the forces acting on the left fin have been extracted, and the forces on the right fin have just been mirrored.

(a) Slices of the robott's fins

(b) Reference systems on which fluid dynamic forces act in the multibody simulation
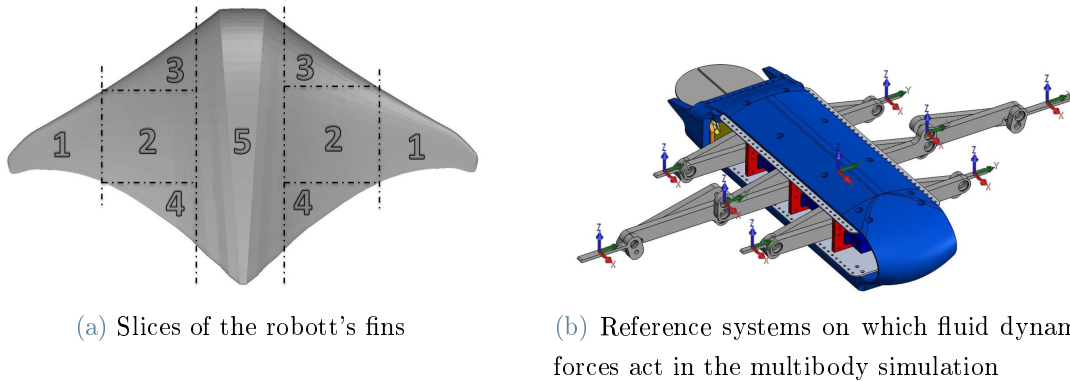
Figure 5.13: Extraction of forced from the CFD analysis and application on the SimMechanics model

The data set for every force and moment consists of a vector with N elements, where N is the time needed for the robot to reach the steady-state velocity starting from the null velocity condition with a discretization of $0.01\,\mathrm{s}$. In the first stage, only the data related to the condition of steady-state velocity were introduced in the model, and they have been converted from functions of time to functions of a cyclical variable α related to the angle of the motor. The movement of the first link connected to the motor is a sinusoidal function, and α is the argument of the sine:

$$\theta = \theta_{max} \sin\left(\omega t + \phi\right) = \theta_{max} \sin \alpha \tag{5.12}$$

Once this process has been completed for all forces and moments of each section in each simulation, some important considerations can be made, with reference to the reference system shown in Figure 5.14. The graphs shown in this paragraph all refer to the simulation made with a frequency of $1\,\mathrm{Hz}$, an amplitude of $60°$, and a wavelength of $0.4\,\mathrm{BL}$, but they are valid in general for all kinematic parameters.
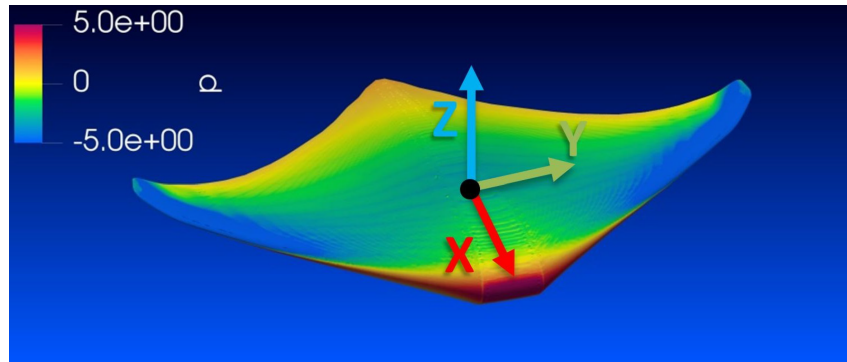
Figure 5.14: Reference system used for the dynamic analysis

Firstly, for all simulated kinematic parameters, the magnitude of the fluid interactions in the central and rear part of the fin (Sections 2 and 4 in Figure 8.24a) are very low compared with the others. The highest fluid dynamic contributions can be found on each fin extremity (Sections 1 and 3). As far as the longitudinal force F_x is concerned (Figure 4.8), it is equal for the two fins, and the two main contributions are found on the fin tip and on the main body, shown in Figure 5.15. On the fin tip, a positive thrust force is produced with a frequency that is twice the flapping frequency, and when the fin is close to being at maximum range, the force F_x goes to zero. On the central body of the robot, the only action produced along x is the drag force; thus, its values are always negative. Once the steady-state velocity has been reached, the drag force can be considered constant.

(a) Thrust force along x axis acting on the fin extremity

(b) Drag force along x axis acting on the central body
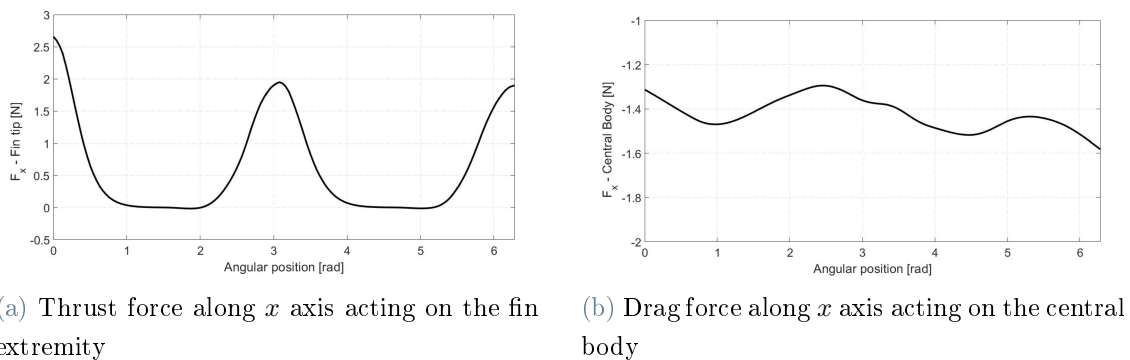
Figure 5.15: Forces acting on the x axis

F_z is the vertical force exerted on the robot. It is equal for the two fins, and in Figure 5.16, its contribution acting on two sections of the fin can be observed. On the fin tip, the maximum force is found again when the fin is almost horizontal, negative during the upstroke and positive during the downstroke. For this reason, the frequency is coincident with the flapping frequency. Another fundamental contribution is provided

by the frontal section of the fin (Section 3 in Figure 8.24a). Each curve concerning F_z is evenly distributed between positive and negative values, obtaining a motion with a height variation of zero mean value.
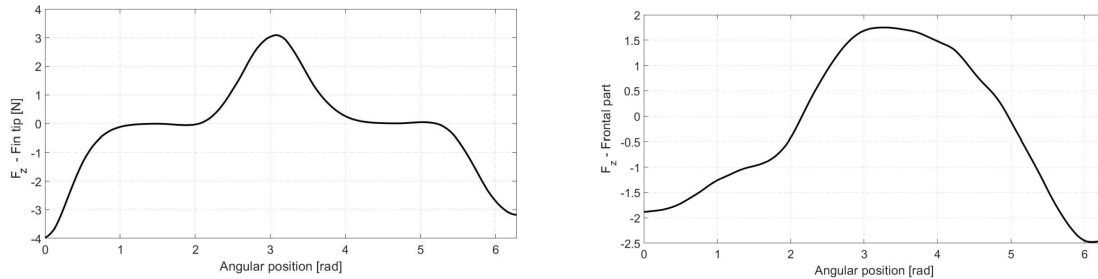
(a) Vertical force along z axis acting on the fin extremity

(b) Vertical force along z axis acting on front

Figure 5.16: Forces acting on the a axis

During straight, forward swimming, both the roll moment M_x and the lateral force F_y on the two fins are equal and opposite because of the symmetry of the problem. Nevertheless, they have to be considered since they affect the torque needed by each servomotor, so it is essential to take them into account for motor sizing. Therefore, the contributions of the lateral force and the roll moment reach their maximum on the fin tip, and they are presented in Figure 5.17.
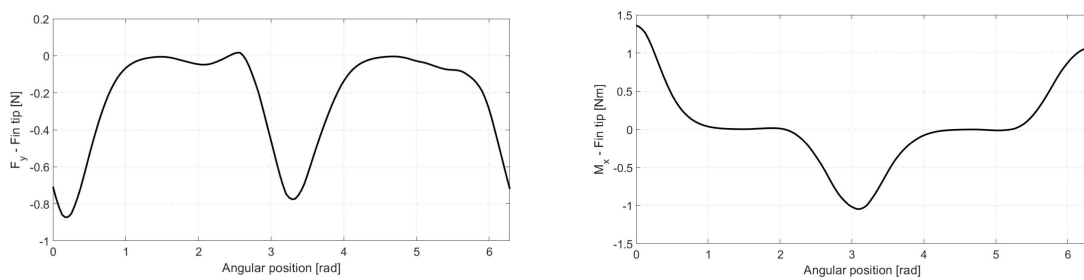
(a) Lateral force along y axis acting on the fin extremity

(b) Roll moment along x axis acting on the fin extremity

Figure 5.17: Lateral force and roll moment

The pitch moment M_y and yaw moment M_z too reach their maximum values on the fin tip, shown in Figure 5.18. The pitch moment M_y is equal for the two fins, and it is fundamental to include it in the analysis to design the control algorithm of the tail, which is supposed to counteract it to minimize the pitch rotation during forward swimming.

Conversely, the yaw moment M_z during forward swimming is equal and opposite for the two fins, and it does not affect motors' torque. However, it has been included in the analysis for the sake of completeness.

(a) Pitch moment along y axis acting on the fin extremity

(b) Yaw moment along z axis acting on the fin extremity
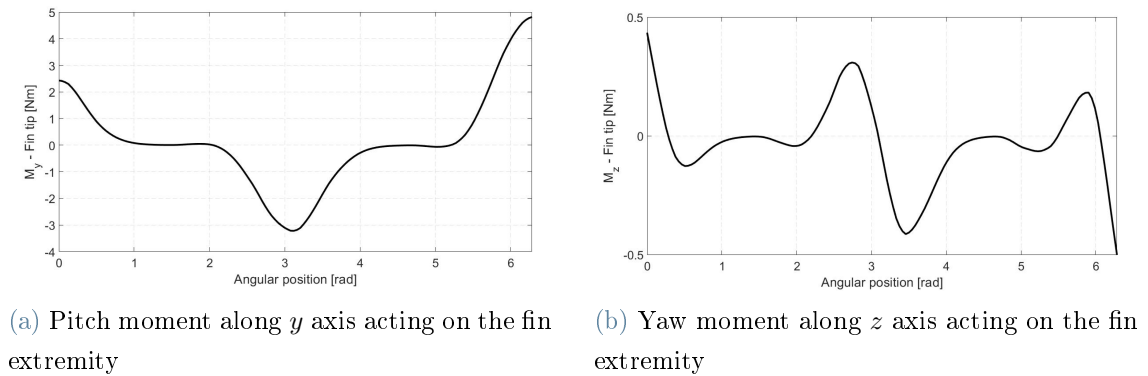
Figure 5.18: Pitch and yaw moments

In order to have a model working in any possible configuration, lookup tables have been introduced to interpolate linearly between consecutive configurations. These lookup tables are multidimensional, since there are four inputs (angular position α, frequency f, wavelength λ, and amplitude θ_{max}) and one output which is the force or the moment in consideration.

(a) Velocity

(b) Force on x axis on the central body

(c) Force dependency on velocity
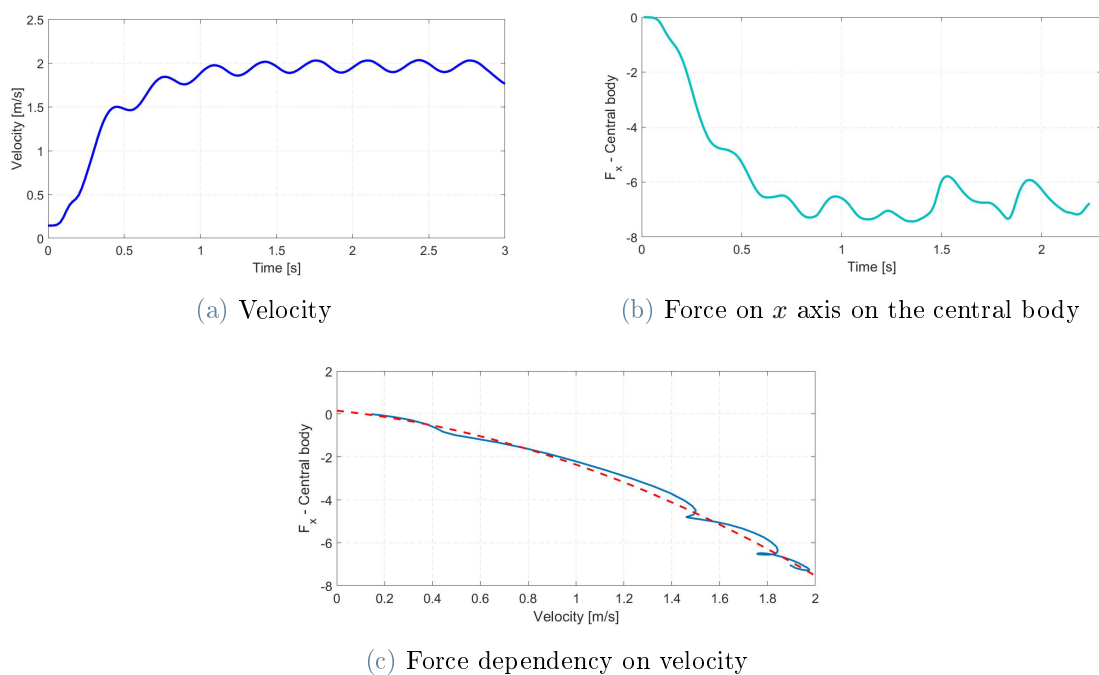
Figure 5.19: Procedure applied to obtain force dependency from velocity

Then, in order to modify the steady-state values accounting for different forward velocities, speed dependence has been introduced. In Figure 5.19c, the relationship between the force (or moment) considered and the velocity of the robot can be observed. This graph has been obtained combining the data of forces and moments(Figure 5.19b) with the velocity variation from null to steady-state velocity (Figure 5.19a).

As previously shown, forces are dependent on the angular positions of the motors; thus, to isolate the dependency on velocity, the data are interpolated with a second-degree polynomial, as shown in Figure 5.19c.
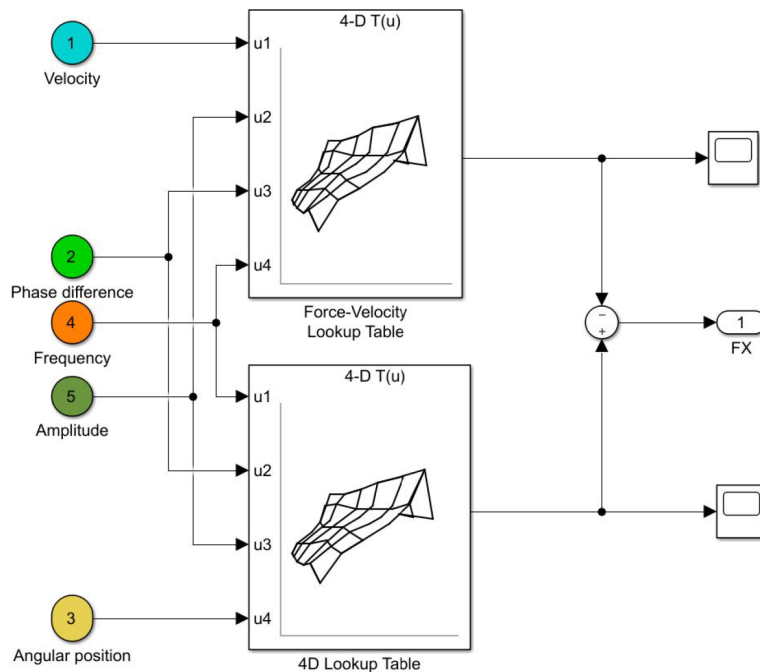
Figure 5.20: Simulink scheme of the force calculation for any possible combination of motor angular position, velocity and kinematic parameters

The same procedure is applied for all the forces and moments for all the CFD simulations, and they have been interpolated by means of a 4D lookup table. The Simulink scheme used to introduce this strategy is depicted in Figure 5.20.

5.2.2. Tail contribution model

The robot uses its tail to stabilize pitch rotation as well as to perform up-floating and diving maneuvers. In order to introduce in the model its contribution, a simplified model of the interaction between the tail and the fluid has been developed. This model is

based on the same assumptions as of the simplified analytical model for the pectoral fins described in Chapter 4. Hence, this model considers only a force normal to the tail elements, neglecting the tangential forces arising due to viscous friction, and it assumes the flow to be two-dimensional, neglecting the lateral flow. In Figure 5.21a, a schematic drawing of the tail is presented. The constraint that fixes it to the base is modeled as a hinge since the only degree of freedom is the rotational one.

(a) Schematic representation of the tail

(b) Calculation of the tail angle θ
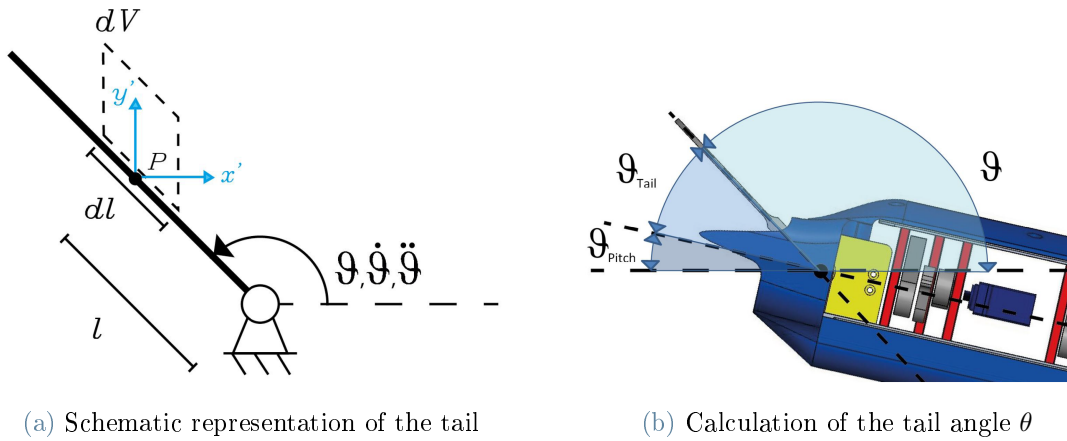
Figure 5.21: Tail model

The angle θ used in the equations is a function of the pitch angle and the tail angle, which is the angle of the tail motor from the horizontal configuration. This is clearly shown in Figure 5.24b. θ can be defined as:

$$\theta = \pi - (\theta_{pitch} + \theta_{tail}) \tag{5.13}$$

The maximum angular displacement θ_{tail} from the horizontal position is $\pm 45°$. This range is set better to mimic the real behavior of the cownose ray and limit the deformation of the elastic coating covering the robot. $\dot{\theta}$ and $\ddot{\theta}$ are respectively the angular velocity and acceleration of the tail.

By considering an infinitesimal volume of water adjacent to the tail surface, schematized in Figure 5.22, it is possible to calculate the infinitesimal force $d\mathbf{F}$ generated by the momentum transfer mechanism as:

$$d\mathbf{F} = \frac{dm \left(\mathbf{v_{out}^n} - \mathbf{v_{in}^n} \right)}{dt} \tag{5.14}$$

where $\mathrm{d}m$ is the infinitesimal mass, defined as:

$$\mathrm{d}m = \rho\mathrm{d}z\mathrm{d}S = \rho\mathrm{d}z|\mathbf{v}_{\mathbf{in}}^{\mathbf{n}}|\mathrm{d}t\mathrm{d}l \tag{5.15}$$
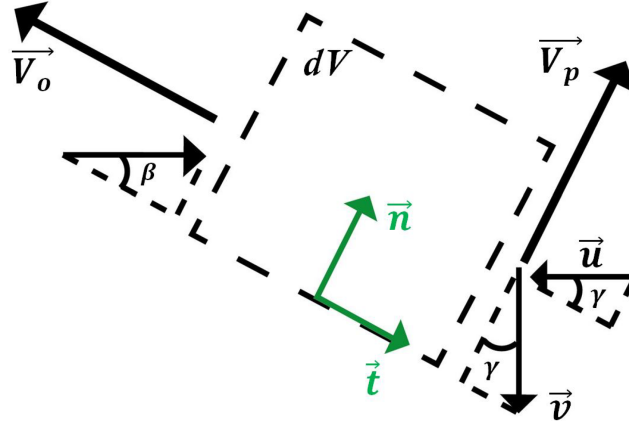
Figure 5.22: Scheme of velocities and forces acting on an infinitesimal element of fluid adjacent to the tail surface

The velocity of the robot is written as:

$$\mathbf{V} = u\mathbf{i} + v\mathbf{j} \tag{5.16}$$

and the velocity of a point P on the tail given by the tail rotation is:

$$\mathbf{V_P} = -\dot{\theta}l\sin\theta\mathbf{i} + \dot{\theta}l\cos\theta\mathbf{j} \tag{5.17}$$

Equations 5.16 and 5.17 allow expressing the normal component of the inlet velocity $\mathbf{v_{in}^n}$ as a function of the robot velocity and the angular velocity of the tail:

$$\mathbf{v_{in}^n} = \left[\dot{\theta}l - v\cos(\pi - \theta) - u\sin(\pi - \theta)\right]\mathbf{n} = \left[\dot{\theta}l + v\cos\theta - u\sin\theta\right]\mathbf{n} \tag{5.18}$$

The outlet velocity $\mathbf{v_{out}}$ is tangential to the tail element, so its normal component is zero. Therefore, the expression of the infinitesimal force $\mathrm{d}\mathbf{F}$ can be obtained:

$$\mathrm{d}\mathbf{F} = -\rho\frac{\mathrm{d}z\left(\dot{\theta}l - u\sin\theta + v\cos\theta\right)^2\mathrm{d}t\mathrm{d}l}{\mathrm{d}t} \tag{5.19}$$

The infinitesimal time $\mathrm{d}t$ can be simplified, and the force acting on the tail can be

calculated integrating Equation 5.19 on the tail surface considering its geometry, as shown in Figure 5.23.
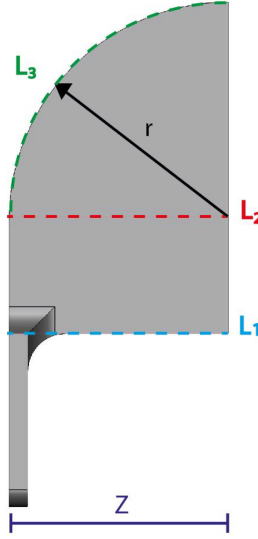
Figure 5.23: Tail geometry

$$\mathbf{F} = -\rho \int_A \left(\dot{\theta} l - u \sin\theta + v \cos\theta \right)^2 \mathrm{d}l \mathrm{d}z =$$

$$= -\rho \int_0^Z \left[\int_L \left(\dot{\theta} l - u \sin\theta + v \cos\theta \right)^2 \mathrm{d}l \right] \mathrm{d}z =$$

$$= -\rho \int_0^Z \left[\int_{L_1}^{L_2} \left(\dot{\theta} l - u \sin\theta + v \cos\theta \right)^2 \mathrm{d}l + \int_{L_2}^{L_3(z)} \left(\dot{\theta} l - u \sin\theta + v \cos\theta \right)^2 \mathrm{d}l \right] \mathrm{d}z$$

$$(5.20)$$

The integral over the tail surface has been split into two parts, and the different sections can be seen in Figure 5.23. $L_3(z)$ is defined as:

$$L_3(z) = L_2 + \sqrt{r^2 - l^2} \tag{5.21}$$

Solving the integrals, it is possible to obtain:

$$\mathbf{F} = -\rho \int_0^Z \left[\frac{\dot{\theta}^2 \left(L_3^3(z) - L_1 \right)}{3} + \underbrace{\left[u^2 \sin\theta^2 + v^2 \cos\theta^2 - uv \sin(2\theta) \right]}_{C_1} \left(L_3(z) - L_1 \right) + \underbrace{\dot{\theta} \left(v \cos\theta - u \sin\theta \right)}_{C_2} \left[L_3^2(z) - L_1^2 \right] \right] \mathrm{d}z =$$

$$= -\rho \underbrace{\int_0^Z \left[\frac{\dot{\theta}^2 L_3^3(z)}{3} + C_2 L_3^2(z) + C_1 L_3(z) \right] \mathrm{d}z}_{I} + \rho \left[\frac{\dot{\theta}^2 L_1^3}{3} + C_2 L_1^2 + C_1 L_1 \right] Z$$

$$(5.22)$$

The integral part can be written as:

$$
I = \frac{\dot{\theta}^2}{3} \underbrace{\int_0^Z \left[L_2 + \sqrt{r^2 - z^2}\right]^3 \mathrm{d}z}_{\alpha} + C_2\left(\theta, \dot{\theta}\right) \underbrace{\int_0^Z \left[L_2 + \sqrt{r^2 - z^2}\right]^2 \mathrm{d}z}_{\beta}
$$
$$
+ C_1\left(\theta\right) \underbrace{\int_0^Z \left[L_2 + \sqrt{r^2 - z^2}\right] \mathrm{d}z}_{\gamma}
$$

(5.23)

The integrals α, β, and γ are numerically computed, and, since they are functions only of the geometry, they are constant which are computed once and for all. Finally, the force of the tail can be obtained, as a function of the robot velocity (v, u) through the coefficients C_1 and C_2, and of the angular position θ and angular velocity $\dot{\theta}$ of the tail:

$$
\mathbf{F} = \rho \left[\frac{\dot{\theta}^2}{3}\left(-\alpha + L_1^3 Z\right) + C_2\left(\theta, \dot{\theta}\right)\left(-\beta + L_1^2 Z\right) + C_1\left(\theta\right)\left(-\gamma + L_1 Z\right)\right] \mathbf{n}
$$

(5.24)

According to the motion conditions, the direction of the normal versor is changed, as shown in Figure 5.24.

(a)   (b)
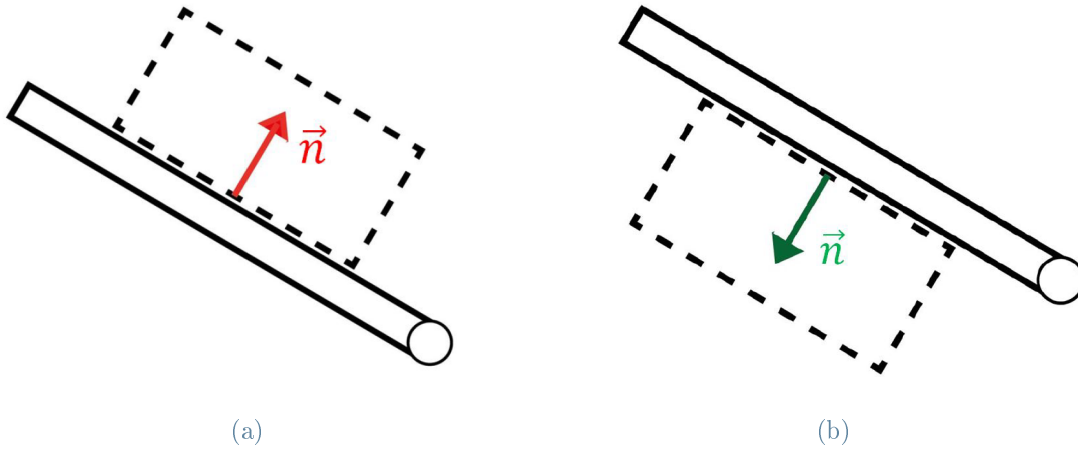
Figure 5.24: Normal versor of the tail

The same procedure can be applied to calculate the moment generated by the forces acting on the tail:

$$
\mathrm{d}\mathbf{M} = -\rho \frac{\mathrm{d}z l \left(\dot{\theta}l - u\sin\theta + v\cos\theta\right)^2 \mathrm{d}t \mathrm{d}l}{\mathrm{d}t}
$$

(5.25)

Integrating it on the tail surface, it becomes:

$$
\mathbf{M} = -\rho \int_0^Z \left[\frac{\dot{\theta}^2 \left(L_3^4(z) - L_1^4\right)}{4} + \underbrace{\frac{1}{2}\left[u\sin\theta - v\cos\theta\right]^2}_{C_3} \left(L_3^2(z) - L_1^2\right) + \underbrace{\frac{2}{3}\dot{\theta}\left(v\cos\theta - u\sin\theta\right)}_{C_4}\left[L_3^3(z) - L_1^3\right] \right] \mathrm{d}z =
$$

$$
= -\rho \underbrace{\int_0^Z \left[\frac{\dot{\theta}^2 L_3^4(z)}{4} + C_4 L_3^3(z) + C_3 L_3^2(z)\right]\mathrm{d}z}_{I} + \rho \left[\frac{\dot{\theta}^2 L_1^4}{4} + C_4 L_1^3 + C_3 L_1^2\right] Z
$$

$$(5.26)$$

The integral part can be written as:

$$
I = \frac{\dot{\theta}^2}{4} \underbrace{\int_0^Z \left[L_2 + \sqrt{r^2 - z^2}\right]^4 \mathrm{d}z}_{\delta} + C_4\left(\theta, \dot{\theta}\right) \underbrace{\int_0^Z \left[L_2 + \sqrt{r^2 - z^2}\right]^3 \mathrm{d}z}_{\alpha}
$$

$$
+ C_3\left(\theta\right) \underbrace{\int_0^Z \left[L_2 + \sqrt{r^2 - z^2}\right]^2 \mathrm{d}z}_{\beta}
$$

$$(5.27)$$

The integrals α and β are the same as for the force expression, and δ is analogously numerically computed since it is a function only of the geometry as well. Finally, the moment of the tail can be obtained, as a function of the robot velocity (v, u) through the coefficients C_3 and C_2, and of the angular position θ and angular velocity $\dot{\theta}$ of the tail:

$$
\mathbf{M} = \rho \left[\frac{\dot{\theta}^2}{4}\left(-\delta + L_1^4 Z\right) + C_2\left(\theta, \dot{\theta}\right)\left(-\alpha + L_1^3 Z\right) + C_1\left(\theta\right)\left(-\beta + L_1^2 Z\right)\right]\mathbf{k} \qquad (5.28)
$$

5.3. Sizing of the components

The electrical circuit which drives and controls the motors is composed of:

- 8 servomotors: 3 motors for each pectoral fin and 2 for the tail

- Arduino Due board

- Battery

5.3.1. Servomotors

From the dynamical model, it is possible to calculate the torque required to each motor during forward swimming. To size motors, a demanding set of parameters has been chosen: the used frequency is $1\,\mathrm{Hz}$, the amplitude is set to the maximum, which is $\frac{\pi}{3}$, the wavelength is 5 body lengths.

The torque required by motors is shown in Figure 5.25.

(a) Frontal

(b) Central

(c) Rear

(d) Tail
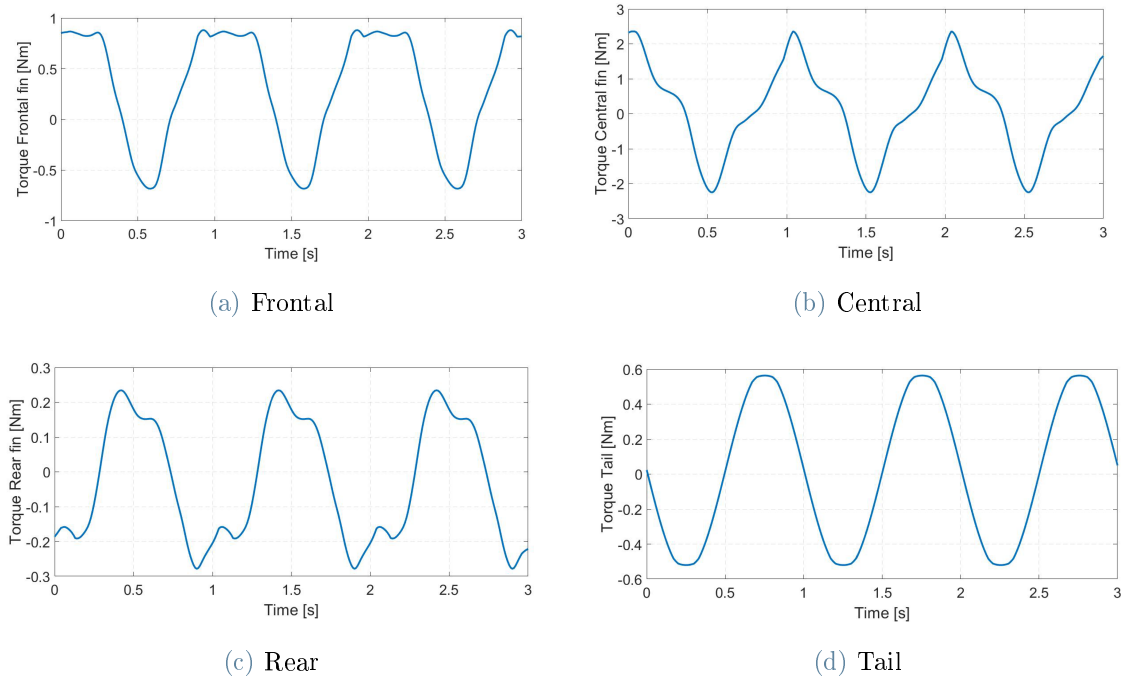
Figure 5.25: Torque needed by every servo motor

The primary contribution is given by the central fin, which requires $2.4\,\mathrm{N\,m}$ in order to fulfill the motion required. The torque demand of the frontal fin is close to $1\,\mathrm{N\,m}$. The contribution of the rear fin is negligible with respect to the others, being $0.23\,\mathrm{N\,m}$. Finally, each motor of the tail requires $0.6\,\mathrm{N\,m}$.

The chosen servomotors are the Feetech-FR5311M-360FB Continuous Rotation, whose characteristics are listed in Table 8.4.1.

Figure 5.26: Feetech-FR5311M-360FB Continuous Rotation servomotor

Torque (7.4 V)	1.96	[Nm]
Voltage	4.8 - 7.4	[V]
Mass	58	[g]
Velocity	60	[rpm]
Dimensions	40.2 x 20 x 38	[mm]

Table 5.1: Servomotor characteristics

These servomotors provide a torque higher than the requirements and can perform a continuous 360° rotation in both directions, and their speed can be controlled with a PWM command. They also provide an analog feedback signal of angular position, which is necessary to control the motor position and synchronize the mechanisms.

5.3.2. Battery

By combining the data regarding the required torque and the knowledge of the angular speed of every servo motor, it is possible to calculate the power consumption of the robot, in order to check the battery suitability and the theoretical battery life. The required power value depends significantly on the wavelength of the fin movement. Considering always a frequency of 1 Hz and an amplitude of $\frac{\pi}{3}$, the required power for different wavelengths is compared: for an hypothetical infinite wavelength, with all the mechanisms moving in synchronism, the peak power consumption is maximum, and it reaches 20 W. If a wavelength of 5 body lengths is considered, the peak power drops to 15 W because the maximum values of power of each motor do not occur simultaneously, and the forces involved are lower as the phase delay increases, as shown in Figure 5.27. The average power decreases too when the wavelength decreases.

(a) Infinte wavelength   (b) 5 BL wavelength
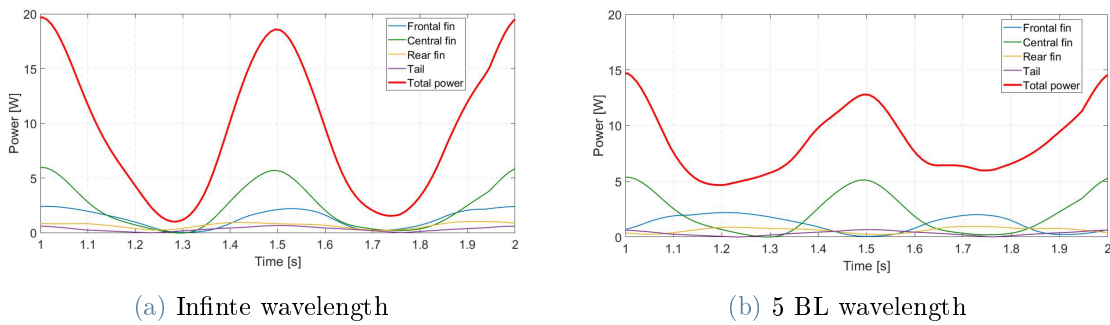
Figure 5.27: Total power consumption

The required current can be calculated by dividing the required power by the voltage of the battery:

$$I = \frac{P}{V} = 1.35\text{A} \tag{5.29}$$

Finally, knowing the battery capacity, the time in which the robot can be used with demanding conditions is:

$$T_{life} = \frac{Capacity}{Current} = \frac{5.2\text{Ah}}{1.35\text{A}} = 3\text{h} \quad 51\text{min} \tag{5.30}$$

The selected battery is the Full Power LiPo 2S 5200 mAh 50C Gold V2, whose features are listed in Table 8.4.3.

Figure 5.28: FullPower 2S battery

Type	LiPo
Voltage	7.4 V
Number of cells	2
Capacity	5200 mAh
Maximum current	260 A
Mass	265 g
Dimensions	163mm x 50mm x 16mm

Table 5.2: Battery characteristics

6 | Control algorithm

THE control algorithm of the robot includes a low-level control algorithm that keeps the mechanisms of the fins synchronized and with the desired phase shift and ensures that their movements have the correct frequency and amplitude, and a high-level control algorithm that takes as input the measurements from sensors and calculates the correct kinematic parameters for each fin and the motion laws of each motor to make the robot move along the desired trajectory.

6.1. Fins' mechanisms synchronization

The low-level control algorithm is designed to keep the two fins synchronized and guarantee the desired phase shift between the mechanisms of each fin. During forward swimming, the phase shift between mechanisms is the same for both fins, and each mechanism is synchronized with the correspondent one on the other fin. During a turning maneuver, the phase shift between mechanisms is opposite for the two fins, the two central mechanisms are again synchronized, but the front mechanisms are synchronized with the back mechanisms of the opposite fin.

For each motor, the velocity is calculated as the sum of a feedforward part and a feedback part. The feedforward part is the reference velocity of motors (ω_{ref}), which is proportional to the frequency of fin motion, it is equal for all motors, and it is provided by the user. The feedback part is a correction needed to maintain the desired phase shift. A PI control logic is adopted in order to correct the phase shift between two mechanisms: the angular position of each motor is measured, and the actual phase shift among all motors is computed; then, the phase shift is corrected, accelerating the motor in delay and slowing the motor in advance, as depicted in the block diagram in Figure 6.1.
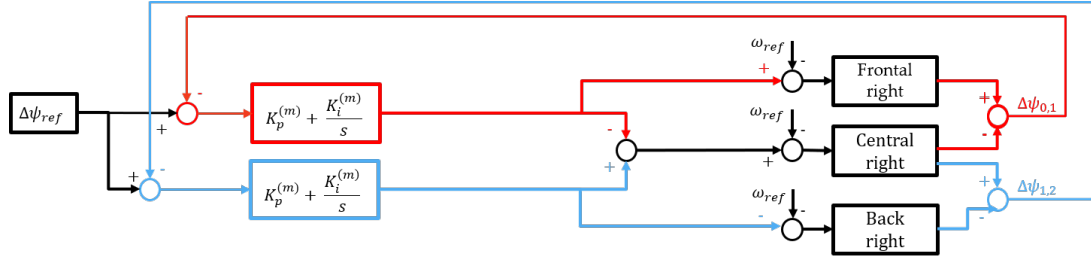
Figure 6.1: Block diagram of the control algorithm correcting the phase shift between mechanisms of the same fin

The block diagram of the complete control algorithm for forward swimming is shown in Figure 6.2. Since the mechanisms are mounted in a mirrored configuration, motors of different fins rotate in opposite directions. Therefore, the phase shift between the same mechanisms of the same fins is calculated as the sum of the two angles instead of their difference.
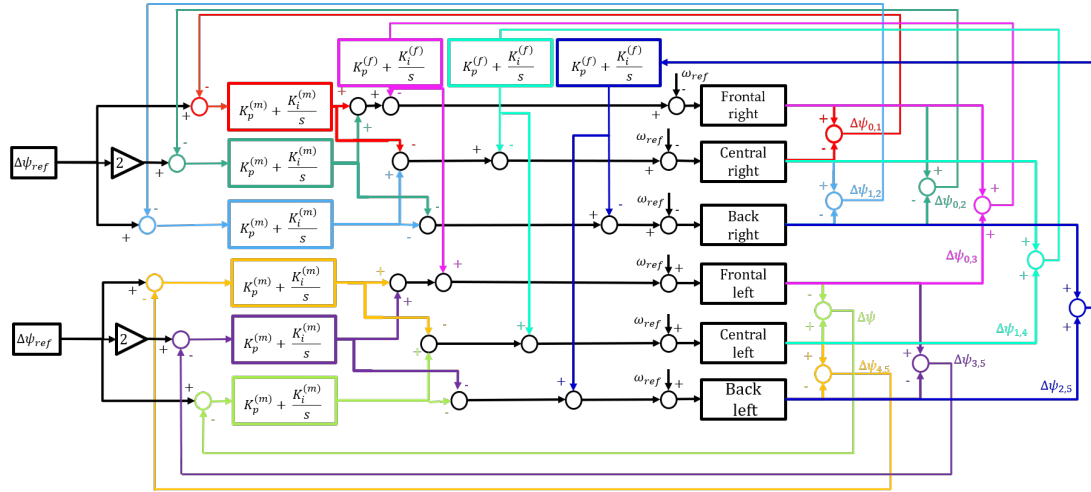
Figure 6.2: Block diagram of the control algorithm for forward swimming

Considering, for example, the central mechanism of the right fin the input velocity given to the motor is calculated as follows:

$$
\begin{aligned}
\omega_1 = \omega_{ref} + \left(k_p^{(m)} + \frac{k_i^{(m)}}{s} \right) (\Delta\psi_{0,1} - \Delta\psi_{ref}) + \\
- \left(k_p^{(m)} + \frac{k_i^{(m)}}{s} \right) (\Delta\psi_{1,2} - \Delta\psi_{ref}) + \left(k_p^{(f)} + \frac{k_i^{(f)}}{s} \right) \Delta\psi_{1,4},
\end{aligned}
\tag{6.1}
$$

where ω_{ref} is the reference velocity given by the input, $\Delta\psi_{ref}$ is the desired phase shift between the mechanisms, and ψ_k is the measured angular position of the motor. The enumeration of motors is the same as in Figure 6.2. The gains $k_p^{(m)}$ and $k_i^{(m)}$ control the phase shift between mechanisms of the same fin and the gains $k_p^{(f)}$ and $k_i^{(f)}$ control the synchronization between the two fins.

The control algorithm acting on all the six motors can be summarized in a matrix form, shown in Equation 6.2 for forward swimming, and in Equation 6.3 for a left turn. In both equations, the integral contribution is omitted to simplify the notation.

$$
\begin{Bmatrix} \omega_0 \\ \omega_1 \\ \omega_2 \\ \omega_3 \\ \omega_4 \\ \omega_5 \end{Bmatrix} = \begin{Bmatrix} \omega_{ref} \\ \omega_{ref} \\ \omega_{ref} \\ -\omega_{ref} \\ -\omega_{ref} \\ -\omega_{ref} \end{Bmatrix} + \begin{bmatrix} -2k_p^{(m)}-k_p^{(f)} & k_p^{(m)} & k_p^{(m)} & -k_p^{(f)} & 0 & 0 \\ k_p^{(m)} & -2k_p^{(m)}-k_p^{(f)} & k_p^{(m)} & 0 & -k_p^{(f)} & 0 \\ k_p^{(m)} & k_p^{(m)} & -2k_p^{(m)}-k_p^{(f)} & 0 & 0 & -k_p^{(f)} \\ -k_p^{(f)} & 0 & 0 & -2k_p^{(m)}-k_p^{(f)} & k_p^{(m)} & k_p^{(m)} \\ 0 & -k_p^{(f)} & 0 & k_p^{(m)} & -2k_p^{(m)}-k_p^{(f)} & k_p^{(m)} \\ 0 & 0 & -k_p^{(f)} & k_p^{(m)} & k_p^{(m)} & -2k_p^{(m)}-k_p^{(f)} \end{bmatrix} \begin{Bmatrix} \psi_0 \\ \psi_1 \\ \psi_2 \\ \psi_3 \\ \psi_4 \\ \psi_5 \end{Bmatrix} + + \begin{bmatrix} -3k_p^{(m)} \\ 0 \\ 3k_p^{(m)} \\ 3k_p^{(m)} \\ 0 \\ -3k_p^{(m)} \end{bmatrix} \Delta\psi_{ref}
$$

$$(6.2)$$

$$
\begin{Bmatrix} \omega_0 \\ \omega_1 \\ \omega_2 \\ \omega_3 \\ \omega_4 \\ \omega_5 \end{Bmatrix} = \begin{Bmatrix} \omega_{ref} \\ \omega_{ref} \\ \omega_{ref} \\ -\omega_{ref} \\ -\omega_{ref} \\ -\omega_{ref} \end{Bmatrix} + \begin{bmatrix} -2k_p^{(m)}-k_p^{(f)} & k_p^{(m)} & k_p^{(m)} & 0 & 0 & -k_p^{(f)} \\ k_p^{(m)} & -2k_p^{(m)}-k_p^{(f)} & k_p^{(m)} & 0 & -k_p^{(f)} & 0 \\ k_p^{(m)} & k_p^{(m)} & -2k_p^{(m)}-k_p^{(f)} & -k_p^{(f)} & 0 & 0 \\ 0 & 0 & -k_p^{(f)} & -2k_p^{(m)}-k_p^{(f)} & k_p^{(m)} & k_p^{(m)} \\ 0 & -k_p^{(f)} & 0 & k_p^{(m)} & -2k_p^{(m)}-k_p^{(f)} & k_p^{(m)} \\ -k_p^{(f)} & 0 & 0 & k_p^{(m)} & k_p^{(m)} & -2k_p^{(m)}-k_p^{(f)} \end{bmatrix} \begin{Bmatrix} \psi_0 \\ \psi_1 \\ \psi_2 \\ \psi_3 \\ \psi_4 \\ \psi_5 \end{Bmatrix} + + \begin{bmatrix} -3k_p^{(m)} \\ 0 \\ 3k_p^{(m)} \\ -3k_p^{(m)} \\ 0 \\ 3k_p^{(m)} \end{bmatrix} \Delta\psi_{ref}
$$

$$(6.3)$$

In both cases, the state matrices have a zero eigenvalue because the reference is given in terms of the difference of angular positions, and no absolute reference position is given to the motors. Nevertheless, this does not represent a singularity problem, but it is just the consequence of the fact that the measured variables are the angular positions, while the control corrects only the difference of angular position among motors. The gains of the PI controllers have been obtained experimentally with a trial-and-error procedure.

The angular positions are acquired at regular intervals of $1\,\mathrm{ms}$, synchronized by the internal clock of the board. Then a low-pass filter with a cut-off frequency of $10\,\mathrm{Hz}$ is applied to the acquired signal to delete some high-frequency noise.

The control algorithm has been tested experimentally, as displayed in Figure 6.3, where the fin mechanisms are shown in different instants of their motion.

(a)

(b)

(c)

(d)
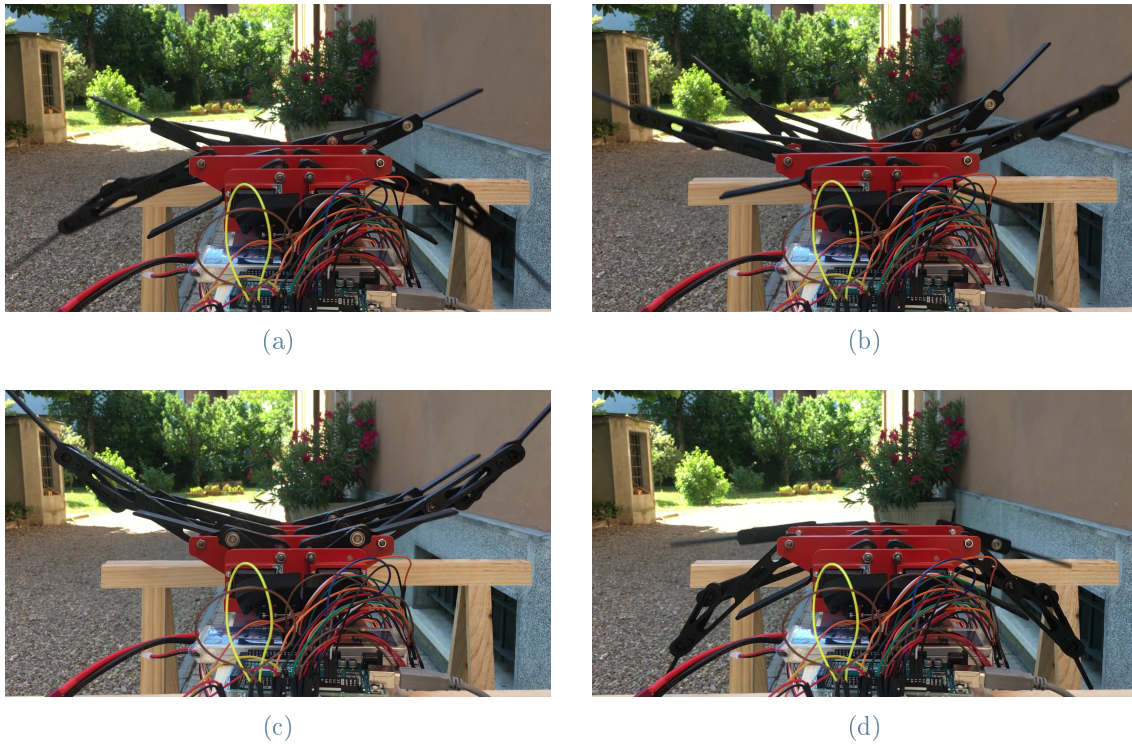
Figure 6.3: Instants of fins motion during forward swimming

The results of the control algorithm can be better appreciated by looking at Figure 6.4, where the signals coming from the encoders are plotted. In Figure 6.4a, the encoders measurements are taken when the fish is swimming forward and it is possible to note that, for both fins, the front mechanisms (Motor 0 and Motor 3) are in advance with respect to the central mechanisms (Motor 1 and Motor 4), and the back mechanisms (Motor 2 and Motor 5) are in delay. On the other side, in figure 6.4b, the measurements come from a left-turn maneuver; for the right fin, the mechanisms have the same phase shift as for forward swimming, whereas for the left fin, the back mechanism (Motor 5) is in advance with respect to the central mechanism (Motor 4), and the front mechanism (Motor 3) is in delay.

(a) Forward swimming (b) Left turn
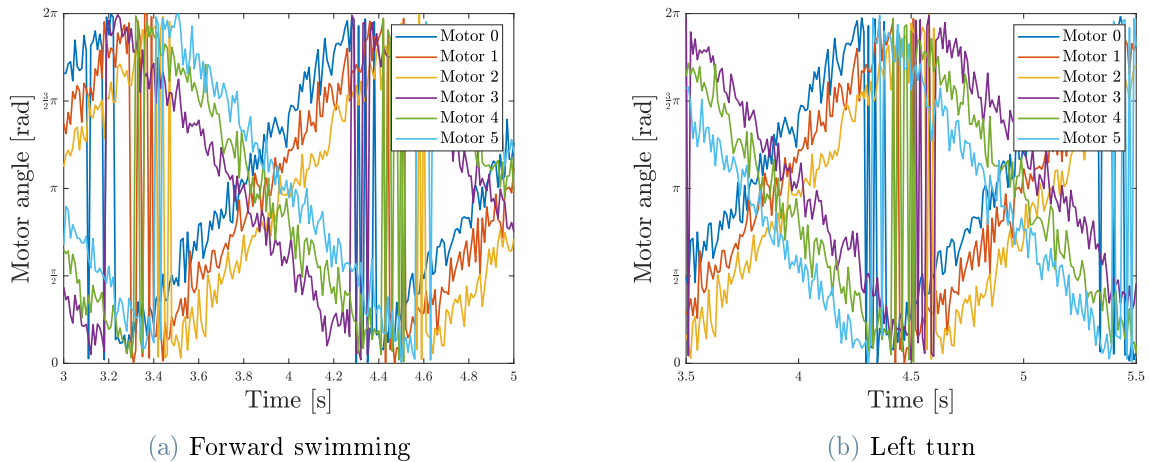
Figure 6.4: Encoder signals

6.2. Trajectory following

The high-level control algorithm is responsible for the correct following of the desired trajectory, which is carried out calculating suitable kinematic parameters for the movement of the fins.

6.2.1. Forward swimming

The first swimming condition studied is the simplest one: the straight motion. The only task that the control algorithm needs to do during straight swimming is correcting the pitch rotation using the tail. Firstly, a feedback control strategy has been implemented, as shown in Figure 6.5. A PI controller is introduced to define the inputs for the tail motors from the error between the robot's actual pitch angle and the target value, which, for straight motion, is set to zero. The acquisition of these data is possible thanks to the inertial measurement unit (IMU) present on the robot.
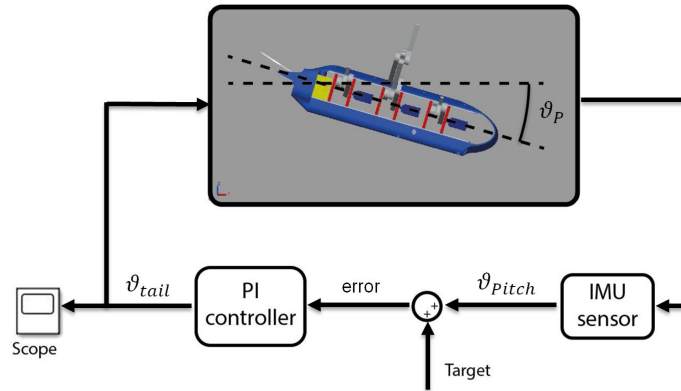
Figure 6.5: Feedback control strategy of the tail

Then, a feedforward control strategy has also been proposed not to depend only on sensors data. By analyzing the tail position given by feedback control, it is possible to recognize a sinusoidal pattern that keeps the robot close to the horizontal position. Therefore, a sine wave has been used as control input for the two motors of the tail mechanism. It has the same frequency of the flapping frequency and amplitude varying according to motion conditions to achieve stability by reducing the pitch angle variation. In this way, it is possible to emulate the feedback strategy results without dealing with sensors noise and inaccuracy. The pitch angle for both feedback and feedforward methods remains bounded between $\pm 10°$, as shown in Figure 6.6. However, the feedback control gives better performance because the tail does not move precisely as a sine wave at the beginning of the motion.
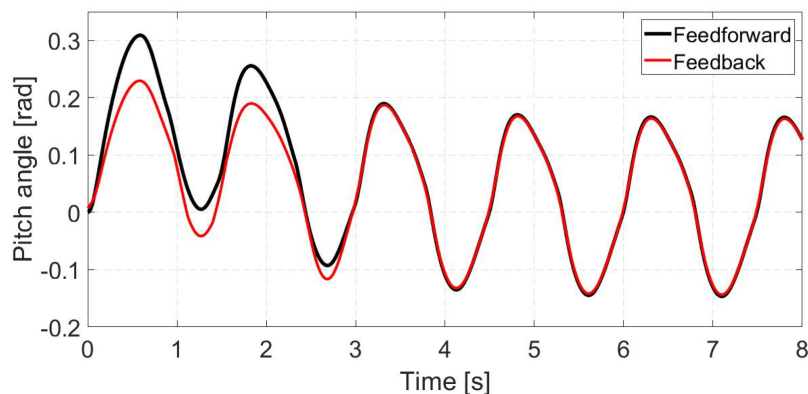
Figure 6.6: Pitch angle of the robot for both feedback and feedforward controls

The vertical displacement variation of the robot in a complete cycle is less than $\pm\,0.05\,\mathrm{m}$, as shown in Figure 6.7.
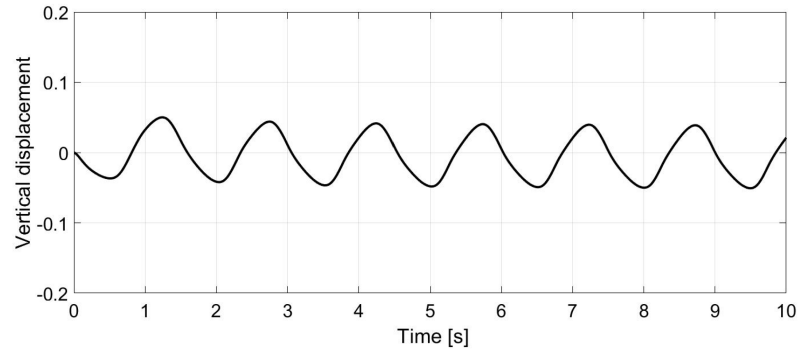
Figure 6.7: Vertical displacement of the robot during forward swimming

As it can be seen in Figure 6.8, the forward velocity resulting from the dynamical analysis is close to the one obtained with the CFD analysis, confirming the reliability of the model.
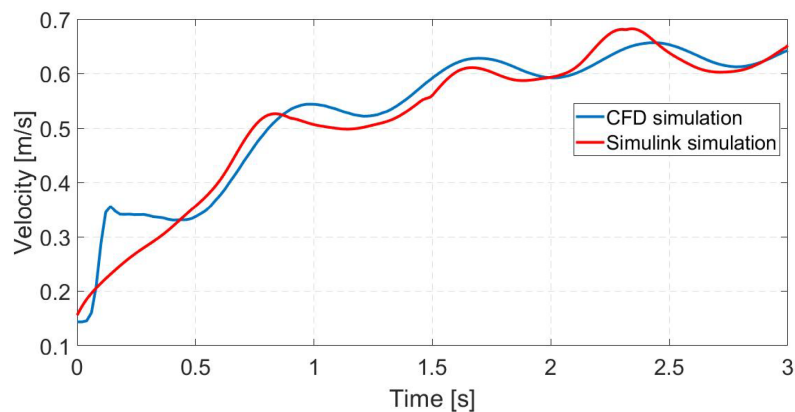
Figure 6.8: Comparison of the velocity of the robot obtained with the CFD and with the multibody model

6.2.2. Floating and diving maneuvers

n this analysis, the robot is considered neutrally buoyant; thus, hydrostatic force and gravity are always perfectly balanced, and any variation of the robot depth is obtained by creating an asymmetrical vertical force with the movement of the fins. In order to perform floating and diving maneuvers, the first step is the study of the behavior of the vertical force acting on each fin section for different swimming parameters. Amplitude, wavelength, and frequency do not change as the robot advances in a straight motion. Consequently, the vertical force is symmetrical and provides the same vertical force during upstroke and downstroke. However, to increase or decrease the actual height of the robot, the vertical component should not be balanced. Therefore, two control strategies have

been proposed: a variation of the amplitude and a variation of the phase difference between the fins as a function of time.

Amplitude variation   The vertical force F_z proportionally increases as the amplitude of the stroke increases and vice-versa. Hence, the idea is to control the motors with a sine wave whose amplitude is variable to obtain a different behavior between upstroke and downstroke, as shown in Figure 6.9. The graphs refer to the fin tip, which is the section providing the most significant contribution.

(a) Constant amplitude control input

(b) Vertical force with a constant amplitude

(c) Variable amplitude control input

(d) Vertical force with a varable amplitude
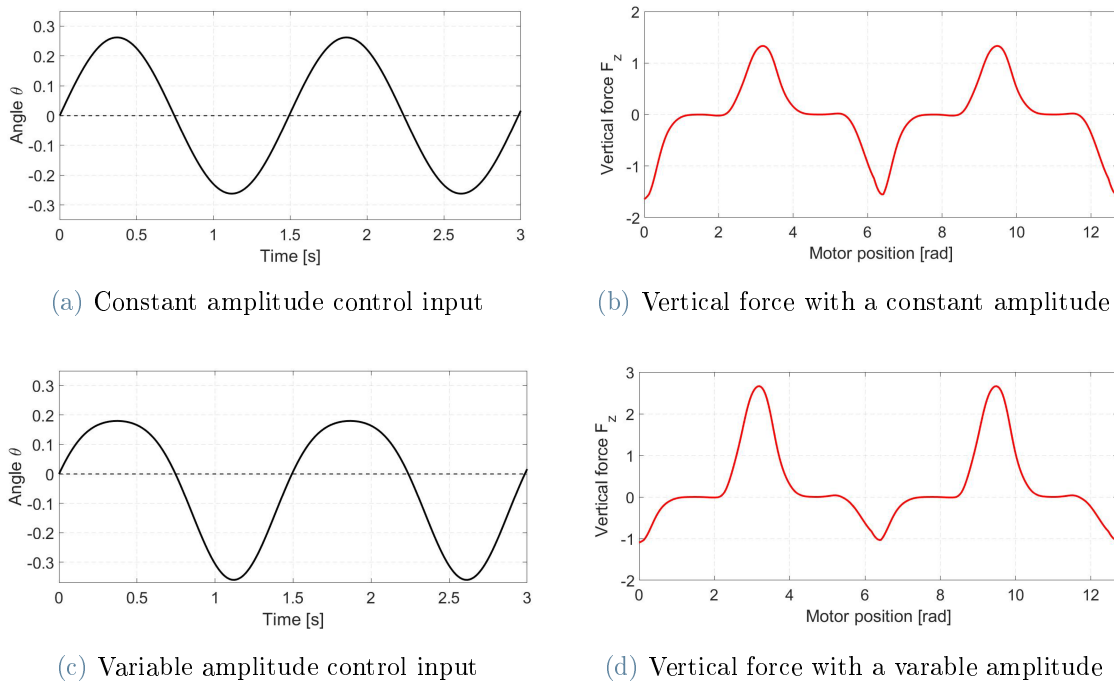
Figure 6.9: Vertical force obtained with variable amplitude

The amplitude is a sine wave with a frequency equal to the principal frequency of fin motion and, after defining the amplitude variation ΔA, it is summed or subtracted from the standard symmetrical value, depending on the aim of the maneuver, as presented in Figure 6.10.

(a) Symmetrical (Forward swimming) (b) Asymmetrical (Floating and diving)
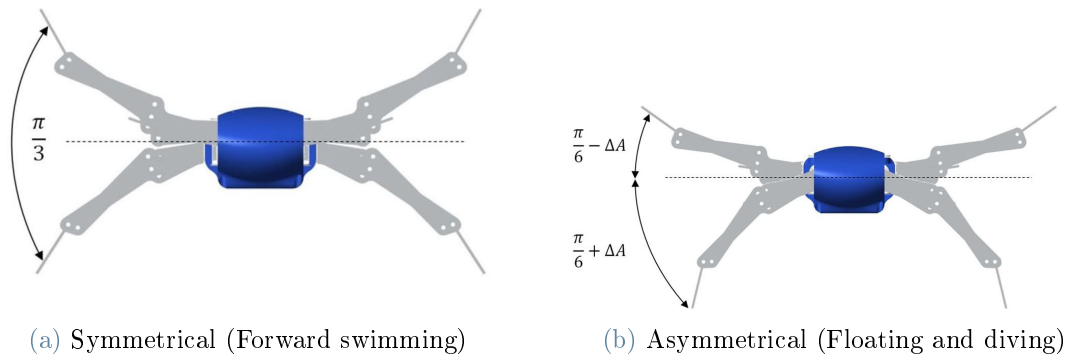
Figure 6.10: Superposition of the configurations with maximum range for symmetrical and asymmetrical amplitude

Wavelength variation   Likewise, the vertical forces increase as the phase delay between the mechanisms decreases. As this tends to zero, all the mechanisms get synchronized, eventually achieving a flat pectoral fin that does not produce a kinematic wave in the direction of motion. Therefore, by varying the phase difference between mechanisms within a reasonable range, it is possible to produce thrust and, at the same time, to vary the vertical force acting on the robot. This result is accomplished by changing the phase difference as a sinusoidal wave with the same frequency as the flapping frequency, as shown in Figure 6.11, where the green line is for frontal mechanism, the blue line for central on, and the red line for the rear one.
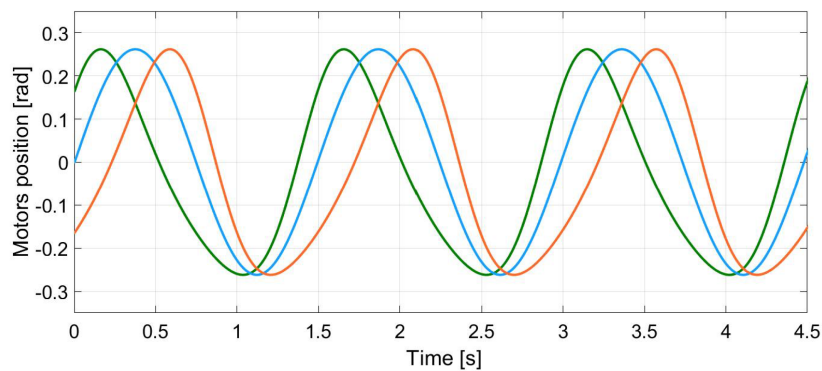
Figure 6.11: Positions of the three servo motors with sinusoidal phase difference variation. $\Delta\phi$ oscillates between 20° and 60°

Mean value and amplitude are defined by looking at the results obtained by the CFD analysis and the lookup table interpolation. Considering the floating maneuver, a flatter fin during downstroke is able to provide a larger contribution in the vertical thrust with respect to the upstroke.

Tail control   During floating and diving maneuvers too, the tail plays a fundamental role because it is needed to orient the robot with its head pointing upwards or downwards. Unlike in the straight motion, where the aim is to keep the robot in a horizontal position, i.e., $\theta = 0$, during floating or diving, the target pitch depends on the chosen trajectory. From the target depth difference H and the target distance L, the pitch angle is calculated as:

$$\theta = \arctan \frac{H}{L} \tag{6.4}$$

A scheme of the control algorithm is presented in Figure 6.12.
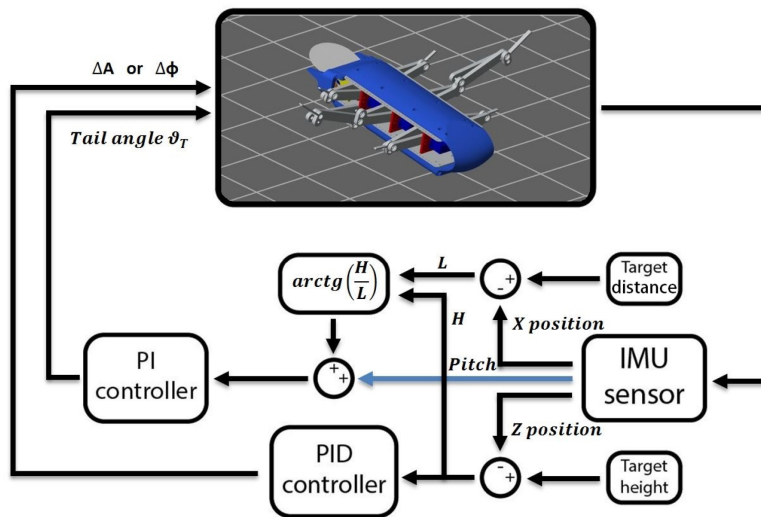
Figure 6.12: Diagram of the control algorithm for floating and diving maneuvers

The target pitch angle is constantly updated, considering the distance traveled by the robot in both directions. For this reason, the IMU unit plays a fundamental role. The three outputs extracted from the sensor are the x position (forward direction), the z position (vertical direction), and the pitch angle. The two positions are obtained by double integrating the accelerations, while the pitch is obtained by analyzing the components of the 3-axes accelerometer to find the orientation of the system. The algorithm compares the actual pitch coming from the IMU sensor with the target pitch angle in order to calculate the error, which is input to the PI controller, and its outcome is the input of the two servomotors moving the tail.

The algorithm compares the actual pitch coming from the IMU sensor with the target pitch angle to calculate the error, which is input to the PI controller, and its outcome is the input of the two servomotors moving the tail. According to which strategy has

been implemented, the only variable influenced in the sinusoidal motion of the fins is the amplitude or the phase delay. They are defined as ΔA or $\Delta \phi$ and correspond respectively to the amplitude variation from the symmetrical motion, added or subtracted from each half depending on the maneuver, and the phase difference variation between the fin mechanisms. This quantity is obtained from the PID controller, considering the difference between the actual and reference depth. Consequently, the gains of the PID controller are different depending on which of the two strategies is employed.

The results obtained with the two approaches are similar. The maximum vertical speed achievable is $0.15\,\mathrm{m\,s^{-1}}$, much lower than the horizontal one due to the larger drag caused by a larger surface and a higher drag coefficient.

In Figure 6.13, it can be seen how the vertical position varies with a target height difference of $0.6\,\mathrm{m}$ and a maximum value of $\Delta A = \frac{\pi}{9}$, with a standard symmetrical value for the amplitude equal to $\frac{\pi}{3}$.
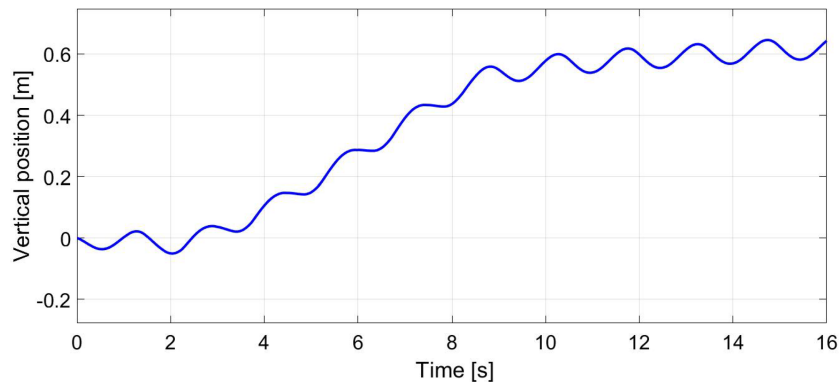
Figure 6.13: Vertical position variation with target at $0.6\,\mathrm{m}$

The main difference between the two approaches concerns power consumption. In both controls, the forces acting on the fins are higher compared to straight linear motion. The main distinction is related to the effect of the phase delay on the power consumption: if the fins are synchronized as in the wavelength control strategy, the peak power and the average power obtained are larger with respect to the amplitude control.

6.2.3. Turning maneuvers

One of the reasons because cownose rays are so attractive is their extraordinary maneuverability, allowing them to perform fast turns even in small spaces. This kind of maneuver is obtained thanks to different thrust forces in the left and right fins, as

discussed in Chapters 2 and 5.

Two turning maneuvers are presented: the highly maneuverable and the banking turns.

Highly maneuverable turn   In highly maneuverable turns, the force generated by one fin is equal and opposite to the one generated by the other. This way, a turn with a curvature radius close to zero can be obtained. In order to get opposite thrust forces, it is possible to change different swimming parameters in the two fins. Since the highest contribution to forces is given by the central mechanisms, they are kept synchronized to avoid stability issues due to the high roll moment that would generate. In this maneuver, except for very large amplitudes, the pitch moment and the vertical force remain small so that the tail can remain horizontal and it does not need to contribute. To get opposite thrust forces in the two fins, the phase difference of the two sinusoidal waves controlling left and right motors are the opposite.

Video frames of this maneuver are shown in Figure 6.14.
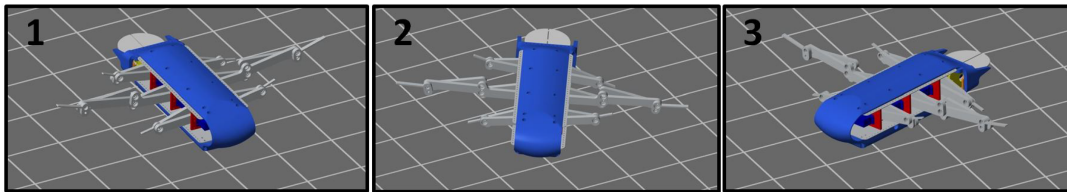
Figure 6.14: Different instants of highly maneuverable turn

The rotational velocity is almost constant throughout the entire turn, as can be seen in Figure 6.15a. In Figure 6.15b, the rotational speed has been calculated for different frequency values, highlighting a linear behavior of the model.
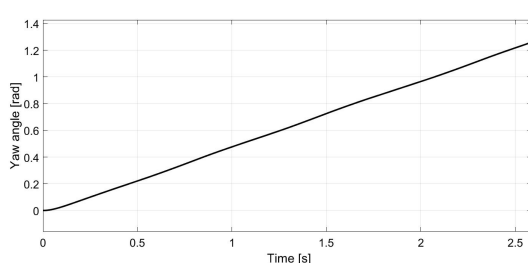
(a) Yaw speed of the robot for a frequency of 0.67 Hz and an amplitude of $\frac{2}{9}\pi$
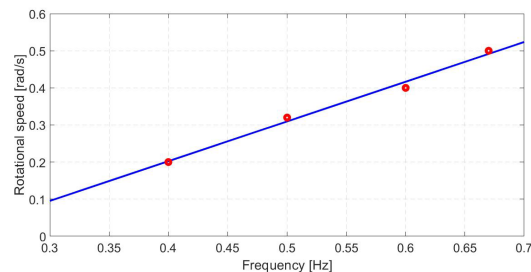
(b) Relationship between rotational speed and flapping frequency

Figure 6.15: Superposition of the configurations with maximum range for symmetrical and asymmetrical amplitude

Banking turn   In order to achieve different curvature radii for turning maneuvers, the strategy applied is related to the differences in the amplitude of motion of each fin. As a result, movements with different amplitudes are generated on the two fins to have different thrust forces on the two fins, as shown in Figure 6.16.
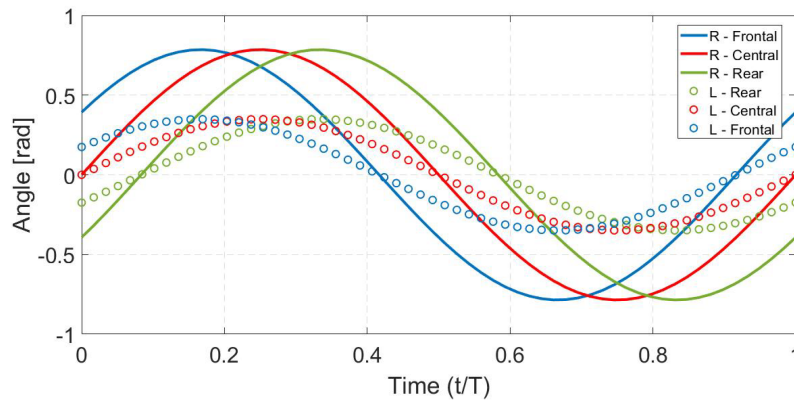
Figure 6.16: Angles of the motors during banking

The amplitude of the left fin movement must be greater than the right fin to perform right turns, whereas to perform left turns, the opposite occurs. During this maneuver, the control of the pitch rotation using the tail is active, and it acts in the same way as during forward swimming. This maneuver can be performed only when the robot already has some kinetic energy, and in this analysis, it is simulated after the robot has reached the steady-state velocity. The variable measured by the IMU sensor is the yaw angle, which is compared with the target yaw, defined with the target trajectory arc. When the yaw is close to the target, both amplitudes tend to their previous symmetrical values to put the robot again in forward swimming mode.

During banking, the roll angle reaches 20° in the middle of the curve, and then it goes back to zero, as the motion of the fins becomes symmetrical again.

7 | Experimental tests on the fins

THE experiments on this prototype are aimed at understanding which are the forces involved when the robot moves in a fluid. The reason why also tests with the robot moving in the air have been carried out is that it has been possible to impose a relative speed between the system and the fluid in a wind tunnel, which would not have been possible in a water tank.

7.1. Experiments in the wind tunnel

To account for the difference of density and viscosity between air and water, all the tests in the wind tunnel have been performed in a flow condition similar to the one of the fish swimming at a steady-state velocity in water, adjusting the flow velocity and the frequency of fin movement to get the same Reynolds number. The meaningful results of this analysis are dimensionless parameters, such as the drag coefficient c_D of the fin. The experiments are conducted in a wind tunnel of section $500\,\mathrm{mm}$ x $500\,\mathrm{mm}$, shown in Figure 7.1, where a large fan is responsible for air movement, and a potentiometer controls the blades' rotational speed.

Figure 7.1: Wind tunnel in which the experiments have been performed

The airspeed is calculated using the Bernoulli equation from a pressure measure inside the tunnel with a Pitot tube.

$$z_0 + \frac{v_0}{2g} + \frac{p_0}{\rho g} = z_1 + \frac{v_1}{2g} + \frac{p_1}{\rho g} \tag{7.1}$$

In Equation 7.1 the subscript 0 stands for the environment outside the wind tunnel, whereas the subscript 1 is meant for inside the wind tunnel. Considering that $z_0 = z_1$ and that the air velocity outside the wind tunnel is zero, it is possible to obtain the air velocity in the wind tunnel:

$$v_1 = \sqrt{\frac{2\,(p_0 - p_1)}{\rho}} \tag{7.2}$$

The air density ρ can be calculated considering it as an ideal gas leading to:

$$\rho = \frac{p}{RT} \tag{7.3}$$

where T is the air temperature, and R represents the ideal gas constant relative to the air, equal to 287.05 J/kg/K. The forces and the moments are measured with a 6-axis force sensor Schunk FT-AXIA 80, which is clamped to the floor of the wind tunnel, as shown in Figure 7.2. Its sensing range is 100 N for F_x and F_y, 360 N for F_z, 8 Nm for the moments about the three axes, and its sampling frequency is 126 Hz.
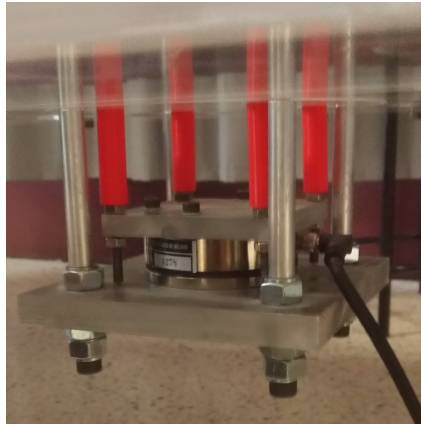
Figure 7.2: Load cell mounted in the wind tunnel

Due to the space constraints, these tests are performed on just one fin of the robot, and the fin is positioned in a vertical direction, which is different from the orientation of the fish during swimming. Nevertheless, this is still representative of the working conditions of the fin since, during swimming, the weight is balanced by the hydrostatic force. Since the fluid air has a much smaller density than water, the measured forces are expected

to be so small that they could be comparable with the noise of the acquisition system. Therefore, for every test in the wind tunnel, the robot has been kept in motion for several cycles so that the signal could be time-averaged. The test setup with the reference system of the load cell is presented in Figure 7.3.
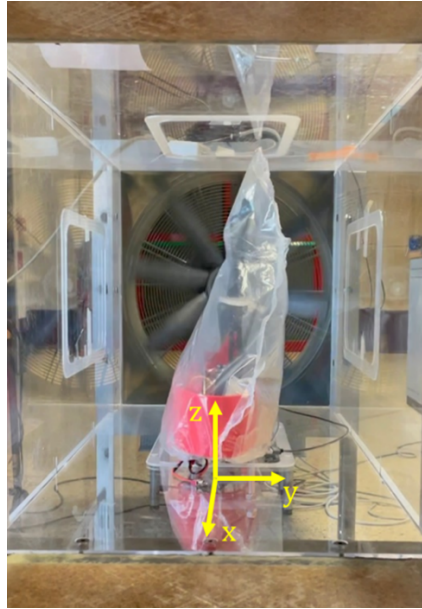
Figure 7.3: Fin in the wind tunnel

7.1.1. Reynolds number equivalence

The forces are measured for a wide range of different air velocities and frequency of motion of the fin. The measured forces are then converted to some non-dimensional parameters to obtain meaningful results representative of the real conditions of a cownose ray swimming in the water, which is a common method used for the evaluation of fluid-dynamic forces [66, 87]. The main flow characteristics are dependent on the Reynolds number, which is equal to:

$$Re = \frac{UD}{\nu} \tag{7.4}$$

Since the kinematic viscosity of water and air are different, as shown in Table 7.1, it is necessary to adjust the velocity U of the relative flow to maintain a Reynolds number of $\sim 10^5$ as for the steady-state swimming in water.

Table 7.1: Kinematic viscosity and density of air and water

Fluid	Kinematic viscosity ν $[m^2/s]$	Density ρ $[kg/m^3]$
Air	1.5×10^{-5}	1.225
Water	1×10^{-6}	997

Thus, being the characteristic length of the fin the same regardless of the fluid, the velocity of the airflow can be calculated with the simple relation:

$$U_{air} = U_{water} \frac{\nu_{water}}{\nu_{air}} \tag{7.5}$$

7.1.2.   Evaluation of the drag coefficient

The drag coefficient is evaluated with the fin still in different positions and with airflow at different velocities from $7.5\,\mathrm{m\,s^{-1}}$ to $10\,\mathrm{m\,s^{-1}}$.
The Reynolds number of the flow in these tests is about 10^5, as for the cownose ray gliding in water at 0.5 - $0.7\,\mathrm{m\,s^{-1}}$. The Reynolds number of the fin still is calculated considering as characteristic length the average chord length, adopting the same procedure as for aerodynamic profiles. Then, the drag coefficient is calculated as follows:

$$c_D = \frac{2F_x}{\rho A U_{air}} \tag{7.6}$$

where A is the area of the projection of the surface of the fin on a plane perpendicular to the yaw axis ($x - z$ plane), equal to $0.1252\,\mathrm{m^2}$.
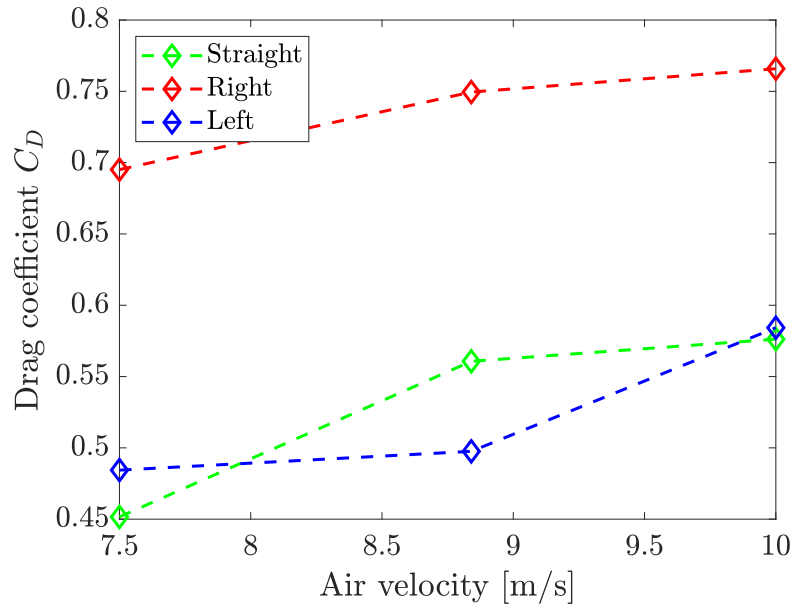
Figure 7.4: Drag coefficient of the fin still at different velocities and with different fin orientations

The drag forces are measured for different fin orientations: with the fin flat and straight and with the fin curved left and right, and the resulting drag coefficient is plotted in Figure 7.4. The drag coefficient c_D increases with an increasing air velocity U_{air} because as the speed reaches a high value, the coating starts folding and creating some local cavities, which make the hydrodynamic profile of the fin less efficient.

7.1.3. Evaluation of the forces with the fin in motion

Several tests with the fin in motion at different frequencies are performed to evaluate the thrust performance of the fin, and the forces are measured with air flowing at different velocities. In all tests, there is a phase shift between consecutive mechanisms of $\frac{\pi}{6}$ to reproduce the traveling wave on the fin surface. To evaluate the forces generated by the fin moving at different frequencies, a measurement of the inertia forces of the mechanism is required. In Figure 7.5 the inertia forces are plotted for the mechanism moving at 0.5 Hz.
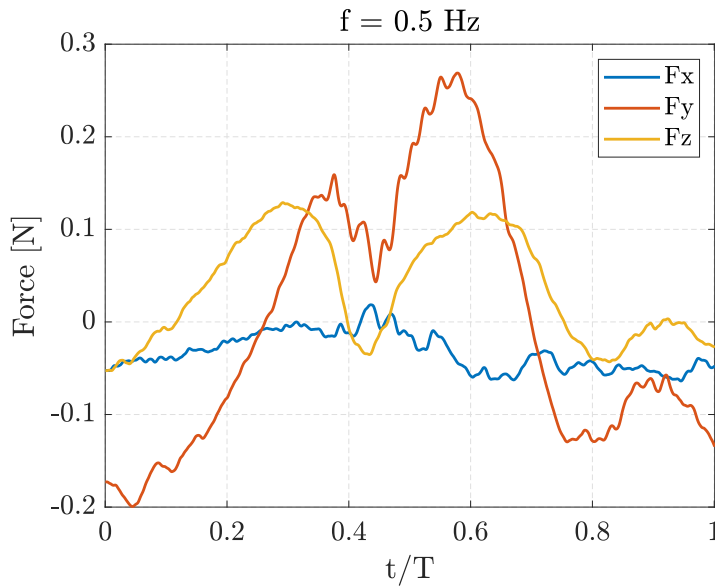
Figure 7.5: Inertia of the mechanisms

The inertia forces are measured without the external surface, so that air cannot be displaced by the motion of the fin. It is possible to note that the lateral force F_y is symmetrical with respect to the x-axis since the motion is symmetrical. It is featured by two peaks occurring when the frontal and the central mechanism, out of phase with each other, have maximum angular acceleration. The vertical force, F_z, is mainly due to the centrifugal inertia force of the mechanisms during rotation and it is featured by two peaks when the angular velocity is maximum. Finally, the longitudinal force F_x is null because the mechanisms move only in y and z directions, and no air is displaced. This measured inertia must be subtracted from the measurements to isolate the fluid-dynamic forces.

The tests with the fin in motion are performed at different wind velocities and for different frequencies. For all of them, the tests have confirmed that a force in the longitudinal direction is generated both during the upstroke and during the downstroke, being the fin motion symmetrical. Hence, the force F_x has a double frequency with respect to the lateral force F_y. The forces are measured for 6 minutes, and then an average over the period is performed to reduce the high frequency noise.

Longitudinal and lateral forces at different frequencies and velocities are presented in Figure 7.6.

(a) Longitudinal force at $0.5\,\mathrm{Hz}$

(b) Lateral force at $0.5\,\mathrm{Hz}$

(c) Longitudinal force at $0.7\,\mathrm{Hz}$

(d) Lateral force at $0.7\,\mathrm{Hz}$

(e) Longitudinal force at $0.9\,\mathrm{Hz}$

(f) Lateral force at $0.5\,\mathrm{Hz}$
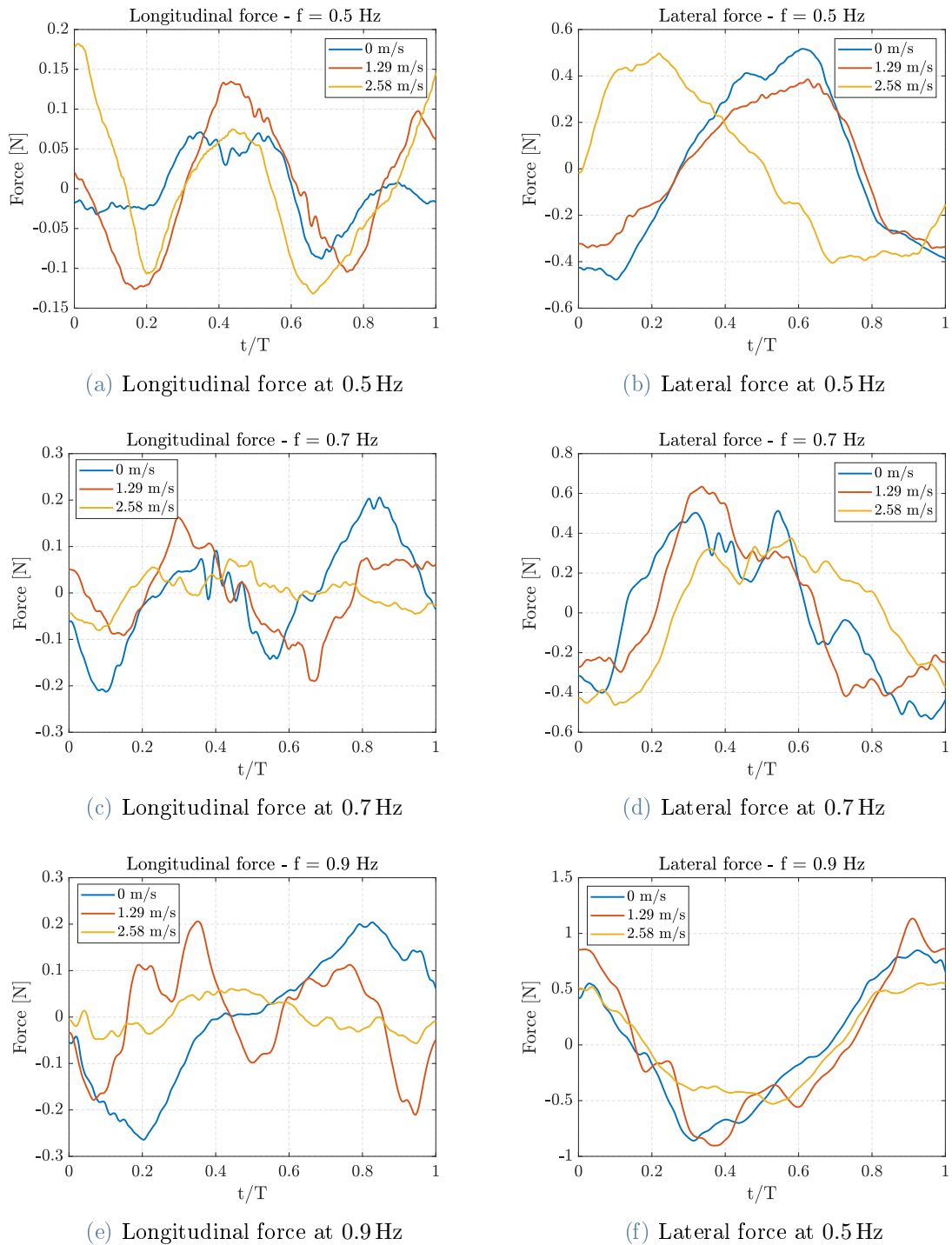
Figure 7.6: Forces on the fin moving at different frequencies and with different air velocities

The amplitude of both longitudinal and lateral forces increases as the frequency increases, whereas the variation of the relative velocity between the fin and the fluid has a small effect on both forces.

From Figure 7.7, it is possible to note that, when the lateral force (F_y) is maximum, the longitudinal force (F_x) is zero, and it is clear that the frequency of the longitudinal force is double.
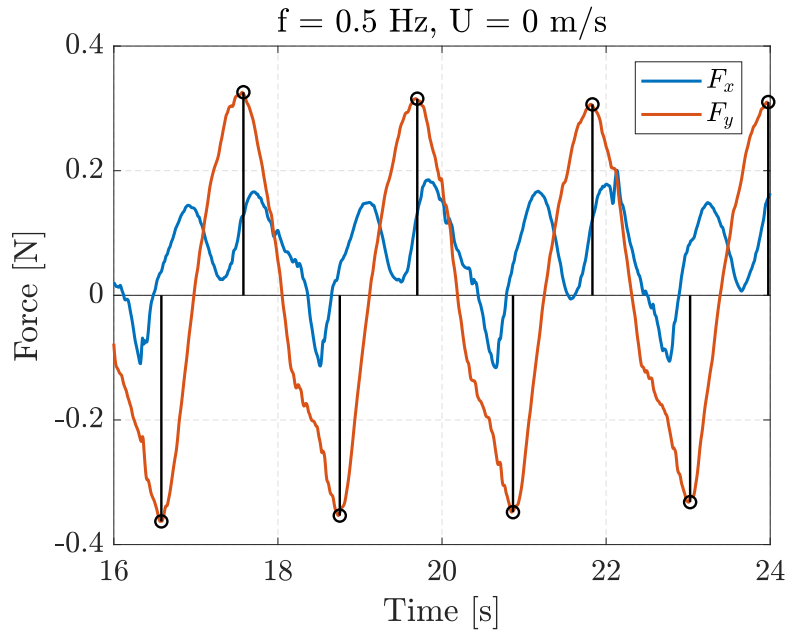
Figure 7.7: Time history of lateral and longitudinal forces. The maximum value of the lateral force, circled in black, is in correspondence of a null value of the longitudinal force.

7.2.　Experiments in the water tank

The experiments in a water tank provide more reliable measures of the forces acting on the fin because it has a higher density with respect to air, so the forces have a superior order of magnitude, and the electric noise coming from measurements is negligible. The forces measurement is carried out using the same 6-axis load cell as in the wind tunnel. For these experiments, just one fin is employed; however, unlike in the experiments in the wind tunnel, the fin is of the robot pointing downwards, whereas, in the wind tunnel, the system is clamped to the load cell with the fin pointing upwards. As a consequence, the load cell must be placed above the robot, requiring an additional support structure to connect the robot to the load cell, which must be characterized by a high stiffness not to alter the force measurements.
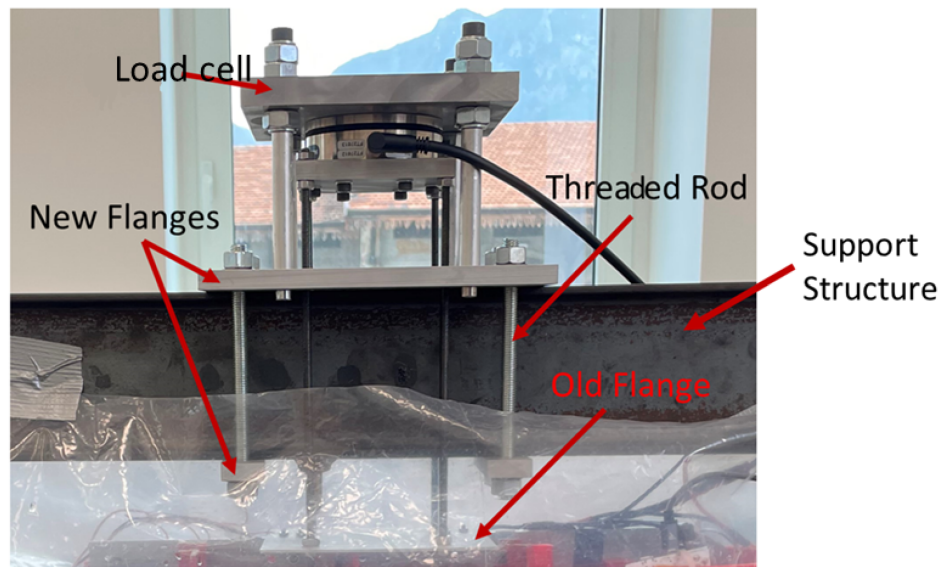
Figure 7.8: Setup of the experiments in a water tank

Hence, the same plate and the two flanges used in the wind tunnel connect the robot to the load cell, in combination with additional plates and threaded rods, which properly fix the load cell on the structure and are useful to adjust the depth of the fin inside water. The experiment setup is shown in Figure 7.8.

The water tank has a volume of 200 l, and the fin is submerged in it, hanging from the top. Unlike in the wind tunnel, nothing moves the fluid except for the fin itself. An aspect to consider is that the tank has a rectangular cross-section; therefore, the most suitable configuration is the one in which the fin is allowed to move along the longest side of the rectangle, as shown in Figure 7.9, to avoid the effect of water bouncing on the sides. This layout affects the reference frame, leading to some changes with respect to the previous configuration. The thrust direction is now the positive y-direction, and the lateral forces are oriented along the x-axis.
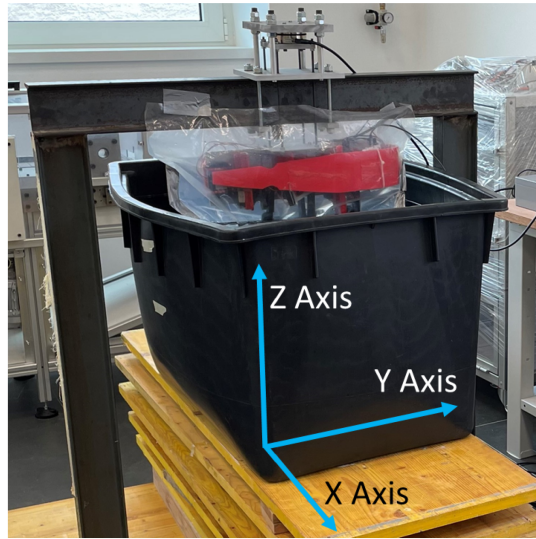
Figure 7.9: Water tank with the reference system used in the experiments

The objective of these tests is to measure the forces exerted by the fin at different frequencies. Combining these results with the values of the drag force that can be calculated thanks to the experiments in the wind tunnel, it is possible to estimate the steady-state velocity of the fish at each frequency.

The drag force acting on the fin moving in water at different velocities is plotted in Figure 7.10 and summarized in Table 7.2. It is computed reverting Equation 7.6 and considering the density of water and the area of both fins.
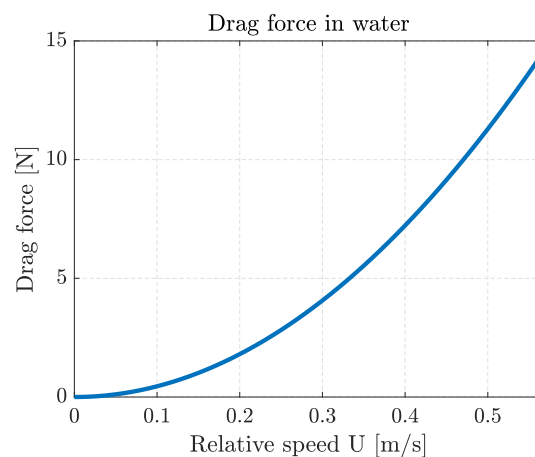
Figure 7.10: Drag force acting on both fins in water

Table 7.2: Drag force on the fin at different flow speed

Relative speed [m/s]	Drag force [N]
0.1	0.4516
0.2	1.8066
0.3	4.0649
0.4	7.2266
0.5	11.292
0.6	20.542
0.7	27.994

Tests have been performed at five different values of frequency: from 0.2 Hz to 0.6 Hz. The measurements have been filtered by using a low pass filter featured by a cutting frequency at 6 Hz. The thrust force, on the y-axis is expected to have a higher component with respect to experiments in air and to have a double frequency compared to the principal one.

However, as for the wind tunnel test, due to vibrations and unwanted movements out of the $y - z$ plane, also components at the principal frequency and at its multiples sum up to the signal. Moreover, in water, the mechanisms are more difficult to control than in the air, as water exerts a much higher force, leading to a worse overall motion than the one in the air, especially at high frequency.

In Figure 7.10 the time histories and the spectra of longitudinal and lateral forces are presented for all the tested frequencies.
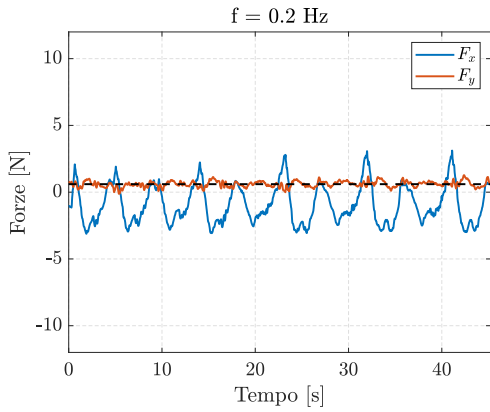
(a) Time history of forces at 0.2 Hz
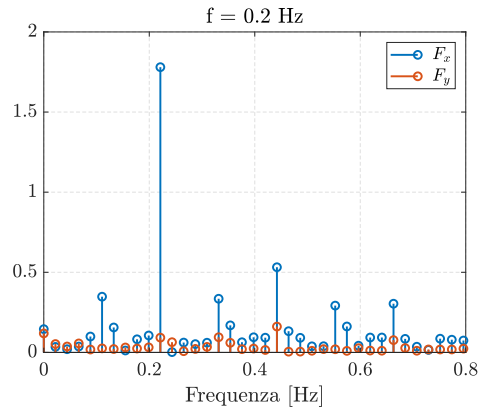
(b) Spectrum of forces at 0.2 Hz
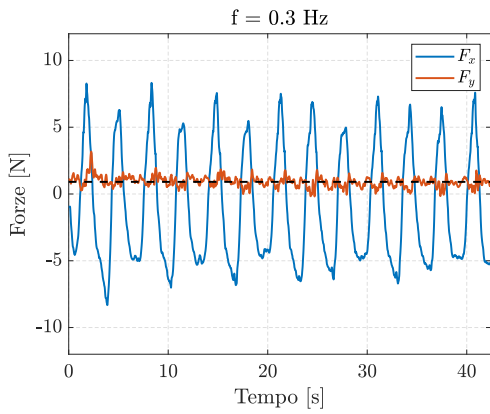
(c) Time history of forces at 0.3 Hz
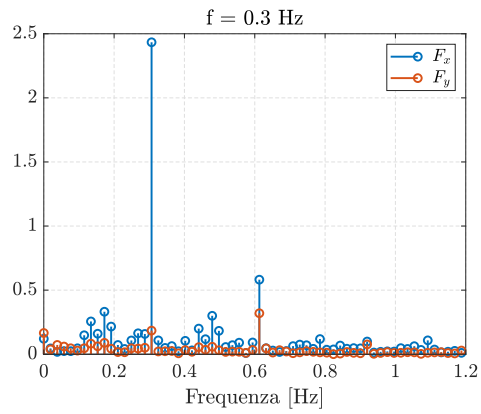
(d) Spectrum of forces at 0.3 Hz
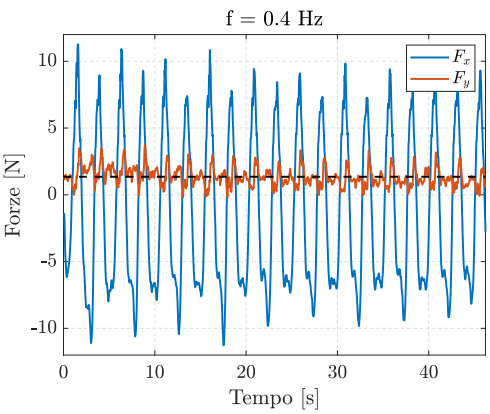
(e) Time history of forces at 0.4 Hz

(f) Spectrum of forces at 0.4 Hz

(g) Time history of forces at 0.5 Hz

(h) Spectrum of forces at 0.5 Hz

(i) Time history of forces at 0.6 Hz
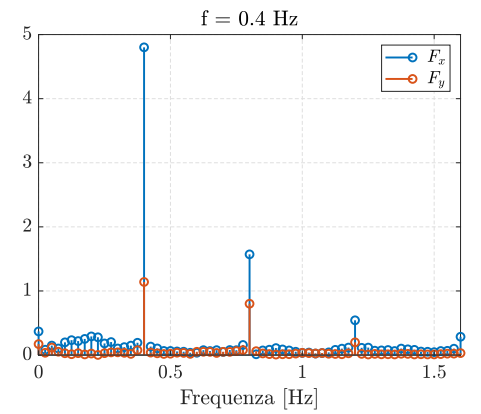
(j) Spectrum of forces at 0.6 Hz
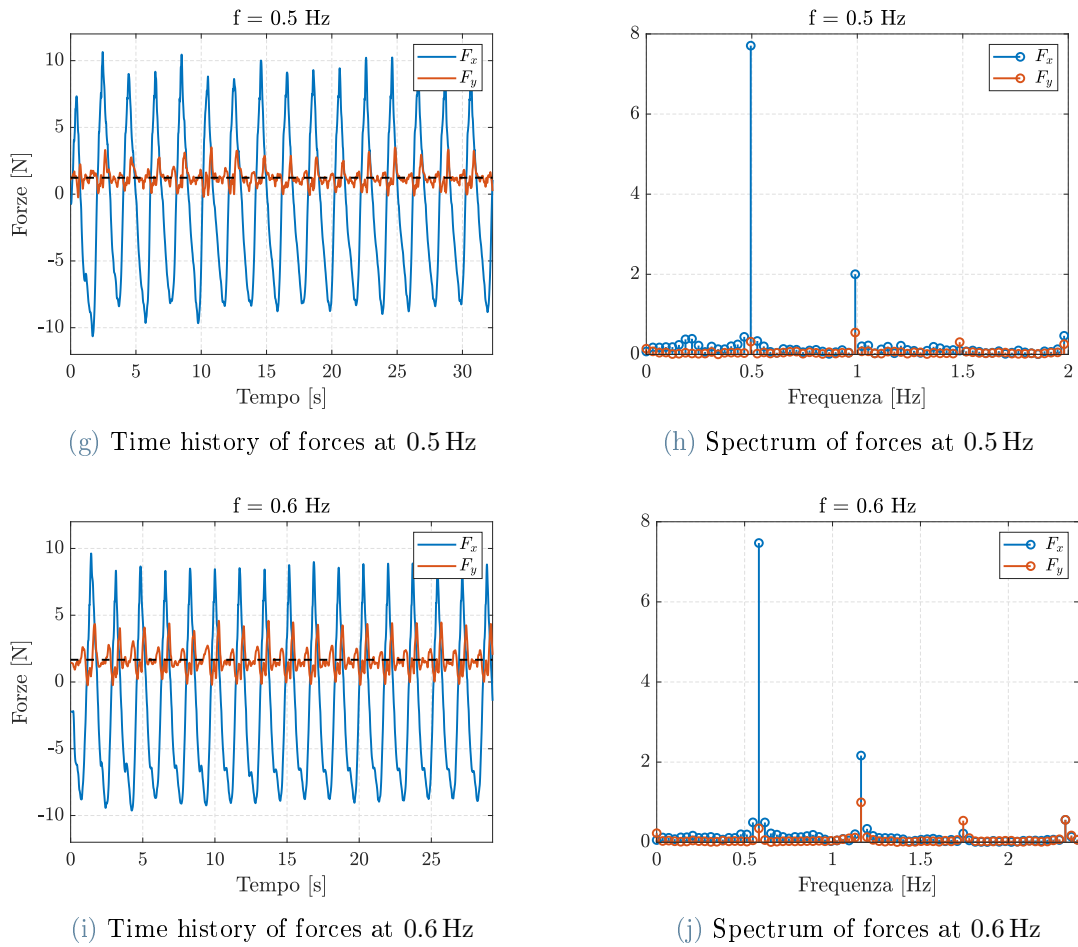
Figure 7.10: Forces on the fin moving at different frequencies in water

As it can be seen, the spectrum highlights the fact that the greatest component of the longitudinal force F_y, exception made for the mean value, is the one at the double of the principal frequency. Then, some other components arise because the fin movement is not perfectly symmetrical. The longitudinal force is positive for almost the whole flapping cycle, meaning that a propulsive force is generated during upstroke and downstroke.

The generated thrust at different frequencies can be interpolated with a second-degree polynomial to understand the relationship between thrust and frequency of fin movement. The result is shown in Figure 7.11, where the yellow area represents the 95% confidence interval of the data fitting.
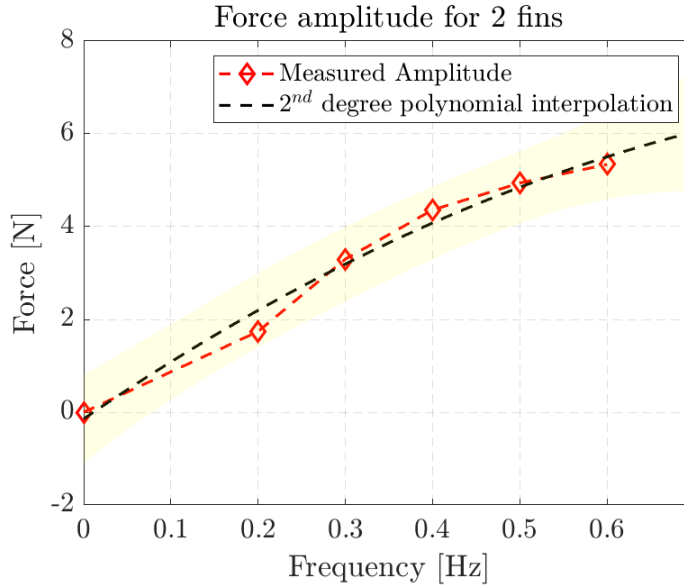
Figure 7.11: Data fitting of the generated thrust and associated frequency

As expected, the relationship between thrust and frequency shows an increasing trend, but there is a substantial difference from the results obtained with the CFD analysis. The relation between thrust and frequency calculated with the CFD analysis is a second-degree polynomial with positive concavity, whereas the experimental results show a negative concavity. In particular, looking at the raw data, it is possible to highlight that the concavity is positive for frequencies lower than 0.4 Hz, and a change of curvature can be observed for higher frequencies.

This can be explained by pointing out that during water experiments, even though the fin has been clamped to the load cell, at high frequencies, some water was also pushed forward due to the interaction with the lateral walls of the tank. Moreover, some folds created in the external surface decreased the thrust generation capability of the fin, which are aspects not considered by the CFD analysis where the fish swims in ideal conditions. Nevertheless, these experiments, recreating a starting swimming condition, where no relative velocity between the fish and the fluid is present, gave results with the same order of magnitude as the CFD analysis, despite all the non-idealities of the tests.

Comparing the thrust force resulting from these experiments and the drag force calculated with the experiments in the wind tunnel, it is possible to find the equilibrium point and calculate the steady-state velocity of the robot for all the frequencies tested. Even at 0.2 Hz, the slowest frequency tested, a positive thrust force is registered, equal to 0.8658 N. Since the tests have been performed on just one fin, the propulsive force in the

real condition is double of the one acquired. Thus, the propulsive force generated with two fins is 1.7313 N, and such thrust force overcomes the drag force for a relative speed $U = 0.19\,\mathrm{m\,s^{-1}}$. Repeating the same procedure for all frequencies, it is possible to obtain the graph shown in Figure 7.12, from which it is possible to understand the relation between frequency and steady-state velocity.
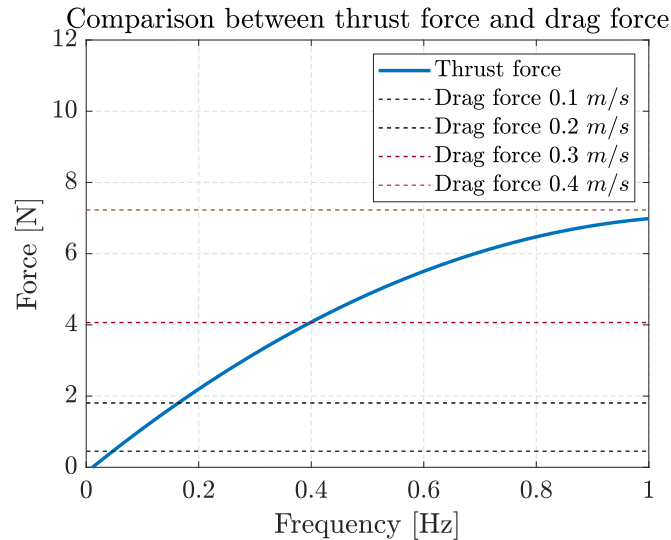
Figure 7.12: Comparison between thrust force and drag force

In conclusion, the results obtained from the experimental tests show that it is possible to generate a thrust and that this thrust force fits the expectations of the CFD model, despite all the limitations of this prototype and the setup of the experiment. Nevertheless, to build a functioning robot, a new design has to be thought of, which can generate higher forces and have a smoother and more flexible external surface.

8 | Improvements to the robot

T HE robot prototype has demonstrated that the locomotion principle adopted by the cownose ray is a viable solution to obtain efficient propulsion underwater. Nevertheless, it has also highlighted several limitations that must be overcome to build a functioning robot exploiting all the advantages of such a locomotion principle and achieving the same swimming performances as its natural counterpart.

The main improvements that have been made to the new version of the biomimetic robot are the following:

- **External surface**: the polyethylene sheets used in the prototype are not flexible enough to follow the deformation of the fins; thus, they are loose to allow movement. Thus, during the mechanism movement, in the external surface, several folds are created, which significantly decrease the hydrodynamic efficiency of the fins and cause undesired stresses on the links. Therefore, in the new design of the robot, fins are entirely redesigned, choosing a different material that meets the elasticity requirements of the application.

- **Fin mechanisms**: although the fin mechanisms reproduce well the deformation of a fin section, sliders are inevitably featured by a large clearance to work, which creates unwanted out-of-plane movements of the mechanisms. Moreover, the presence of a four-bar linkage connected to a motor with continuous rotation does not allow changing the amplitude of fin motion, reducing the controllability of the robot. In the new version of the robot, these problems are overcome by designing a mechanism with only hinges and without sliders and removing the four-bar linkage.

- **Motors**: such a choice of the mechanism requires servomotors with position control to adjust the amplitude of the movement. Furthermore, the selected motors for the final design of the robot have a higher torque.

- **Material**: the links made of ABS show a very large deflection under the load of the hydrodynamic forces, especially in the central mechanism where the bending moment is the highest. Moreover, ABS is too light, and the robot requires a considerable amount of additional weight to counteract the hydrostatic force. Therefore, in the final version of the robot, all the links and the main components are made of aluminum.

The overall dimensions of the robot are the same as those of the prototype, replicating the dimensions of the real cownose ray, so the length of the robot is $0.58\,\mathrm{m}$ and its width from fin tip to fin tip corresponds to $1\,\mathrm{m}$. In addition, the robot is supposed to be neutrally buoyant, so the mass of the robot is tuned to reach the corresponding mass of the water volume displaced.

8.1. Pectoral fin kinematics

The fin is still composed of three mechanisms, but the front mechanism and the rear mechanism are exactly the same, while the central one is an extension of the frontal one. The most significant change is the elimination of the four-bar linkage, which makes the system easier to control because it allows the implementation of a position control rather than a velocity control. Moreover, this new system is simpler as there is no more the necessity of introducing clearance after eliminating the sliders, limiting the out-of-plane movement.

The kinematic diagram of the front and rear mechanisms is shown in Figure 8.1

(a) CAD model   (b) Kinematic diagram
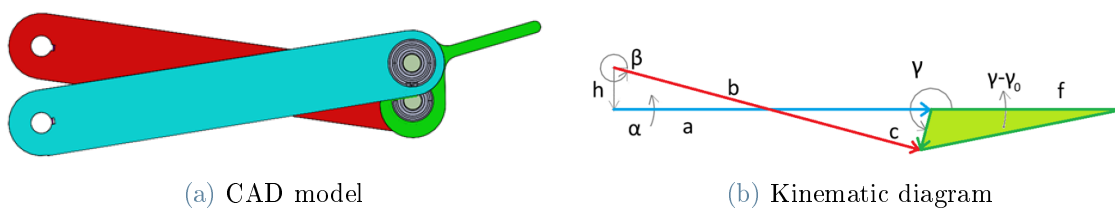
Figure 8.1: Frontal and rear mechanism of the pectoral fins

The procedure used to optimize the link lengths so to reproduce at best the shape of the fin cross-section is the same as the one used for the mechanisms of the prototype. Hence, the first step is to solve the kinematics of the mechanism to calculate the area below it. Since the motor is connected to the link a, shown in light-blue, the angle α corresponds

to the rotation of the motor and it is convenient to express all other variables as functions of α. By projecting on the x and y axes, the following expression is obtained:

$$\begin{cases} b\cos\beta = a\cos\alpha + c\cos\gamma \\ h + b\sin\beta = a\sin\alpha + c\sin\gamma \end{cases} \tag{8.1}$$

Rearranging the terms, Equation 8.1 becomes:

$$\begin{cases} c\cos\gamma = -a\cos\alpha + b\cos\beta \\ c\sin\gamma = -a\sin\alpha + h + b\sin\beta \end{cases} \tag{8.2}$$

Squaring both equations and summing them together, it is possible to obtain an equation with the only variable β, which, after some goniometric simplifications, is equal to:

$$c^2 = a^2 + b^2 + h^2 - 2h\left(a\sin\alpha - b\sin\beta\right) - 2ab\cos\left(\alpha - \beta\right) \tag{8.3}$$

Then, it is possible to find the angles β and γ.

$$\beta = 2\arctan\left(\frac{\sqrt{2a^2c^2 - b^4 - c^4 + 6a^2b^2 - a^4 + 2b^2c^2 - 2a^2h^2\left(1 - 2\sin^2\alpha\right) + 2b^2h^2 + 2c^2h^2 + 4ah\sin\alpha\left(-h^2 - a^2 + b^2 + c^2\right)} + 2bh + 2ab\sin\alpha}{a^2 + 2ab\cos\alpha + 2ah\sin\alpha + b^2 - c^2 + h^2}\right) \tag{8.4}$$

$$\gamma = \arccos\left(\frac{b\cos\beta - a\cos\alpha}{c}\right) \tag{8.5}$$

Another critical aspect of the kinematics of the frontal and rear mechanism is that the c link, shown in green, must be in a horizontal position when the angle α is equal to zero. According to Figure 8.1, when α is 0, also $\gamma - \gamma_0$ must be equal to zero. Hence, it is necessary to find the correct value of γ_0 to satisfy this condition, which for this configuration is equal to $-105.07°$. The central mechanism of the fin, shown in Figure 8.2, is featured by the same kinematic diagram repeated twice; thus, the kinematics can be solved using the same set of equations, and the angle δ_0, which allows the final link to be in a horizontal position when $\alpha = 0$ is $-105.07°$.
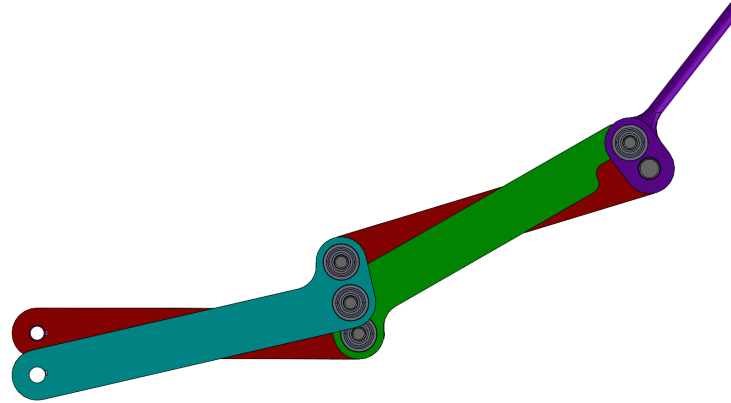
(a) CAD model
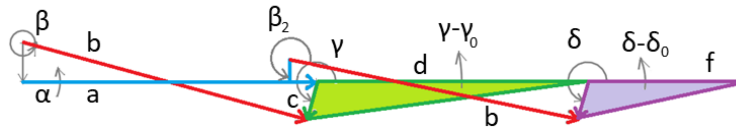
(b) Kinematic diagram

Figure 8.2: Central mechanism of the pectoral fins

After having solved the kinematics of the mechanisms, it is possible to apply the same procedure that was applied for the mechanisms of the prototype to find the link lengths that reproduce at best the fin deformation. The only difference is the area below the links, which is:

$$
\begin{aligned}
\tilde{A} = & \frac{a^2 \sin\alpha \cos\alpha}{2} + \frac{(2a\sin\alpha + c\sin(\gamma - \gamma_0))\, c\cos(\gamma - \gamma_0)}{2} \\
& + \frac{(2a\sin\alpha + 2c\sin(\gamma - \gamma_0) + d\sin(\delta - \delta_0))\, d\cos(\delta - \delta_0)}{2}
\end{aligned}
\tag{8.6}
$$

The length of the mechanisms is determined in order to obtain an overall extension of the system from fin to fin equal to $1\,\mathrm{m}$. This means that the central mechanisms are $0.4\,\mathrm{m}$ long since the central body is $0.15\,\mathrm{m}$ wide and a few centimeters are left for the external profile around the tip.

The result of the link lengths optimization is shown in Figure 8.3, and the resulting link lengths are listed in Table 8.1.
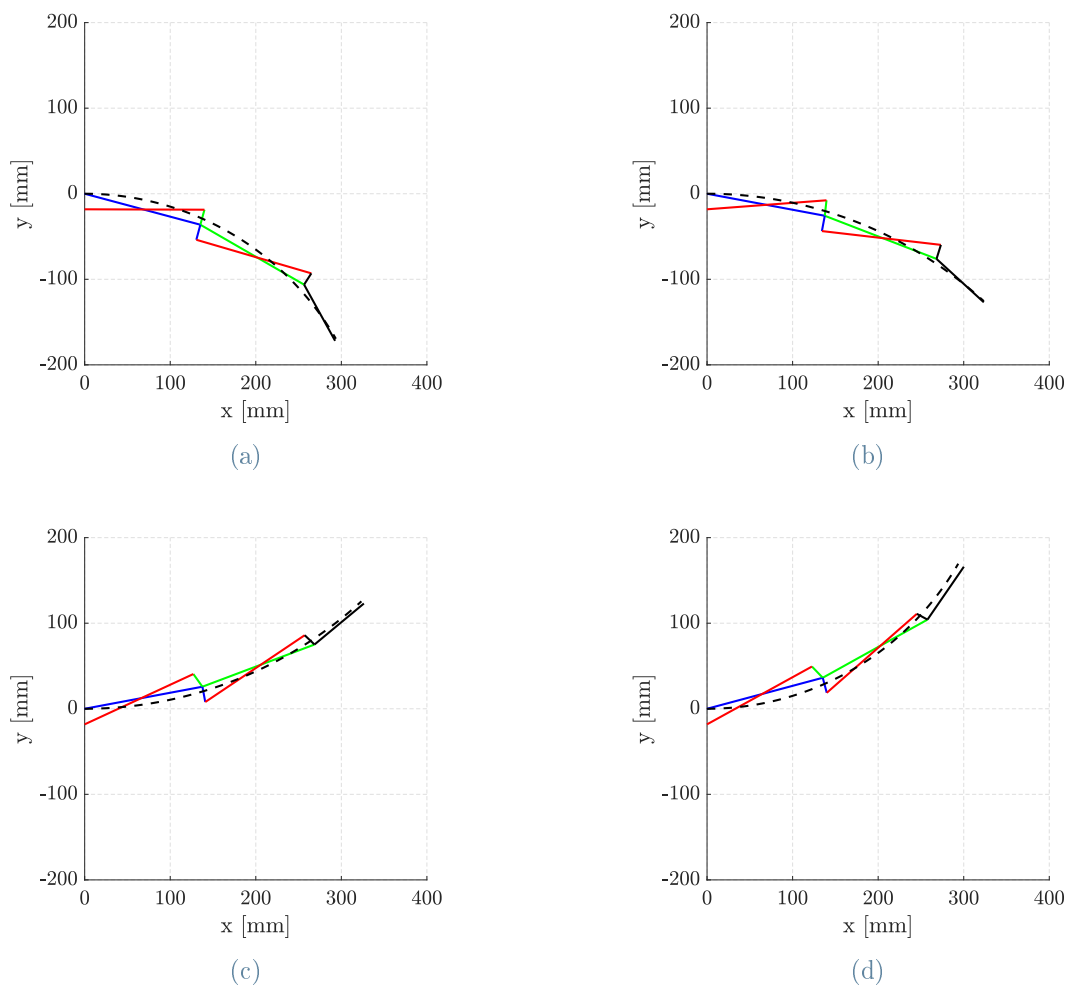
Figure 8.3: Result of the optimization of link lengths

Table 8.1: Link lengths resulting from optimization

Link	Length
a	140 mm
b	140 mm
c	18.2 mm
d	140 mm
f	70.5 mm
h	18.2 mm

When the mechanisms move with a great phase shift, the distance between corresponding points of different mechanisms increases, requiring that the external surface is stretchable

enough to allow such a large deformation. Although the material of which fins are made is highly flexible and able to bear such an elongation, this is still not desirable, as the elastic force would be an additional load for the motors reducing the torque available to move the surrounding water. Therefore, to limit this problem, the last link, c, shown in green, in the front and rear mechanisms, is connected by means of spherical bearings to a and b links so that an out-of-plane rotation is allowed and the tip of the front and the rear mechanisms can bend toward the center when a great phase shift makes the distance increase. Conversely, all the bearings of the central mechanisms are cylindrical.
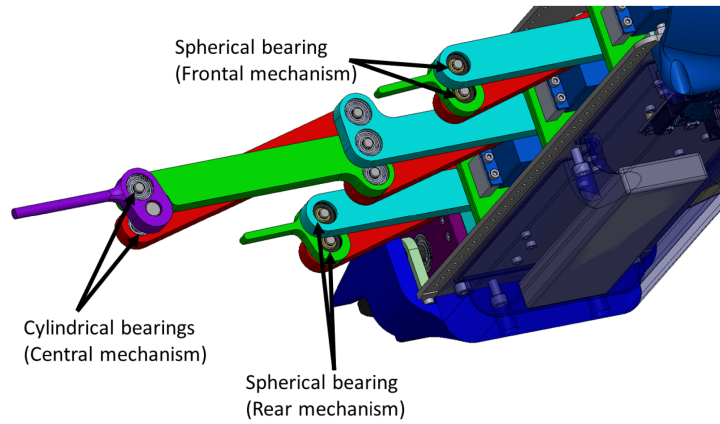
Figure 8.4: CAD model showing the different bearings according to the mechanism

It is of interest to quantify the transmission ratio of the overall mechanism. The transmission ratio is defined as the ratio between the displacement observed of the output, $\delta - \delta_0$ for the central mechanism or $\gamma - \gamma_0$ for the frontal and rear mechanism, over the input rotation α. The mechanism is thought with the idea of multiplying the angle given by the servomotor, and the higher the number of links in series, the higher this ratio. The central mechanism, thus, is expected to have a higher transmission ratio than the frontal and rear ones. Such configuration replicates well the deformation of the fin, which is featured by an increasing amplitude towards the tip. The transmission ratios of the mechanisms, defined in Equations 8.7 and 8.8, are shown in Figure 8.5, in the range of feasible angles α from $-15°$ to $15°$.

$$\tau_\gamma = \frac{\gamma - \gamma_0}{\alpha} \tag{8.7}$$

$$\tau_\delta = \frac{\delta - \delta_0}{\alpha} \tag{8.8}$$

(a) Front and rear mechanisms   (b) Central mechanism
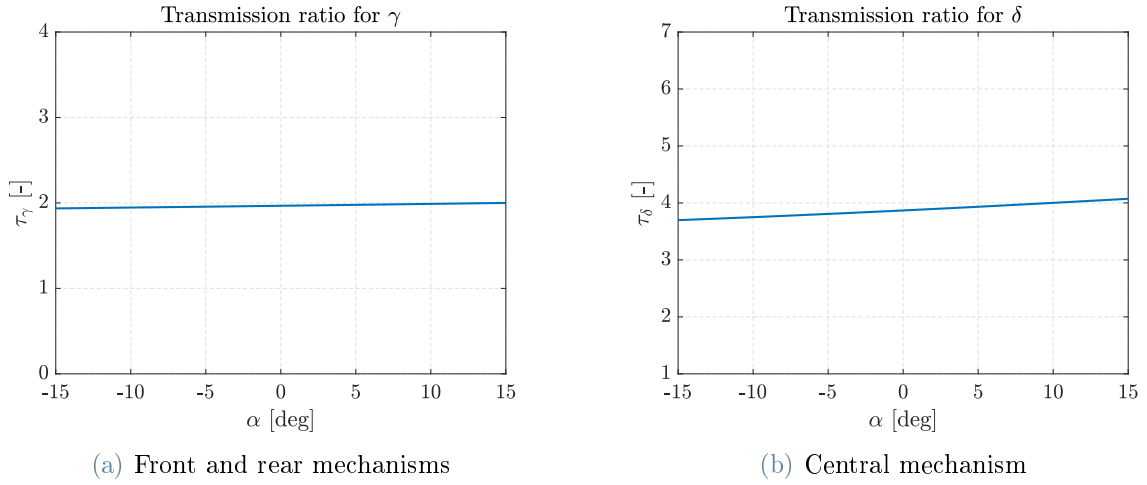
Figure 8.5: Transmission ratios of the mechanisms

In the end, it is interesting to check which is the highest force that the system can withstand in the worst possible case in order to correctly size motors. Since it would be unnecessarily complex to include the kinematics of the mechanism in the CFD analysis, as the worst possible case, it is considered the simplified scenario in which the central mechanism of the fin is loaded with a force concentrated at its tip and directed orthogonally to its orientation.

The ratio between this force and the motor torque is calculated with the principle of virtual work (PVW).

$$C \cdot \delta\alpha = \vec{F_\perp} \cdot \delta\vec{s_{tip}} \tag{8.9}$$

Since the force is perpendicular to the mechanism orientation, it is always oriented with an angle $\delta - \delta_0 + \frac{\pi}{2}$, the relation between the force and the motor torque is the following:

$$C = -|F| \sin{(\delta - \delta_0)} \delta x_{tip} + |F| \cos{(\delta - \delta_0)} \delta y_{tip} \tag{8.10}$$

In the CFD analysis and the experiments on the prototype of the robot, the maximum vertical force at the steady-state was about $10\,\mathrm{N}$. Since there are three mechanisms for each fin, but the central fin is more loaded than the other two, it is reasonable to consider that the load applied on the tip of the central mechanism is $5\,\mathrm{N}$. The torque required to balance this load for all feasible angular position is displayed in Figure 8.6.
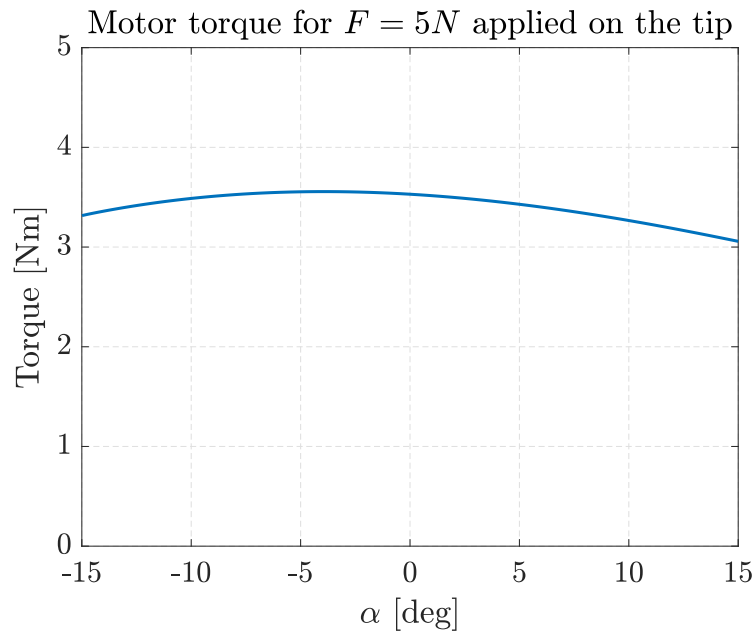
Figure 8.6: Motor torque for a force of 5 N at the fin tip

It is possible to observe that the ratio between force and torque remains almost constant in all the feasible range of the angle α and that the maximum required torque is $3.55\,\mathrm{N\,m}$. This is the worst possible configuration, as in general, there cannot be a concentrated force on the tip, but there is rather a distributed load along the whole mechanism. Therefore, it is expected to deal with lower torques in normal working conditions. This is just an approximation of the torque requirements of the motors needed to understand the order of magnitude of the required torque. More accurate sizing is performed with the multi-body analysis shown in the following sections of this chapter.

8.2. Tail

The tail of the robot acts as a rudder, and it has the function of correcting the pitch rotation during forward swimming and of improving the robot's maneuverability during floating and diving maneuvers. The tail shape and dimensions are the same as for the prototype, and the only difference is that its material is aluminum. The tail is composed of two rudders so that they can be moved independently and help stability during turning maneuvers, and the motors moving the tail are the same as those moving the mechanisms of the pectoral fins. The CAD model of the tail is shown in Figure 8.7.
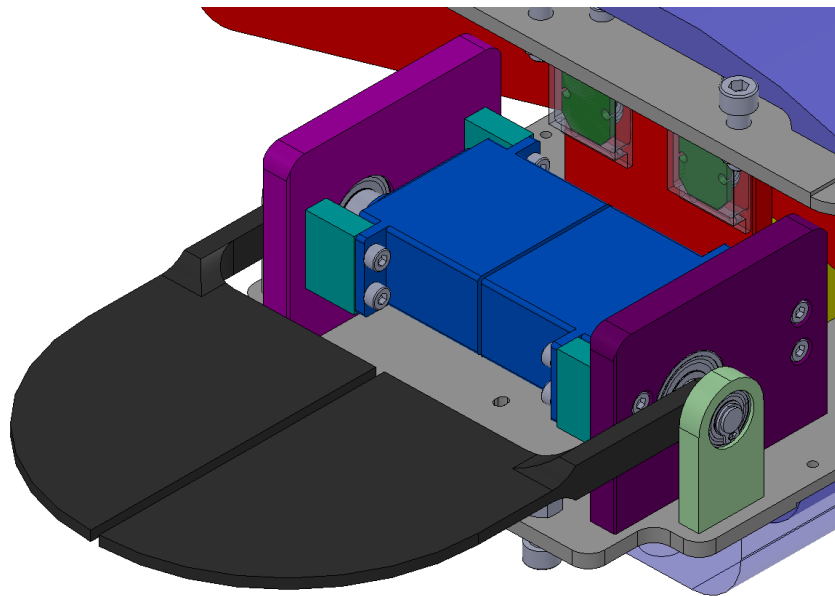
Figure 8.7: Tail of the robot

8.3. Robot assembly

Each mechanism requires three frames called anterior, central, and posterior. The anterior frame connects the motor with the first link of the mechanism; the central frame sustains both the first and the second link of the mechanism; finally, the posterior frame completes the support of the second mechanism and allows the positioning of the encoder for the control of the system.

This way, the motor's shaft is loaded only with its torque. Both mechanisms for left and right fins are mounted in a mirrored configuration on the same frame. In Figure 8.8, a section view of the mechanism block is shown. The frames and the links are connected through bearings, and, in order to avoid relative rotation between the shafts and the links, a room for a feather key, coupled with the respective hub in the link, has been designed on the shafts.
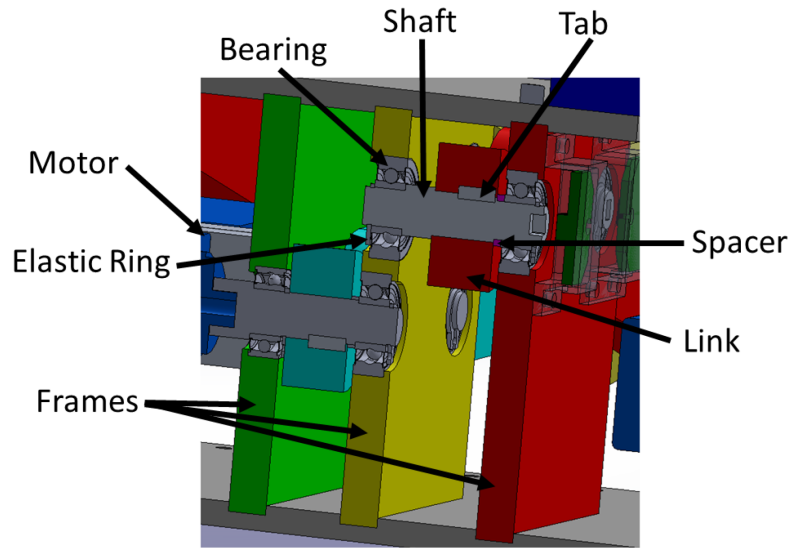
Figure 8.8: Section view of the mounting configuration of the links

The two shafts sustaining the links are different since one is connected to the motor, whereas the other must have a pocket for a magnet. The two shafts are presented in Figure 8.13.

(a) First link shaft
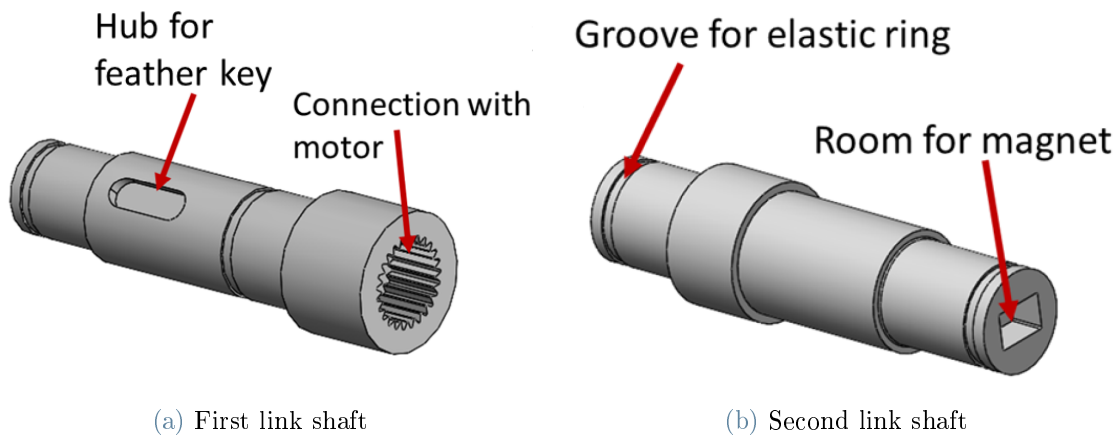
(b) Second link shaft

Figure 8.9: Shafts of each mechanism

Since there is no space to place an encoder in front of the shaft directly connected to the motor, the measured angle is not α, but β and the encoder is placed in front of the shaft connected to the second link. Nevertheless, since the kinematic relation between α and β is known, it is possible to calculate α from the measurement of β. Since the encoder is magnetic, a small magnet is placed inside a purposefully made pocket inside the shaft. The encoder mounting configuration is shown in Figure 8.10. Since the encoders are not

waterproof, they are placed inside a box filled with dielectric gel and sealed with silicone.
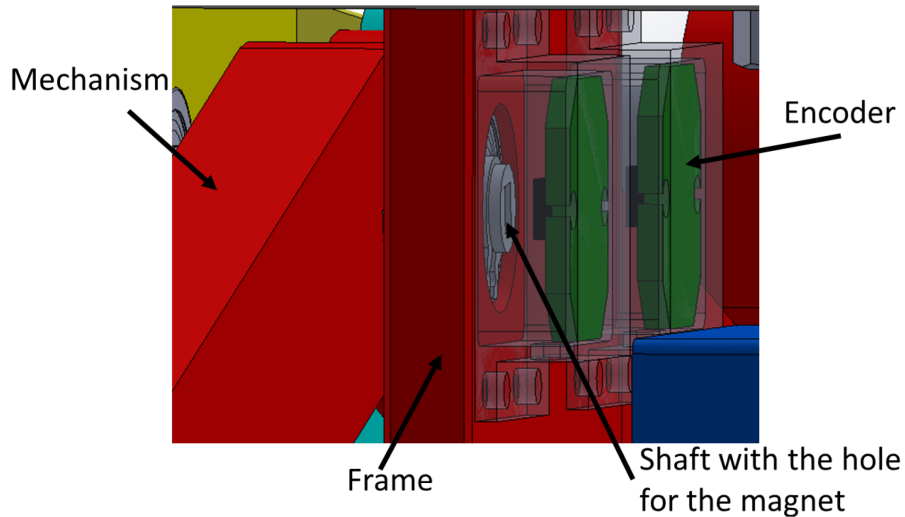
Figure 8.10: Magnetic encoders mounted on the frame

The three frames supporting the mechanisms are blocked between two aluminum bases. The bases are made so that frames can be inserted into small pockets of the same size as the frames, and they are mounted with screws. The two aluminum bases, shown in Figure 8.11, are equal, with the only difference being that they are flipped one with respect to the other.
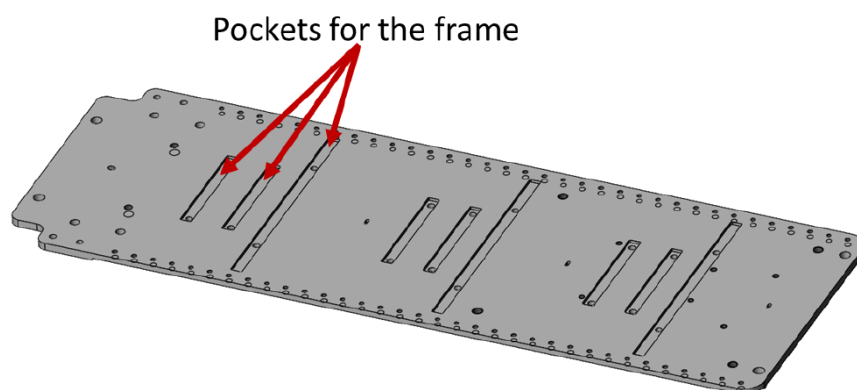
Figure 8.11: Aluminum base

The tail block, as visible in Figure 8.7 is featured by only two frames supporting just one shaft.

All the electronic components are placed in a box that uses the aluminum base of the robot as a lid, as shown in Figure 8.12. The first important requirement is, indeed, the impermeability both from the external environment and from the internal part of the robot, so that even in case of holes in the external coating of the fins, water never gets in contact either with the battery or with the electronics. Hence, a groove is present on the top surface of the box, as room for an elastomeric seal, and cable glands are present in the base to waterproof the holes for the passage of cables. In addition, every electronic component is contained in a 3D printed box filled with dielectric gel, and IP68 certified connectors are used to connect all the devices. Two holes are present on the side of the box: one is needed for the switch, and the other for a connector used to recharge the battery and reload the program into the board.
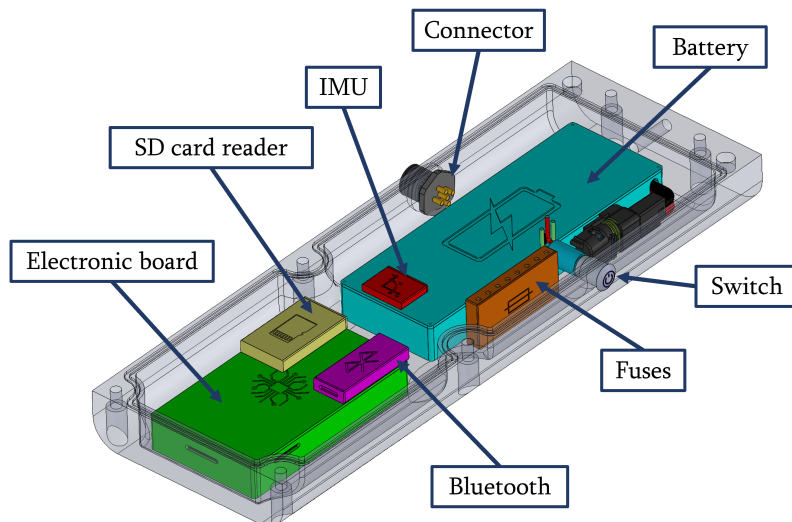
Figure 8.12: Box containing the battery and the electronic devices

In order to have a hydrodynamic profile, some 3D printed parts with the desired shape are placed on the top, in the front, and in the robot's back. The part on the top is just a rounded shell to avoid sharp angles between the fins and the aluminum base and to cover the heads of the screws which connect the frames to the base. Conversely, the parts in the front and the back not only improve the hydrodynamics of the body but also have other functions, since the part in the front, shown in Figure 8.13a, has a pocket to hold a video camera, and the part in the back, shown in Figure 8.13b, has some features tailored to mount the external surface covering the tail.

(a) Front   (b) Back
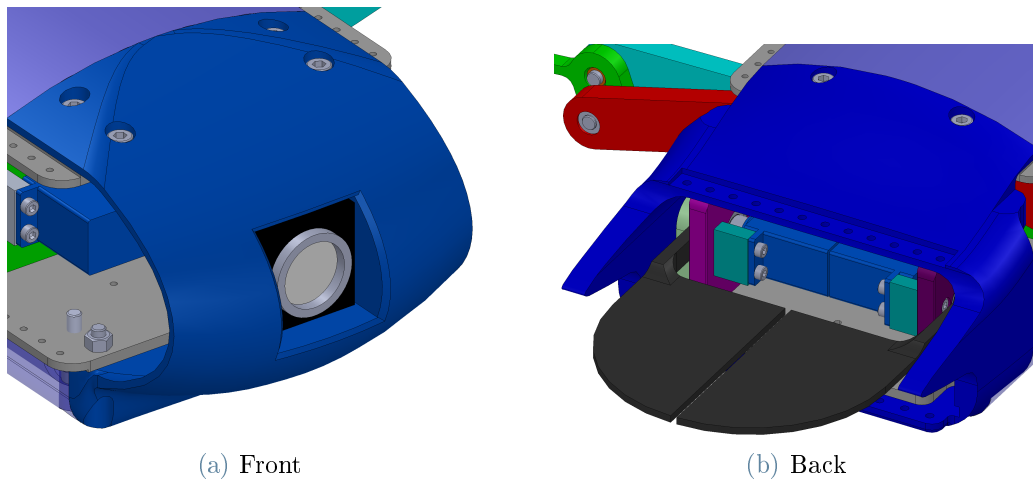
Figure 8.13: 3D printed parts in the front and in the back of the robot

8.4. Components

The electronic board of the robot is Arduino Due, which is featured by high computational power and a large number of input and output pins while remaining economical and simple to program. The electronic circuit of the robot includes:

- **8 servomotors**: three motors move each pectoral fin, and two are employed to move the tail;

- **6 encoders**: they measure the angular position of the fin mechanisms since it is fundamental to have reliable feedback in order to synchronize fin mechanisms and give them the correct phase shift;

- **Inertial Measurement Unit (IMU)**: it is composed of a 3-axes accelerometer and a 3-axes gyroscope needed to control the robot position and orientation while swimming;

- **Bluetooth module**: it is used to communicate wirelessly with the operator without removing sealing when the robot is outside of water;

- **SD card module**: it is needed to store navigation data since it is impossible to communicate wireless underwater;

- **Battery**.

In Figure 8.14, a scheme of the circuit is presented.
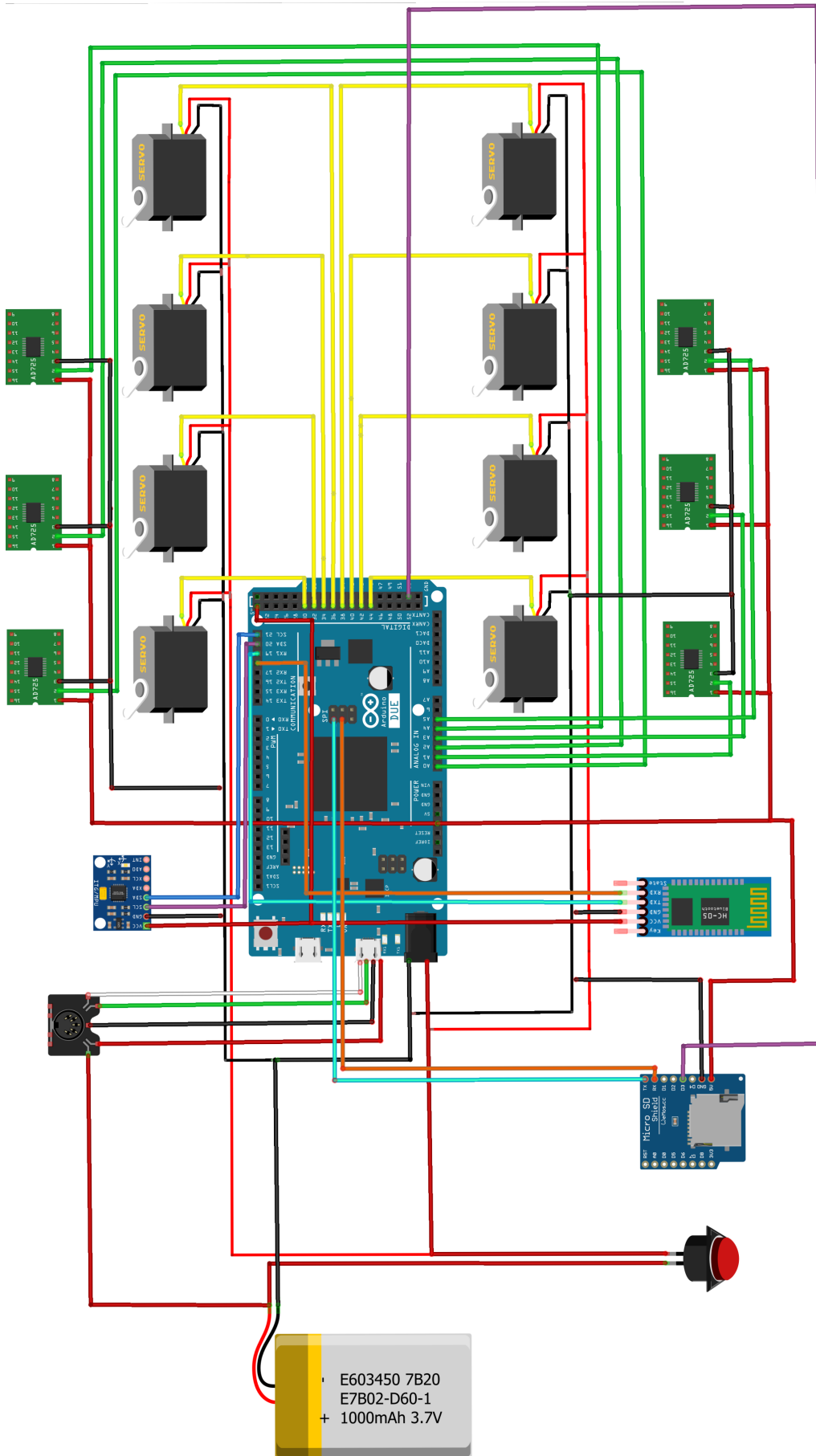
Figure 8.14: Scheme of the circuit of the robot

8.4.1. Motors

In order to enhance performances with respect to the prototype, more powerful motors have been selected. All the torque requirements are well below the motors' maximum available torque, which is 3.92 N m.

The new motors are PowerHD 40 waterproof, which are IP68 certified. Their characteristics are listed in Table 8.4.1.

Torque (7.4 V)	3.92	[Nm]
Voltage	6.0 - 8.4	[V]
Mass	82	[g]
Velocity	60	[rpm]
Dimensions	40.7 x 20.5 x 38.5	[mm]

Figure 8.15: PowerHD 40 waterproof servomotor

Table 8.2: Servomotor characteristics

Despite the internal part of the robot not being supposed to be in contact with water, the selected motors are waterproof with IP68 certification to avoid damaging them even if some water leaks through the sealings of the external surface, which might be possible, especially during the first test. These are brushless servomotors with steel and titanium gears that allow high torque. Their angular position is controlled using a PWM signal, and they do not provide any feedback signal; thus, it is necessary to measure with an encoder the angular position of the links to keep mechanisms synchronized.

8.4.2. Encoders

The selected encoders are the AS5600 magnetic encoders.

Type	Magnetic
Voltage	3.3 V
Resolution	12 bits (0.088°)
Signal	Analog
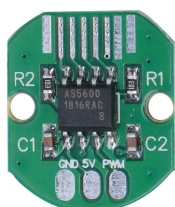
Figure 8.16: AS 5600 encoder

Table 8.3: Encoder characteristics

8.4.3. Battery

The chosen battery is the same as for the prototype, and its characteristics are reported in Table 8.4.3.

Figure 8.17: FullPower
2S battery

Type	LiPo
Voltage	7.4 V
Number of cells	2
Maximum current	260 A
Mass	265 g
Dimensions	163mm x 50mm x 16mm

Table 8.4: Battery characteristics

8.4.4. IMU

The IMU sensor is attached to the rigid central body of the robot, and it consists of a 3-axes accelerometer and a 3-axes gyroscope, whose measurements are useful to control the robot's position and orientation during swimming. This device, by the way, is also equipped with a thermometer that is not used for this application. It communicates with the electronic board using the I^2C standard and provides a 16-bit signal. The measurement range can be modified by changing the value in the corresponding register, and the resolution changes accordingly. In Table 8.4.4, the IMU characteristics refer to the selected measurement range
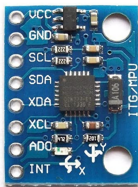
Figure 8.18: MPU 6050
IMU

Voltage	5 V
Accelerometer full scale	$\pm\,78.5\,\mathrm{m\,s^{-2}}$
Accelerometer resolution	$0.0024\,\mathrm{m\,s^{-2}}$
Gyroscope full scale	$\pm\,17.4\,\mathrm{rad\,s^{-1}}$
Gyroscope resolution	$5\times 10^{-4}\,\mathrm{rad\,s^{-1}}$
Communication protocol	I^2C
Mass	$20\,\mathrm{g}$

Table 8.5: IMU characteristics

8.4.5. Bluetooth module

Radio signals, including Bluetooth, do not propagate underwater, but it is still convenient to have the possibility to communicate wireless with the robot even though it can only be made when the robot is not swimming. The reason is that the connector used to communicate with the board is sealed with a lid and quite impractical to remove. Hence, the connector is used only to reload the program on the board, whereas the Bluetooth module can be used to modify some parameters of the motion law or communicate stored data. The selected Bluetooth module communicates via serial port, and its characteristics are listed in Table 8.4.5.
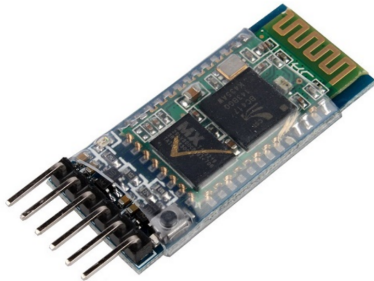
Figure 8.19: HC-05 Bluetooth module

Voltage	5 V
Maximum Baudrate	460800
Accelerometer resolution	$0.0024\,\mathrm{m\,s^{-2}}$
Data bit	8

Table 8.6: Bluetooth module characteristics

8.4.6. SD card reader module

Since it is impossible to communicate in real-time with the robot, especially during the first tests, it is necessary to store some navigation data such as the measurements of the accelerometer and the gyroscope to tune the control algorithm. However, it is impossible to store a large amount of data in the flash memory of the Arduino Due, a memory expansion is required, and this is done by connecting an SD card reader to the board, whose characteristics are listed in Table 8.4.6.
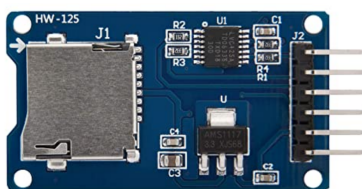
Figure 8.20: SD card reader module

Voltage	5 V
Maximum memory supported	16GB
Communication protocol	SPI

Table 8.7: SD card reader characteristics

8.5.   Fins

The fins are the most crucial part of the robot because they generate thrust with their movement and deformation. Therefore, it is fundamental to design fins that follow the movement imposed by the mechanisms generating a traveling wave on the fin without creating folds and losing hydrodynamic efficiency so that all the advantages of this locomotion principle are exploited. Another essential requirement of the fins is their impermeability because they represent the external surface of the robot, and they must waterproof the internal part. If the system is not completely sealed, the electronic devices could be irreversibly damaged, and the weight of the water inside the robot could unbalance it or even make it sink.

In this project, two different versions of the fins having the aforementioned characteristics have been developed, and they are described in the following subsections.

8.5.1.   Silicone sheet fins

In this fins version, silicone rubber sheets are the robot skin. This material is immensely elastic, allowing a maximum elongation of 600% before breaking. Its elastic behavior is not linear, and its Young modulus is between 0.2 and 4 MPa, whereas the Young modulus of the polyethylene sheets of the prototype is between 200 and 300 MPa.

Using sheets 0.2 mm thick, it is possible to attach them to the central body and the mechanisms keeping them stretched so that they are never loose and never create folds, but, thanks to the material elasticity, they do not generate undesired stresses on the mechanisms.

To always keep the sheets in the correct position, a flexible structure is created along the fin edges, represented in Figure 8.21, showing the complete assembly of the robot with fins made of silicone sheets.
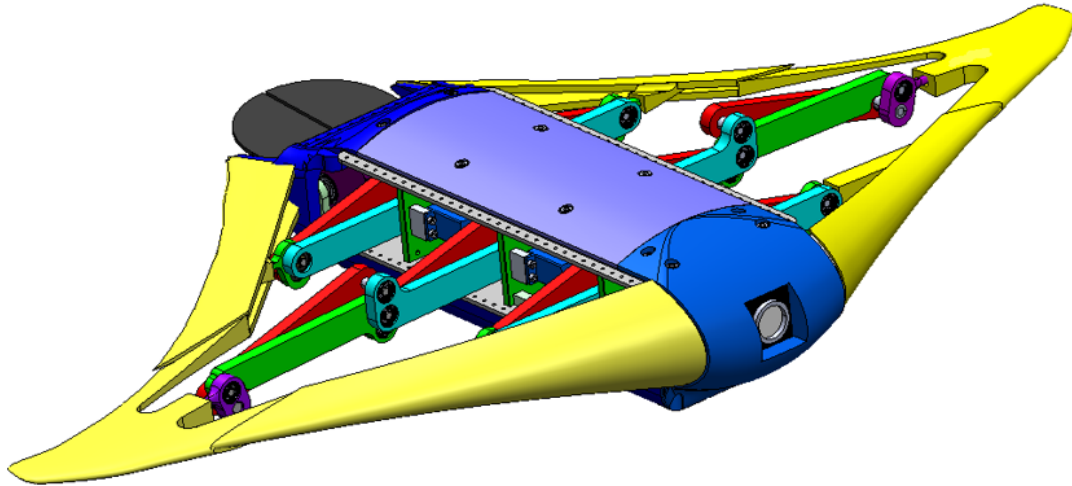
Figure 8.21: Robot with the support structure for the fins made of silicone sheet

Not to deplete the elastic properties of the fins, this structure must allow a high deformation, so it is made of TPU, which is a material suitable for 3D printing with mechanical characteristics similar to rubber since it is composed of a fraction of rubber and a fraction of polyurethane. The Young modulus of TPU is about $40\,\mathrm{MPa}$; thus, this structure would significantly increase the stiffness of the fin, especially against tension, while leaving its bending stiffness almost unchanged.

However, this problem can be worked around by designing a constraint that allows a certain amount of relative motion between this structure and the mechanisms. The structure and the silicone rubber sheets are glued to the central part of the robot, whereas the constraint between the structure and the mechanisms is a mechanical coupling. The last link of each mechanism is inserted in a pocket of the same shape present in the TPU structure, leaving a few centimeters of axial clearance so that, when there is a great phase shift between mechanisms, the structure needs to elongate of a small quantity. On the other side, the lateral clearance is just of few tenths of a millimeter so that the vertical displacement imposed by the mechanism is followed accurately. Moreover, the last link of the central mechanism has a circular cross-section so that the structure is also free to rotate around it to avoid stresses when the phase shift between mechanisms is significant, and the front and the rear mechanisms move in opposite directions.

8.5.2. Silicone rubber fins

An alternative to the fins made of silicone sheets is constituted by fins realized with silicone rubber. This material has suitable elastic properties since it has a very small Young modulus, a density similar to the water density, and it vulcanizes at room temperature so that it is effortless to produce customized complex parts with this material by molding. The elastic behavior of this material is strongly non-linear, showing a significant softening behavior for large elongations. The Young modulus for small stresses and strains can be calculated starting from the shore hardness using an empirical formula known as the Gent's equation [46]:

$$E = \frac{0.0981\,(56 + 7.62336S)}{0.137505\,(254 - 2.54S)} \tag{8.11}$$

where S is the shore hardness. Elastomers are usually characterized using this index instead of Young modulus E. The Young modulus is very difficult to estimate with accuracy because it depends on the value of the applied load and the type of applied load, showing different behaviors for monoaxial tension, planar tension, and shear.

Conversely, the shore hardness can be easily tested with a durometer measuring the penetration depth. The selected silicone rubber is featured by a shore hardness of 10, which is one of the lowest available for casting at room temperature. Its mechanical properties are summarized in Table 8.8.

Table 8.8: Mechanical characteristics of silicone rubber

Shore hardness	10 A
Young modulus	$0.44\,\mathrm{MPa}$
Density	$1210\,\mathrm{kg\,m^{-3}}$
Poisson's ratio	0.5
Tensile strength	$2.4\,\mathrm{MPa}$

By adopting such a soft material, it is possible to fill a lot of the empty space that is present with the silicone sheet fins, adding mass without increasing the stiffness too much. This is advantageous because it results in a more uniform mass distribution inside the robot, requiring fewer ballasts under the central body and leading to a more symmetrical load condition for the motors. The CAD model of the fin made of silicone rubber is shown in Figure 8.22.
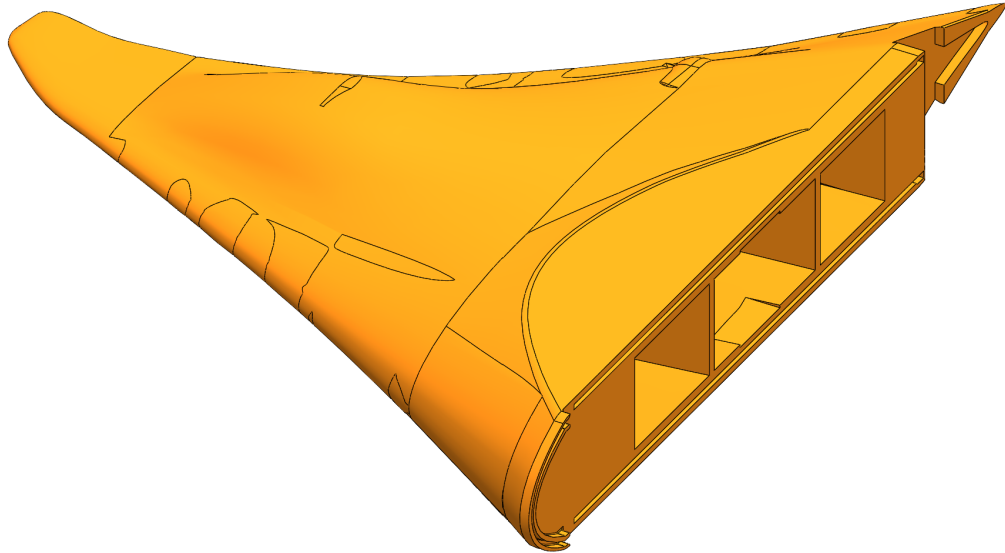
Figure 8.22: Fin made of silicone rubber

The edge of the fin is the same as the one obtained with the silicone sheets fin, but in the center of the body, a slight bulge is added to allow the central mechanism to have more space and avoid it touching the external surface while bending. This ensures a better and more reliable kinematics of the mechanisms, and it impacts very little on the hydrodynamics of the robot. What differs most from the fin made of silicone sheets is the internal part, as shown in Figure 8.23.
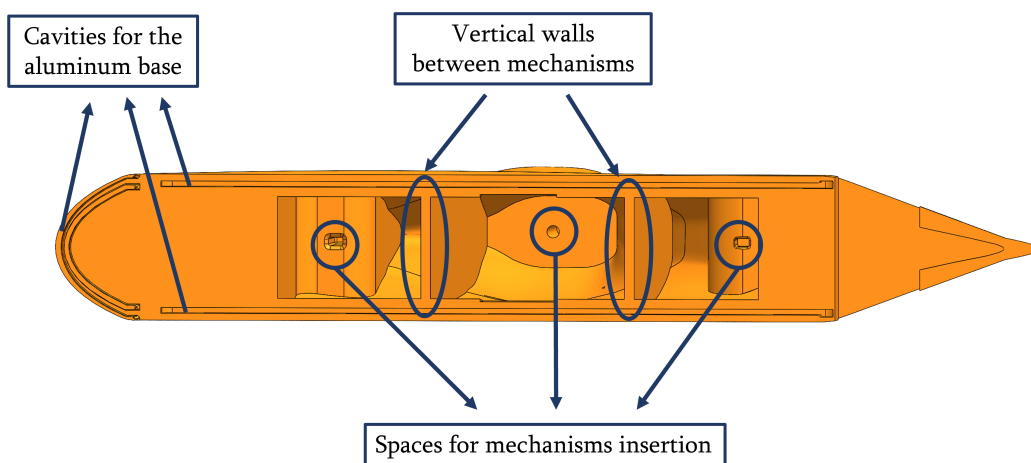
Figure 8.23: Features of the silicone rubber fin

Some empty space is present around mechanisms to allow them to move freely; in particular, the largest amount of empty space is left around the central mechanism because the central part of the fin is the one subject to the highest stretching, so the thickness of the surface is reduced to 2 mm to minimize the elastic forces. Conversely, the leading and the trailing edge are subject mainly to a bending load, to which silicone rubber opposes almost zero resistance as it can be bent and folded very easily. Therefore, it is possible to increase the thickness of the fin up to fill all the empty space wherever a stretching deformation is not required. Moreover, some vertical walls have been added between mechanisms to avoid a fin collapse under the pressure of the surrounding water. Together with the mechanisms inside, these walls are an obstacle to the shrinking of the fin and prevent the fin from changing its volume so that the air present inside cannot be displaced. Since these walls develop only laterally, they do not increase the longitudinal stiffness of the fin.

The holes in which mechanisms are inserted are the same as in the fin made of silicone sheets, having the same shape and axial clearance. In order to ensure better sealing and coupling with the aluminum bases and with the head of the robot, a small cavity is present on the internal surface of the fin.

As these fins are realized by molding, they have been designed considering that no undercut can be present.

The deformation of the fin has been simulated using a FEM analysis with the software Abaqus. The most challenging situation has been considered, corresponding to when the maximum stretching of the surface is required. This occurs when the mechanisms move with maximum amplitude and the phase difference among them is maximum too, which means that the front mechanism is pointing upwards, the rear mechanism is pointing downwards, and the central mechanism is in the middle. The model is non-linear as it considers both the non-linearity given by the geometry, as large deformations occur, and the non-linearity of the material since a Neo-Hookean elastic model has been adopted with coefficients automatically estimated by the software. Being the Poisson's ratio close to 0.5, the material is almost incompressible, so elements with hybrid formulation needed to be used. The fin is constrained with a clamping along the surface in contact with the central body, and the load is considered applied a displacement and rotation boundary condition on the surfaces in contact with the mechanisms. This is done by constraining these surfaces to some reference points, which are in turn linked to other reference points with rigid body constraints reproducing the kinematics of the mechanisms. This way, not only the fin movement is reproduced correctly, but also the effect of the elastic force of

the fin surface on the torque required to motors can be evaluated.

The results are shown in Figure 8.24.

(a) (b)
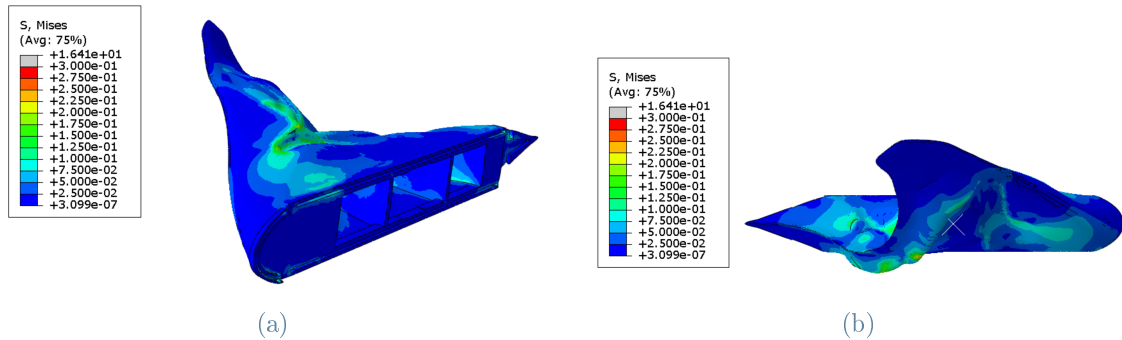
Figure 8.24: Fin deformation resulting from the FEM model

As it is possible to observe, the stresses are smaller than the limit of the material everywhere, and that the deformation of the fin is accomplished correctly, giving it the desired shape with the presence of a traveling wave. The motor torque needed to overcome the elastic force is $0.5\,\mathrm{N\,m}$ for the front motor, $0.15\,\mathrm{N\,m}$ for the central motor, and $0.3\,\mathrm{N\,m}$ for the rear motor.

The tail too is covered by a silicone rubber fin, shown in Figure 8.25.
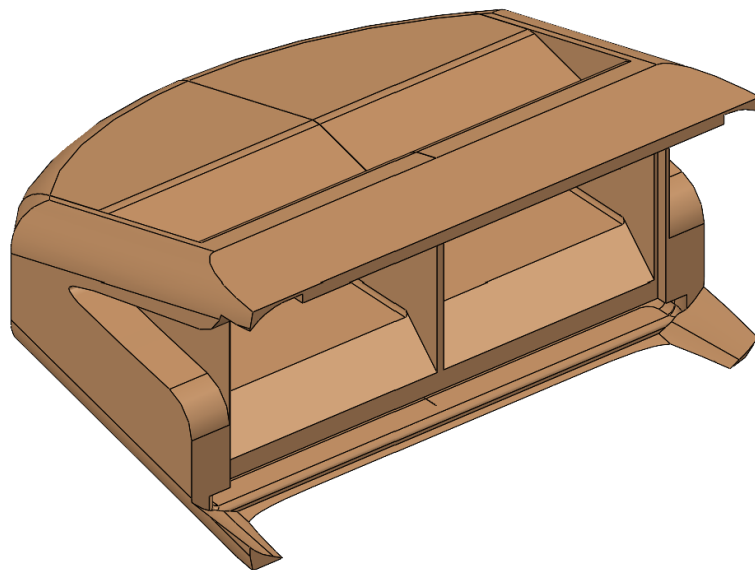
Figure 8.25: Silicone rubber fin covering the tail

Since the tail is composed of two parts that move independently, the silicone rubber fin covering it must be composed of two separate structures to avoid excessive deformation between the two parts of the tail. Hence, thin cuts are present in the middle and on the two sides. Since this structure is needed to waterproof the robot, these cuts cannot extend up to the internal surface of the tail fin, but they finish before. The tail fin is realized with casting too.

The robot with the silicone rubber fins is presented in Figure 8.26.
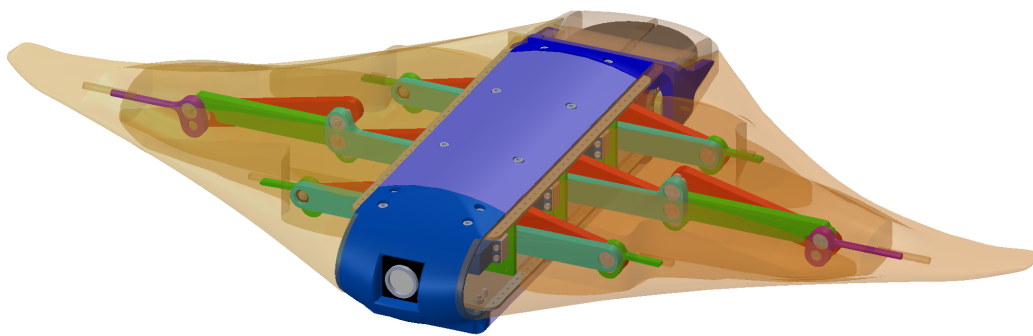
Figure 8.26: Bioinspired robot with silicone rubber fins

8.6.   Robot construction

The assembly of fin mechanisms is relatively straightforward, and the only complicated assembly sequence is the one concerning the mounting of the links with the shafts and the frames since parts are coupled with an interference fit and the mounting is irreversible. The first step is to couple the shafts with the motors, then bearings are inserted in the first frame, and the motor is screwed on the supports present on the frame.

A Seeger ring is placed on the groove of the shaft and, after having inserted the feather key on the hub, the first link is connected with the shaft. A spacer is then required to adjust the axial distance and avoid the out-of-plane motion of the link. The remaining part of the shaft is put on the second frame with another bearing, and it is closed with a Seeger ring.

Then, this link is connected with the third link of the mechanism thanks to a pin and a bearing, with a spacer in between. The second shaft is placed on the second frame, once again with the respective bearings and Seeger ring.

After positioning the feather key, it is possible to mount the second link, which, as the first one, is connected to the third link. After that, the spacer and the third frame with its bearings are placed. Finally, the magnet is placed on the shaft, and the encoder is screwed on the last frame.

In Figure 8.27, the result of this assembly procedure is shown.

(a)   (b)
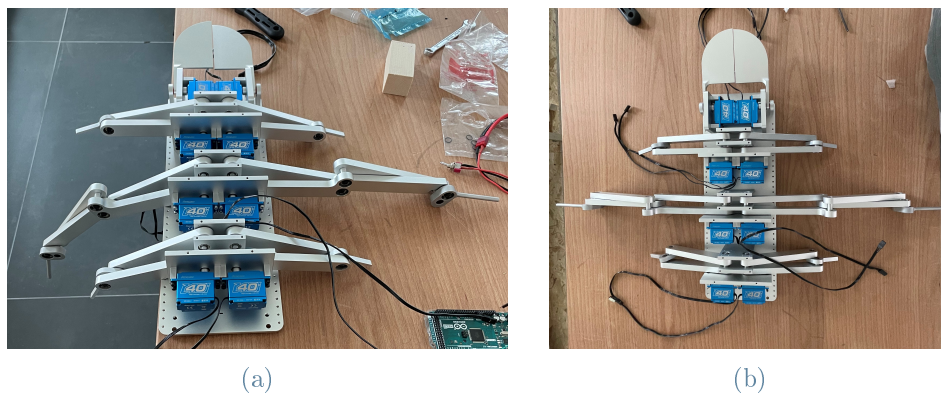
Figure 8.27: Assembly of the mechanisms of the robot

Then, the mechanism blocks are mounted on the lower and upper aluminum bases, and the parts composing the external profile are mounted together with the box containing the electronics, as shown in Figure 8.28.

Figure 8.28: Assembled robot without the fins

8.7.   Fins made of silicone rubber sheets

The external structure is made of three separate parts, due to the dimension limits of the 3D printer, that have been glued together before being mounted on the mechanisms, as shown in Figure 8.29.

Figure 8.29: Structure of the fin mounted on the mechanisms

Then, the silicone rubber sheets are glued on the structure and the rigid body of the robot,

covering the structure to make it waterproof. The final result of the robot assembly is presented in Figure 8.30.

Figure 8.30: Robot with the fins made of silicone rubber sheets

As it is possible to see, the surface of the fins remains stretched when the fins move, and it accurately follows the deformation imposed by the mechanisms. With these fins the overall mass of the robot is $5.5\,\text{kg}$, while its volume is $0.0104\,\text{m}^3$, so $4.5\,\text{kg}$ of ballast have been added. The fin has been tested, and it has been observed that it can allow an accurate replication of the traveling wave without generating high elastic forces; nevertheless, it is featured by three major limitations:

- the mass of the fin is too low. Although it is always possible to add ballasts under the central body of the robot to meet an overall neutral buoyancy, it is also essential that the mass is evenly distributed, and having lead ballasts in the center and empty air inside the fins is precisely the opposite. Such a mass distribution would be perfect for the robot's stability, but fins would receive a very high hydrostatic force directed upwards and would act as floaties for the robot. In such a way, the fin movement would require much torque to motors during the downstroke, and it would also be challenging to control the mechanisms and keep them synchronized.

- The air inside the fins is free to move. Since the external structure is highly flexible, the external pressure of water presses against the fin surface and tends to make it shrink till it adheres to the mechanism. However, this is not possible for both fins at the same time since air is present inside them. Hence, as one fin shrinks, the other one inflates like a balloon, totally changing the mass distribution inside the

robot and making it rotate about the roll axis.

- It is very difficult to waterproof. Since the structure at the edges is 3D printed layer-by-layer, it is not waterproof; thus, it must be covered with silicone sheets to protect it from water. In order to avoid folds, it is necessary to adapt them to the edge shape, which can be done only by cutting them into many smaller parts, which are then glued and sealed together. Nevertheless, the more the joints are, the more likely one of them breaks and allows leaking inside the robot.

8.8.   Fins made of silicone rubber

The silicone rubber fins are realized by molding, and the exploded view of the mold is presented in Figure 8.31.
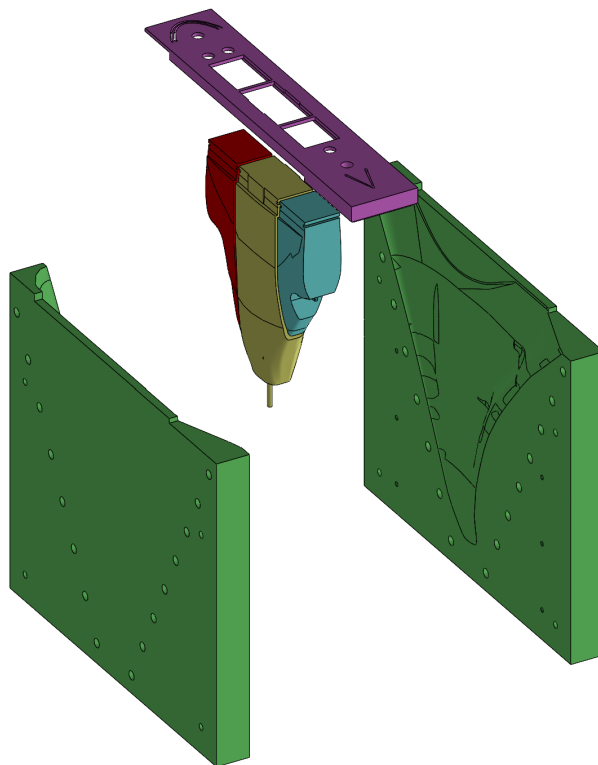
Figure 8.31: Exploded view of the molds for the fins

The mold comprises two symmetrical external parts, a cover, and three mold cores. The external parts have been realized with traditional machining with resin, whereas the cover and the mold cores have been 3D printed and chemically treated with acetone to smooth them and make them easier to extract.

In Figure 8.32 the two molds are displayed, and, in Figure 8.33 the cores are presented.
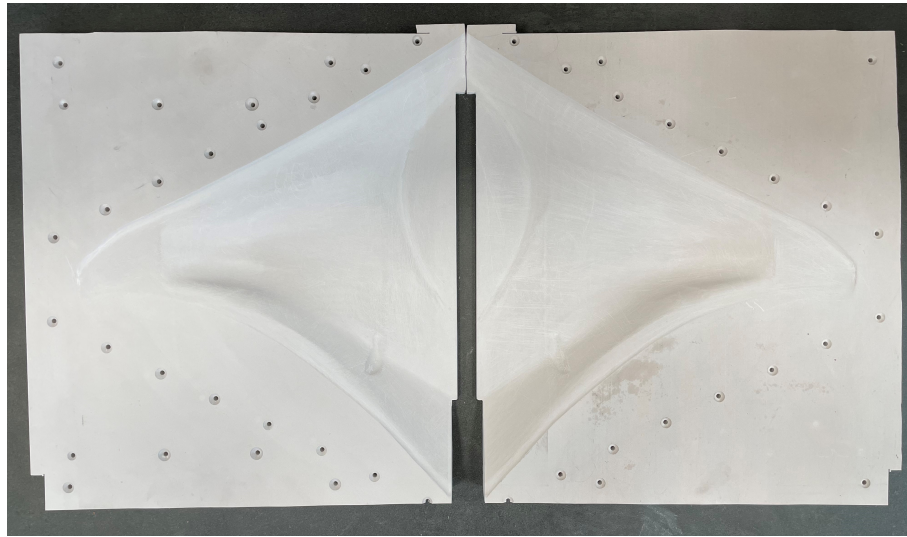
Figure 8.32: Mold for the fins
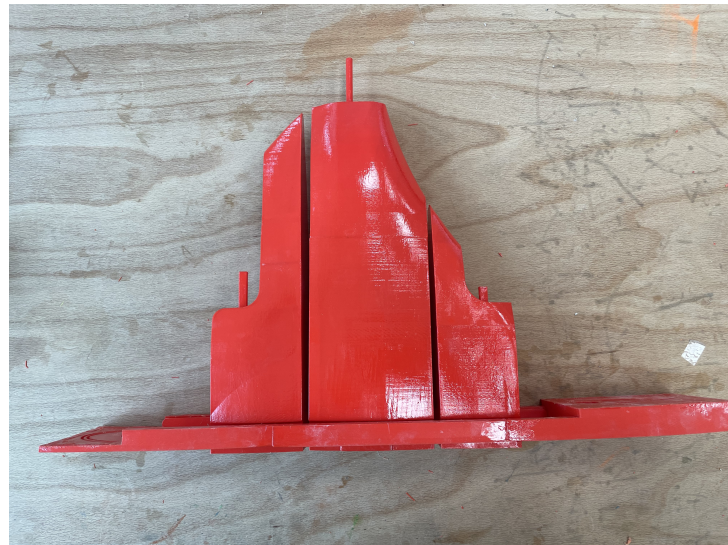
Figure 8.33: Cores of the mold

The liquid silicone rubber is mixed in proportion of 1:1 with a platinum-based catalyst and some colorant is added in the process. The obtained fin is shown in Figure 8.34.

Figure 8.34: Fin made of silicone rubber

The mold of the fin of the tail instead is composed of three parts, all 3D printed. It has been divided into three parts instead of two to have the possibility to extract the tail fin even in the presence of some undercuts that were unavoidable to meet the deformation requirements imposed by the tail mechanisms. In order to realize the cuts separating the two mechanisms, some thin papers are inserted into the mold.
An exploded view of the mold is shown in Figure 8.35.
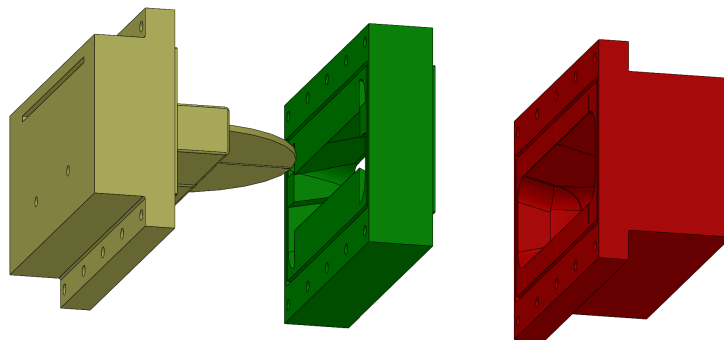
Figure 8.35: Mold of the tail fin

The fin of the tail is presented in Figure 8.36.

Figure 8.36: Fin of the tail

The fins are glued to the aluminum bases of the robot with silicone sealing the connection, and the final assembly of the robot is shown in Figure 8.37.

Figure 8.37: Final assembly of the robot

9 | Conclusion

THE research work presented in this thesis describes the study of an efficient locomotion strategy present in nature and its adaptation to a biomimetic robot. The research topic is the swimming locomotion of live beings, with an emphasis on energy efficiency. Biological motion techniques are efficient and allow moving in unstructured environments with great agility and maneuverability. Nature offers several examples of underwater locomotion strategies, from which inspiration can be taken to develop robots and vehicles. Bioinspired robots can move in uneven and dangerous environments not accessible neither to humans nor to traditional vehicles, so they find application, for example, in search and rescue operations, surveillance, or environmental monitoring.

After a thorough investigation of all the different swimming strategies present in nature, the locomotion principle adopted by batoid fishes, in particular by the cownose ray, has been identified as the most promising source of inspiration for autonomous underwater vehicles. The reasons why the characteristics of this species are suitable for bioinspired applications are its high energy efficiency, which allows a long endurance, and its extraordinary maneuverability. Hence, this swimming strategy represents a valid alternative to thrusters for propulsion generation in underwater vehicles, and this research aims to generate new knowledge about underwater locomotion using a bioinspired approach. This objective is pursued developing innovative models to describe and understand the fluid mechanics of swimming locomotion and recreating its locomotion strategy with a biomimetic robot.

The underlying physical principle is common to several fishes and cetaceans, and it consists of a traveling wave on the fin, which moves from the head to the tail and pushes backward the surrounding water so that the fish receives a forward thrust as a consequence of momentum conservation. In order to understand the reason for its energy efficiency, a model of the dynamics of the swimming locomotion of a cownose ray has been developed.

Firstly, a model of fin kinematics has been created based on the observation of the fin motion and the biological data found in the literature. This allows calculating the position and the velocity of each point of the fin, which are used as inputs for a CFD model. The numerical simulations concern a cownose ray in a forward swimming motion, the simplest and the most common gait among all the possible swimming modes. The deformation of the fin is prescribed, whereas the rigid motion in the swimming direction is calculated together with the surrounding fluid's pressure and velocity. The model uses an overset mesh consisting of two domains for the simulation, one fixed in the background and another surrounding the fish advancing with it and deforming with its fins.

These simulations have put in evidence that the vortices in the wake form a reverse Karman Street, consisting of vortices of alternate signs forming a propulsive jet in the center of the wake, and it is a direct consequence of a positive thrust acting on the fins. Moreover, the shape of the fin and the curvature created during its movement are optimized to reduce the losses due to the fin-tip vortex.

The swimming efficiency of a self-propelled body has been defined in a novel way, and it has been calculated for all the combinations of the kinematics parameters, relating it to the difference in vortex structures in the wake.

A robot prototype has been built, and tests in a water basin and a wind tunnel have been carried out. The experiments in the wind tunnel demonstrated that the generated thrust decreases as the relative velocity of the fluid increases. This is due to the increase of the drag force and the difference of velocity between the traveling wave and the forward velocity reduces.

The experiments in the water basin confirmed that the generated thrust varies periodically, with a double frequency with respect to the fin movement and that the relationship between frequency of fin movement and the generated thrust is quadratic, as expected from the numerical analysis.

The design of the final version of the biomimetic robot has been carried out, optimizing the kinematics of the mechanisms that move the fins to replicate at best their natural movement. The three mechanisms of each fin are crossed four-bar linkages in series, which accurately approximate the curvature of fin deformation.

Two different versions of the fins have been realized. In the first version, they are featured by a flexible contour, 3D printed using TPU, and a surface made of thin silicone rubber sheets; in the second version, the fins are entirely made of silicone rubber and manufactured by molding. While the former is much simpler to realize, the latter shows

better performances in many aspects since it makes the mass distribution of the robot more balanced and the waterproofing more effective.

The final version of the robot has been realized, and the control logic which keeps the two fins synchronized and the mechanisms in each fin with the correct phase shift has been tested with success.
A dynamic model of the robot during forward swimming and during turning and diving maneuvers has been implemented in Simulink, and it will be a starting point for the development of the complete control algorithm of the robot.

Some preliminary tests in water of the robot showed that the realized fins can effectively displace water and generate a force which moves the robot. As a future development the control algorithm of the robot will be designed and tested.

Bibliography

[1] J. Anderson, K. Streitlien, D. Barrett, and M. Triantafyllou. Oscillating foils of high propulsive efficiency. *Journal of fluid mechanics*, 360:41–72, 1998.

[2] AskNature. Biomimicry taxonomy, 2021. URL https://asknature.org/resource/biomimicry-taxonomy/.

[3] AskNature. Light-reflecting coating inspired by butterfly wings, 2021. URL https://asknature.org/innovation/light-reflecting-coating-inspired-by-butterfly-wings/#ray-of-hope-prize.

[4] K. Autumn, Y. Liang, S. Hsieh, W. Zesch, W. Chan, T. Kenny, R. Fearing, and R. Full. Adhesive force of a single gecko foot-hair. *Nature*, 405(6787):681–685, 2000.

[5] R. Bale, M. Hao, A. S. Bhalla, and N. Patankar. Energy efficiency and allometry of movement of swimming and flying animals. *PNAS*, 111(21):7517–7521, 2014.

[6] Y. Bar-Cohen. *Biomimetics: Biologically Inspired Technologies*. Taylor & Francis, 2005.

[7] Y. Bar-Cohen. *Biomimetics: Nature Based Innovation*. Taylor & Francis, 2011.

[8] Y. Bar-Cohen. Nature as a model for mimicking and inspiration for new technologies. *International Journal of Aeronautical & Space Science*, 13(1):1–13, 2012.

[9] D. N. Beal, F. Hover, M. S. Triantafyllou, J. Liao, and G. Lauder. Passive propulsion in vortex wakes. *Journal of Fluid Mechanics*, 549:385–402, 2006.

[10] S. Behbahani and X. Tan. Bio-inspired flexible joints with passive feathering for robotic fish pectoral fins. *Bioinspiration & Biomimetics*, 11:036009, 2016.

[11] G. Bledt, M. Powell, B. Katz, J. D. Carlo, P. Wensing, and S. Kim. Mit cheetah 3: Design and control of a robust, dynamic quadruped robot. In *2018 IEEE/RSJ International Conference on Intelligent Robots and Systems (IROS)*, 2018.

[12] R. Bogue. Underwater robots: a review of technologies and applications. *Industrial Robot: An International Journal*, 42(3):186–191, 2015.

[13] E. Bonabeau, M. Dorigo, and G. Theraulaz. Inspiration for optimization from social insect behavior. *Nature*, 406:39–42, 2000.

[14] I. Borazjani and M. Daghooghi. The fish tail motion forms an attached leading edge vortex. *Proceedings of the Royal Society B*, 280:20122071, 2012.

[15] R. Bottom, I. Borazjani, E. L. Blevins, and G. Lauder. Hydrodynamics of swimming in stingrays: numerical simulations and the role of the leading-edge vortex. *Journal of Fluid Mechanics*, 788:407–443, 2016.

[16] Y. Cai, S. Bi, and L. Zhang. Design and implication of a bionic pectoral fin imitating cow-nosed ray. In *The 2010 IEEE/RSJ International Conference on Intelligent Robots and Systems*, 2010.

[17] Y. Cai, S. Bi, and L. Zheng. Design and experiments of a robotic fish imitating cow-nosed ray. *Journal of Bionic Engineering*, 7:120–126, 2010.

[18] Y. Cai, S. Bi, and L. Zheng. Design optimization of a bionic fish with multi-joint fin rays. *Advanced Robotics*, 26:177–196, 2012.

[19] Y. Cai, S. Bi, G. Li, H. Hildre, and H. Zhang. From natural complexity to biomimetic simplification: Realization of bionic fish inspired by the cownose ray. *IEEE Robotics and automation magazine*, 99:1–13, 2018.

[20] Y. Cao, Y. Liu, Y. Chena, L. Zhua, Y. Yana, and X. Chen. A novel slithering locomotion mechanism for a snake-like soft robot. *Journal of the Mechanics and Physics of Solids*, 99:304–320, 2017.

[21] Z. Chen, T. Um, J. Zhu, and H. Bart-Smith. Bio-inspired robotic cownose ray propelled by electroactive polymer pectoral fin. In *Proceedings of the ASME 2011 International Mechanical Engineering Congress & Exposition*, 2011.

[22] C. Chew, Q. Lim, and K. Yeo. Development of propulsion mechanism for robot manta ray. In *Proceedings of the 2015 IEEE Conference on Robotics and Biomimetics*, 2015.

[23] W. Chi and K. Low. Review and fin structure desing for robotic manta ray (roman iv). *Journal of Robotics and Mechatronics*, 24(4):620–628, 2012.

[24] R. Clark and A. Smits. Thrust production and wake structure of a batoid-inspired oscillating fin. *Journal of Fluid Mechanics*, 562:415–429, 2006.

[25] A. Crespi and A. J. Ijspeert. Amphibot ii: An amphibious snake robot that crawls and swims using a central pattern generator. In *Proceedings of the 9th International Conference on Climbing and Walking Robots Brussels, Belgium*, 2006.

[26] A. Crespi, A. Badertscher, A. Guignard, and A. Ijspeert. Amphibot i: an amphibious snake-like robot. *Robotics and Autonomous Systems*, 50:163–175, 2005.

[27] O. Curet, N. Patankar, G. Lauder, and M. MacIver. Mechanical properties of a bio-inspired robotic knifefish with an undulatory propulsor. *Bioinspiration & Biomimetics*, 6:026004, 2011.

[28] A. Debray. Manipulators inspired by the tongue of the chameleon. *Bioinspiration & Biomimetics*, 6:026002, 2011.

[29] P. Dewey, A. Carriou, and A. Smits. On the relationship between efficiency and wake structure of a batoid-inspired oscillating fin. *Journal of Fluid Mechanics*, 691: 245–266, 2012.

[30] E. Drucker and G. Lauder. Locomotor forces on a swimming fish: three-dimensional vortex wake dynamics quantified using digital particle image velocimetry. *Journal of Experimental Biology*, 202:2393–2412, 1999.

[31] E. G. Drucker and G. V. Lauder. Locomotor function of the dorsal fin in teleost fishes: experimental analysis of wake forces in sunfish. *The Journal of Experimental Biology*, 204:2943–2958, 2001.

[32] O. Dumele, J. Chen, J. Passarelli, and S. Stupp. Supramolecular energy materials. *Advanced Materials*, 32:1907247, 2020.

[33] J. D. Eldredge and A. R. Jones. Leading-edge vortices: Mechanics and modeling. *Annual Review of Fluid Mechanics*, 51:75–104, 2019.

[34] C. Eloy. Optimal strouhal number for swimming animals. *Journal of Fluids and Structures*, 30:205–218, 2012.

[35] EvoLogics, S. . S. M. Tech, and F. H. Lubeck. Boss project. manta ray auv. Technical report, 2017.

[36] P. Fayemi, K. Wanieck, C. Zollfrank, N. Maranzana, and A. Aoussat. Biomimetics: process, tools and practice. *Bioinspiration & Biomimetics*, 12:011002, 2017.

[37] F. Fei, Z. Tu, J. Zhang, and X. Deng. Learning extreme hummingbird maneuvers on flapping wing robots. In *2019 International Conference on Robotics and Automation*, 2019.

[38] Festo. Aqua ray. Technical report, 2007.

[39] F. E. Fish, C. M. Schreiber, K. W. Moored, G. Liu, H. Dong, and H. Bart-Smith. Hydrodynamic performance of aquatic flapping: Efficiency of underwater flight in the manta. *Aerospace*, 3(20):3030020, 2016.

[40] S. Flamand, J. Saldien, P. Deconinck, F. Wyffels, S. Verstockt, and R. Terryn. Innovative design of a hexapod scorpion through digital production techniques. 2016.

[41] B. Flammang and M. Porter. Bioinspiration: Applying mechanical design to experimental biology. *Integrative and Comparative Biology*, 51(1):128–132, 2011.

[42] J. Gao, S. Bi, Y. Xu, and C. Liu. Development and design of a robotic manta ray featuring flexible pectoral fins. In *Proceedings of the 2007 IEEE International Conference on Robotics and Biomimetics*, 2007.

[43] Y. Gao, A. Ellery, M. Sweeting, and J. Vincent. Bioinspired drill for planetary sampling: Literature survey, conceptual design, and feasibility study. *Bioinspiration & Biomimetics*, 44(3):703–709, 2007.

[44] M. Gazzola, M. Argentina, and L. Mahadevan. Scaling macroscopic aquatic locomotion. *Nature Physics*, 10:758–761, 2014.

[45] B. J. Gemmell, K. D. Clos, S. Colin, K. Sutherland, and J. H. Costello. The most efficient metazoan swimmer creates a virtual wall to enhance performance. *The Royal Society Publishing Proceedings B*, 288:20202494, 2020.

[46] A. Gent. On the relation between indentation hardness and young modulus. *Institution of Rubber Industry - Transactions*, 34:46–57, 1958.

[47] M. Gordon, R. Blickhan, J. Dabiri, and J. Videler. *Animal locomotion: physical principles and adaptations*. CRC Press - Taylor & Francis Group, 2017.

[48] S. Gorumlu and B. Aksak. Sticking to rough surfaces using functionally graded bio-inspired microfibres. *Royal Society Open Science*, 4:161105, 2017.

[49] K. Hall, P. J. Hundt, J. D. Swenson, A. P. Summers, and K. D. Crow. The evolution of underwater flight: The redistribution of pectoral fin rays, in manta rays and their relatives (myliobatidae). *Journal of Morpholgy*, 279:1155–1170, 2018.

[50] P. Han, G. Lauder, and H. Dong. Hydrodynamics of median-fin interactions in fish-like locomotion: Effects of fin shape and movement. *Physics of Fluids*, 32:011902, 2020.

[51] J. He, Y. Cao, Q. Huang, Y. Cao, C. Tu, and G. Pan. A new type of bionic manta ray robot. In *Global Oceans 2020: Singapore U.S. Gulf Coast*, 2020.

[52] M. Helms, S. Vattam, and A. Goel. *Biologically inspired design: process and products.* Elsevier, 2009.

[53] S. Ho, H. Nassef, N. Pornsinsirirak, Y. Tai, and C. Ho. Unsteady aerodynamics and flow control for flapping wing flyers. *Progress in Aerospace Sciences*, 39:635–681, 2003.

[54] A. Hoover, B. Griffith, and L. Miller. Quantifying performance in the medusan mechanospace with an actively swimming three-dimensional jellyfish model. *Journal of Fluid Mechanics*, 813:1112–1155, 2017.

[55] J. Hopkins, B. W. Spranklin, and S. Gupta. A survey of snake-inspired robot designs. *Bioinspiration & Biomimetics*, 4:021001, 2009.

[56] D. Hu, J. Nirodya, T. Scotta, and M. J. Shelleya. The mechanics of slithering locomotion. *PNAS*, 106:10081–10085, 2009.

[57] H. Hu, J. Liu, I. Dukes, and G. Francis. Design of 3d swim patterns for autonomous robotic fish. In *Proceedings of the 2006 IEEE/RSJ International Conference on Intelligent Robots and Systems*, 2006.

[58] H. Huang, C. Sheng, J. Wu, G. Wu, C. Zhou, and H. Wang. Hydrodynamic analysis and motion simulation of fin and propeller driven manta ray robot. *Applied Ocean Research*, 108:102528, 2021.

[59] J. Hughes, U. Culha, F. Giardina, F. Guenther, A. Rosendo, and F. Iida. Soft manipulators and grippers: A review. *Frontiers in Robotics and AI*, 3, 2016.

[60] T. Ichikizaki and I. Yamamoto. Development of robotic fish with various swimming functions. In *2007 Symposium on Underwater Technology and Workshop on Scientific Use of Submarine Cables and Related Technologies*, 2007.

[61] A. J. Ijspeert, A. Crespi, D. Ryczko, and J. Cabelguen. From swimming to walking with a salamander robot driven by a spinal cord model. *Science*, 315:1416–1420, 2007.

[62] R. K. Katzschmann, J. DelPreto, R. MacCurdy, and D. Rus. Exploration of underwater life with an acoustically controlled soft robotic fish. *Science Robotics*, 3:3449, 2018.

[63] J. L. Kendall, K. S. Lucey, E. A. Jones, J. Wang, and D. J. Ellerby. Mechanical

and energetic factors underlying gait transitions in bluegill sunfish (lepomis macrochirus). *The Journal of Experimental Biology*, 210:4265–4271, 2007.

[64] G. O. Koca, D. Korkmaz, C. Bal, Z. H. Akpolat, and M. Ay. Implementations of the route planning scenarios for the autonomous robotic fish with the optimized propulsion mechanism. *Measurement*, 93:232–242, 2016.

[65] J. Koh and K. Cho. Omega-shaped inchworm-inspired crawling robot with large-index-and-pitch (lip) sma spring actuators. *IEEE/ASME Transactions on Mechatronics*, 18:419–429, 2013.

[66] A. Kozlov, H. Chowdhury, I. Mustary, B. Loganathan, and F. Alam. Bio-inspired design: aerodynamics of boxfish. In *6th BSME International Conference on Thermal Engineering (ICTE 2014)*, 2014.

[67] S. Kuindersma, R. Deits, M. Fallon, A. Valenzuela, H. Dai, F. Permenter, T. Koolen, P. Marion, and R. Tedrake. Optimization-based locomotion planning, estimation, and control design for the atlas humanoid robot. *Autonomous Robots*, 40:429–455, 2016.

[68] C. Laschi, M. Cianchetti, B. Mazzolai, L. Margheri, M. Follador, and P. Dario. Soft robot arm inspired by the octopus. *Advanced Robotics*, 26:709–727, 2012.

[69] E. Lauga and T. Powers. The hydrodynamics of swimming microorganisms. *Reports on Progress in Physics*, 72:096601, 2009.

[70] A. Li, K. Putra, L. Chen, J. Montgomery, and A. Shih. Mosquito proboscis inspired needle insertion to reduce tissue deformation and organ displacement. *Scientific Reports Nature Research*, 10:12248, 2020.

[71] J. Liao. A review of fish swimming mechanics and behaviour in altered flows. *Phylosophical Transaction of the Royal Society B*, 362:1973–1993, 2007.

[72] M. Lighthill. Hydromechanics of aquatic animal propulsion. *Annual Reviews on Fluid Mechanics*, 1:413–446, 1969.

[73] M. Lighthill. Note on the swimming of slender fish. *Journal of Fluid Mechanics*, 9: 305–317, 1969.

[74] P. Liljeback, K. Pettersen, O. Stavdahl, and J. T. Gravdahl. Snake robot locomotion in environments with obstacles. *IEEE Transactions on Mechatronics*, 20:1–12, 2011.

[75] P. Liljeback, O. Stavdahl, K. Y. Pettersen, and J. T. Gravdahl. Mamba - a

waterproof snake robot with tactile sensing. In *2014 IEEE/RSJ International Conference on Intelligent Robots and Systems (IROS 2014)*, 2014.

[76] G. Liu, H. Lin, H. Lin, S. Chen, and P. Lin. A bio-inspired hopping kangaroo robot with an active tail. *Journal of Bionic Engineering*, 11:541–555, 2014.

[77] G. Liu, Y. Ren, J. Zhu, H. Bart-Smith, and H. Dong. Thrust producing mechanisms in ray-inspired underwater vehicle propulsion. *Theoretical and Applied Mechanics Letters*, 5:54–57, 2015.

[78] X. Liu, T. Iwasaki, and F. Fish. Dynamic modeling and gait analysis of batoid swimming. In *2013 American Control Conference (ACC)*, 2013.

[79] K. H. Low, C. Zhou, G. Seet, S. Bi, and Y. Cai. Improvement and testing of a robotic manta ray (roman-iii). In *Proceedings of the 2011 IEEE International Conference on Robotics and Biomimetics*, 2011.

[80] H. Lu, K. Yeoy, and C. Chew. Effect of pectoral fin kinematics on manta ray propulsion. *Modern Physics Letters B*, 32(12):1840025, 2018.

[81] H. Ma, Y. Cai, Y. Wang, S. Bi, and Z. Gong. A biomimetic cownose ray robot fish with oscillating and chordwise twisting flexible pectoral fins. *Industrial Robot: An International Journal*, 42(3):214–221, 2015.

[82] J. T. Machado and M. Silva. An overview of legged robots. In *Proceedings of the International Symposium on Mathematical Methods in Engineering*, 2006.

[83] A. Maertens, M. Triantafyllou, and D. Yue. Efficiency of fish propulsion. *Bioinspiration & Biomimetics*, 10:046013, 2015.

[84] A. Mainong, A. Acob, and M. Archad. Investigating pectoral shapes and locomotive strategies for conceptual designing bio-inspired robotic fish. *Journal of Engineering Sicence and Technology*, 12(1):1–14, 2017.

[85] H. Marvi, C. Gong, N. Gravish, H. Astley, M. Travers, R. L. Hatton, J. Mendelson, H. Choset, D. Hu, and D. Goldman. Sidewinding with minimal slip: Snake and robot ascent of sandy slopes. *Science*, 346:224–228, 2014.

[86] Y. Meng, Z. Wu, H. Dong, J. Wang, and J. Yu. Toward a novel robotic manta with unique pectoral fins. *IEEE transactions on systems, man and cybernetics: systems*, 1:1–11, 2020.

[87] D. Miklosovic, M. Murray, L. Howle, and F. Fish. Leading-edge tubercles delay

stall on humpback whale (megaptera novaeangliae) flippers. *Physics of fluids*, 16 (39), 2004.

[88] K. Moored, P. Dewey, M. Leftwich, H. Bart-Smith, and A. Smits. Bioinspired propulsion mechanisms based on manta ray locomotion. *Marine Technology Society Journal*, 45(4):110–118, 2011.

[89] J. Najem, S. A. Sarles, B. Akle, and D. Leo. Biomimetic jellyfish-inspired underwater vehicle actuated by ionic polymer metal composite actuators. *Smart Materials and Structures*, 21:094026, 2012.

[90] C. Niu, L. Zhang, S. Bi, and Y. Cai. Development and depth control of a robotic fish mimicking cownose ray. In *Proceedings of the 2012 IEEE International Conference on Robotics and Biomimetics*, 2012.

[91] J. M. Parson, F. Fish, and A. Nicastro. Turning performance of batoids: Limitations of a rigid body. *Journal of Experimental Marine Biology and Ecology*, 402:12–18, 2011.

[92] M. Plotkin, I. Hod, A. Zaban, S. Boden, D. Bagnall, D. Galushko, and D. Bergman. Solar energy harvesting in the epicuticle of the oriental hornet (vespa orientalis). *The Science of Nature*, 97(12):1067–1076, 2010.

[93] T. Prescott, M. Pearson, B. Mitchinson, J. Charles, W. Sullivan, and A. Pipe. Whiskiing with robots. *IEEE Robotics & Automation Magazine*, 1070-9932:42–50, 2009.

[94] P. Ramdya, R. Thandiacka, R. Cherney, T. Asselborn, R. Benton, A. Ijspeert, and D. Floreano. Climbing favours the tripod gait over alternative faster insect gaits. *Nature Communications*, 8:14494, 2017.

[95] K. Ramesh, K. Granlund, M. Ol, A. Gopalarathnam, and J. Edwards. Leading-edge flow criticality as a governing factor in leading-edge vortex initiation in unsteady airfoil flows. *Theoretical and Computational Fluid Dynamics*, 32:109–136, 2018.

[96] T. Ranzani, G. Gerboni, M. Cianchetti, and A. Menciassi. A bioinspired soft manipulator for minimally invasive surgery. *Bioinspiration & Biomimetics*, 10: 035008, 2015.

[97] Z. Ren, W. Hu, X. Dong, and M. Sitti. Multi-functional soft-bodied jellyfish-like swimming. *Nature Communications*, 10:2703, 2019.

[98] L. Rosemberger. Pectoral fin locomotion in batoid fishes: undulation versus oscillation. *Journal of Experimental Biology*, 204:379–394, 2001.

[99] L. Rosemberger and M. W. Westneat. Functional morphology of undulatory pectoral fin locomotion in the stingray taeniura lymma (chondrichthyes: Dasyatidae). *Journal of Experimental Biology*, 202:3523–3539, 2009.

[100] M. Rubenstein, A. Cornejo, and R. Nagpal. Programmable self-assembly in a thousand-robot swarm. *Science*, 345(6198):795–799, 2014.

[101] R. Russo, S. Blemker, F. Fish, and H. Bart-Smith. Biomechanical model of batoid (skates and rays) pectoral fins predicts the influence of skeletal structure on fin kinematics: implications for bio-inspired design. *Bioinspiration & Biomimetics*, 10: 046002, 2015.

[102] M. Saadat, F. E. Fish, A. G. Domel, V. D. Santo, G. V. Lauder, and H. Haj-Hariri. On the rules for aquatic locomotion. *Physical review fluids*, 2:083102, 2017.

[103] A. Sadeghi, A. Mondini, and B. Mazzolai. Toward self-growing soft robots inspired by plant roots and based on additive manufacturing technologies. *Soft Robotics*, 4 (3):211–223, 2017.

[104] P. Saffman and J. Schatzmann. An inviscid model for the vortex-street wake. *Journal of fluid mechanics*, 122:467–486, 1982.

[105] R. Salazar, V. Fuentes, and A. Abdelkefi. Classification of biological and bioinspired aquatic systems: A review. *Ocean Engineering*, 148:75–114, 2018.

[106] S. Sane. Bioinspiration and biomimicry: What can engineers learn from biologists? *Journal of Applied Science and Engineering*, 19(1):1–6, 2016.

[107] V. D. Santo and C. P. Kenaley. Skating by: low energetic costs of swimming in a batoid fish. *Journal of Experimental Biology*, 219:1804–1807, 2016.

[108] J. Schaefer and A. Summers. Batoid wing skeletal structure: Novel morphologies, mechanical implications, and phylogenetic patterns. *Journal of Morphology*, 264: 298–313, 2005.

[109] T. Schnipper, A. Andersen, and T. Bohr. Vortex wakes of a flapping foil. *Journal of Fluid Mechanics*, 633:411–423, 2009.

[110] S. Seok, C. Onal, K. Cho, R. Wood, D. Rus, and S. Kim. Meshworm: A peristaltic soft robot with antagonistic nickel titanium coil actuators. *IEEE/ASME Transactions on Mechatronics*, 18:1485–1497, 2013.

[111] M. Sfakiotakis, D. Lane, and J. Davies. Review of fish swimming modes for aquatic locomotion. *IEEE Journal of Oceanic Engineering*, 24(2):237–252, 1999.

[112] N. Sharp, V. Hagen-Gates, E. Hemingway, M. Syme, J. Via, J. Feaster, J. Bayandor, S. Jung, F. Battaglia, and A. Kurdila. Computational analysis of undulatory batoid motion for underwater robotic propulsion. In *Proceedings of the ASME 2014 4th Joint US-European Fluids Engineering Division Summer Meeting*, 2014.

[113] G. Shi, Q. Xiao, Q. Zhu, and W. Liao. Fluid-structure interaction modeling on a 3d ray-strengthened caudal fin. *Bioinspiration & Biomimetics*, 14:036012, 2019.

[114] L. Shu, K. Ueda, I. Chiu, and H. Cheong. Biologically inspired design. *CIRP Annals - Manufacturing Technology*, 60:673–693, 2011.

[115] P. Sitorus, Y. Nazaruddin, E. Leksono, and A. Budiyono. Design and implementation of paired pectoral fins locomotion of labriform fish applied to a fish robot. *Journal of Bionic Engineering*, 6:37–45, 2009.

[116] J. Sparemberg. Survey of the mathematical theory of fish locomotion. *Journal of Engineering Mathematics*, 44:395–448, 2002.

[117] W. Stoll and H. Frontzek. *BionicOpter*. Festo AG & co., 2013.

[118] W. Stoll and D. Mankau. *Bionic Motion Robot*. Festo AG & co., 2017.

[119] W. Stoll, H. Frontzek, and E. Knubben. *Bionic Kangaroo*. Festo AG & co., 2014.

[120] W. Stoll, H. Frontzek, and E. Knubben. *Flex Shape Gripper*. Festo AG & co., 2015.

[121] W. Stoll, K. V. Hafen, and E. Knubben. *Bionic Swift*. Festo AG & co., 2021.

[122] J. C. Sullivan, B. Mitchinson, M. J. Pearson, M. Evans, N. F. Lepora, C. W. Fox, C. Melhuish, and T. Prescott. Tactile discrimination using active whisker sensors. *IEEE Sensors Journal*, 12(2):350–362, 2012.

[123] G. Taylor. Simple scaling law predicts peak efficiency in oscillatory propulsion. *PNAS*, 115(32):8063–8065, 2018.

[124] G. K. Taylor, R. Nudds, and A. Thomas. Flying and swimming animals cruise at a strouhal number tuned for high power efficiency. *Letters to nature*, 425:707–710, 2003.

[125] N. Thekkethil, A. Sharma, and A. Agrawal. Three-dimensional biological hydrodynamics study on various types of batoid fishlike locomotion. *Physical Review Fluids*, 5:023101, 2020.

[126] G. Triantafyllou, M. S. Triantafyllou, and M. Grosenbaugh. Optimal thrust development in oscillating foils with application to fish propulsion. *Journal of fluids and structures*, 7:205–224, 1993.

[127] M. Triantafyllou, G. S. Triantafyllou, and R. Gopalkrishnan. Wake mechanics for thrust generation in oscillating foils. *Physics of fluids A*, 3:2835–2837, 1991.

[128] A. Vargas, R. Mittal, and H. Dong. A computational study of the aerodynamic performance of a dragonfly wing section in gliding flight. *Bioinspiration & Biomimetics*, 3:026004, 2008.

[129] B. Vehkam and M. Sitti. Design methodology for biomimetic propulsion of miniature swimming robots. *Journal of Dynamic Systems, Measurement and Control*, 128:36–43, 2006.

[130] A. Vidyasagar, J. Zufferey, D. Floreano, and M. Kovac. Performance analysis of jump-gliding locomotion for miniature robotics. *Bioinspiration & Biomimetics*, 10: 025006, 2015.

[131] A. Villanueva, C. Smith, and S. Priya. A biomimetic robotic jellyfish (robojelly) actuated by shape memory alloy composite actuators. *Bioinspiration & Biomimetics*, 6:036004, 2011.

[132] P. Vukusic, J. R. Sambles, C. R. Lawrence, and R. J. Wootton. Quantified interference and diffraction in single morpho butterfly scales. *Proceedings of the Royal Society B: Biological Sciences*, 266, 1999.

[133] P. Webb. Simple physical principles and vertebrate aquatic locomotion. *American Zoology*, 28:709–725, 1988.

[134] C. Wei-shan, W. Zhi-Jun, L. Jun-Kao, S. Sheng-Jun, and Z. Yang. Numerical simulation of batoid locomotion. *Journal of Hydrodynamics*, 23(5):594–600, 2011.

[135] A. Winter, R. Deits, D. Dorsch, A. Slocum, and A. Hosoi. Razor clam to roboclam: burrowing drag reduction mechanisms and their robotic adaptation. *Bioinspiration & Biomimetics*, 9:036009, 2014.

[136] J. Wu. Theory for aerodynamic force and moment in viscous flows. *AIAA Journal*, 19(4):432–441, 1981.

[137] T. Wu. Swimming of a waving plate. *Journal of Fluid Mechanics*, 10:321–344, 1960.

[138] T. Wu. Hydromechanics of swimming of fishes and cetaceans. *Advances in Applied Mechanics*, 11:1–63, 1971.

[139] T. Wu.   Hydromechanics of swimming propulsion. part 1. swimming of a two-dimensional flexible plate at variable forward speeds in an inviscid fluid. *Journal of Fluid Mechanics*, 46:337–355, 1971.

[140] T. Wu. Hydromechanics of swimming propulsion. part 3. swimming and optimum movements of slender fish with side fins. *Journal of fluid mechanics*, 46:545–568, 1971.

[141] T. Wu, C. Brochaw, and C. Brennen. *Swimming and Flying in Nature - Volume 2.* Springer Science+Business Media, 1975.

[142] H. Xie, H. Zhou, L. Shen, and D. Yin.   Mechanism design, dynamics modelling and experiments of bionic undulating fins. *International Journal of Robotics and Automation*, 31(2):146–155, 2016.

[143] S. Yoon and S. Park.   A mechanical analysis of woodpecker drumming and its application to shock-absorbing systems. *Bioinspiration & Biomimetics*, 6:016003, 2011.

[144] J. Yu, Z. Su, Z. Wu, and M. Tan. Development of a fast-swimming dolphin robot capable of leaping. *IEEE/ASME transactions on mechatronics*, 21(5):2307–2316, 2016.

[145] J. Zhan, Y. Gong, and T. Li. Effect of angles of attack on the hydrodynamic forces of manta ray. In *Proceedings of the Eleventh (2014) Pacific/Asia Offshore Mechanics Symposium*, 2014.

[146] Y. Zhang, S. Wang, X. Wang, and Y. Geng. Design and control of bionic manta ray robot with flexible pectoral fin. In *2018 IEEE 14th International Conference on Control and Automation (ICCA)*, 2018.

List of Figures

List of Tables